CPPM-T-2017-10

AIX-MARSEILLE UNIVERSITÉ

Faculté des Sciences – Département de Physique

Centre de Physique des Particules de Marseille

Thèse présentée pour obtenir le grade universitaire de docteur

Discipline : Physique et Sciences de la Matière
Spécialité: Physique des Particules et Astrophysique

Venugopal ELLAJOSYULA

Search for a doubly charged Higgs boson decaying to same-sign W bosons in a triplet-doublet extension of the Standard Model with the ATLAS detector at the LHC

Soutenue le 18 Décembre 2017 devant le jury composé de:

Dr. Jean-Baptiste DE VIVIE DE RÉGIE	LAL/CNRS	Rapporteur
Dr. Cristinel DIACONU	CPPM/CNRS	Directeur de thèse
Dr. Sabine KRAML	LPSC/CNRS	Examinateur
Dr. Gilbert MOULTAKA	CNRS	Invité
Dr. Emmanuel PEREZ	CERN Geneva	Rapporteur
Prof. Mossadek TALBY	AMU/CPPM	Examinateur

Acknowledgments

Through my three years a CPPM, until the very end, there have been many who have supported me and pushed me. I would like to acknowledge them here.

My supervisor, Cristinel Diaconu, has been a constant presence. He was one of the most hardworking people at CPPM and cares about the academic success of his students. He made sure that my work was of good quality and was always there to guide me when I lost direction in research. He attended all my talks and was there to support me when needed. My understanding of statistics has improved significantly because of him, and so have my problem solving skills. For this, and much more, I'm forever grateful to him.

My unofficial co-supervisor, Gilbert Moultaka, helped me with the theoretical and phenomenological work. He had the patience to help answer all of my stupid questions in order to understand our model. His rigor in work is something I hope to carry along wherever I go next. Thanks to him, I'm much more capable of independently working across the theory-experiment border. He has supported me emotionally throughout my PhD. I'm very glad he was around when needed.

I would like to take this opportunity to thank the members of my jury as well. Emmanuel, one of the two referees, had very insightful questions and comments during the review. Thanks to him, even in the final minutes of my PhD, I was able to learn. Sabine, the only external theorist on the jury, posed questions which would certainly help me in the on-going work. She was very nice during our short interaction. Mossadek, the president of the jury and also the former director of the doctoral school of physics and material sciences, has known me since the start of my time at CPPM. At the lab, it was always nice to see him since he was always so positive, polite, and greeted us all with a warm smile. My second referee, Jean-Baptiste, was also the convener of the group I worked in within ATLAS. During my work in ATLAS, he was by far the best convener I have seen. His emphasis on the quality and rigor of work was refreshing and inspiring. As a referee and a convener, he is very helpful to all those he works with.

My colleagues and friends at CPPM have also been there for me all the way. We had a lot of interesting discussions, and a lot of fun evenings together. Thank you Thomas, Kazuya, Asma, Sebastien, Yulia, Michael, Robert, Romain, Liam, Joan,and Ana. Kazuya, my first friend at CPPM, has been a mentor and a friend in times of need. Whenever I was stuck with some problem in physics, he'd give me hints to solve the problem instead of feeding me with the solutions. For this, I'm very grateful. This approach has helped me improve my skills in programming by leaps and bounds. Outside of physics, he was always there for me. When I was ill, or upset or happy, I could always share my thoughts with him. I was really touched to see that he drove for seven hours just to be at my defence.

Romain started working as a post-doc with me when he first joined. Over time, we've become very good friends. He introduced me to the French way of living, took the time to tell me about their culture, and invited me to so many of trips that became legendary for one reason or another. We have had interesting conversations about everything under the sun, from physics to capitalism to Bollywood. My perspectives on subjects outside of physics have become so much more refined because of him. I am forever grateful to that. The structure of his doctoral work was similar to mine. So he was aware of the problems I had encountered and was about to encounter. He always spared time to actively help me out with the issues I faced during the last year of my PhD.

Liam and Joan, a year junior to me, have made sure my life outside of work and during coffee breaks never got boring. We have spent the best of times together. Yulia and Robert are two friends I'm less similar to than anyone else. Nevertheless, all our interactions have been enjoyable and a learning experience.

That brings me to my climbing group, a family away from home. Andrey, Vlad, Clara, and Cedric. I started climbing with them during the last few months of my PhD. It started as a way to reduce some stress. Somewhere along the way, I found myself going camping with them to climb and realized that I had found a new passion in life. We've had adventures like no other and shared a lot our precious times with each other. They helped me become stronger mentally and physically. They taught me what it means to get over fear and grow. My few months with them made me realize the importance of a balance between work and life. I'm in their debt for all of this.

A few people have been there for me in spirit but not physically. My friends in the USA- Ankur, Priyam, Ashok, and Kiran. They are all such lovely people. It was always a refreshing change to meet them in person. Thanks for all the great times. They have definitely help me work harder and more diligently during my PhD.

A handful of people have supported me much longer than those I've mentioned above. My family, the only constant in my life. My parents have made sure that they did everything in their power so that I could follow my goals in life. They've been infinitly patient with me and have sacrificed a lot for me. My brother, who hasn't failed to be there when I needed him. I owe him everything for who I am and will ever be. Thank you, Srikar!

Contents

Introduction

The Standard Model of physics describes all known elementary particles and their interactions. It also provides a mechanism to generate masses of the weak gauge bosons and all the fermions except the neutrinos via electroweak symmetry breaking (EWSB). This mechanism is called the Brout-Englert-Higgs (BEH) mechanism and requires a scalar field, now called the Higgs field, to generate all the masses. Before the LHC began its operations, the only piece from the SM that was not observed was the Higgs boson. This changed in July 2012, when the ATLAS and CMS collaborations announced the discovery of a new particle with a mass of about $125\ \mathrm{GeV}$. Higgs and Englert were subsequently awarded the Nobel prize for their work on the BEH mechanism in 1964. This particle was eventually found to be compatible with the Higgs boson predicted by the SM. Since the discovery of the Higgs boson, there have been no significant deviations from the SM at any of the experiments at the LHC. The SM has withstood the rigorous tests of precision measurements over the past few decades. But several questions such as the the ones about dark matter, matter- antimatter asymmetry, fine tuning etc. still remain unanswered.

One of these problems concerns the neutrinos. In the SM, they are predicted to be massless. But the discovery of neutrino oscillations for which Arthur B. McDonald and Takaaki Kajita were awarded the Nobel Prize in physics in 2015, suggest that neutrinos are indeed massive. There are several propositions to fix the SM and generate massive neutrinos. The most popular propositions in literature involve either the addition of sterile neutrinos or very-heavy neutrinos to the SM particle content. The obvious issue with such possibilities is that they cannot be tested, especially at the LHC. This problem can be circumvented by extending the scalar sector of the SM to include a triplet with a hypercharge, $Y = 2$. EWSB in such a model results in very light Majorana masses for the neutrinos, consistent with experimental observations. The mass-mixing caused by the EWSB also results in a very rich scalar structure which includes a doubly charged Higgs boson, unique only to models with high scalar representation. It will be shown in the following sections that this model brings to light very interesting topologies which can be exploited to search for the doubly charged Higgs boson.

This thesis includes a theoretical/phenomenological description of the model, and the experimental search for the doubly charged Higgs boson decaying to same-sign $W-$bosons using the 2015-2016 data collected by the ATLAS detector. The first chapter provides the theoretical background of the SM, the triple-doublet extension of the SM, and the theoretical constraints that need to be taken into account. The second chapter discusses various phenomenological aspects of the model, and also explains how the parameters for event generation were chosen. The third chapter describes the Large Hadron Collider and ATLAS detector. The fourth chapter is dedicated to the identification and reconstruction of the different physics objects in the ATLAS detector. Chapter 5 deals with the various experimental aspects of the search such as the background estimation, signal optimization, and chapter 6 details the interpretation of the results. Variations of the model that could help increase the sensitivity are discussed in the seventh chapter.

1. Theoretical Background

1.1. The Standard Model

The Standard Model (SM) of particle physics describes all known elementary particles and their interactions with each other. The following sections describe the gauge structure and the particle content of the SM and the mechanism by which the particles get their masses.
The SM is a relativistic quantum field theory desrcibed by the Glashow-Weinberg-Salam model of electroweak interactions, and Quantum Chromodynamics (QCD). The principle symmetry in the SM is the gauge symmetry given by,

$$SU(3)_C \times SU(2)_L \times U(1)_Y, \tag{1.1}$$

where C, L, and Y denote color, left-handedness, and the weak hyper-charge respectively. The strong interactions are described by Quantum Chromodynamics (QCD) and are represented by the $SU(3)_C$ group. On the other hand, the electromagnetic and weak interactions are unified into the electroweak interactions, described by the $SU(2)_L \times U(1)_Y$ group. The electroweak unification was achieved by Sheldon Glashow, Abdus Salam, and Steven Weinberg awarding them a Nobel prize in 1978. This was shown to be renormalizable by Gerardus 't Hooft and Martinus Veltman for which they received the Nobel prize in 1999. The SM Lagrangian is required to be invariant under these groups in addition to being Lorentz invariant (invariant under the $SO(1,3)$ group).

Field Content

SM, as a field theory, consists of the matter fields, and the gauge fields.

- the fermion fields, ψ, which have a half-integer spin and make up the matter particles
- the electroweak boson fields, W_a ($a = 1, \cdots, 3$), and B
- the gluon field, G_a ($a = 1, \cdots, 8$), which is responsible for the strong force
- the Higgs field, ϕ, which is the only scalar field in the SM. It is responsible for generating masses for the fermions and gauge bosons.

The electroweak and gluon fields are together called the gauge fields. The matter fields consist of three families of spin-1/2 quarks and leptons, and a spin 0 Higgs boson, as shown in Table 1.1. Q^i_L, u^i_R, d^i_R represent the quark fields, and L^i_L, e^i_R denote the lepton fields. The index i is the family or generation index ($i = 1, 2, 3$). The subscripts L and R denote left-handed and right-handed fields respectively,

$$\psi_L = P_L \psi, \quad \psi_R = P_R \psi, \tag{1.2}$$

where the projection operators P_L and P_R are given by,

$$P_L = \frac{1}{2}(1 - \gamma_5), \quad P_R = \frac{1}{2}(1 + \gamma_5)$$

where γ_5 denotes the product of the four Dirac matrices.

Field	$SU(3)$	$SU(2)$	$U(1)$	$SO(3,1)$
$Q_L^i = \begin{pmatrix} u_L^i \\ d_L^i \end{pmatrix}$	3	2	1/6	(1/2,0)
u_R^i	3	1	2/3	(0,1/2)
d_R^i	3	1	-1/3	(0,1/2)
$L_L^i = \begin{pmatrix} \nu_L^i \\ e_L^i \end{pmatrix}$	1	2	-1/2	(1/2,0)
e_R^i	1	1	-1	(0,1/2)

Table 1.1: Matter fields in the SM. The index i denotes the quark and lepton family. The group $SO(3,1)$ is the Lorentz group.

Electroweak symmetry breaking

The SM does not allow bare mass terms for these particles by default because such terms are not invariant under the SM gauge group. Spontaneous symmetry breaking in the electroweak sector (EWSB) provides a mechanism to generate mass terms for the gauge bosons, and fermions. The terms in the Lagrangian that involve only the scalar Higgs doublet

$$\phi = \begin{pmatrix} \phi^+ \\ \phi^0 \end{pmatrix} \tag{1.3}$$

are,

$$\mathcal{L} = (D_\mu \phi)^\dagger (D_\mu \phi) - V(\phi). \tag{1.4}$$

$\phi^+ = \frac{1}{\sqrt{2}}(\phi_3 + i\phi_4)$ and $\phi^0 = \frac{1}{\sqrt{2}}(\phi_1 + i\phi_2)$, with all ϕ_i's being real. The covariant derivative of the doublet is given by,

$$D_\mu \phi = \left(\partial_\mu - \frac{i}{2} g \tau^i W_\mu^i - \frac{i}{2} g' Y B_\mu\right) \phi. \tag{1.5}$$

where τ^i are the weak $SU(2)$ generators, and Y denotes the $U(1)$ hypercharge. The $SU(2)$ and $U(1)$ couplings are denoted by g and g' respectively. The most general scalar potential, $V(\phi)$ is given by,

$$V(\phi) = \frac{m^2}{2} \phi^\dagger \phi + \frac{\lambda}{4} (\phi^\dagger \phi)^2. \tag{1.6}$$

m (the bare mass of the new scalar) and λ are free parameters of the model. The minimum of this potential depends on the sign of m^2. For positive values, the minimum of the potential is at $\phi = 0$. For negative values, this occurs at $\left(\phi^\dagger \phi\right)_0 = -\frac{m^2}{\lambda}$. We restrict ourselves to the isospin frame where $\langle \phi_1 \rangle = -\frac{m^2}{\lambda}, \langle \phi_2 \rangle = \langle \phi_3 \rangle = \langle \phi_4 \rangle = 0$. Considering this, the local $SU(2)$ symmetry can be used to rotate the doublet such that,

$$\phi(x) = \begin{pmatrix} 0 \\ \eta + \frac{\sigma(x)}{\sqrt{2}} \end{pmatrix},$$

where $\sqrt{2}\eta = \sqrt{-\frac{m^2}{\lambda}}$ and $\sigma(x)$ is a real function of space and time. A symmetry being local just implies that the symmetry rotation affects the field differently at different points in space. Expanding the covariant derivative using the expressions for τ^i and writing them as matrices gives,

$$D_\mu\phi = \begin{pmatrix} 0 \\ \frac{1}{\sqrt{2}}\partial_\mu\sigma \end{pmatrix} - \left[\frac{ig}{2}\begin{pmatrix} W_\mu^3 & W_\mu^1 - iW_\mu^2 \\ W_\mu^1 + iW_\mu^2 & -W_\mu^3 \end{pmatrix} + \frac{ig'}{2}B_\mu\right] \times \begin{pmatrix} 0 \\ \eta + \frac{\sigma}{\sqrt{2}} \end{pmatrix}$$

Substituting this in the kinetic term of the scalar field and expanding it further gives,

$$\begin{aligned}(D_\mu\phi)^\dagger(D_\mu\phi) = \frac{1}{2}(\partial_\mu\sigma)^2 + \frac{g^2\eta^2}{4}\left[(W_\mu^1)^2 + (W_\mu^2)^2\right] \\ + \frac{\eta^2}{4}\left(gW_\mu^3 - g'B_\mu\right)^2 + \text{cubic and quartic terms.}\end{aligned}$$

We, now, define Z_μ, and the orthogonal field A_μ as,

$$Z_\mu = \frac{gW_\mu^3 - g'B_\mu}{\sqrt{g^2+g'^2}} = \cos\theta_W W_\mu^3 - \sin\theta_W B_\mu, \text{ and} \tag{1.7}$$

$$A_\mu = \frac{g'W_\mu^3 + gB_\mu}{\sqrt{g^2+g'^2}} = \sin\theta_W W_\mu^3 + \cos\theta_W B_\mu \tag{1.8}$$

where θ_W, known as the Weinberg angle, is given by,

$$\cos\theta_W = \frac{g}{\sqrt{g^2+g'^2}}, \tag{1.9}$$

$$\tan\theta_W = \frac{g'}{g}. \tag{1.10}$$

Plugging this back in, and collecting the terms quadratic in the gauge fiels show that W_μ^1, W_μ^2, and Z_μ gain masses which are given by,

$$M_{W_1}^2 = M_{W_2}^2 = \frac{g^2\eta^2}{2}, \tag{1.11}$$

$$M_Z^2 = \frac{M_W^2}{\cos^2\theta_W}. \tag{1.12}$$

On the other hand, A_μ, which can be identified as the electromagnetic field does not gain a mass, which is to be expected.
This mechanism wherein the Higgs field acquires a non-zero vacuum expectation value and results in massive weak gauge bosons and a massless photon is called the BEH mechanism.

The Yukawa terms in the Lagrangian are given by,

$$\mathcal{L}_{\text{Yukawa}} = Y_u^{ij}\bar{u}_R^i\phi^T\epsilon Q_L^j - Y_d^{ij}\bar{d}_R^i\phi^\dagger Q_L^j - Y_e^{ij}\bar{e}_R^i\phi^\dagger L_L^j + \text{h.c.} \tag{1.13}$$

Since ϕ has a vacuum expectation value, the Yukawa couplings in Eq. 1.13, give rise to 3×3 quark and lepton mass,

$$\mathcal{M}_u^{ij} = \eta Y_u^{ij}/\sqrt{2}, \qquad \mathcal{M}_d^{ij} = \eta Y_d^{ij}/\sqrt{2}, \qquad \mathcal{M}_e^{ij} = \eta Y_e^{ij}/\sqrt{2}. \tag{1.14}$$

Such a term does not exist for the neutrinos due to absence of right handed neutrinos, which explains why they are massless in the Standard Model. The mass-matrices, above, are not diagonal but can be diagonalized via separate unitary transformations on left- and right-handed quark and lepton fields. These separate transformations can be written as,

$$u_L = \mathcal{U}_L^u u'_L, \quad u_R = \mathcal{U}_R^u u'_R, \tag{1.15}$$

$$d_L = \mathcal{U}_L^d d'_L, \quad d_R = \mathcal{U}_R^d d'_R, \tag{1.16}$$

$$e_L = \mathcal{U}_L^e e'_L, \quad e_R = \mathcal{U}_R^e e'_R. \tag{1.17}$$

Here u, d, and e are three-component column vectors in the flavor space for the quarks and leptons. The primed fields represent the corresponding mass-eigenstates. The expressions to diagonalize the mass-matrices using the 3×3 unitary matrices can be written as,

$$\mathcal{U}_R^{u\dagger} u_L \mathcal{M}_u \mathcal{U}_L^u = \begin{pmatrix} m_u & 0 & 0 \\ 0 & m_c & 0 \\ 0 & 0 & m_t \end{pmatrix} \tag{1.18}$$

$$\mathcal{U}_R^{d\dagger} d_R \mathcal{M}_d \mathcal{U}_L^d d_L = \begin{pmatrix} m_d & 0 & 0 \\ 0 & m_s & 0 \\ 0 & 0 & m_b \end{pmatrix} \tag{1.19}$$

$$\mathcal{U}_R^{e\dagger} e_R \mathcal{M}_e \mathcal{U}_L^e = \begin{pmatrix} m_e & 0 & 0 \\ 0 & m_\mu & 0 \\ 0 & 0 & m_\tau \end{pmatrix} \tag{1.20}$$

But u_L and d_L are parts of the same $SU(2)_L$ doublet, $\mathcal{Q}_L$, which can be re-written using the unitary matrices as,

$$\begin{pmatrix} u_L \\ d_L \end{pmatrix} = \begin{pmatrix} \mathcal{U}_L^u u'_L \\ \mathcal{U}_L^d d'_L \end{pmatrix} = \mathcal{U}_L^u \begin{pmatrix} u'_L \\ V d'_L \end{pmatrix}, \tag{1.21}$$

where V denotes the Cabibbo-Kobayashi-Masakawa (CKM) matrix defined as, $V = \mathcal{U}_L^{u\dagger} \mathcal{U}_L^d$. It is important to note that the up-type and down-type fields transform differently.

The 3×3 unitary matrix is completely specified by nine parameters. But an overall phase rotation of all quark doublets eliminates four of the nine parameters. The CKM matrix can then be expressed in the Kobayashi-Maskawa parametrization as,

$$V_{\text{CKM}} = \begin{pmatrix} c_1 & s_1 c_3 & s_1 s_3 \\ -s_1 c_2 & c_1 c_2 c_3 - s_2 s_3 e^{i\delta} & c_1 c_2 s_3 + s_2 c_3 e^{i\delta} \\ -s_1 s_2 & c_1 s_2 c_3 + c_2 s_3 e^{i\delta} & c_1 s_2 s_3 - c_2 c_3 e^{i\delta} \end{pmatrix}, \tag{1.22}$$

where c_i and s_i denote $\sin\theta_i$, and $\cos\theta_i$, repectively where $i = 1, 2, 3$ and the angles are chosen to lie in the first quadrant where the sines and cosines are both positive. The phase, δ, if non-zero leads to CP violation in the weak sector. The CKM matrix, hence, can be viewed as the transformation matrix from the flavor basis to the mass basis. The general notation for the mass-basis is $u'_1 = u$, $u'_2 = c$, $u'_3 = t$ and $d'_1 = d$, $d'_2 = s$, $d'_3 = b$. Due to the absence of right handed neutrinos, this mechanism does not generate neutrino masses.

1.2. The triplet-doublet extension of the SM

In order to accommodate the observation of neutrino oscillations, several modifications to the SM were proposed. If the SM is assumed to be an incomplete theory and valid only until a certain energy scale, it is possible to add non-renormalizable, dimension-5 term to generate neutrino masses [1]. Another possibility is the popular canonical seesaw mechanism [2]. While it is, in principle, a sound alternative, it involves energy scales of the order of the GUT scale. The seesaw mechanism introduces lepton number violation and an associated scale. Via the seesaw mechanism, neutrinos acquire tiny masses and the scale associated with lepton number violation is related to a grand unified theory scale. This is not an attractive option because the new physics occurs at GUT scale due to which such models lack testability at the LHC and other accelerators in the foreseeable future. Instead, adding a $Y = 2$ scalar triplet to the SM field content provides an alternative that is testable at the LHC. This section briefly describes one such model, and its theoretical constraints. A detailed description can be found in [3].

The Standard Model can be extended by including a scalar triplet, Δ, with a hypercharge $Y_\Delta = 2$, which transforms under the SM gauge group, $SU(3) \times SU(2) \times U(1)$ as $(1, 3, 2)$, while H, the SM Higgs field, transforms as $(1, 2, 1)$[a]. The most general renormalizable Lagrangian for such an extension can be written as,

$$\mathcal{L} = (D_\mu H)^\dagger (D^\mu H) + Tr(D_\mu \Delta)^\dagger (D^\mu \Delta) - V(H, \Delta) + \mathcal{L}_{Yukawa}. \tag{1.23}$$

The covariant derivatives, like in the SM, is defined as,

$$D_\mu H = \partial_\mu H + igT^a W^a_\mu H + i\frac{g'}{2} B_\mu H, \tag{1.24}$$

$$D_\mu \Delta = \partial_\mu \Delta + i\left[T^a W^a_\mu, \Delta\right] + ig'\frac{Y_\Delta}{2} B_\mu \Delta. \tag{1.25}$$

As described in section 1.1, W^a_μ and B_μ denote the $SU(2)_L$ and $U(1)_Y$ gauge fields respectively and g, g' denote the corresponding gauge couplings. The T^a's are $\frac{\sigma^a}{2}$ where $a = 1, 2, 3$, σ_a's being the usual Pauli matrices. Also, for the sake of simplicity of calculations, the triplet is written in the adjoint representation of $SU(2)$ as a 2×2 matrix,

$$\Delta = \begin{pmatrix} \delta^+/\sqrt{2} & \delta^{++} \\ \delta^0 & -\delta^+/\sqrt{2} \end{pmatrix}, \tag{1.26}$$

and H, the SM Higgs doublet is written in its standard form as $H = \begin{pmatrix} \phi^+ \\ \phi^0 \end{pmatrix}$.

The potential of the scalar sector is given by,

$$V(H, \Delta) = - m_H^2 H^\dagger H + \frac{\lambda}{4}(H^\dagger H)^2 + m_\Delta^2 Tr(\Delta^\dagger \Delta) + [\mu(H^\dagger i\sigma^2 \Delta^\dagger H) + h.c.] \tag{1.27}$$

$$+ \lambda_1 (H^\dagger H) Tr(\Delta^\dagger \Delta) + \lambda_2 (Tr\Delta^\dagger \Delta)^2 + \lambda_3 Tr\left(\Delta^\dagger \Delta\right)^2 + \lambda_4 H^\dagger \Delta \Delta^\dagger H. \tag{1.28}$$

---

[a] The normalization used is here is different compared to the SM section by a factor of 2.

The only additional contribution from the BSM fermion sector can be seen in $\mathcal{L}_{Yukawa}$,

$$\mathcal{L}_{Yukawa} \supset -Y_\nu L^T \otimes C \otimes i\sigma^2 \Delta L \tag{1.29}$$

where L denotes the $SU(2)_L$ doublets, and Y_ν denotes the Yukawa couplings in the lepton flavor space, C the charge conjugation operator, and σ_2 the second Pauli matrix. The tensor products indicate that the operators act on different spaces. When the neutral component of the triplet acquires a vev, Eq. 1.29 provides a term quadratic in neutrino fields. This results in tiny majorana masses for the neutrinos. The mass is proportional to $y_\nu v_t$, v_t being the vev of the triplet.

When the neutral components of the doublet and triplet acquire a vev (v_d, v_t), the doublet and triplet can be re-written as,

$$\Delta = \begin{pmatrix} 0 & 0 \\ v_t/\sqrt{2} & 0 \end{pmatrix}, \text{ and } H = \begin{pmatrix} 0 \\ v_d/\sqrt{2} \end{pmatrix}. \tag{1.30}$$

Using Equations 1.28, 1.30, 1.26 and the definition of H, and minimizing $V(\Delta, H)$, like in the SM as shown in the previous section, the following conditions are obtained,

$$M_\Delta^2 = \frac{2\mu v_d^2 - \sqrt{2}\,(\lambda_1+\lambda_4)\,v_d^2 v_t - 2\sqrt{2}\,(\lambda_2+\lambda_3)\,v_t^3}{2\sqrt{2}v_t}, \tag{1.31}$$

$$m_H^2 = \frac{\lambda v_d^2}{4} - \sqrt{2}\mu v_t + \frac{(\lambda_1+\lambda_4)}{2} v_t^2. \tag{1.32}$$

Replacing the coefficients in the potential (Eq. 1.28) with Eqs. 1.31 and 1.32, the 10×10 squared-mass matrix can be obtained by evaluating the double derivative of the potential w.r.t to all the fields at the minimum of the potential,

$$\mathcal{M}^2 = \frac{1}{2}\frac{\partial^2 V}{\partial \eta_i^2}|_{\Delta=\langle\Delta\rangle} \tag{1.33}$$

The matrix is block-diagonal and contains the doubly degenerate mass eigenvalue, $m^2_{H^{\pm\pm}}$ corresponding to δ^{++}, and four 2×2 matrices denoted by $\mathcal{M}_\pm$ corresponding to terms with $\delta^\pm$ and $\phi^\pm$, $\mathcal{M}_{\mathcal{CP}_{odd}}$, and $\mathcal{M}_{\mathcal{CP}_{even}}$. Diagonalizing the matrices gives the transformation relations between the flavor-eigenstates which in turn results in mass-mixing. and the mass-eigenstates.
The quadratic terms for $\delta^{\pm\pm}$ give the squared mass,

$$m^2_{H^{\pm\pm}} = \frac{\sqrt{2}\mu v_d^2 - \lambda_4 v_d^2 v_t - 2\lambda_3 v_t^3}{2v_t}. \tag{1.34}$$

In the case of the doubly charged Higgs bosons, the flavour eigenstate is the same as the mass eigenstate. The story is slightly different for the other Higgs bosons. The mass-squared matrix for the singly charged components is found to be,

$$\mathcal{M}_\pm^2 = \left(\sqrt{2}\mu - \frac{\lambda_4 v_t}{2}\right)\begin{pmatrix} v_t & -v_d/\sqrt{2} \\ -v_d/\sqrt{2} & v_d^2/2v_t \end{pmatrix},$$

which can be diagonalized with a rotation matrix, with a rotation angle, say, β'. The squared-mass matrix has two eigenvalues; one of these is 0 and corresponds to the Goldstone boson while the other gives the mass of the singly charged Higgs,

$$m_{H^\pm}^2 = \frac{(v_d^2 + 2v_t^2)[2\sqrt{2}\mu - \lambda_4 v_t]}{4v_t}. \tag{1.35}$$

It is important to note that the two mass eigenstates, $G^\pm$ and $H^\pm$, are obtained by rotating the flavour eigenstates, $\phi^\pm$ and $\delta^\pm$ and hence involve the mixing of the two flavour eigenstates.Working out the diagonalization conditions yields the following relation for β'

$$\tan\beta' = \left(\sqrt{2}\frac{v_t}{v_d}\right). \tag{1.36}$$

From Eq.1.34 and 1.35, assuming $v_t \ll v_d$, it can be seen that the singly charged and doubly charged Higgs bosons should be nearly degenerate in order for the model to remain perturbative.
It is possible to evaluate the mass matrices for the neutral Higgs bosons. The mass-squared matrices for the neutral Higgs bosons are,

$$\mathcal{M}^2_{\mathcal{CP}_{even}} = \begin{pmatrix} A & B \\ B & C \end{pmatrix} \tag{1.37}$$

$$\mathcal{M}^2_{\mathcal{CP}odd} = \sqrt{2}\mu \begin{pmatrix} 2v_t & -v_d \\ -v_d & v_d^2/2v_t \end{pmatrix} \tag{1.38}$$

where A, B, C denote,

$$A = \frac{\lambda}{2} v_d^2, \tag{1.39}$$

$$B = v_d \left(-\sqrt{2}\mu + (\lambda_4 + \lambda_1)\, v_t\right), \tag{1.40}$$

$$C = \frac{\sqrt{2}\mu v_d^2 + 4\,(\lambda_2 + \lambda_3)\, v_t^2}{2v_t}. \tag{1.41}$$

These matrices can be diagonalized using rotation matrices with angles, say, α and β for the CP-even and CP-odd matrices respectively. The rotation of the CP-even squared-mass matrix gives the relation between the flavor- and mass-eigenstates

$$h^0 = c_\alpha h + s_\alpha \xi^0, \tag{1.42}$$

$$H^0 = -s_\alpha h + c_\alpha \xi^0 \tag{1.43}$$

where h and ξ^0 are the real parts of the neutral components of the scalar doublet and triplet respectively. If α, is small or 0, the mixing between the doublet-like and triplet-like Higgs bosons is negligible. This allows h^0 to precisely be the SM Higgs that has been observed. The masses are the the eigenvalues of the rotated squared-mass matrix and found to be,

$$m_{h^0}^2 = \frac{1}{2}\left[A + C - \sqrt{(A-C)^2 + 4B^2}\right] \tag{1.44}$$

$$m_{H^0}^2 = \frac{1}{2}\left[A + C + \sqrt{(A-C)^2 + 4B^2}\right]. \tag{1.45}$$

The diagonalization demands the angles to satisfy the following conditions,

$$\tan 2\alpha = \frac{2B}{A-C}, \tag{1.46}$$

$$\tan\beta = \frac{2v_t}{v_d} \tag{1.47}$$

Proceeding along similar lines, the rotation of the CP-odd squared-mass matrix yields the following relation between the mass- and flavor eigenstates,

$$A^0 = -s_\beta Z_1 + c_\beta Z_2, \tag{1.48}$$

$$G^0 = c_\beta Z_1 + s_\beta Z_2 \tag{1.49}$$

where Z_1 and Z_2 are the imaginary parts of ϕ^0 and δ^0 respectively. G^0 is the Goldstone boson while A^0 is the massive physical state with the mass given by,

$$m_A^2 = \frac{\mu\left(v_d^2 + 4v_t^2\right)}{\sqrt{2}v_t}. \tag{1.50}$$

The masses shown in this section are bounded by some theoretical constraints, listed below:

- the potential should be bounded from below (BFB)
- tree-level unitarity should be preserved by various scattering processes
- tachyonic modes should be absent.

These are described in more detail in [3]. These constraints impose bounds on the λ_i's and μ that need to be taken into account to choose a parameter space of interest for an experimental analysis.

2. Phenomenology and event generation of the TDHM

In order to explore the various possibilities to search for the doubly charged Higgs bosons at the LHC, it is important to understand the mechanisms by which it can be produced, and also its decay modes. This section explains these production and decay modes in detail, describes the various parameters required for the event generation and shows the expected number of events within the acceptance of the detector and the kinematics of various objects in these events.

2.1. Production of $H^{\pm\pm}$

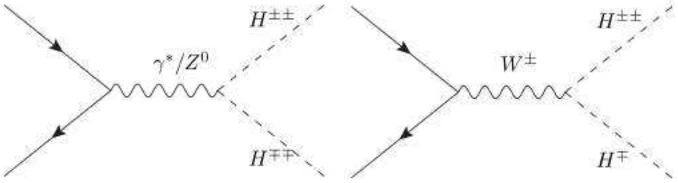

Fig. 2.1: Feynman diagrams showing the pair production and associated production modes for $H^{\pm\pm}$

The triplet Higgses couple to the gauge bosons via the terms involving the covariant derivatives, as shown in the previous section. Also, the triplet Higgses are fermiophobic and couple to fermions with a strength which is directly proportional to the neutrino masses, which tend to be of the order of a few eV. Thus, the doubly charged Higgs can be produced only via the gauge bosons. The important modes by which the doubly charged Higgs can be produced are,

- Pair production: $pp \rightarrow Z^*/\gamma^* \rightarrow H^{\pm\pm}H^{\mp\mp}$
  The coupling for this production mode is $-2ie_V(p_{H^{\pm\pm}} - p_{H^{\mp\mp}})$, where $p_{H^{\pm\pm}}$ is the four-momentum of $H^{\pm\pm}$ abd e_V is just the standard gauge coupling. The only new parameter on which this cross-section depends on is the mass of $H^{\pm\pm}$.
- Associated production: $pp \rightarrow W^{\pm *} \rightarrow H^{\pm\pm}H^{\mp}$
  The coupling for this mode is $ig(p_{H^{\pm\pm}} - p_{H^{\mp}})$; g corresponds to the $SU(2)$ gauge coupling and $p_{H^{\pm\pm}(H^{\pm})}$ stands for the four-momentum of $H^{\pm\pm}(H^{\pm})$. The cross-section for this mode depends on the masses of $H^{\pm\pm}$ and $H^{\pm}$. When $H^{\pm}$ is significantly heavier than $H^{\pm\pm}$ (about $200-300$ GeV at least), this mode is suppressed by an order of magnitude. For nearly-degenerate masses, the cross-section is comparable to that of the pair-production mode.
- Single production: $pp \rightarrow W^{\pm *}W^{\pm *} \rightarrow H^{\pm\pm}qq$
  In this case, the coupling is $-i\sqrt{2}g^2 v_t g_{\mu\nu}$. The cross-section, then, depends on the vev of the triplet. For low values of the vev, this mode is also suppressed.

In the analysis presented in this thesis, only the pair-production mode will be investigated. The associated production mode is briefly discussed in the chapter dedicated to the future prospects.

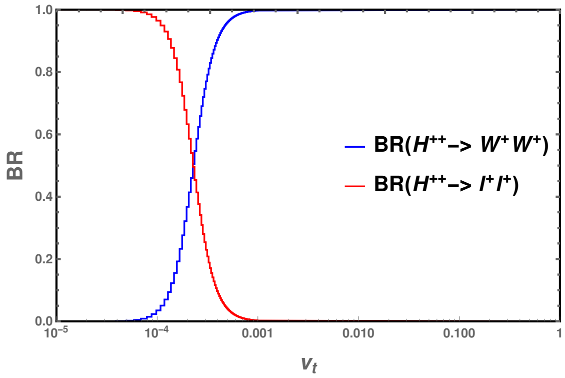

Fig. 2.2: Dependence of the branching ratio of $H^{\pm\pm}$ on the vacuum expectation value of the triplet.

2.2. Decay modes of $H^{\pm\pm}$

The next important factor that needs to be fixed is the decay mode of the doubly-charged Higgs since this dictates the signatures of $H^{\pm\pm}$ in the detectors. The case where $H^{\pm\pm}$ decays to $W^{\pm}H^{\pm}$ will be ignored since this is allowed only when $m_{H^{\pm}} < m_{H^{\pm\pm}}$. The only possible decays, then, are,

$$H^{\pm\pm} \rightarrow \ell^{\pm}\ell^{\pm}, \tag{2.1}$$

$$H^{\pm\pm} \rightarrow W^{\pm}W^{\pm}. \tag{2.2}$$

Both the decay modes depend on v_t, the vev of the triplet. Thus, it is possible to find the dependence of the branching ratio on v_t. This is shown in figure 2.2. The WW decay mode is suppresed at tiny values of v_t and dominates at relatively higher values of v_t.

2.3. Experimental constraints

It is not possible to consider arbitrarily high values of v_t. The most stringent constraint on v_t is obtained from the precision measurements of the eletroweak ρ parameter. At tree-level, in the SM, $\rho = 1$. This arises from the fact that the scalar potential is a function of $H^{\dagger}H$, not just H. In the model being investigated here, at tree level, ρ is modified to be,

$$\rho = \frac{v_d^2 + 2v_t^2}{v_d^2 + 4v_t^2}. \tag{2.3}$$

The modified ρ is less than one. At 2σ level, the measured value, $\rho = 1.004 \pm 0.0048$. This imposes an upper bound on v_t of 1.6 GeV. It is important to note that this bound holds only at tree-level.[a]

There have been several searches for the doubly charged Higgs at CMS, ATLAS, OPAL, Delphi, CDF which assume 100% branching into leptons. The lower bounds on $m_{H^{\pm\pm}}$ set by these experiments range from $400-600$ GeV. There is no previous dedicated search in the WW channel. In various phenomenological studies, with the assumption that the branching into WW is 100%, the bounds and sensitivity of the model w.r.t. the mass of the doubly charged Higgs is re-evaluated [4]. It is shown that the previous experimental searches designed for dilepton decays were not sensitive to WW decay mode. The lower limit on $m_{H^{\pm\pm}}$ was evaluted to be 85 GeV with 20 fb^{-1} of data at

---

[a] The radiative corrections from the purely BSM sector pushes the value of ρ higher and thus, relaxes the bound on v_t.

a centre of mass energy of 14 TeV. This shows that the high v_t region is still sensitive despite the previous searches for the doubly charged Higgses. The rest of the analysis focuses on pair production of doubly charged Higgs with $v_t = 0.1$ GeV, well within the experimental constraints where the WW decay mode dominates.

Futhermore, the measurement of the electroweak precision data also constrains the allowed mass-splitting between the charged Higgs bosons. In the scenario where $\sin\alpha$ is very small and h^0 is SM-like, the maximum allowed mass-splitting between $H^\pm$ and $H^{\pm\pm}$ is 40 GeV [5].

2.4. Event generation and fiducial cross-sections

In order to perform the analysis, event generation of the above mentioned decays is necessary. For this purpose, CalcHEP was used [6]. The benchmark $m_{H^{\pm\pm}}$ points were chosen to be 200-700 GeV in steps of 100 GeV. Since we benchmark on the mass of $H^{\pm\pm}$, the masses of the Higgs bosons are given as input to CalcHEP instead of the parameters that appear in Eq. 1.28 (λ_i's and μ). To choose a set of masses, the parameters of the Lagrangian need to be fixed. These depend on the various theoretical constraints mentioned in the previous chapter. Furthermore, the set of parameters of the Lagrangian can be written in terms of the masses of the various Higgses by using the equations described in the previous section as,

$$\lambda_1 = -\frac{2}{v_d^2 + 4v_t^2}.m_A^2 + \frac{4}{v_d^2 + 2v_t^2}.m_{H^\pm}^2 + \frac{\sin 2\alpha}{2v_d v_t}.\left(m_{h^0}^2 - m_{H^0}^2\right) \tag{2.4}$$

$$\lambda_2 = \frac{1}{v_t^2}\left[\frac{s_\alpha^2 m_{h^0}^2 + c_\alpha^2 m_{H^0}^2}{2} + \frac{1}{2}.\frac{v_d^2}{v_d^2 + 4v_t^2}.m_A^2 - \frac{2v_d^2}{v_d^2 + 2v_t^2}.m_{H^\pm}^2 + m_{H^{\pm\pm}}^2\right] \tag{2.5}$$

$$\lambda_3 = \frac{1}{v_t^2}\left[-\frac{v_d^2}{v_d^2 + 4v_t^2}.m_A^2 + \frac{2v_d^2}{v_d^2 + 2v_t^2}.m_{H^\pm}^2 - m_{H^{\pm\pm}}^2\right] \tag{2.6}$$

$$\lambda_4 = \frac{4}{v_d^2 + 4v_t^2}.m_A^2 - \frac{4}{v_d^2 + 4v_t^2}.m_{H^\pm}^2 \tag{2.7}$$

$$\lambda = \frac{2}{v_d^2}\left[c_\alpha^2 m_{h^0}^2 + s_\alpha^2 m_{H^0}^2\right] \tag{2.8}$$

$$\mu = \frac{\sqrt{2}v_t}{v_d^2 + 4v_t^2}.m_A^2 \tag{2.9}$$

The only remaining parameters are m_H^2 and M_Δ^2 which are related via the electroweak symmetry breaking conditions (equations 1.31 and 1.32). To remain in the phase space where the two CP even Higgses have no mixing, α is chosen to be 10^{-4}. The theoretical constraints are then applied on these parameters, and several sets of parameters allowed by these constraints and have values close to 1 are chosen. The above equations are then inverted to get the masses in terms of the allowed sets of parameters. The charged Higgses are required to be nearly degenerate (less than 10 GeV mass-splitting). The neutral BSM Higgs bosons, A^0 and H^0, are degenerate. This can be understood by considering equations 1.39 - 1.41, 1.45, $m^2_{H^0}$ can be rewritten as,

$$m^2_{H^0} = \frac{1}{2}\left[\frac{\lambda v_d^2}{2} + \frac{\sqrt{2}\mu v_d^2 + 4\left(\lambda_2+\lambda_3\right)v_t^3}{2v_t}\right. \tag{2.10}$$

$$\left. + \sqrt{\left(\frac{\lambda v_d^2}{2} - \frac{\sqrt{2}\mu v_d^2 + 4(\lambda_2+\lambda_3)v_t^3}{2v_t}\right)^2 + 4v_d^2\left(-\sqrt{2}\mu + (\lambda_1+\lambda_4)v_t\right)^2}\right]. \tag{2.11}$$

In the limit $v_t \ll v_d$,

$$m^2_{H^0} = \frac{\mu v_d^2}{\sqrt{2}v_t}. \tag{2.12}$$

Using equation 1.50 and the limit, $v_t \ll v_d$, it can be concluded that $m^2_{H^0} = m^2_{A^0}$. The mass-splitting between these neutral Higgs bosons and the charged Higgs bosons is driven by λ_1. However, the exact masses of H^0 and A^0 do not affect the analysis presented in this thesis.

These masses are then used as an input to CalcHEP to then generate events for the requested decay,

$$pp \to H^{\pm\pm}H^{\mp\mp} \to W^{\pm}W^{\pm}W^{\mp}W^{\mp}. \tag{2.13}$$

by setting $v_t = 0.1$ GeV. The chosen parameters relevant to the analysis are shown in table 2.3. Details about all the parameters required to generate events can be found in Appendix A.

The CTEQ6l parton distribution function (PDF) is used to generate the events. The cross-sections, at leading order (LO), for the various benchmark points are shown in table 2.1. Given the four W bosons, it is possible to investigate various final states, as shown in table 2.2. Of these final states, the channels with 0ℓ, 1ℓ, and $2\ell^{os}$ are faced with a high background from SM processes. Thus, an analysis in $2\ell^{ss}$ (total charge$= \pm 2$), 3ℓ (total charge$= \pm 1$), and 4ℓ (total charge$= 0$) final states is considered.

H^{++} mass (GeV)	200	300	400	500	600	700
cross section (fb)	64.58	13.34	3.998	1.466	0.610	0.276

Table 2.1: Cross sections of the signal samples

The events generated by CalcHEP are fed to Delphes to perform a fast simulation of the ATLAS detector and evaluate the fiducial cross-sections. The leptons are required to be within $|\eta| < 2.5$ and have a $P_T > 10$ GeV. The number of events that pass these fiducial cuts in various channels at 36 fb^{-1} are evaluated for $m_{H^{\pm\pm}} = 200$ GeV. These are shown in Table 2.4.

These events are then used to compare observables that could be used in the analysis. Figure 2.3 shows the distributions of the invariant mass of the same-sign leptons originating from the same doubly-charged Higgs boson via W-decays as a function of the mass of the doubly charged Higgs

$H^{\pm\pm}H^{\mp\mp} \to 4W$	BR (in %)
$\to 0\ell + 8$ jets	31.3
$\to 1\ell + \not{E}_T + 6$ jets	42.4
$\to 2\ell^{ss/os} + \not{E}_T + 4$ jets	21.6
$\to 3\ell + \not{E}_T + 2$ jets	4.9
$\to 4\ell + \not{E}_T +$ no jets	0.4

Table 2.2: Branching ratios for various final states

Parameter	Value
v_t	0.1 GeV
$\sin\alpha$	10^{-4}
$m_{H^{\pm\pm}}$	200 – 700 GeV in steps of 100 GeV

Table 2.3: Summary of parameters relevant to the analysis.

$\text{N}_{\text{leptons}}$	Channel	N_{tot}	Percentage of events within fiducial acceptance
$2\ell^{ss}$	ee	34.8	85
	$e\mu$	69.5	85
	$\mu\mu$	34.7	85
3ℓ	eee	9.9	75
	$ee\mu$	29.7	75
	$e\mu\mu$	29.7	75
	$\mu\mu\mu$	9.9	75
4ℓ	$eeee$	0.4	69
	$eee\mu$	1.4	69
	$ee\mu\mu$	2.1	68.2
	$e\mu\mu\mu$	1.4	69
	$\mu\mu\mu\mu$	0.4	69

Table 2.4: The fraction of events, at 36fb^{-1}, that survive the fiducial cuts is shown. The 3 lepton channels are required to have a total charge of ±1, the di-lepton channel is required to have a total charge of ±2 while the four lepton channel is required to have a total charge of 0.

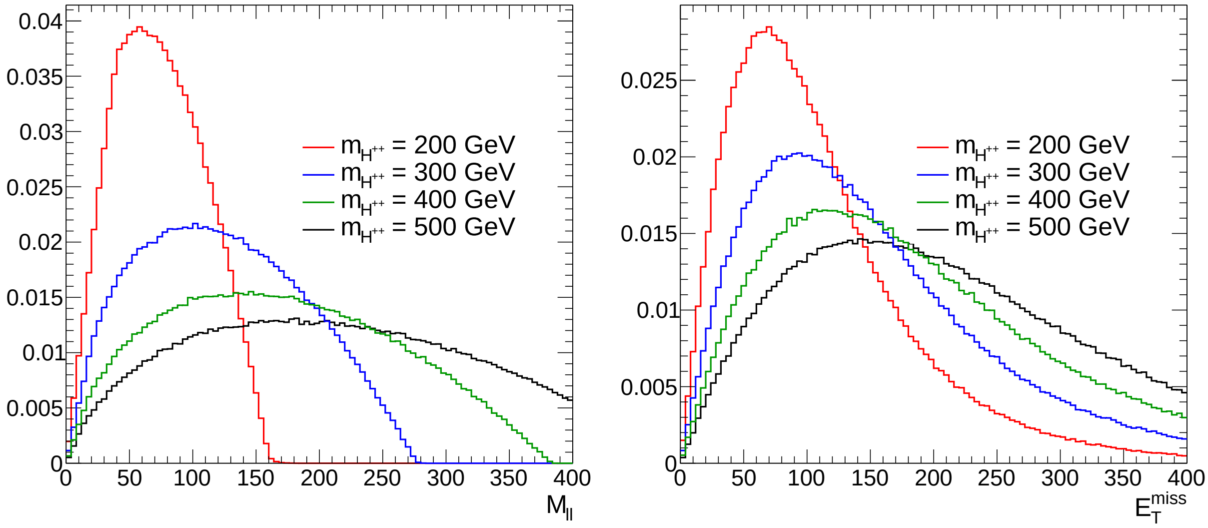

Fig. 2.3: Left: Invariant mass distribution of same-sign leptons from W decays of the doubly charged Higgs boson as a function of $M_{H^{\pm\pm}}$ at the generator level.
Right: $\mathrm{E}_{\mathrm{T}}^{\mathrm{miss}}$ distributions in events with $H^{\pm\pm} \rightarrow W^{\pm}W^{\pm}$ as a function of $M_{H^{\pm\pm}}$ at the generator level. The distributions are normalized to 1.

boson.

To summarize the chapter, the various possible production and decay modes of the doubly charged Higgs boson and their dependence on different parameters is described. Taking into consideration the experimental constraints, the generation of events for pair-production of the doubly charged Higgs boson in the WW decay mode is explained with the specific choice of parameters (summarized in Table 2.3) for the same. These events are then used for the experimental analysis.

3. The ATLAS experiment at the Large Hadron Collider

This chapter describes a series of accelerators including the Large Hadron Collider and the ATLAS detector built at the European Organization for Nuclear Research (CERN) in sections 3.1 and 3.2, respectively. Additionally, the software tools and computing facilities used for the simulation and analyses of collision data are discussed.

3.1. Large Hadron Collider

A wide program of research in fundamental physics at the European Center for Nuclear Physics (CERN) is pursued with a system of many accelerators, the cornerstone of which is the Large Hadron Collider (LHC). The LHC [7] is the world's largest synchrotron, built underground at about 100 m depth near Geneva, Switzerland. Its diameter is about 9 km, lying across the border between France and Switzerland.

All protons at CERN originate from a source canister of hydrogen gas. The hydrogen atoms are ionized and the resulting protons are accelerated into an initial beam energy of 50 MeV by a linear accelerator, LINAC2. This beam then enters the Proton Synchrotron (PS) booster. The PS booster increases the beam energy to 1 or 1.4 GeV before sending the beam to the PS, which further increases the beam energy to 25 GeV before transferring the beam to the Super Proton Synchrotron (SPS). The SPS increases the beam energy to 450 GeV, the minimum beam energy the LHC is capable of accepting.

The LHC further accelerates the protons to an energy of 6.5 TeV before colliding them at several interaction points (IPs) around the LHC ring. The collisions at the LHC have reached a centre-of-mass energy of $\sqrt{s} = 13$ TeV. The design energy is $\sqrt{s} = 14$ TeV, the largest ever produced in a laboratory setting.

Once the LHC accepts the beam, it is locked to the machine by operating the Radio Frequency (RF) cavities, which drive the acceleration of the proton beam, at a harmonic of the accelerator's revolution frequency,

$$f_{\text{RF}} = h f_{rev}. \tag{3.1}$$

This procedure creates stable regions called buckets along the path of the beam. In these buckets, the beam is not accelerated and the protons are localized around these regions. As the magnetic field of the synchroton is increased, the momentum of these buckets increases. This in turn accelerates the protons. At the LHC, $f_{rev} = 11.2455$ Hz and $f_{RF} = 40$ MHz. This gives $h = 35642$ stable regions along the beam. Typically only one in ten of these buckets is filled with protons to ensure a safe extraction of the LHC beam during a fill. At design specifications 2808 of the available 3564 bunches are filled, and grouped into larger structures called trains. The spacing between bunches within a train can be as low as 25 ns corresponding to the nominal RF frequency. The distance between the trains, however, is several bunches long. This is done to accommodate the beam dump kicker rise time of $3\ \mu$ s and the SPS injection kicker rise time of $0.95\ \mu$s. The nominal filling scheme for operations at 25 ns can be written as,

$$
\begin{aligned}
3564 = & [2 \times (72b + 8e) + 30e] && (3.2)\\
& + [3 \times (72b + 8e) + 30e] + [4 \times (72b + 8e) + 30e] && (3.3)\\
& + 3 \times \{2 \times [3 \times (72b + 8e) + 30e] + [4 \times (72b + 8e) + 31e]\} && (3.4)\\
& + 80e, && (3.5)
\end{aligned}
$$

where b denotes a filled bucket and e denotes an empty bucket. The filling scheme can also be written in terms of the SPS cycles and the number of proton batches provided from the pre-injection chain during each cycle:

$$234 \quad 334 \quad 334 \quad 334 \tag{3.6}$$

where the first cycle contains a pair of 72-bunch batches from pre-injection, the second contains a triplet, and so on for the 12 injection cycles required to fill each LHC beam. Every SPS injection cycle requires 21.6 seconds to perform. Thus, the nominal filling of the LHC beam is about 4 minutes. Following the filling, the magnetic field is ramped up (increased adiabatically) from an initial strength of 0.54 T up to maximum design specification of 8.33 T. This process takes more than half an hour.

After the LHC has been filled and the beams brought up to the required energy, collisions are provided to each of the LHC experiments. The rate of collisions is typically written in terms of the instantaneous luminosity, $\mathcal{L}_{int}$, and the total cross-section of the proton-proton interaction,

$$R = \mathcal{L}_{int}\sigma_{pp}. \tag{3.7}$$

At the LHC, the TOTEM collaborations and ATLAS ALFA detectors use roman pot detectors and particle telescopes to measure σ_{pp}. The instantaneous luminosity may be expressed as,

$$\mathcal{L}_{int} = f_{rev}\frac{n_c N_1 N_2}{4\pi\sigma^2}, \tag{3.8}$$

where n_c is the number of colliding bunch pairs in the LHC filling scheme, N_i are the number of protons in the respective beams, and σ is the transverse size of the beam at the interaction point. A precise measurement of N and σ allows for a calibration of the instantaneous luminosity. Dedicated beam-current monitors installed along the LHC ring are used to measure N. The transverse size can be factorized into the $x-$ and $y-$ components of the beam size,

$$\sigma^2 = \sigma_x\sigma_y. \tag{3.9}$$

These quantities are measured at every interaction point using Van der Meer scans. These scans are performed periodically during the LHC operations when the LHC beams are slightly displaced w.r.t each other and scanned across one another, first horizontally and then vertically. This allows for an accurate determination of the beam size. Such a scan was first developed and applied by Simon van der Meer in order to measure the size of the proton beams at Cern's intersecting storage rings during the 1970s.

Since the beams are formed of dense bunches (about $100,000$ million protons per bunch), it is very likely that more than one proton from each beam will interact. This phenomenon is called pile-up and presents a major challenge for the physics performed at the LHC. The additional pp interactions produce several low-p_T particles which generates spurious noise in the detector systems and may lead to the degradation of the performance of particle identification.

In total, there are seven experiments positioned at different points along the LHC ring. A couple of general purpose detectors, ATLAS and CMS, were designed to search for the Higgs boson, and for new TeV-scale physics. LHCb is designed to study the physics of b-hadrons and CP violation. ALICE is designed to study the collisions of relativistic lead ions produced by the LHC. Sharing the same interaction point as ATLAS, the LHCf experiment studies the origin of ultra-high-energy cosmic rays by investigating the cascade of particles produced at very low angles by LHC collisions. The MOEDAL experiment, situated in the same cavern as LHCb, searches for magnetic monopoles and highly ionizing massive, yet stable, particles. The TOTEM experiment measures the total proton-proton interaction cross-section.

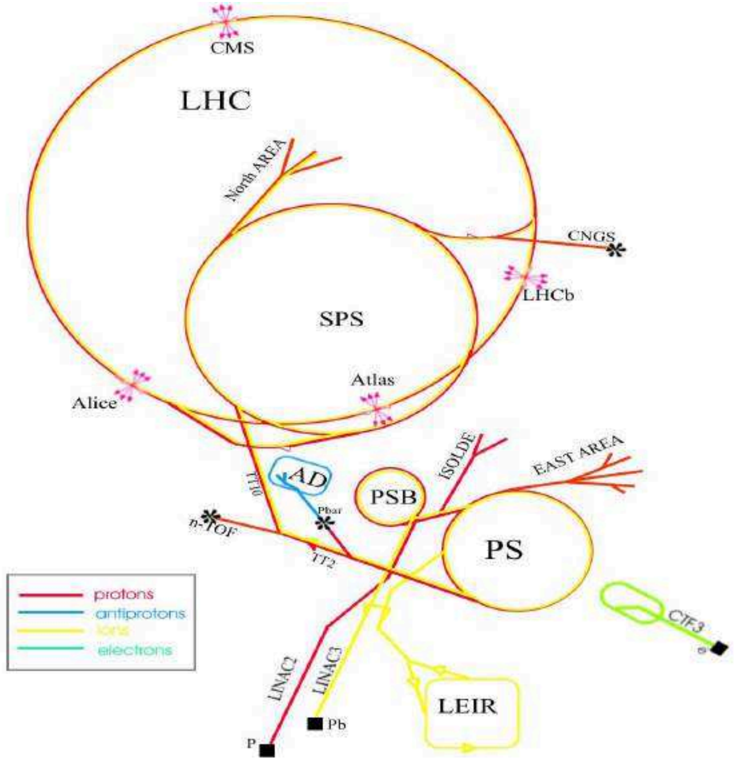

Fig. 3.1: The CERN accelerator complex.

3.2. The ATLAS detector

This section describes the ATLAS detector, indicated as Atlas in fig 3.1, located at CERN Point-1, one of the collisions points in the LHC. The detector is installed in an underground cavern, and the main control room is located over ground, almost right above the detector. The overview of the ATLAS detector is shown in fig 3.2. The ATLAS detector is composed of an Inner Detector (ID), the electromagnetic and hadronic calorimeters, the muon spectrometer, and a system of magnets.

3.2.1. Experimental coordinates and quantities

The right handed-system is used for the coordinates of the ATLAS experiment. The $+x$ direction points towards the center of the LHC ring, while the $+y$ direction points vertically upwards. The z axis

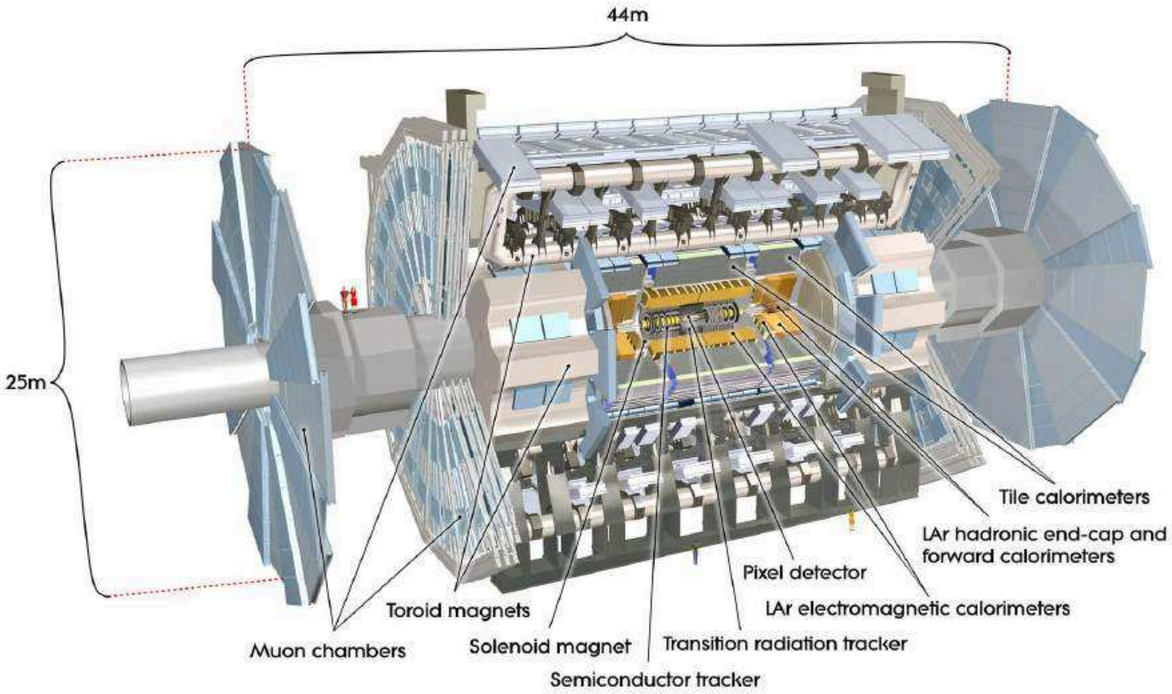

Fig. 3.2: Overview of the ATLAS detector. It is composed of three main sub-detectors which are the Inner Detector, the calorimeter, and the Muon Spectrometer.

corresponds to the path traversed by the beams, and the $+z$ direction indicates the counterclockwise rotation along the z-axis when the LHC is seen from above.

The cylindrical coordinate system (r, ϕ, θ) is also used along with the Cartesian system, r denotes the radius from the beam axis (z-axis) in the x-y plane, ϕ denotes the azimuthal angle from x-axis $(-\pi < \phi \leq +\pi)$ in the transverse plane, and θ, the polar angle measured from z-axis.

Rapidity y, in which the distance Δy is Lorentz-invariant, is defined as,

$$y = \frac{1}{2} \ln \frac{E + p_z}{E - p_z}, \tag{3.10}$$

where E is the energy of the particle and p_z is the z component of the particle momentum. If the rest-mass of the particle is negligible, y in eq 3.10 becomes the pseudo-rapidity:

$$\eta = -\frac{1}{2} \ln \left(\tan \frac{\theta}{2} \right). \tag{3.11}$$

and is frequently used instead of θ since it is Lorentz-invariant. The distance between two particles, ΔR, in the pseudo-rapidity-azimuth space is defined as:

$$\Delta R = \sqrt{(\Delta\eta)^2 + (\Delta\phi)^2}, \tag{3.12}$$

where $\Delta\eta$ and $\Delta\phi$ are the angular separation between the two particles in the corresponding angular variable.

The particle transverse momentum, p_T, is defined as:

$$p_{\mathrm{T}} = \sqrt{p_x^2 + p_y^2}. \tag{3.13}$$

Since ATLAS is a proton collider experiment, the longitudinal energy of the initial colliding partons cannot be measured. However, the vectorial sum of particle momenta on the transverse plane should be conserved. This provides the missing transverse momentum, which can be a hint of neutrinos' momenta. The missing transverse momentum magnitude, $E_{\mathrm{T}}^{\mathrm{miss}}$, is defined as:

$$E_{\mathrm{T}}^{\mathrm{miss}} = \sqrt{(E_x^{\mathrm{miss}})^2 + (E_y^{\mathrm{miss}})^2}. \tag{3.14}$$

Details about $E_{\mathrm{T}}^{\mathrm{miss}}$ are discussed in section 4.4.

3.2.2. Inner Detector

Approximately 100 particles emerge from the interaction point every 25 ns. The inner detector is designed to function in such a busy environment with a very high track density. The ID is composed of

- Pixel Detector
- Semi-conductor tracker (SCT)
- Transition Radiation Tracker (TRT).

It provides the track and vertex resolution required to identify the various particles that emerge from the collisions. The ID is immersed in a 2T solenoid field. The IBL forms the innermost layer and is surrounded by discrete high-resolution semiconductor pixel and strip detectors. These are arranged as concentric cylinders around the beam axis in the barrel region. The end-cap layers are installed as disks perpendicular to the beam axis. The pixel and SCT detectors provide a coverage of $|\eta| < 2.5$. The intrinsic accuracy and alignment tolerances are detailed in Table 3.1 and a schematic of the ID is shown in figure 3.3.

Table 3.1: Intrinsic measurement accuracy and mechanical alignment tolerances for the Inner Detector sub-systems. The numbers in the table correspond to the single-module accuracy for pixels, to the effective single-module accuracy for the SCT, and to the drift-time accuracy of a single straw for the TRT [8].

Item	intrinsic accuracy (μm)	alignment tolerances (μm)		
		radial (r)	axial (z)	azimuth (r-ϕ)
Pixel				
Layer-0	10 (r-ϕ) 115(z)	10	20	7
Layer-1 and -2	10 (r-ϕ) 115(z)	20	20	7
Disks	10 (r-ϕ) 115(r)	20	100	7
SCT				
Barrel	17 (r-ϕ) 580(z)	100	50	12
Disks	17 (r-ϕ) 580(r)	50	200	12
TRT	130			30

An important factor that has a significant impact of the ID performance is the material distribution. Multiple scattering in the detector can be a hindrance to particle identification. A higher material budget is needed to achieve mechanical stability in face of high radiation exposure. On the other hand, a low material budget is required for optimal performance. The current material distribution as a function of the radiation length X^0 in the ID is shown in figure 3.7. This distribution implies that approximately 40% of the photons are converted in electron-positron pairs before reaching the calorimeter. Such conversions can act as important backgrounds in analysis.

The trajectory of a charged particle is bent in the magnetic field generated by the solenoid. The curvature is then used to measure the charge and the momenta of the particles. Fitting the tracks to the hits in the various layers of the ID can then be used for the reconstruction of the interaction points and the decay vertices of short lived particles. The TRT enhances the accuracy of electron identification via the measurement of transition radiation, used to reject fake electrons from light, charged hadrons. The semiconductor trackers allow precision measurements of the impact parameters and reconstruction of displaced vertices for heavy flavour or τ-lepton tagging. The innermost pixel layers aid the secondary vertex measurement, at a radius of about 5 cm. The ID provides a good momentum and vertex resolution for tracks with a $p_T > 0.5$ GeV in a coverage of $|\eta| < 2.5$. It is helpful in identification of electrons with $0.5 < p_T < 150$ GeV and $|\eta| < 2.0$. These sub-detectors are described below in more detail.

Pixel Detector

Located closest to the collision point, the pixel detector is required to have the highest tolerance to radiation damage among all the sub-detectors. The high resolution of the Pixel detector aids in identying and tagging short lived particles such as $\tau-$leptons and $b-$hadrons. The Insertable B-Layer (IBL), added in 2014, has contributed significantly to b-tagging and was used to improve electron

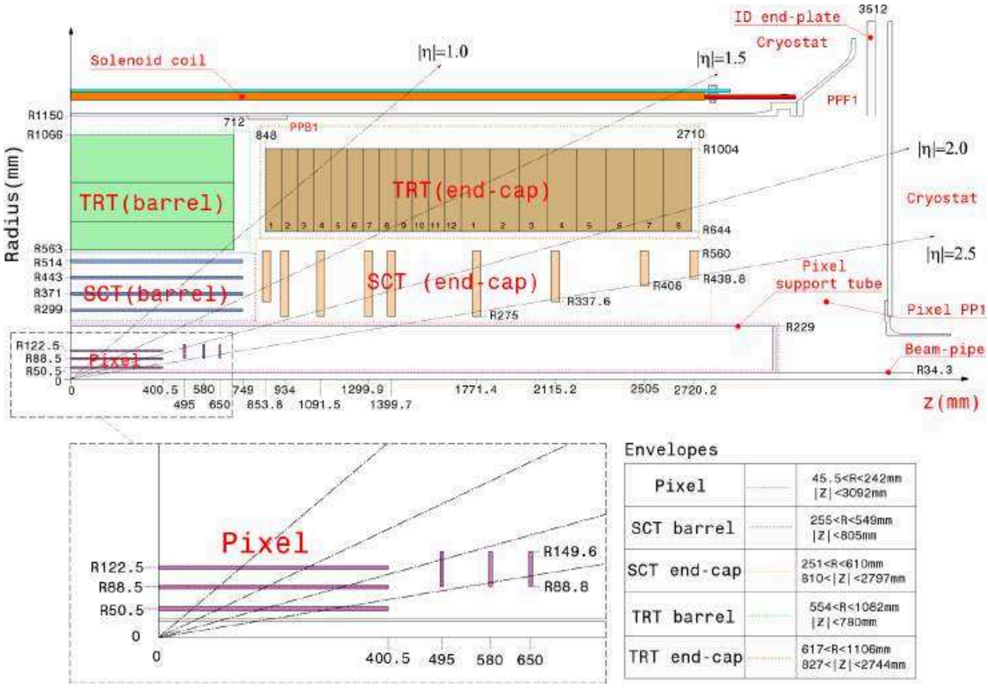

Fig. 3.3: The quarter section of the Inner Detector showing each of the major detector elements with its active envelopes. The labels PP1, PPB1 and PPF1 indicate the patch-panels for the services [8].

identification during Run 2 so far and is discussed in the next sub-section. The pixel detector is segmented in the $R - \phi$ plane and along the $z - axis$. The barrel region consists of three concentric cylinders around the beam axis at radii of 50.5, 88.5, and 122.5 mm respectively. The endcap region is made of disks perpendicular to the beam axis on both sides of the collision point.

The schematic of the picture is shown in figure 3.4. All modules are identical and have a size of 19×63 mm^2. Each pixel has a size of 50×400 μm^2 in $r\phi \times z$. Each of the above mentioned modules consist of 46080 pixels, directly linked to 16 front-end chips for readout. Every front-end chip has 2880 channels to amplify the signal from the pixels. There are a total of 1744 pixel modules with 80 million channels.

In the barrel region, 13 modules are attached to a stave. The staves are mounted on a cylindrical support with $20°$ tilt angle to form a layer. The three layers forming the barrel region are shown in figure 3.3. The endcap disks are made of 8 sectors, and each sector has six pixel modules. Figure 3.5 shows photographed examples of the barrel stave and disk sector.

The pixel detector can provide information about the energy lost by a particle as it traverses a certain distance, dE/dx, by using Time-over-Threshold (ToT) [10]. The charge is estimated by measuring the time during which the signal lies above the threshold in the 25 ns intervals. dE/dx as a function of momentum can be used to identify the charged particle.

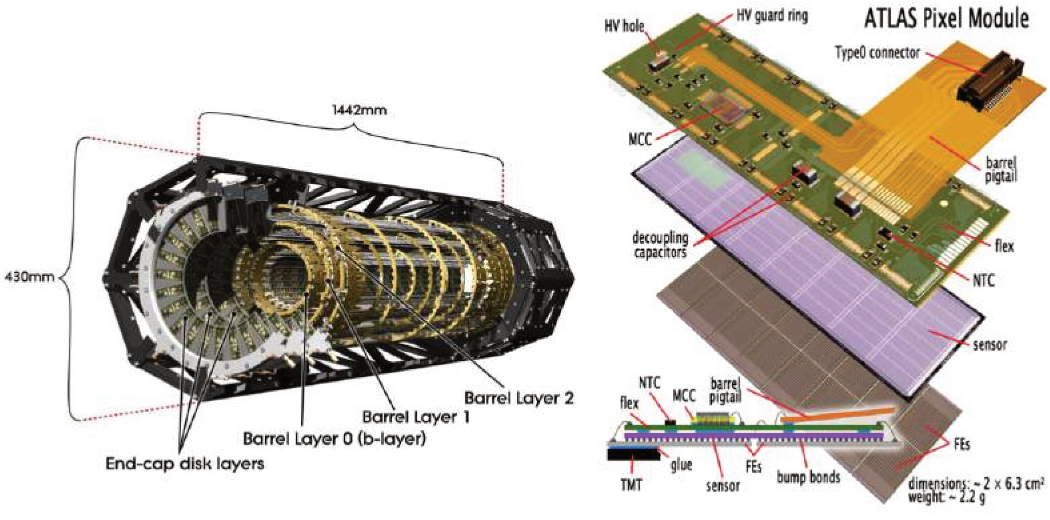

(a) (b)

Fig. 3.4: (a) Schematic of the ATLAS Pixel Detector. The detector consists of three barrel layers with three disks in each endcap sides. The detector modules are mounted on carbon fiber support structures with integrated cooling circuits. (b) Assembly and cut views of an ATLAS Pixel Detector module. The bump-bonded front-end chips are indicated as FEs [9].

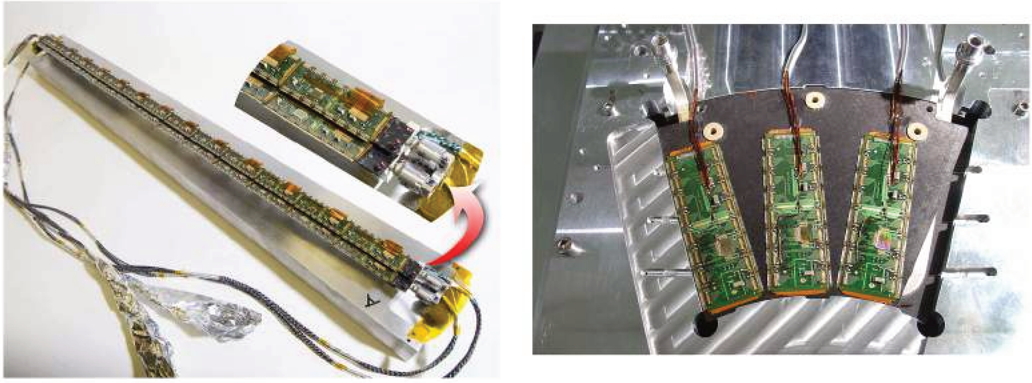

Fig. 3.5: Close up of bi-stave loaded with modules (left). Pixel disk sector during the attachment of modules (right). There are also three modules on the back of the sector [8].

Insertable B-layer (IBL)

The IBL is the newest member of the ID, added before Run-2 in order to cope with the increased number of pile-up interactions planned for Run-2, and to reduce radiation damage to the other pixel layers. The IBL is directly mounted on the beam pipe at a mean radious of 33.25 mm with a coverage of $|\eta| < 2.58$. The IBL pixel size is $50 \times 250\mu\text{m}^2$, smaller than the size of the pixels in the other layers. There are 224 modules on 14 staves,forming about 6 million channels. Figure 3.6 (top) shows a 3D view of IBL modules in the ATLAS geometry. Figure 3.6 (bottom) shows a collision event display with IBL recorded in June 2015. IBL has resulted in a significant improvement in the impact parmeter measurements. It also helps to distinguish between electrons from photon conversions, and electrons resulting from prompt decays. The material distribution is also changed accordingly to the insertion of the IBL in Run 2 (see fig 3.7).

Semiconductor Tracker

The Semiconductor Tracker (SCT), is made of silicon micro strips. The barrel and end-cap regions are composed of 4 concentric cylindrical layers and nine disks on each side of the interaction point, respectively. The total number of modules in the four barrel layers and 18 end-cap disks are 2112 and 988 respectively.

Figure 3.8 shows the SCT barrel module which is made of the sensor, the read-out chip, and the base-board. Each sensor consists of 768 strips in 80 μm pitch and the length of each strip is 128 mm. A pair of sensors are glued onto either side of the base-board. This provides a 2D position measurement. Unlike the sensors in the pixel detector, the SCT sensors are made of p-in-n type semiconductors. The SCT wafer is 285 μm in thickness with silicon strips implanted on one side. The strips are highly doped p-type semiconductors while the wafers are n-type silicon semiconductors

The end-cap disks consist of trapezoidal modules with strips radially disposed. There are three types of modules for the disks, and they are called inner, middle, and outer types. The pitch between the strips are $54 - 69$, $70 - 95$, and $71 - 90$ μm for inner, middle, and outer types, respectively.

Transition Radiation Tracker

The Transition Radiation Tracker (TRT) forms the outermost part of the ID. It extends the tracking volume in the radial direction thereby increasing the resolution of momentum measurement. The TRT is made of straw tube gas chambers. The gas used in Run-1 was Xenon mixed with CO_2 and O_2. During Run-2, the Xenon was replaced by a mixture of Xenon and Argon in some parts of the detector. This change was necessary because the TRT is plagued with leakages. Mixing Xenon with Argon significantly reduces the cost. The Xenon-Argon mixture absorbs X-rays while the CO_2 stabilizes the gas amplification. At the center of the straw tube (4 mm in diameter) is a Tungsten string which provides read-out.

The barrel region is divided at $z = 0$ and each half consists of $52,544$ tubes parallel to the beam axis. The transition radiation material, polypropylene fiber, is interleaved in between the tubes. The barrel and end-cap regions provide a coverage of $|\eta| < 0.7$ and $0.7 < |\eta| < 2.0$ respectively. A minimum of 36 and 22 tubes are traversed by a particle with $p_T > 0.5$ GeV in the barrel and endcap regions respectively. The endcap part is composed of $122,880$ tubes aligned radially in the $+z$ and $-z$ sides, respectively. Figure 3.9 shows the endcap wheel of TRT with the readout circuits along the outer ring. The TRT enhances pattern recognition and improves the momentum resolution within $|\eta| < 2.0$ which helps electron identification complementary to that of the calorimeter over a wide range of energies.

The efficiencies of data-taking by the ID are shown in table 3.2.

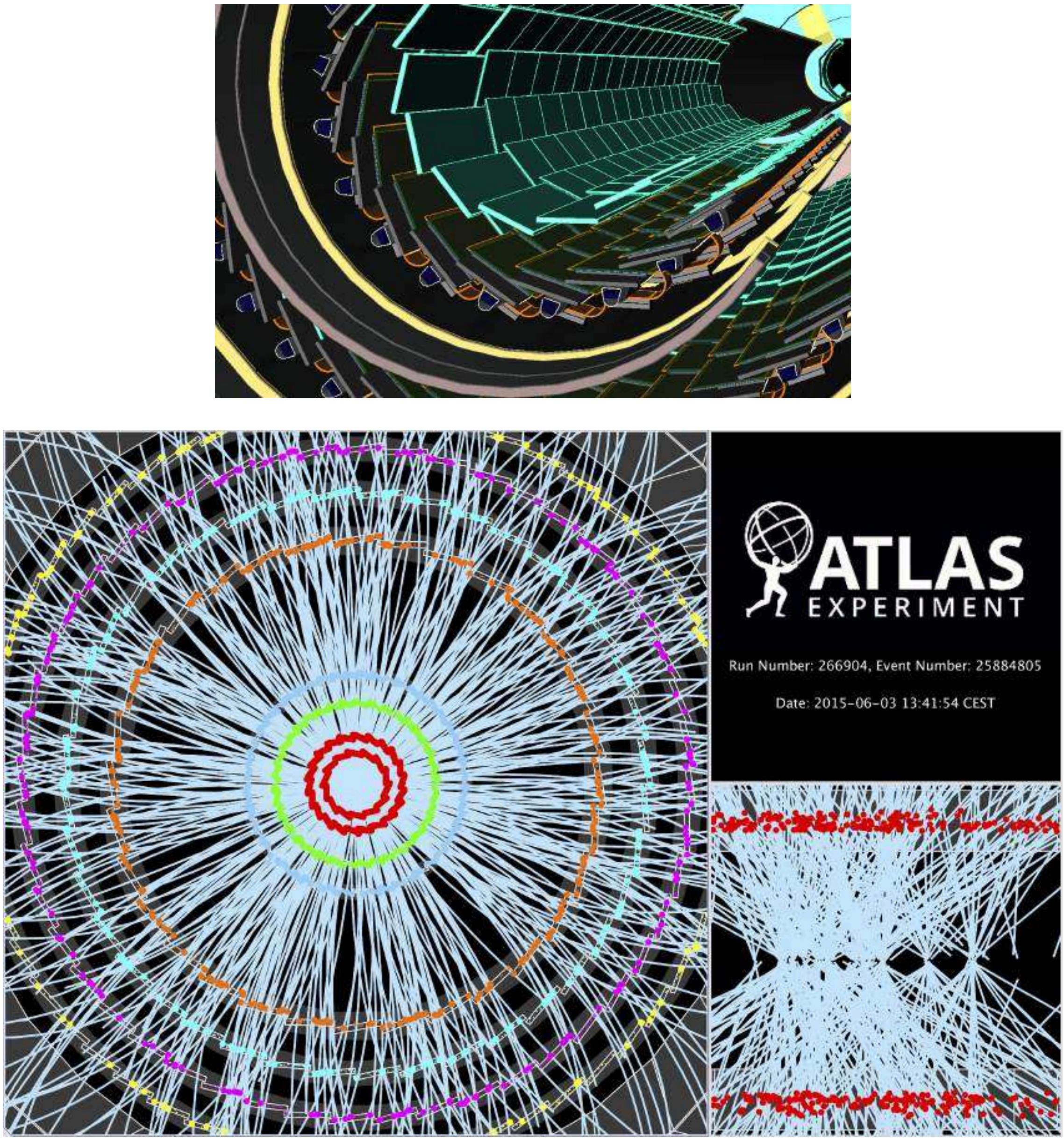

Fig. 3.6: The IBL modules highlighted in cyan in a 3D view, together with the other pixel layers (top) [11]. A collision event display after the IBL insertion (bottom), the IBL is highlighted in red together with the old innermost layer [12].

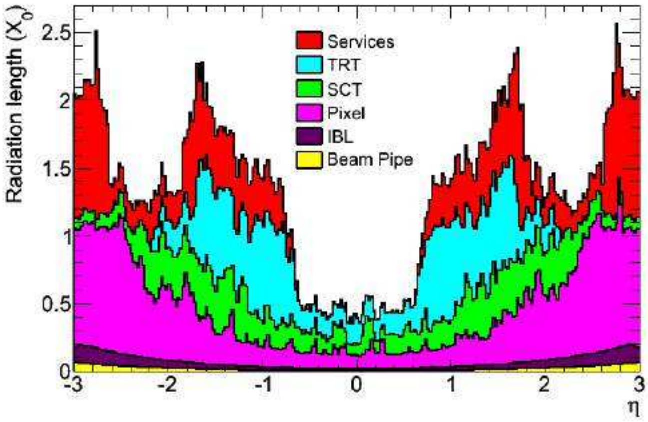

Fig. 3.7: Simulated material distribution expressed in the radiation length as a function of η. The IBL material amount is compared to the other Inner Detector components [11].

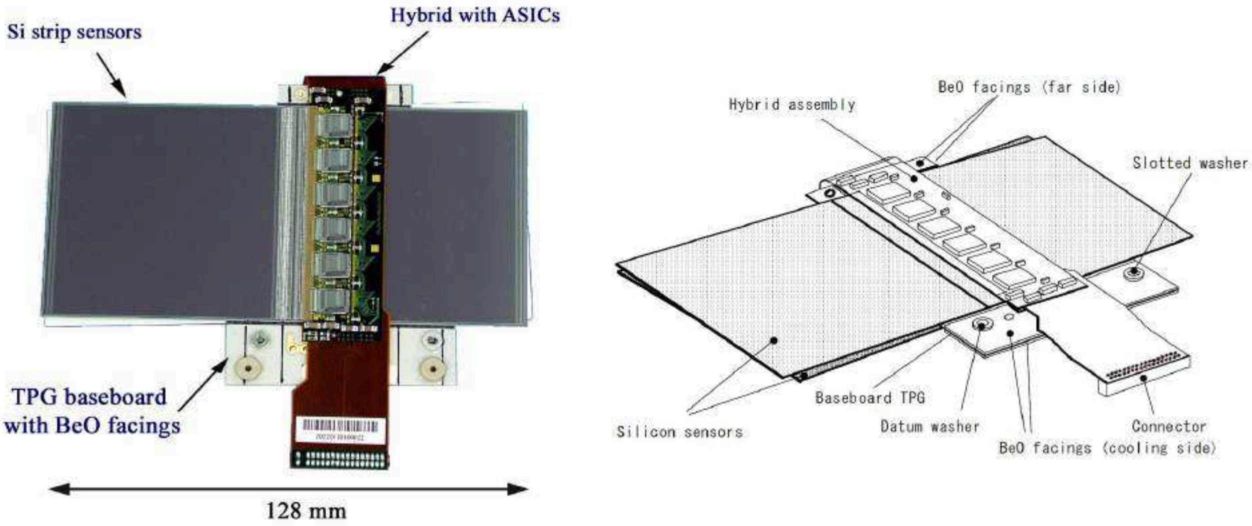

Fig. 3.8: Photograph (left) and drawing (right) of the SCT barrel module, showing its components. The high thermal conductivity between the coolant and sensors are kept by the base-board which is made of thermal pyrolytic graphite (TPG). The TPG base-board has also excellent electric conductivity so that it is used for applying the bias voltage to the micro strip sensors [13, 14].

Fig. 3.9: Photograph of TRT endcap wheel during assembly. The inner and outer C-fiber rings can be seen, as well as the first layer of straws and the first stack of polypropylene radiator foils beneath it [8].

Detector sub-system	2015 (in %)	2016 (in %)
IBL	93.8	99.8
Pixel	93.7	98.9
SCT	99.8	98.9
TRT	98.3	99.9
All	91.8	98.5

Table 3.2: The data taking efficiency of the various sub-system of the ID during the 2015 and 2016 data taking periods.

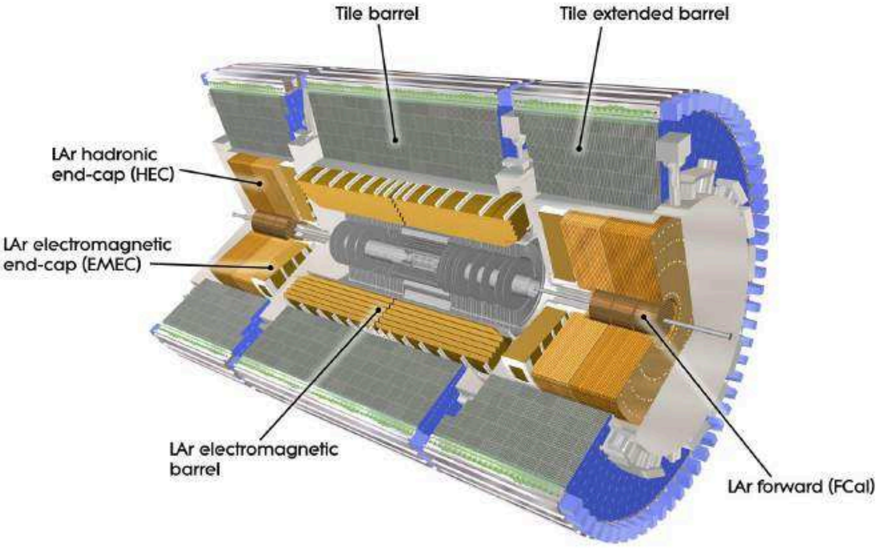

Fig. 3.10: The overview of the ATLAS calorimeter system.

3.2.3. Calorimeter

The calorimeter provides the measurement of energy and helps in the identification of electrons, charged hadrons, and neutral particles like photons and neutral hadrons which don't leave tracks in the ID. The calorimeter covers the range $|\eta| < 4.9$, which allows an accurate measurement of the missing transverse energy, $E_{\mathrm{T}}^{\mathrm{miss}}$.

The calorimeter consists of the electromagnetic calorimeter (EMCAL), and the hadronic calorimeter (HCAL). Both these sub-detectors are divided into barrel and end-cap regions. The EMCAL and the forward HCAL use liquid Argon (LAr) while scintillation tiles are used in the barrel region of the HCAL. The overview of the calorimeter is illustrated in figure 3.10. Figure 3.11 illustrates the electromagnetic and hadronic calorimeter positions and the forward calorimeters.

Electromagnetic Calorimeter

The EMCAL measures the energies of electrons and photons. It is made of lead plates in a structure with LAr layers. The barrel and end-cap regions provide coverages of $|\eta| < 1.475$ and $1.375 < |\eta| < 3.2$, respectively. Each of these is housed in their own cryostat. Like the TRT, the EMCAL barrel is divided at $z = 0$.

The Electromagnetic Endcaps (EMEC) of LAr calorimeters are segmented into coaxial wheels. The outer (inner) wheel covers $1.375 < |\eta| < 2.5$ $(2.5 < |\eta| < 3.2)$. The accordion structure of the EM calorimeter provides complete coverage in ϕ, without azimuthal cracks, while allowing fine segmentation in the $\eta - \phi$ plane(see fig 3.12). The thickness of lead in the absorber plates has been chosen to optimize the energy resolution in the η-direction. In the range of $|\eta| < 1.8$, a pre-sampler detector is used to correct for the energy lost by electrons and photons before entering the calorimeter. There are sets of three high voltage (HV) lines in the EM calorimeter. Two are used to maintain a HV, one at $+1000$ volts and the other at -1000 V. The third line is used to maintain a voltage across the purity

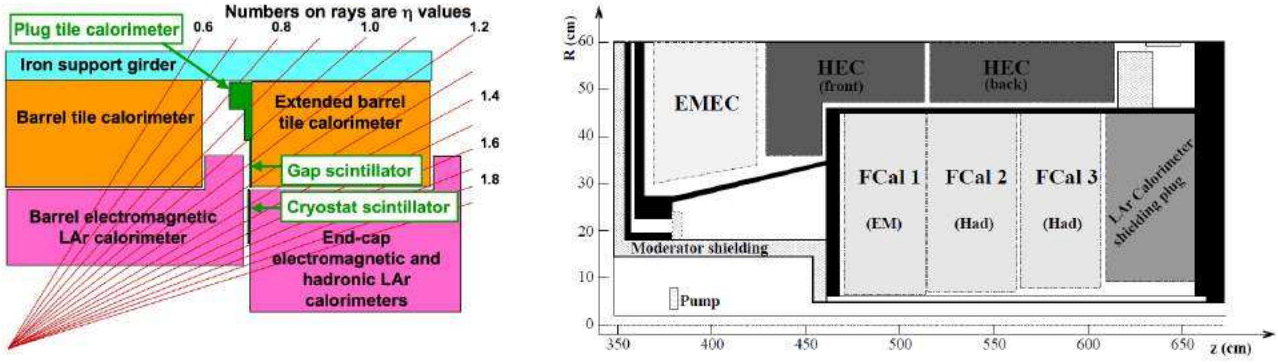

Fig. 3.11: Schematic of the transition region between the barrel and endcap cryostats, where additional scintillator elements are installed to provide corrections for energy lost in inactive material (not shown), such as the LAr cryostat and the inner-detector services (left). Schematic diagram showing the three FCal modules located in the endcap cryostat (right). The material in front of the FCal and the shielding behind it are also shown. The diagram has a larger vertical scale for clarity [8].

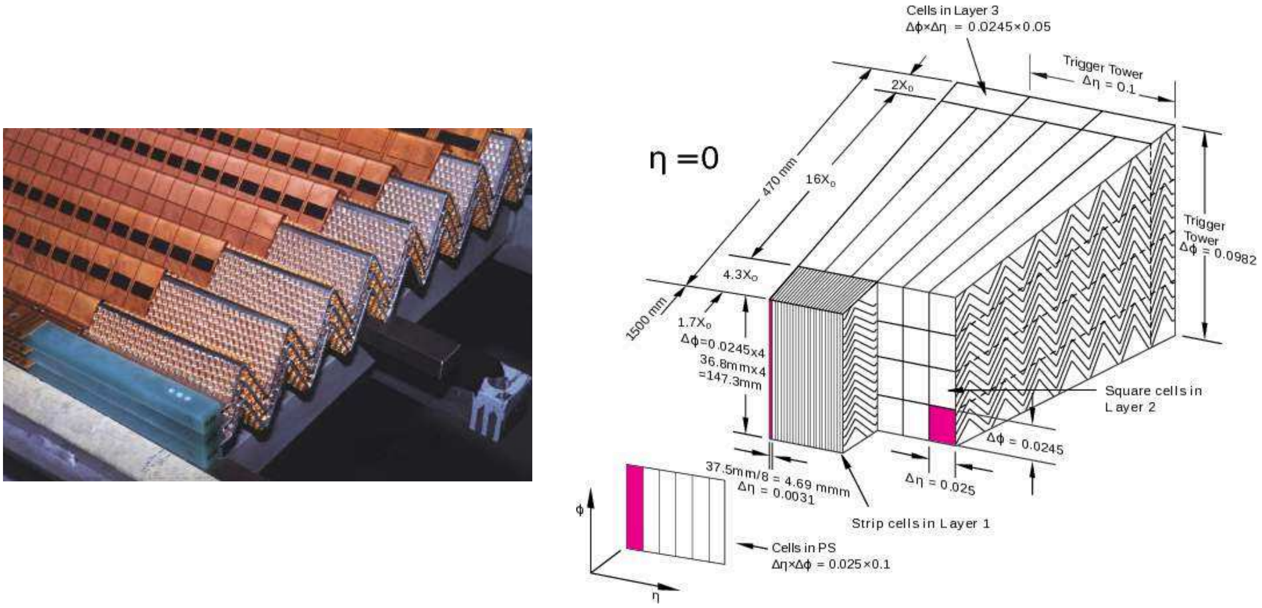

Fig. 3.12: The photographed accordion shape of LAr calorimeter (left), the honey-comb structured spacers are also visible. Sketch of a barrel module where the different layers are clearly visible with the ganging of electrodes in ϕ (right). The granularity in η and ϕ of the cells of each of the three layers and of the trigger towers is also shown.

probes, which measure the levels of impurity in LAr.

Hadronic Calorimeter

The ATLAS hadronic calorimeter is consists of two sub-systems.

Tile calorimeter: The scintillation tile hadronic calorimeter is installed directly outside the LAr EM calorimeter. The coverage is $|\eta| < 1.0$ ($0.8 < |\eta| < 1.7$) for the (extended) barrel(s) as shown in fig 3.11. It uses steel as the absorber and scintillating tiles as the active material. There are 64 modules installed azimuthally in the barrel and extended barrels. The inner and outer radii of the barrel and extended barrels are 2.28 m and 4.25 m, respectively.

Hadronic endcap calorimeter: The Hadronic Endcap Calorimeter (HEC) consists of two wheels for each endcap. The front wheel is closer to the interaction point than the back wheel. These two sets of front and back wheels cover $1.5 < |\eta| < 3.2$. Each wheel is composed of 32 identical wedge-shaped modules which are divided into two segments in depth, have a total of four layers per endcap. The front endcap wheels are made of 25 mm thick parallel copper plates, while back wheels use 50 mm copper plates. The inner and outer radii of the copper plates are 0.475 and 2.03 m, respectively. The radius of copper plates in the front wheel is 0.372 m in the region overlapping with the forward calorimeter. There are LAr gaps in between the copper plates, providing the active medium for the sampling calorimeter.

Forward Calorimeter

The Forward Calorimeter (FCal) is integrated into the endcap cryostats. It provides a good coverage and reduces radiation background in the muon spectrometer. FCal covers the forward region of $3.1 < |\eta| < 4.9$, and consists of three modules in each endcap: the LAr EM module uses copper for the absorber, while the other two are made of tungsten, which mostly measure the hadronic energy. Each module consists of a metal matrix, with regularly spaced longitudinal channels filled with the electrode structure consisting of concentric rods and tubes parallel to the beam axis. Table 3.3 shows the efficiencies of the various sub-detectors during 2015 and 2016. The major reasons for the inefficiencies tend be HV trips and noiseburts. When such an HV trip occurs, the operating voltage jumps suddenly and the corresponding energy measurements become unreliable. Thus, the lumiblocks[a] in which these HV trips occur are removed from the data and are not considered for physics analyses.

Detector sub-system	2015 (in %)	2016 (in %)
EMCAL	99.5	99.3
Tile	100	98.9
HEC	99.6	99.4
LAr FCAL	99.5	99.4
All	99.5	98.6

Table 3.3: The data taking efficiency of the various sub-systems of the calorimeter during the 2015 and 2016 data taking periods.

---

[a] A lumiblock is defined as roughly one minute of data-taking

3.2.4. Muon Spectrometer

The muon spectrometer (MS) is built to measure charged particles that exit the calorimeter.

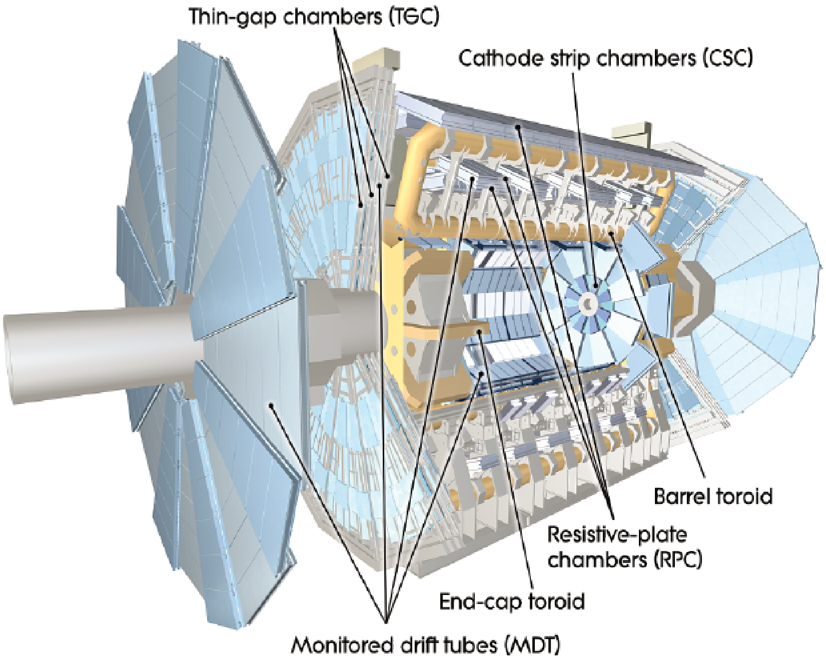

Fig. 3.13: Cut-away view of the ATLAS muon system.

The layout of the MS is shown in Fig. 3.13. The barrel toroid provide the magnetic field in the pseudo-rapidity range $|\eta| < 1.4$, while two end-cap magnets which are inserted in both ends of the toroid provide the magnetic field in the region $1.6 < |\eta| < 2.7$. In the transition region, $1.4 < |\eta| < 1.6$, the magnetic field is provided by a combination of the barrel and end-cap magnets. The shape of the magnetic fields in these regions as a function of η is very complex, as shown in Fig. 3.14.
Tracks in the barrel region are measured in three concentric cyclindrical chambers while those in the transition and end-cap regions are measured by planar chambers installed perpendicular to the beam axis. These different sub-detectors of the muon system are: Monitored Drift Tube chambers (MDT), Cathode Strip Chambers (CSC), Resistive Plate Chambers (RPC), and Thin Gap Chambers (TGC), as shown in fig. 3.13. The coverage of the MDTs include the range $|\eta| < 2.7$, whereas, the CSC provides a coverage of $2.0 < |\eta| < 2.7$. The trigger signals are provided by the RPC and TGC in the $\eta-$ranges $|\eta| < 1.05$ and $1.05 < |\eta| < 2.7$ respectively.
The essential element of the MDT is a pressurized drift tube with a diameter of 29.97 mm, composed of a mixture of Ar (93%) and CO_2 (3%) gases at 3 bar. These gases are selected because of good ageing properties. For example, formation of polymers, which tend to reduce signal pulse heights, are not observed thanks to the lack of Hydrogen. The transverse and longitudinal sections of an MDT are shown in 3.15. The electrons resulting from ionisation are collected by the central tungsten-rhenium wire which is held at a potential of 3080 V. The connections to the readout electronics and the HV power supply are placed at opposite ends of the tube. Building the MDT chambers out of individual drift tubes allows a high mechanical precision while maintaining robustness, and operational reliability because the failure of one tube does not affect the function of the rest. The MDT has a resolution of 80 μm but can only be used with counting rates upto 150 kHz/cm^2. These counting rates tend to be

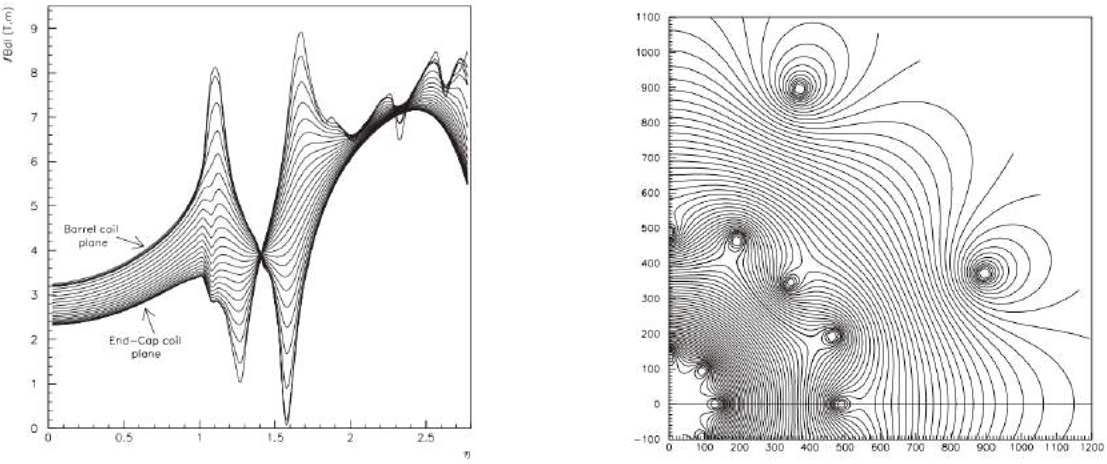

Fig. 3.14: The bending power dependence on pseudo rapidity η (left). The structure of the toroidal magnetic field in the transition region on the x-y plane (right) [15].

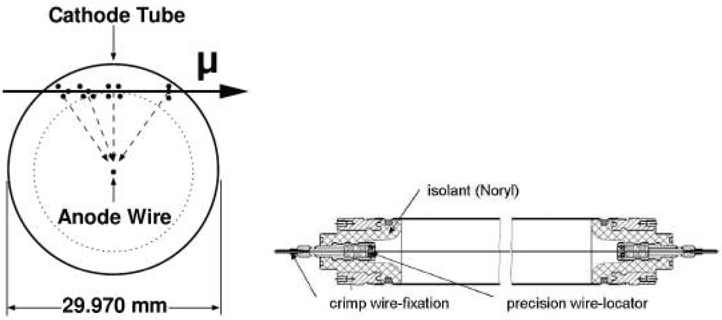

Fig. 3.15: The transverse and longitudinal section of the MDT drift tube.

higher in the forward region which necessitates the use of the CSCs.

The CSCs combine high spatial, time, and double track resolution with low neutron sensitivity and extend the operational point upto counting rates of about 1000 Hz/cm^2. The CSCs are divided into large and small chambers in ϕ. It consists of two disks with eight small and eight large chambers in each disk. The CSC's are multiwire proportional chambers. The wires act as anodes while the plates, which mount the cathode, are segmented into strips which run parallel and perpendicular to the wires. The tracks are then obtained by interpolation between the charges induced on neighbouring cathode strips. The anode wire, on the other hand, is not connected to the read-out electronics.The CSC offers a resolution of 60 μm which is significantly better than what the MDT offers.

The RPCs are gas chambers which use a mixture of $C_2H_2F_2$ (97%) and C_4H_{10} (3%). The RPCs provide a spatial and time resolution of 1mm and 1ns respectively. RPC-1 and RPC-1 are used to trigger at low p_T ($6 - 9$ GeV), and RPC-3 is used to trigger on events with higher p_T ($9 - 35$ GeV).

The TGCs, on the other hand, relies on multi-wire proportional chambers (MWPC), with copper wires that run radially and carbon strips that run in the ϕ direction. This results in a possibility of 2D position measurement with very fast response times for triggering.

The efficiencies of the various parts of the the muon spectrometer during these periods are summarized in Table 3.4.

Detector sub-system	2015 (in %)	2016 (in %)
MDT	100	99.8
RPC	100	99.8
CSC	100	99.9
TGC	100	99.9
All	99.9	99.6

Table 3.4: The data taking efficiency of the various sub-system of the muon spectrometer during the 2015 and 2016 data taking periods.

3.2.5. Trigger

The collision rate in the LHC is incredibly high and storing information from every collision is not possible due to immense requirements of storage capacity. In order to reduce the rate, it is important to select events which are more likely to be useful for the various physics analyses. The trigger system is designed to select events of interest and to lower the data recording rate from 40 MHz to about $500 - 1000$ Hz.

The ATLAS trigger system is divided into three levels. The first level is based on customized hardware and uses information with coarse granularity from the calorimeter and muon systems. The second and third levels are together called the higher level trigger (HLT) and uses software algorithms which exploit the granularity of the detectors. Figure 3.16 shows the overview of the ATLAS trigger and data-acquisition (DAQ) flow.

Level-1 trigger

The L1 trigger is based on the information gathered by the calorimeter and muon system. It reduces the event-rate from 40 MHz to about 100 kHz. Since the events are recorded on-the-fly, the trigger

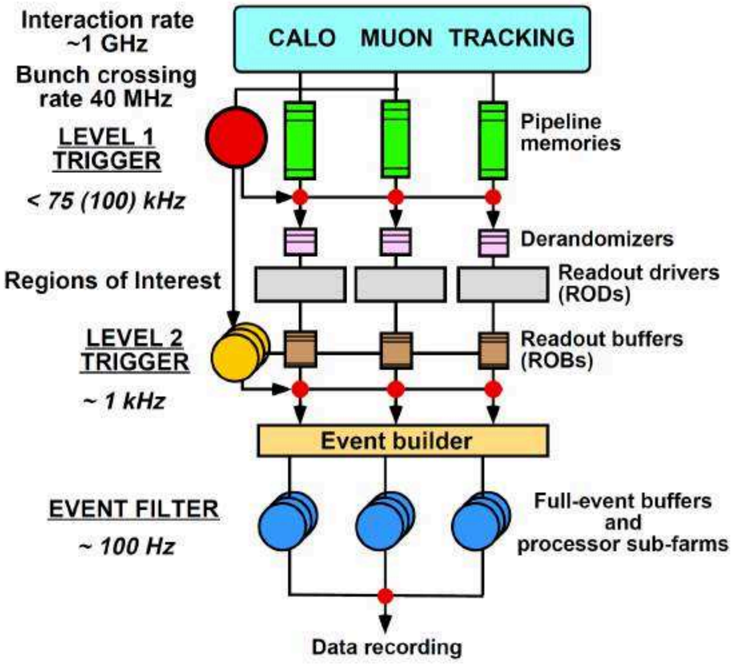

Fig. 3.16: Block diagram of the Trigger/DAQ system [16]. Along with the levels of trigger system, the original design rate acceptances are indicated.

decisions need to be made in time period as low as $2.5\ \mu$s. During this time, data from all detectors are sent down the pipelines for further processing in the level-2 trigger systems. The L1 decision is typically based on the transverse momentum threshold and the multiplicity of various physics objects, such as electrons, muons, jets, and photons, in the events. The algorithms use the energy deposited in the calorimeter with a granularity of 0.1×0.1 in the $\Delta\eta \times \Delta\phi$ frame. A region of interest (ROI) is associated to the objects which pass the L1 thresholds. This information is then passed on to the level 2 trigger for further processing.

Higher level trigger

The level-2 and event filter are together called the HLT. The L2 algorithms are designed to reduce the trigger rates down to a few kHZ. The L2 latency is about $10\ \mu$s with averaging processing times of about 40 ms. The ROI information from L1 is at level-2 used to further reduce the event rates.

The event filter uses the L2 information such as the seeds to increase the precision. The algorithms, at this level, are very similar to the reconstruction algorithms used offline. At this stage, the event rate is reduced to less than 1kHz with processing times of about 4 s. Once the event is selected by the HLT, it is permanently stored at the CERN Computing Center (a.k.a Tier-0) and processed by the offline reconstruction software frameworks which include the most up-to-date version of calibrations etc. The processed data is then distributed to the grid computing centers located all over the globe, as described below.

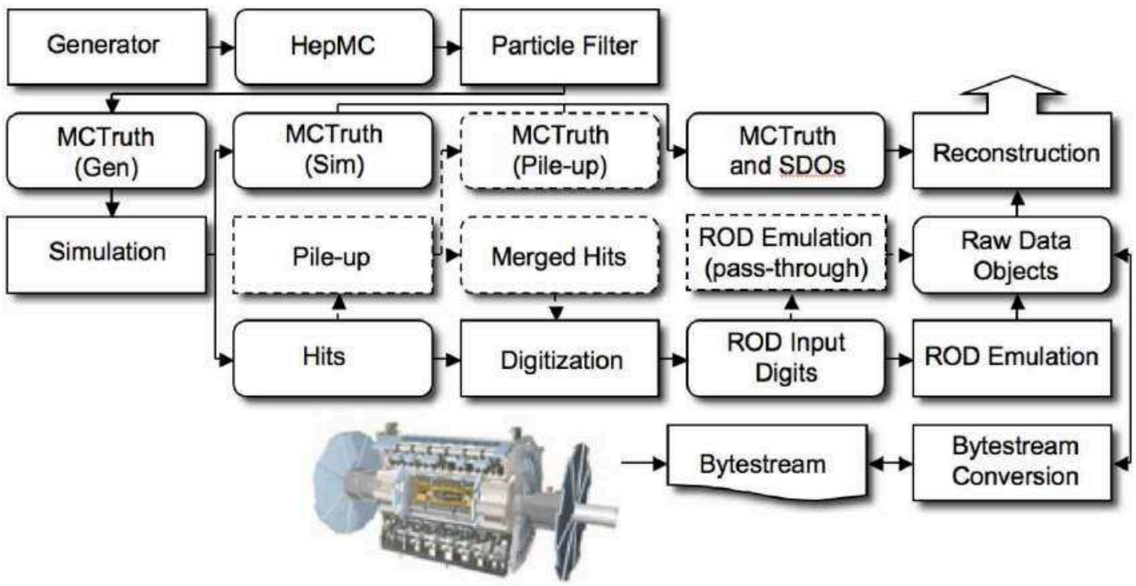

Fig. 3.17: The flow of the ATLAS simulation software, from event generators (top left) to reconstruction (top right). Algorithms are placed in square-cornered boxes and persistent data objects are placed in rounded boxes. The optional pileup portion of the chain, used only when events are overlaid, is dashed. Generators are used to produce data in HepMC format. Monte Carlo truth is saved in addition to energy depositions in the detector (hits). This truth is merged into Simulated Data Objects (SDOs) during the digitization. Also, during the digitization stage, Read Out Driver (ROD) electronics are simulated.

3.2.6. Simulation

The simulation of the proton-proton collisions is based on random number generation using the Monte-Carlo (MC) method. The various stages involved in a full simulation and fast simulation are shown in Figure 3.17 . The data recorded by the detector is eventually processed and stored in a data format that is used as the output format for the simulation. In this section, the computing tools, both software and resources, used in the collaboration are discussed.

Event generation

In order to simulate the physics processes originating from the LHC collisions, event generators are used to produce events as they are predicted to occur in theory during the experiment. For each event, the four-momenta of the final state particles are provided by for each pp collision.

The event generation is done in stages through the *hard process*, *parton shower*, and *hadronization*. The hard process refers to the main interaction between the partons during a head-on collision. During the stage involving the parton shower, photon and gluon emissions are generated using QED and QCD, respectively. Finally, during hadronization, the process of formation of various hadrons from quarks is generated using results from various QCD experiments since this process is non-perturbative and cannot be solved analytically. The event generators used in this thesis are CalcHEP, PYTHIA6, PYTHIA8, HERWIG, SHERPA, and POWHEG. Details about which generators are used to simulated which processes are given in section.

Detector simulation

Once the collision events are generated, they are passed through a process called detector simulation. In the ATLAS experiment, two approaches for detector simulation are used, *fast simulation* and *full simulation*.

Full simulation is based on GEANT4 and simulates the interaction between the final state particles and the detector components and material. The electronic detector readout is also simulated. The *digitization* process emulates the detector response. Finally, the process of *reconstruction* uses the digitized detector response to generate physical objects such as tracks and calorimetric clusters.

The full simulation is expected to reproduce, in detail, the physics phenomena occurring during the particle detection, but its major drawback is that it consumes vast amounts of computing resources and requires a lot of time per event (roughly 15 minutes per event). This issue was overcome by developing a fast simulation called ATLFAST. It simplifies the showering process in the calorimeter; a process that takes up 80% of the entire simulation time. This is done by removing electromagnetic particles with low energy and replacing them by pre-simulated showers. The three main detector sub-systems (ID, calorimeter, and MS) can be simulated using this method. Each system can independently employ either fast simulation or full simulation based on the requirements. This strategy significantly improves the speed of simulation. For example, if the ID uses full simulation while the calorimeter and the MS use fast simulation, the speed of simulation is increased ten-fold compared to full simulation in all sub-systems.

3.2.7. ATLAS Distributed Computing

The high-level triggers in ATLAS record each event in the 'RAW' format at the rate of 1 kHz. In this format, each event takes up $1-2$ MB, depending on the pile-up conditions. This cannot analyzed easily. The RAW events are transferred from the HLT farm to the CERN Tier-0 computing center which is responsible to maintain a copy of the RAW data and to convert it into more manageable formats such as the Event Summary Data (ESD) format or the Analysis Object Data (AOD) format[b]. The Tier-0 computing center distributes the raw data and the derived formats to the Tier-1 centers for archival and downstream accessibility respectively. A typical user in the collaboration cannot access the Tier-0 facility directly. This makes it necessary to distribute the raw data downstream to the Tier-1 centers. There are 10 ATLAS Tier-1 centers situated across the globe. These centers store a second copy of all the raw data as a backup in-case of possible failure or accidents in the Tier-0 facility. The Tier-1 centers also produce the derived versions of the raw data and pass the replicas downstream to the Tier-2 centers. These are located at 155 collaborating universities across the globe.

The Tier 2 sites store two copies of the AOD in order to ensure reliable and fast access to the data. These sites are also computing resources used for producing MC simulations for various physics processes. Copies of these simulations are passed back upstream to the Tier-1 sites for long-term storage and re-processing.

Most physicists in the collaboration interact directly with the Tier-3 sites. A Tier-3 site is generally a computing cluster with enough storage and computing power required to perform routine tasks. It also provides a connection to the Worldwide LHC Computing Grid, most commonly known as the *grid*. For large-scale tasks that require high computing power and storage, users can submit the tasks to the LHC grid. These tasks are then performed at the Tier-2 and Tier-3 sites. In most cases, the user reduces the size of the files on which the analysis is performed by applying basic cuts that remove events irrelevant to their analysis. This significantly reduces the size of the files and makes analysis at the Tier-3 site feasible. Final stages of most analyses, such as statistical interpretations or graphic visualizations, are performed at the local Tier-3 sites using common analysis tools such as ROOT which are provided and maintained by the respective sites.

---

[b] Most users begin their analysis from the AOD format

4. Particle and object identification

In this chapter, the reconstruction and identification of different physics objects are discussed. These physics objects are tracks, vertices, photons, electrons, muons, taus, jets, and missing transverse momentum.

Figure 4.1 shows a partial transverse cut view of the ATLAS detector with many particles traversing.

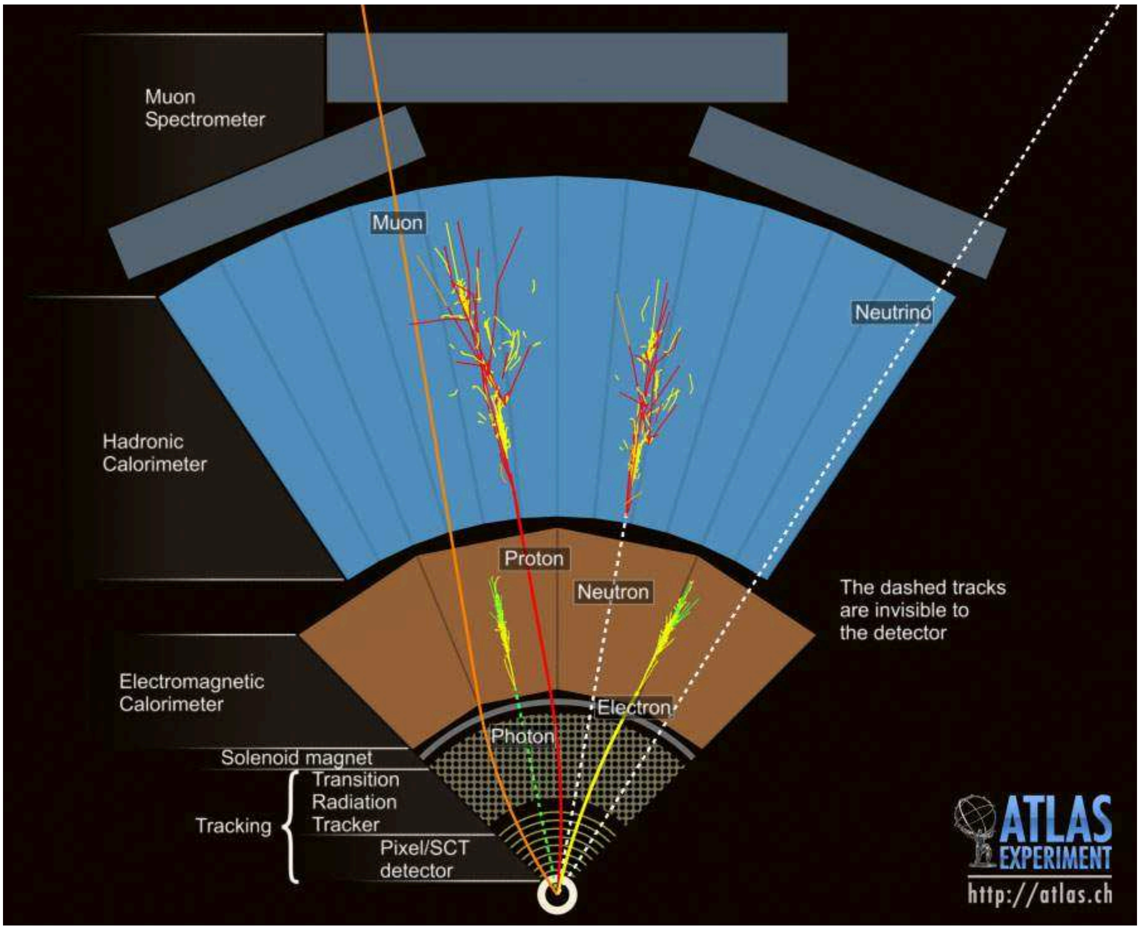

Fig. 4.1: An overview of particle identification in the ATLAS detector. The solid and dashed curves show the tracks of charged and neutral particles. Arising from the interaction region (beam axis), the muon goes through the whole detector while being tracked by the Inner Detector and the Muon Spectrometer, the electron and the photon are caught by mainly the EM calorimeter with and without being tracked, respectively, the proton and the neutron are trapped by mainly the hadronic calorimeter with and without leaving a track, respectively, and the neutrino passes through the entire detector without leaving its signal in any of the sub-detectors.

4.1. Electrons and photons

Electrons and photons have similar signatures in the EMCAL. The use of these signatures to reconstruct electrons and photons is described below.

Electrons

Reconstruction

An electron leaves hits in the ID and then deposits some energy in the EMCAL. Reconstruction of the electron seeded by the EM cluster associated to the track in the ID is then possible. The clustering is done using the sliding-window algorithm [17] in the EMCAL. The algorithm consists of three steps:

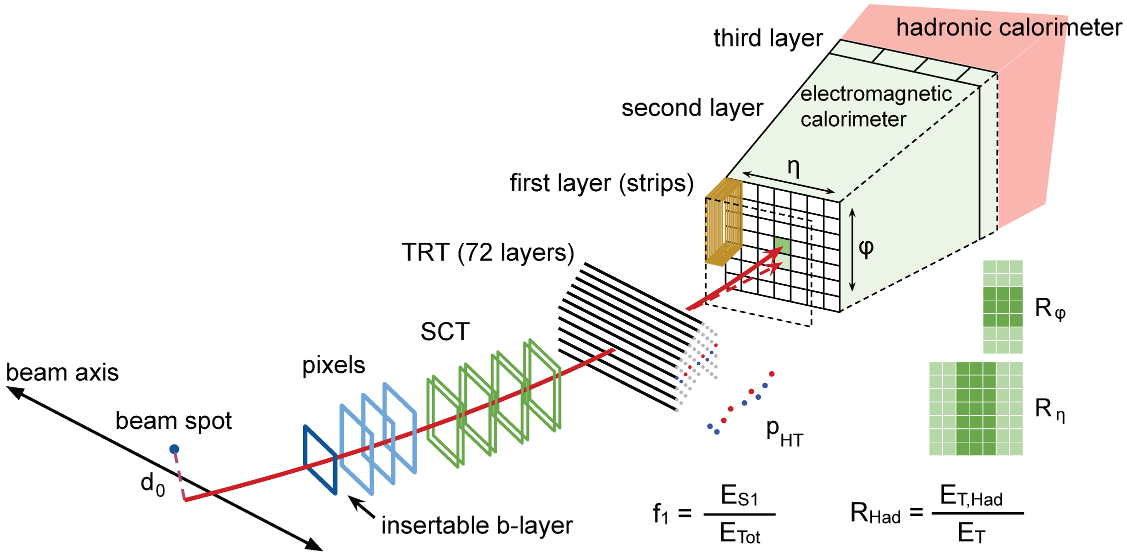

Fig. 4.2: A schematic representation of the various sub-detectors the electrons pass through and the variables corresponding to each layer of each sub-detector that differentiate electrons from other charged particles such as light pions.

- Tower building
  The EM calorimeter is divided into 200×256 squares in the $\eta - \phi$ plane. Contributions from each layer are summed up in each square thus forming a 'tower'.
- Sliding-window seed finding
  A window of 3×5, in units of 0.025×0.025, scans each element of the tower grid in steps of $\Delta\eta$ and $\Delta\phi$. When the scan finds the total transverse energy above a pre-defined threshold (2.5

GeV), a seed is formed. The clustering algorithm used to form the clusters around the seed removes duplicates from the clusters.

- Track reconstruction: This involves pattern recognition and a fit of the track. For pattern recognition, ATLAS uses the pion hypothesis for the energy loss due to interaction with the detector material which is then improved a modified algorithm which allows upto 30% energy loss due to interactions of the track with the detector material to take into account possible bremsstrahlung. A track seed consists of three hits in different silicon layers. If this seed corresponds to a transverse momentum larger than 1 GeV and cannot be extended to a full track of at least 7 hits using the pion hypothesis, and corresponds to an energy deposit in the EM cluster region of interest, the new pattern recognition algorithm is used with the electron hypothesis that allows for higher energy loss. Tracks are then fit with either the electron or pion hypothesis using a global χ^2 Track Fitter [18].

- Electron specific track fit: The reconstructed tracks are loosely matched to the EM clusters using the distance in η and ϕ between the direction of the track and the position of the energy deposit in the middle layer of the calorimeter and the cluster barycenter. This matching also takes into account the possibility of bremsstrahlung. Tracks that have a high enough number of precision hits in the silicon detector (> 3), and are loosely matched to electron clusters, are refit using an optimized Gaussian Sum Filter [19].

- Electron candidate reconstruction: The final step of the reconstruction procedure is completed after matching the track of the candidate to a cluster seed. A matching similar to the one described above is used for the refit track with tighter conditions. When several tracks match the cluster seed, the choice of the primary track is made using an algorithm that relies on the distance between the matched track and the cluster seed. The electron cluster is reformed using a 3×7 (5×5) longitudinal towers in the barrel (end-cap) regions of the EM calorimter. The energy of the electron is then calibrated to the original energy of the electron using various multivariate techniques [20] which are based on simulations.

Electron identification

This method of reconstructing an electron candidate is not perfect and often mis-identifies other particles as electrons. In order to reduce the mis-identification, cut-based and log-likelihood based menus are built using various discriminating variables in different parts of the various detector components. A schematic of such variables is shown in the figure above. A description of the variables used for electron identification is given in Table 4.1.

Two algorithms for electron ID are available in ATLAS: the cut-based method and the likelihood method. The standard ID algorithm used for physics analyses is the likelihood method (LLH). The LLH is a multivariate method that uses the signal ($Z \rightarrow ee$) and background (di-jet MC) probability distribution functions (PDFs) of the variables defined in Table 4.1. Using these PDFs, a probability is evaluated for the candidate to be signal or background. The signal and background probabilities are then used to define a discriminant. A cut is then applied on this discriminant. The value of the cut is determined by the working point that is to be used. There are three working points available using LLH: *loose*, *medium*, and *tight*. These working points are designed such that all events that pass the *tight* requirement also pass the *medium* and *loose* requirement. Furthermore, the electrons selected by the *medium* working point are also selected by the *loose* working point. The signal and background efficiencies corresponding to these working points are shown in Figure 4.3.

Table 4.1: Definitions of electron discriminating variables.

Type	Description	Name
Hadronic leakage	Ratio of E_T in the first layer of the hadronic calorimeter to E_T of the EM cluster (used over the range $\|\eta\| < 0.8$ or $\|\eta\| > 1.37$)	R_{had_1}
	Ratio of E_T in the hadronic calorimeter to E_T of the EM cluster (used over the range $0.8 < \|\eta\| < 1.37$)	R_{had}
Back layer of EM calorimeter	Ratio of the energy in the back layer to the total energy in the EM accordion calorimeter. This variable is only used below 100 GeV, because it is known to be inefficient at high energies.	f_3
Middle layer of EM calorimeter	Lateral shower width, $\sqrt{(\Sigma E_i \eta_i^2)/(\Sigma E_i) - ((\Sigma E_i \eta_i)/(\Sigma E_i))^2}$, where E_i is the energy and η_i is the pseudorapidity of cell i and the sum is calculated within a window of 3×5 cells	W_η
	Ratio of the energy in 3×3 cells over the energy in 3×7 cells centered at the electron cluster position	R_ϕ
	Ratio of the energy in 3×7 cells over the energy in 7×7 cells centered at the electron cluster position	R_ϕ
Strip layer of EM calorimeter	Shower width, $\sqrt{(\Sigma E_i (i - i_{\max})^2)/(\Sigma E_i)}$, where i runs over all strips in a window of $\Delta\eta \times \Delta\phi \approx 0.0625 \times 0.2$, corresponding typically to 20 strips in η, and $i_{\max}$ is the index of the highest-energy strip	$W_{s,tot}$
	Ratio of the energy difference between the largest and second largest energy deposits in the cluster over the sum of these energies	ΔE_{max}
	Ratio of the energy in the strip layer to the total energy in the EM accordion calorimeter	f_1
Track quality	Number of hits in the innermost pixel layer; discriminates against photon conversions	n_{Blayer}
	Number of hits in the pixel detector	n_{Pixel}
	Number of total hits in the pixel and SCT detectors	n_{Si}
	Transverse impact parameter with respect to the beam-spot	track d_0
	Significance of transverse impact parameter defined like the ratio of track d_0 and its uncertainty	σ_{d_0}
	Momentum lost by the track between the perigee and the last measurement point divided by the original momentum	$\Delta E/P$
TRT	Likelihood probability based on transition radiation in the TRT	$e_{ProbabilityHT}$
Track-cluster matching	$\Delta\eta$ between the cluster position in the strip layer and the extrapolated track	$\Delta\eta$
	$\Delta\phi$ between the cluster position in the middle layer and the track extrapolated from the perigee	$\Delta\phi$
	Defined as $\Delta\phi$, but the track momentum is re-scaled to the cluster energy before extrapolating the track from the perigee to the middle layer of the calorimeter	$\Delta\phi_{res}$
	Ratio of the cluster energy to the track momentum	E/p

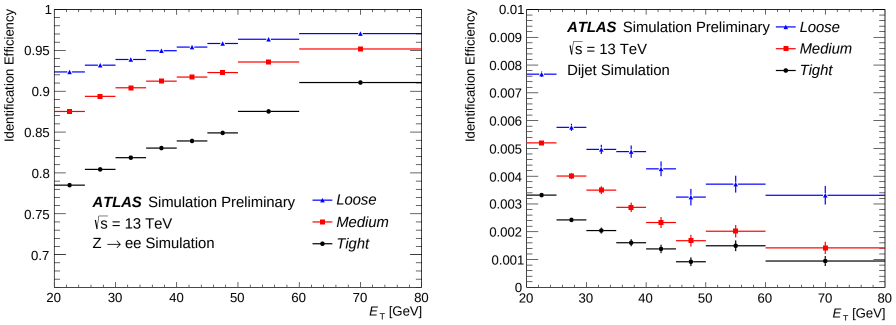

Fig. 4.3: The efficiency to identify electrons from $Z \to ee$ (left) and the efficiency to identify identify hadrons as electrons estimated using simulated dijet samples. The efficiencies are measured with respect to reconstructed electrons [21].

The cut-based method uses a set of rectangular cuts on the variables described in table 4.1. The method used to optimize the cut-based method is described in detail in Appendix B.

Electron isolation

Requiring the electrons to fulfill isolation criteria helps further discriminate between the signal and background. The isolation variables quantify the energy of the particles detected around the electron candidate. This allows to differentiate prompt electrons from non-isolated candidates such as those being produced from heavy flavor decays or photon conversions. Two discriminating variables are defined as follows:

- E_T^{cone20}: The sum of the transverse energies of topological clusters in the calorimeter within a cone of $\Delta R < 0.2$ around the lepton candidate. The transverse energy contained in a rectangular cluster of size $\Delta\eta \times \Delta\phi = 0.125 \times 0.175$ centered around the cluster barycentre is subtracted.
- $p_T^{varcone20}$: The scalar sum of the transverse momenta of all tracks that certain pass track-quality requirements within a cone of $\Delta R = \min(0.2, 10\text{ GeV}/E_T)$ around the candidate track and originating from the reconstructed primary vertex of the hard collision excluding the tracks associated to itself.

Various operating points are defined using these variables, as shown in Table 4.2

Electron trigger

Besides the reconstruction, identification, and isolation, the efficiency to find and select an electron in the ATLAS detector also depends on the L1 and HLT triggers. The L1 electron triggers use the energies deposited in the EM and hadronic calorimeters with regions of $\Delta\eta \times \Delta\phi = 0.4 \times 0.4$ to calculate the energy in the inner region and the surrounding (isolation) region. The E_T thresholds are set differently for different η regions. A veto on the hadronic leakage is applied, by requiring the energy deposits in the hadronic calorimeter behind the core of the EM cluster to be less than a certain value w.r.t. the EM cluster energy. Furthermore, an isolation cut can also be applied using the cluster energy around the EM candidate relative to the cluster transverse energy. The cuts on isolation and hadronic leakage are used only for the electron candidates with $E_T < 50$ GeV.

At the HLT, electron candidates are selected in several stages in such a way that the earlier steps reject candidates and thus reduce the event rate to a level where more precise algorithms can be used within the allowed latency range. These steps are as follows:

Operating point	calorimeter isolation	track isolation	total efficiency
LooseTrackOnly	-	99%	99%
Loose	99%	99%	98%
Tight	96%	99%	95%
Gradient	$0.1143\% \times E_T + 92.14\%$	$0.1143\% \times E_T + 92.14\%$	90/99% at 25/60 GeV
GradientLoose	$0.057\% \times E_T + 95.57\%$	$0.057\% \times E_T + 95.57\%$	95/99% at 25/60 GeV

Operating point	calorimeter isolation	track isolation
FixedCutLoose	0.20	0.15
FixedCutTightTrackOnly	0.06	0.06

Table 4.2: Different operating points using the electron isolation variables. The upper table illustrate the efficiencies corresponding to requirements that can be constant or vary as a function of the energy. The E_T used for Gradient and GradientLoose is in GeV. The fixed requirement operating points are shown in the lower table. In this case, the upper cut on the isolation variables, for a given operating point is always constant.

- Fast EM calorimeter algorithms are used to build clusters from the calorimeter cells in the region of interest identified at L1. Cuts are applied on R_{had}, R_η, E_{ratio}, and E_T of the electron candidate. Tracks with a minimum p_T reconstructed using fast algorithms are matched to clusters within $\Delta\eta < 0.2$.
- The HLT then employs more precise algorithms based on candidates selected in the first step. Additional cuts are applied on various shower shape variables to reduce the rate further before precision tracking.
- Clusters corresponding to the candidates are matched to precision tracks and extrapolated to the second layer of the EM calorimeter within $\Delta\eta < 0.05$ and $\Delta\phi < 0.05$.
- The ID of electrons at the HLT is performed using the variables in Table 4.1, same as the offline identification.

The efficiency to find and select an electron in the detector are measured with data as well as simulations using a tag-and-probe method. The difference between the two are used as scale factors which are dependent on the E_T and η of the electron candidate. Further details concerning the methods used for these efficiency measurements can be found in Ref. [21].

Photons

Since photons are electrically neutral, they don't leave tracks in the ID unless they convert into a pair of leptons. This makes them invisible in the entire tracking volume. Depending whether the photon candidate corresponds to a conversion vertex, the candidate is classified as a converted or an unconverted photon. The unconverted photon candidate can be reconstructed without an associated conversion vertex while the reconstruction of the converted photon uses the conversion vertex. Electrons from converted photons are often mis-identified as prompt leptons if the photon conversion takes place before it passes through the IBL. Photons are not directly used in the analysis presented in this thesis but are used in the calculation of E_T^{miss}.

4.2. Muons

Reconstruction and identification

Reconstruction of muons in the ATLAS detector uses the Inner Detector and the Muon Spectrometer independently. These are then combined to form muon tracks which are then used in the physics analyses. In the ID, the reconstruction of muons is similar to that of electrons, or any other charged particle.

The hit patterns in each muon chamber is searched for to form segments. In every MDT chamber and the corresponding trigger chamber, using a Hough transform, a search is performed to find the hits aligned on a trajectory in the bending plane of the detector. Similarly, a combinatorial search is performed in the $\eta \times \phi$ plane in order to form segments in the CSCs. The muon candidates are then identified by fitting together the hits from different segments in each layer. The essential criteria to select segments to build tracks are hit-multiplicity, the fit quality, and the relative position and angles between the segments. To build a track, it is required that at least two matching segments are found unless it is in the transition region, where only one high quality segment is enough.

Depending on the information provided by the ID, calorimeter, and the MS, various algorithms are used to reconstruct muons. These are described below:

- Combined (CB) muons: Track reconstruction is done independently in the ID and MS, and using a global refit, a combined track is formed. The muons are reconstructed in the MS and extrapolated inward to the ID and matched to the track in the ID.
- Segment-tagged (ST) muons: A track in the ID is identified as a muon if it is associated to at least one track in a segment of either the MS or the CSC. This algorithm is used in case the muon has low p_T or if the muon is in a low acceptance region of the MS.
- Calorimeter-tagged (CT) muons: Since muons are weakly ionizing particles, they don't have significant deposits in the calorimeter. A track in the ID can still be identified as a muon if the associated energy deposits in the calorimeter is compatible with a minimally-ionizing particle. This algorithm has low purity but it can be used for muons in some low acceptance regions such as areas with low MS coverage due to cables etc.
- Extrapolated (ME) muons: This algorithm uses only the MS track and a rather loose requirement on the associated impact parameter to classify a particle as a muon. The algorithm requires the muon to pass through at least two (three in forward region) layers of the MS. This algorithm is used when the muon is out of ID coverage.

Once an algorithm is selected, additional quality cuts are applied to select prompt muons and suppress the background, which mostly tend to originate from pion- and kaon-decays. Using the $t\bar{t}$ MC, classifying muons from W bosons as signal, muons from light-hadron decays as background, several variables are identified to discriminate between signal and background muons [22]. For example, the variables used for CB muons are:

- the q/p significance: It is defined as the absolute value of the difference between the ratio of the charge and momentum of the muons measured in the ID and the MS divided by the sum, in quadrature, of the corresponding uncertainties.

$$\frac{|(q/p)_{ID} - (q/p)_{MS}|}{\sigma^2_{q/p}(ID) + \sigma^2_{q/p}(MS)}.$$

- ρ': It is defined as the absolute value of the difference between the transverse momentum measured in the ID and the MS, divided by the p_T of the combined track.

$$\frac{\left|p_T^{ID} - p_T^{MS}\right|}{p_T^{CB}}$$

- the normalized χ^2 of the combined track fit.

Using such variables, several working points which offer different signal efficiencies and background rejections are defined:

- Medium muons: The CB tracks are required to have at least 3 hits in at least two MDT layers. The ME tracks are required to have hits in at least three MDT/CSC layers. Besides, the q/p significance is required to be at least 7. The ME muons, as mentioned above, are used only outside the geometric coverage of the ID.
- Loose muons: These are generally used in Higgs analyses with four leptons in the final state. All types of muons are used. The CB and ME muons are required to have the same quality as medium muons. The CT and ST muons are restricted to $|\eta| < 0.1$.
- Tight muons: This working point offers the highest purity at the cost of some signal efficiency. Only CB muons with hits in at least two stations of the MS, while satisfying the Medium selection are used. χ^2 is required to be at most 7 to remove bad tracks. An additional 2-D cut on ρ' and q/p significance is applied for a stronger background rejection.
- High p_T: These are used only for muons with $p_T > 100$ GeV and require a special treatment since they have a smaller bending, the track fit criteria need to be stronger.

Depending on the background contributions, different analyses choose different working points. As an example, the purity of loose working point is shown in Figure 4.4 as a function of the η of the muons using the $t\bar{t}$ sample. In this study, muons originating from W bosons are called signal-like muons while muons originating from any other source are called background-like muons. The figure shows the purity of signal like muons i.e. the number of signal-like muons that pass the loose working point divided by the total number of loose muons. The background contamination as $1 -$ signal purity. The most dominant origin of background muons tends to be from semi-leptonic decays of $b-$hadrons.

Isolation

Muons originating from prompt decays of heavy particles such as W- and Z-bosons are isolated from other particles. Muons originating from the semi-leptonic b-decays, on the other hand, are embedded in jets and are badly isolated. The measurement of energy deposits or track hits around the muon candidate is known as the muon isolation.

As for the electrons, track-based and calorimeter-based variables are defined to quantify the isolation of the muon candidate as follows:

- $p_T^{\text{varcone30}}$: Scalar sum of the transverse momenta of the tracks with $p_T > 1$ GeV in a cone size of $\Delta R = \min(10\ \text{GeV}/p_T^{\mu}, 0.3)$ around the muon of transverse momentum p_T^{μ}, excluding the muon track itself.
- $E_T^{topocone20}$: Sum of the transverse energy of topological clusters in a cone size of $\Delta R = 0.2$ around the muon, excluding the contribution from the energy deposit of the muon itself, and applying corrections for effects from pile-up.

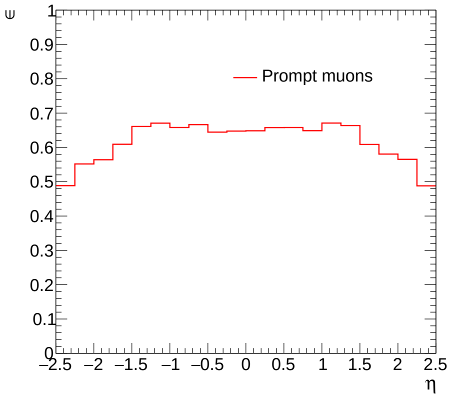

Fig. 4.4: Purity of signal like muons and contamination of background muons in the Loose working point using the $t\bar{t}$ simulation.

There are several working points being used in ATLAS [22], but the working points used in the analysis presented in this analysis are:

- LooseTrackOnly: A cut is applied on $p_T^{\text{varcone30}}$ such that a constant efficiency of 99% is obtained in η and p_T.
- FixedCutTightTrackOnly: $p_T^{\text{varcone30}}$ is required to be less than 0.06.

The other working points defined in ATLAS also apply cuts on $E_T^{topocone20}$.

Efficiency measurements

The muon reconstruction and isolation efficiency measurements are performed using $Z \to \mu\mu$ decays. The muon reconstruction efficiency is close to 99% over $|\eta| < 2.5$ for $p_T > 5$ GeV. The efficiency is measured with a precision of about 0.2% for $p_T > 20$ GeV. The reconstruction efficiency corresponding to the different working points are shown in Figure 4.5. The isolation efficiency for the different working points varies from 93% to 100% depending on the selection and the p_T of the particle. Furthermore, the momentum and scale resolution studies are used to correct the simulation to minimize the systematic uncertainties in physics analyses.

4.3. Jets

Jets, collimated sprays of particles, are frequently observed objects in high energy proton collisions, due to fragmentation and hadronization of high energy partons emerging from the hard interactions, or as a result of hard gluon radiation.

The final state particles are combined into jets using various jet definition algorithms. These algorithms are required to fulfill two main criteria in order to be well-defined.

- Collinear safety: jets should not be changed by collinear splitting such as gluon emission from a quark.
- Infrared safety: jets should not be changed by soft emission such as very low energy particles produced in hadronization.

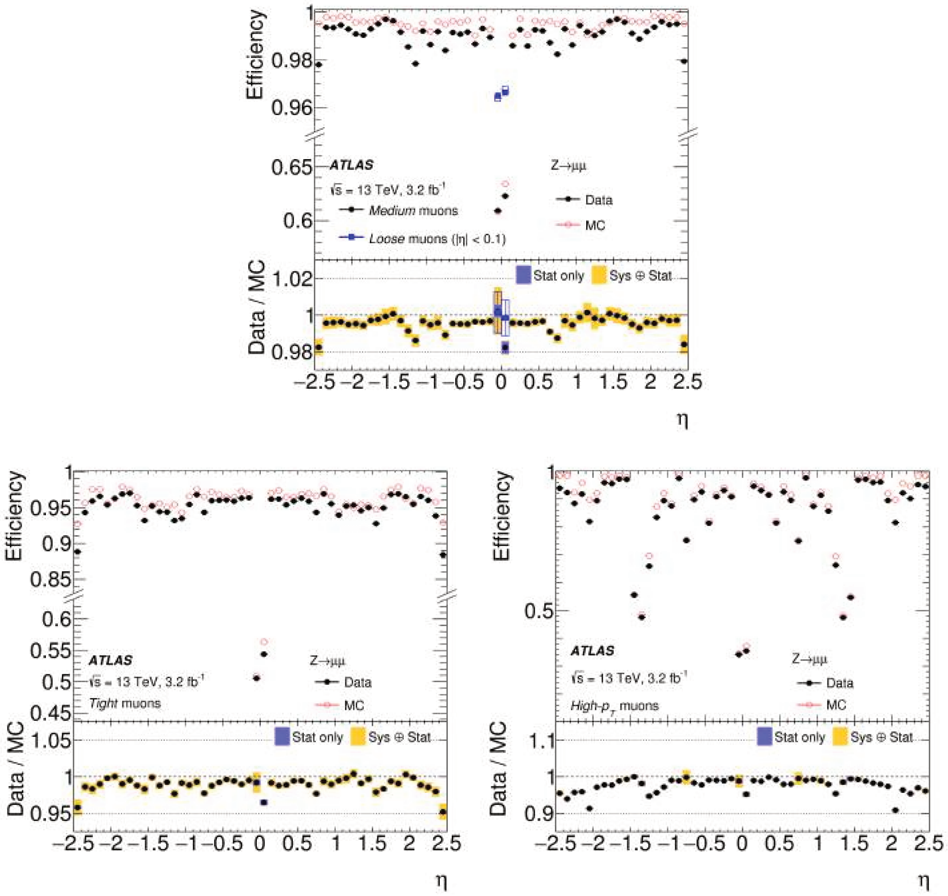

Fig. 4.5: Reconstruction efficiency for the Medium (top), Tight (bottom left), and High-p_T muons originating from a Z boson is shown as a function of η. In addition, the top plot also shows the efficiency corresponding to the loose working point. A comparison with the efficiency measure using the $Z \to \mu\mu$ is also shown [22].

Based on these requirements and the fact that the reconstruction should be very efficient, roughly two types of jet reconstruction algorithms are developed: the *cone* algorithms which were used in Tevatron experiments, and *sequential recombination* algorithms mainly used in LHC experiments.

In the ATLAS experiment, the anti-k_t algorithm, a sequential recombination algorithm, is used. The noise-suppressed clusters of energy in the calorimeter are used as inputs for the anti-k_t algorithm [23]. The anti-k_t algorithm computes the following quantities for all the input constituents:

$$d_{ij} = \min\left(\frac{1}{k_{T_i}}, \frac{1}{k_{T_j}}\right)\frac{\Delta R_{ij}^2}{R^2}, \tag{4.1}$$

$$d_{iB} = \frac{1}{k_{T_i}^2}, \tag{4.2}$$

where $\Delta R_{ij}^2 = (\eta_i - \eta_j)^2 + (\phi_i - \phi_j)^2$, R is a parameter of the algorithm that controls the size of the jet, and k_T is the transverse momentum of the ith constituent. d_{ij} denotes the distance between the ith and jth constituents, and d_{iB} is the distance between the beam and the i-th constituent. These distances are defined to differentiate between the constituents originating from hard interactions and those from proton remnants.

The algorithm compares d_{ij} and d_{iB} for the most energetic particles first. If d_{ij} is smaller, it recombines the ith and jth constituents. On the other hand, if the smaller distance is d_{iB} is termed as a jet, and removed from the set of constituents. This process is continued for the remaining constituents until no further constituents are remaining. An advantage of this method is that it produces rather circular jets in the $\eta - \phi$ plane. A detailed explanation of the anti-k_t algorithm can be found in [24]. Figure 4.6 shows jets clustered by the anti-k_t algorithm in the η-ϕ plane.

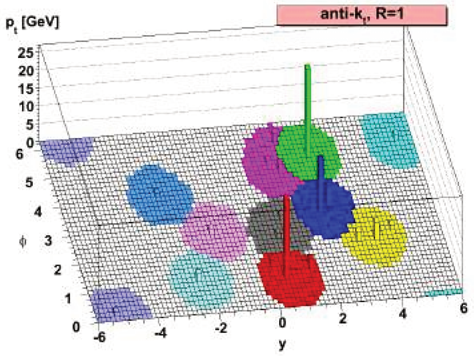

Fig. 4.6: A sample parton-level event, together with many random soft momentum particles (called ghost), clustered with the anti-k_t algorithm [24].

Jets with a cone size parameter of 0.4 in the calorimeter, called AntiKt4EMTopo jets, are used as the baseline in ATLAS.

Studies on using tracks for the jet clustering algorithm are on-going in ATLAS since using track jets is robust against pileup interactions. This allows to identify the primary vertex of interest.

Jets can easily be contaminated by particles originated in pileup interactions since there is no way to distinguish particles in the jets from the particles originating from pileup interactions. The fact that jet reconstruction is based entirely on calorimetry makes the contamination easier.

To identify the origin of jets, tracks associated to jets are used to construct a quantity called jet vertex fraction (JVF) [25]. For a given jet in an event, JVF is defined as follows:

$$\mathrm{JVF} = \frac{\sum\limits_{\mathrm{tracks} \in \mathrm{jet} \cap \mathrm{PV}} p_{\mathrm{T}}^{\mathrm{track}}}{\sum\limits_{\mathrm{tracks} \in \mathrm{jet}} p_{\mathrm{T}}^{\mathrm{track}}}, \tag{4.3}$$

where the denominator is the sum of p_{T} of tracks associated to the jet, and the numerator is the sum of p_{T} of tracks associated to both the jet and the primary vertex in the event.

The left sketch in fig 4.7 shows an example case of JVF for two vertices and two jets, and the right plot in fig 4.7 shows simulated JVF distributions for jets from hard scatter vertices and pileup vertices. In Run 1, JVF worked well for the reduction of pileup-originated jets. However, its robustness against the number of primary vertices was not perfect. In order to recover the performance of JVF, the jet vertex tagger (JVT) has been developed for Run 2, which is based on a 2D likelihood using two new variables: JVF corrected for the number of reconstructed vertex in the event, and ratio of summed p_{T} of the tracks originated from the hard-scatter in the jet to $p_{\mathrm{T}}^{\mathrm{jet}}$ [27].

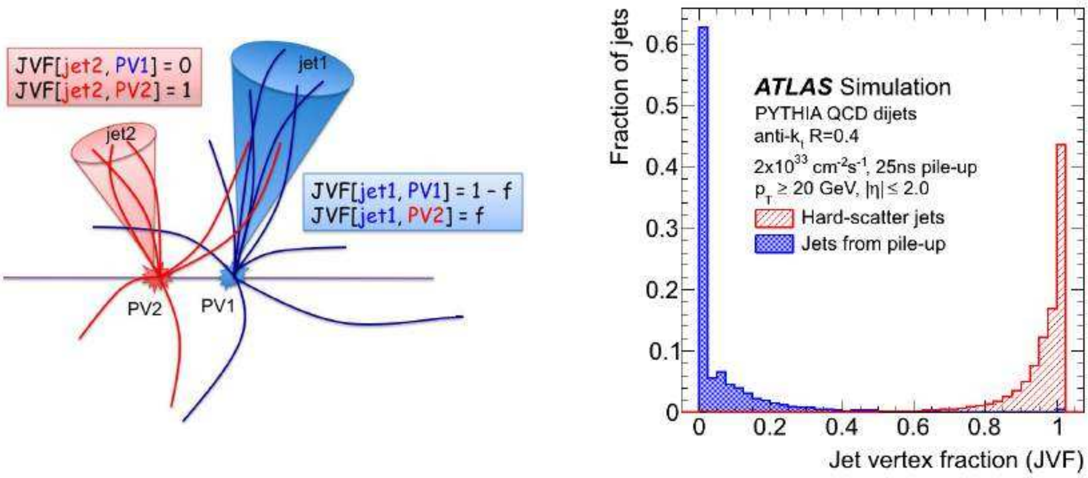

Fig. 4.7: A sketch of the JVF quantities for a case with two jets and two vertices [26] (left). The JVF distributions (right) for the blue histogram for jets originated in pileup vertex and the red histogram for jets originated in hard scattering vertex [25].

b-tagging

The identification of jets originating from $b-$quarks, called $b-$tagging, plays an important role in physics analyses within ATLAS. The elementary $b-$tagging algorithms use tracks of charged particles to discriminate between different jet flavours. ATLAS uses three distinct algorithms, all of which provide complementary information:

- Impact Parameter based algorithms (IP2D and IP3D):
  These make use of the significance of the signal impact parameters of the tracks matched to the jet. The probability density functions constructed using these significances of the impact parameters of the matched tracks are used to define a Likelihood Ration (LLR) discriminant. IP3D uses both, the transverse and longitudinal impact parameters, while IP2D uses only the transverse impact parameters.

- Secondary Vertex finding Algorithm (SV):
  It attempts to explicitly reconstruct the displaced secondary vertex within a jet. The first step involves reconstructing two-track vertices using candidate tracks. Some of these tracks are rejected if the corresponding secondary vertex can be easily identified to be originating from either photon conversions or decays of long-lived hadrons. Using the tracks that pass this test, a single vertex is reconstructed, with outlier tracks removed iteratively.

- Decay Chain Multi-Vertex Algorithm:
  It exploits the topological difference between the $b-$quark and $c-$quark weak decays inside the jet. It then attempts to reconstruct the entire decay chain, PV $\to b \to c-$hadrons. Whenever the resolution allows it, this helps to resolve the $b-$hadron and $c-$hadron vertices when only a single track is attached to each of them.

- Multivariate Algorithm (MV2):
  The input variables obtained from the above mentioned algorithms are used as an input to a boosted decision tree (BDT) algorithm from light jets and $c-$jets. This is referred to as the MV2c10 algorithm. The '10' in MV2c10 indicates that the background is composed of 90% light-jets and 10% $c-$jets as background. The various working points in ATLAS include 70% and 85% $b-$tagging efficiencies.

The most important detector upgrade that has helped with $b-$tagging was the addition of the IBL. Further details about the performance of different algorithms can be found in ref [28].

4.4. Missing transverse energy

Protons are composite particles, so the center-of-mass momentum of the interacting partons along the beam axis cannot be measured on an event-by-event basis. However, the momentum conservation in the transverse plane is useful since the initial partons have negligible transverse momenta. This momentum conservation in the transverse plane provides a quantity called missing transverse momentum, by reversing a vectorial sum of the transverse momenta of all objects in the event. Its magnitude is $E_{\mathrm{T}}^{\mathrm{miss}}$, the missing transverse energy.
In ATLAS, $E_{\mathrm{T}}^{\mathrm{miss}}$receives contributions from two sources, the hard event signals which comprise of fully reconstructed and calibrated particles and jets, and the second contribution arises due to soft signals which consist of reconstructed charged particle tracks not associated with hard physics objects. As mentioned above, all particles and jets have dedicated reconstruction algorithms. A candidate reconstructed as an electron, for example, is often also reconstructed as jets. This causes a double counting which is accounted for by an explicit signal ambiguity resolution in ATLAS.
The missing transverse momentum reconstruction in ATLAS allows for some observables to be constructed. The x- and y- components of the missing transverse momentum is given by,

$$E_{x(y)}^{miss} = -\sum_{i\in\text{hard objects}} p_{x(y),i} - \sum_{j\in\text{soft signals}} p_{x(y),j}. \tag{4.4}$$

This can be used to define the variables used in this, and other analyses in ATLAS,

$$E_T^{miss} = \sqrt{(E_x^{miss})^2 + (E_y^{miss})^2}, \phi^{miss} = \arctan(E_y^{miss}/E_x^{miss}). \tag{4.5}$$

High energy neutrinos can result in a large $E_{\mathrm{T}}^{\mathrm{miss}}$, since they usually do not interact with any of the material in the ATLAS detector. Hence, $E_{\mathrm{T}}^{\mathrm{miss}}$ measurement is a very important key for a lot of physics analyses, such as analyses involving $W \rightarrow \ell\nu$, like the analysis presented in this thesis. If a certain event has one neutrino, ideally $E_{\mathrm{T}}^{\mathrm{miss}}$ corresponds to the neutrino's p_{T}.

4.5. Taus

The τ leptonic decays lead to final states with isolated light leptons and some amount of E_T^{miss}. When τ originates from W decays ($W \rightarrow \tau\nu_\tau$), the leptonic decays of τ lead to final states identical to $W \rightarrow e\nu_e, \mu\nu_\mu$ with the charged leptons that have a lower momentum on average. For the final state presented in this thesis, leptonic τ decays are associated to the main signature or background predictions.

The hadronic τ decays contribute to the hadronic final state in the event. While ATLAS does provide a τ identification algorithm (τ-jets), this is not used in this analysis.

5. Search for $H^{\pm\pm}H^{\mp\mp} \to W^{\pm}W^{\pm}W^{\mp}W^{\mp}$

The search for $H^{\pm\pm}$ is performed in multi-lepton final states. This chapter mainly describes the 3ℓ analysis. The final results are combined with the results of the analyses in the $2\ell^{ss}$ and 4ℓ final states.

Sections 5.1 to 5.3 describe the various simulations and datasets, the triggers and object selections used in the analyses. These are common for all three channels. Section 5.4 is dedicated to the analysis in the 3ℓ final state. Section 5.5 summarizes the analyses in the $2\ell^{ss}$ and 4ℓ final states.

5.1. Data and simulation samples

5.1.1. Data

This analysis uses 36.1 fb^{-1} of data collected from proton-proton collision recorded by the ATLAS detector at $\sqrt{s} = 13$ TeV during 2015 and 2016 with a bunch crossing of 25 ns. Only the data collected when the IBL was on is considered.

5.1.2. Signal simulation

For the pair production of $H^{++}H^{--}$, the partonic events, generated with the CalcHEP [6] generator as described in section 2, are subsequently showered using PYTHIA8 [29] with A14 tune [30], and passed through the official ATLAS detector simulation and reconstruction. Additional minimum-bias pp interactions (pileup) are modeled using the Pythia 8.1 generator with the MSTW2008LO parton distribution function (PDF) set [31] and the A2 tune [32], and are added to simulated events according to the luminosity profile of the recorded data.

Samples have been simulated with $m_{H^{\pm\pm}} = 200$, 300, 400, 500, 600 and 700 GeV respectively. A filter that selects events with at least two light leptons (electron or muons) with $p_T > 10$ GeV and $|\eta| < 10$ is applied at the truth level. The filter efficiencies for the various benchmark points are shown in Table 5.1. Note that in all tables in this thesis, the expectations for the 'signal' correspond to the prediction of the model described above.

H^{++} mass (GeV)	200	300	400	500	600	700
filter efficiency	0.2858	0.3031	0.3198	0.3264	0.3362	0.3451

Table 5.1: Filter efficiencies for the signal samples

5.1.3. Standard Model simulation

Processes such as WZ, ZZ, $t\bar{t}V$ contribute as the dominant backgrounds with 2 or more true leptons. Processes such as $4t$, $t\bar{t}WW$, VH, and $t\bar{t}$ can contribute in small amounts. Processes such as $t\bar{t}$ and $Z + jets$ contribute as backgrounds with one or more objects (such as a jet or a lepton originating from semi-leptonic b-decays) that are misidentified as leptons. The simulations corresponding to such misidentified leptons are used only as reference. Additionally, the $Z \to ee$ simulations are used to understand backgrounds originating from mis-identification of charge (opposite-sign leptons being categorized as same-sign leptons). Accordingly, the list of simulations used for the search are shown in table 5.2.

Process	ME Generator	Parton Shower	PDF	Tune
$t\bar{t}H$	MG5_aMC [33]	Pythia 8 [29]	NNPDF 3.0 NLO [34]/ NNPDF 2.3 LO [35]	A14 [30]
VH	Pythia 8	Pythia 8	NNPDF 2.3 LO	A14
$tHqb$	MG5_aMC	Pythia 8	CT10 [36]/NNPDF 2.3 LO	A14
$t\bar{t}W$	MG5_aMC	Pythia 8	NNPDF 3.0 NLO/2.3 LO	A14
$t\bar{t}(Z/\gamma^*)$	MG5_aMC	Pythia 8	NNPDF 3.0 NLO/2.3 LO	A14
$t(Z/\gamma^*)$	MG5_aMC	Pythia 6 [37]	CTEQ6L1	Perugia2012 [38]
$tW(Z/\gamma^*)$	MG5_aMC	Pythia 8	NNPDF 2.3 LO	A14
$t\bar{t}t\bar{t}$	MG5_aMC	Pythia 8	NNPDF 2.3 LO	A14
$t\bar{t}W^+W^-$	MG5_aMC	Pythia 8	NNPDF 2.3 LO	A14
$t\bar{t}$	Powheg-BOX [39]	Pythia 6	CT10/CTEQ6L1	Perugia2012
s-, t-channel, Wt single top	Powheg-BOX [40, 41]	Pythia 6	CT10/CTEQ6L1	Perugia2012
VV, $qqVV$, VVV	Sherpa 2.1.1 [42]	Sherpa	CT10	Sherpa default
$Z \to \ell^+\ell^-$	Sherpa 2.2	Sherpa	NNPDF 3.0 NLO	Sherpa default
$W \to \ell\nu$	Sherpa 2.2	Sherpa	NNPDF 3.0 NLO	Sherpa default

Table 5.2: Configurations used for event generation of background processes. If only one parton distribution function (PDF) is shown, the same one is used for both the matrix element (ME) and parton shower generators; if two are shown, the first is used for the matrix element calculation and the second for the parton shower. 'V' refers to production of an electroweak boson (W or Z/γ^*). 'Tune' refers to the underlying-event tune of the parton shower generator. 'MG5_aMC' refers to MadGraph5_aMC@NLO 2.2.1; 'Pythia 6' refers to version 6.427; 'Pythia 8' refers to version 8.2; 'Herwig++' refers to version 2.7. The samples have heavy flavor hadron decays modeled by EvtGen 1.2.0 [43], except for samples generated with Sherpa.

Event generators and configurations used for simulating the Standard Model processes are shown in Table 5.2. Detailed descriptions of the generator configurations may be found in Refs. [44–47]. The generated events are used as input to a full GEANT4 [48] simulation of the ATLAS detector. Similar to the signal simulation described above, additional minimum-bias pp interactions (pileup) are modeled with the PYTHIA 8.1 generator with the MSTW2008LO PDF set [31] and the A2 tune [32], and are added to simulated events by taking into consideration the luminosity profile of the recorded data.

The production of $t\bar{t}H$, $t\bar{t}W$, and $t\bar{t}Z$ is simulated with a next-to-leading order (NLO) QCD matrix element computed by MADGRAPH5_AMC@NLO, matched to the PYTHIA 8 parton shower. In the case of $t\bar{t}Z$, the full $t\bar{t}\ell\ell$ matrix element is computed, including off-shell Z and γ^* contributions with $m(\ell\ell) > 5$ GeV. For studies of systematic variations, samples with variations of the QCD factorization and renormalization scales by factors of 2 and 0.5 are used. Production VH is simulated at leading order with PYTHIA 8 and the A14 tune. Production of VV, $VVqq$, and VVV are simulated with a NLO QCD matrix element computed by SHERPA and matched to the SHERPA parton shower which uses the CT10 PDF. Note that some of the processes lead to events with three prompt leptons while others may only contribute if a hadron is misidentified as a lepton. The latter contribution is studied using data driven methods as explained later in the chapter.

5.2. Trigger

2015	2016
HLT_e26_lhmedium_L1EM20VH for data set	HLT_e26_lhtight_nod0_ivarloose
HLT_e60_lhmedium	HLT_e60_lhmedium_nod0
HLT_e120_lhloose	HLT_e140_lhloose_nod0
HLT_mu20_iloose_L1MU15	HLT_mu26_ivarmedium
HLT_mu50	HLT_mu50

Table 5.3: Summary of triggers used by data taking period.

Triggers used in this analysis, summarized in table 5.3, are single lepton triggers with different energy thresholds. These consist of electron (thresholds of $E_T > 26, 60, 120, 140$ GeV) and muon (thresholds of $E_T > 20, 26, 50$ GeV) triggers. The L1EM20VH denotes the following set of cuts at L1:

- $p_T > 20$ GeV.
- Hadronic core isolation is applied (H).
- p_T thresholds vary with η to account for energy losses.

Furthermore, L1MU15 implies that the muon is required to satisfy $p_T > 15$ GeV at L1. The electron triggers use the log-likelihood identification method optimized by taking into account the resolution of various sub-detectors at the HLT level. Similarly, the muon triggers use identification methods developed for the HLT. The triggers HLT_e24_lhtight_nod0_ivarloose, HLT_e26_lhtight_nod0_ivarloose use loose isolation ($p_T^{\text{varcone20}}/E_T < 0.1$), while HLT_mu24_ivarmedium, HLT_mu26_ivarmedium use medium isolation conditions ($p_T^{\text{varcone30}}/p_T < 0.07$). Triggers with _nod0 remove the d_0 cut at the HLT level in order to reduced effects from mis-alignment.

5.3. Object selection

Several observables related to lepton identification are used to further classify the leptons in each event.

Leptons

To further suppress hadronic background, the electron candidates are required to be isolated using the variables defined in section 4. Cuts are applied on E_T^{cone20}/P_T and $p_T^{varcone20}/P_T$ of the lepton candidates to obtain a flat efficiency of 99% in the $\eta - E_T$ plane.

The impact parameter cuts are applied along both, the longitudinal and the transverse, directions from the interaction point. These cuts help to reduce non-prompt backgrounds that arise from particles which have a larger lifetime, fly a certain distance before producing jets and leptons and also help to reject tracks that are badly reconstructed.

Particles reconstructed in events that pass the trigger conditions are stored as candidates. These candidates are further selected using specific requirements to maximize acceptance while rejecting backgrounds from QCD. In analyses, *loose* leptons are used when the background is low to begin with. This allows to accept as much signal as possible. When the background is high, a *tight* selection is used to reject the excessive background at the cost of some signal efficiency. In such cases, the effect of the *tight* selection is much lower on the signal in comparison to that on the background. In the current analysis, however, a combination of *loose* and *tight* leptons is used.
The two working points of LooseLH and TightLH are used for the identification of electrons. The muons are required to pass only the loose identification criterion in order to increase the statistics. The selections used for *loose* and *tight* leptons are summarized in table 5.4.

Lepton	Electrons		Muons	
Condition	Loose	Tight	Loose	Tight
p_T	$p_T^e > 10$ GeV		$p_T^\mu > 10$ GeV	
Pseudo-rapidity	$\lvert\eta_e\rvert < 2.47$, not in crack $1.37 : 1.52$		$\lvert\eta_\mu\rvert < 2.5$	
Identification	LooseLH	TightLH	Loose	Loose
Isolation	Loose	FixedCutTight	LooseTrackOnly	FixedCutTightTrackOnly
PV longitudinal	$\lvert z_0 sin\theta\rvert < 0.5$ mm	$\lvert z_0 sin\theta\rvert < 0.5$ mm	$\lvert z_0 sin\theta\rvert < 0.5$ mm	$\lvert z_0 sin\theta\rvert < 0.5$ mm
PV transverse	$\lvert d_0/\sigma(d_0)\rvert < 5$	$\lvert d_0/\sigma(d_0)\rvert < 5$	$\lvert d_0/\sigma(d_0)\rvert < 3$	$\lvert d_0/\sigma(d_0)\rvert < 3$

Table 5.4: Summary of electron and muons selection conditions used in the analysis.

Jets

As described in section 4, jets are reconstructed from topological clusters using the anti-k_T algorithm with a radius parameter of $R = 0.4$. Only jets with $p_T > 25$ GeV and $|\eta| < 2.5$ are considered. For jets with $p_T < 50(60)$ GeV and $|\eta| < 2.4$, the output of the jet vertex tagger - JVT - is required to be larger than 0.59 in order to suppress jets originating from pile-up. Jets are discarded if they overlap with leptons, as explained below. The identification of jets containing b-hadrons (b-tagged jets) is described in section 4. The working point used to reject b-jets for this search corresponds to an average efficiency of 70% for b-jets with $p_\mathrm{T} > 20$ GeV and $|\eta| < 2.5$ in $t\bar{t}$ events. The expected rejection factors against light and c-jets are 380 and 12, respectively.

Overlap removal and E_T^{miss}

In absence of a coherent particle flow algorithm implemented at reconstruction level, an ad-hoc overlap removal is performed among objects in the events that pass the above mentioned baseline selection. The removal procedure is summarized in Table 5.5. The electron is removed if it shares track with a muon. A jet is removed if it is close to any electron within $\Delta R < 0.2$. Then any electron is removed if it is close to any remaining jet within $\Delta R < min(0.4, 0.04 + 10/P_T[\text{GeV}])$. Furthermore, a jet is removed if it is close to a muon within $\Delta R < min(0.4, 0.04 + 10/P_T[\text{GeV}])$ and is associated with less than three tracks, otherwise the respective muon is removed.

Keep	**Remove**	**Cone size (Δ R) or track**
electron	CaloTagged muon	shared track
muon	electon	shared track
electron	jet	0.2
jet	electron	$\Delta R < min(0.4, 0.04 + 10/P_T[\text{GeV}])$
muon	jet	(0.2 or ghost-matched to muon) and (numJetTrk $\leq$2)
jet	muon	$\Delta R < min(0.4, 0.04 + 10/P_T[\text{GeV}])$

Table 5.5: Summary of overlap removal between electrons, muons and jets. The tau hadronic decays are not treated in this event final state decomposition and are part of the hadronic final state (included in jets reconstruction).

The calculation of E_T^{miss} (described in 4.4) is done using all the above mentioned objects after the overlap procedure is applied.

5.4. Analysis in the 3ℓ final state

This section is dedicated to the details of the analysis in the 3ℓ final state. The event pre-selection used to suppress dominant backgrounds is described in section 5.4.1. Section 5.4.2 details the methods used for background estimation. In section 5.4.3, the optimization of cuts on various variables that can discriminate between signal and background, and the consequent background estimates in the signal region are detailed.

5.4.1. Event preselection

In the 3ℓ final state, a significant part of the expected SM contribution to the background originates from di-boson production. In particular, the WZ production, where both bosons decay to leptons, presents also other signal features like significant $E_{\mathrm{T}}^{\mathrm{miss}}$and absence of b-jets for most of the production cross section. The same-flavour opposite sign lepton pairs are predominantly produced in the Z bosons mass window. A second major type of background involves process with top quarks, $t\bar{t}$ for example. These backgrounds always correspond to a $b-$jet.

The event pre-selection, illustrated in Table 5.6, is used to suppress the above mentioned background processes without reducing the signal yields significantly. It involves the following steps:

A Event cleaning and tri-lepton selection: Only events with exactly three loose leptons with a total charge ±1 are selected. The event cleaning includes a trigger requirement (as explained above) and the presence of at least one primary vertex.

B Suppression of processes involving a Z boson and low mass resonances: A veto is imposed on events for which at least one same-flavour opposite-sign lepton pair has an invariant mass within a ± 10 GeV window around the Z-boson mass. Furthermore, events with a pair of same-flavor opposite leptons with an invariant mass less than 15 GeV are rejected. Moreover, only events with at least two hadronic jets are selected.

C Suppression of processes involving a top quark: Events with one or more jets tagged as b-jet are rejected.

D The same-sign leptons are required to be *tight*.

Step	Selection Criteria	*Data*	Signal $M_{\mathrm{H}^{\pm\pm}} = 200$
A	Three leptons with total charge of ± 1, $P_T^{0,1,2} > 10, 20, 20 GeV$	23905	38.8 ± 0.2
B	$\lvert M_{\ell^+\ell^-} - M_Z \rvert > 10$ GeV	10064	34.2 ± 0.2
	$M_{\ell^+\ell^-} > 15$ GeV	8131	33.9 ± 0.2
	$E_{\mathrm{T}}^{\mathrm{miss}} > 30$ GeV	4198	31.0 ± 0.2
	$N_{\mathrm{jet}} >= 2$	1895	20.7 ± 0.1
C	$N_{\mathrm{b-jet}} = 0$	905	19.6 ± 0.1
D	Tight same-sign leptons	392	16.4 ± 0.1

Table 5.6: Cut flow for the 3ℓ analysis. The leptons definitions used in steps A-C are "Loose", such that these can also be used for fake leptons studies. Step D is the pre-selection region, and denoted as XS in the rest of this document.

The total lepton charge requirement to be ± 1 imposes that two leptons are of the same sign and the third lepton has an opposite sign. The opposite sign lepton is assigned the lepton index 0. The same sign leptons are assigned indices 1 and 2, with the condition $\Delta R_{01} < \Delta R_{02}$. The fraction of events in which lepton 0 tends to be prompt is expected to be very high[a]. Indeed, the dominant backgrounds often involve a Z boson or $t\bar{t}$. In both these cases, two prompt leptons are expected which form one opposite sign pair. The third lepton, which can be any object misidentified as a true lepton, enters as one of the two same-sign leptons. Hence, in the rest of this analysis, lepton 0 will be required to pass only the loose selection. Thus, the signal region selection will include *tight* selection requirement for leptons 1 and 2.

5.4.2. Background estimation

There are two types of background contributions: fake and prompt background sources. Processes with final states similar to that of the signal region which consist of leptons originating promptly from the parent particles (for example, leptonic decays of W and Z bosons) are classified as prompt backgrounds. In cases when a jet is reconstructed in the detector as a lepton, or when the lepton originates via an non-prompt decay (such as semi-leptonic b-decays) or from photon conversions[b], the lepton is classified as fake. The fake background contribution is very difficult to model and is estimated using data driven techniques. The fake leptons originate mostly from $t\bar{t}$ and Z+jets processes, with further contributions from rare top processes (detailed contributions in the appendix). The irreducible prompt background is dominated by the WZ process.

---

[a] Using simlations for processes with at least one fake lepton, and requiring the same-sign leptons to be tight, the fraction of events in which lepton 0 passes the loose selection but not the tight was found to be less than 5%

[b] This is valid in all cases except $Z\gamma$ for which the simulations are used.

The strategy to study the fake background is based on the lepton identification criteria described in Table 5.4: for a given event topology, the *tight* lepton requirement defines the signal-like region, with a suppressed fake lepton contribution, while the *loose* (and not *tight*) requirement on one of the leptons enriches the sample in fake lepton contributions and allows the estimation of the fake background.

Regions defined for fake estimation

Since the signal region is designed such that the SM contribution is minimized, it contains very low statistics and there is little handle to check the background in-situ. Therefore, in order to study and estimate the fake leptons contributions, four samples are defined as follows:

X This is the event pre-selection sample described above. It is selected with three loose leptons, all quality cuts (trigger, matched), the Z-veto, $M_{\text{os}} > 15$ GeV, $E_{\text{T}}^{\text{miss}} > 30$ GeV, $N_{\text{jets}} \geq 2$ and a veto on b-jets $N_{\text{b-jets}} = 0$. This sample corresponds to step C in Table 5.6, re-described here for completeness.

Y This event sample correspond to most of the pre-selection criteria, except that selects events at low jet multiplicity. It is defined by requiring three loose leptons, all quality cuts (trigger, matched), the Z-mass veto and $N_{\text{jets}} = 1$. This region is a low jet multiplicity sample disjoint from the signal region and also from the test samples described hereafter. This region is used to calculate the extrapolation factor (called "fake factor") from *loose-not-tight* to *tight* regions, as described below.

Z This sample is enriched in Z+jets events, an opposite-sign lepton pair is required, with the invariant mass within the Z mass window, a b-jet veto is applied: $N_{\text{b-jets}} = 0$, and a jet multiplicity corresponding to the preselection is required $N_{\text{jets}} \geq 1$.

T This sample is enriched in $t\bar{t}$: the pre-selection step A and B are applied and the b-jets condition is modified to $N_{\text{b-jets}} \geq 1$.

All above samples are split in "signal-like" region XS/YS/ZS/TS, where the same-sign leptons are required to be *tight* , and the "fake-enriched" XF/YF/ZF/TF regions, where at least one of the two same-sign leptons is required to be *loose* but not *tight*. The region XS is designed to be the pre-selection for the final selection, the events in which are used for the signal region optimization. The Y region is used as a baseline for the fake factor determination, XS region is used as the signal pre-selection region (XF is used to estimate the fakes in the XS region) while Z and T regions are pure control regions, enriched in heavy/light fake contributions.

The fake factor method

The fake factors are calculated in the YS and YF regions using the formula:

$$\theta_{\text{e}/\mu} = \frac{(N_{\text{Data}} - N_{\text{prompt}})_{\text{xee}/\text{x}\mu\mu}}{(N_{\text{Data}} - N_{\text{prompt}})_{\text{xe}\not{e}/\text{x}\mu\not{\mu}}} \tag{5.1}$$

Here, $\not{e}$ and $\not{\mu}$ indicate the electrons and muons that are *loose* and not *tight* (therefore events from YF region) while e and μ indicate the electrons and muons that pass the *tight* selection. Lepton 0 is indicated by "x" to imply that they include both the flavours. The numerator is therefore calculated by counting events from the YS region, while the denominator is calculated with events from the YF region after subtracting the prompt contributions, defined in section 5.1 and estimated using MC

Cut name	X (pre-selection)	Y	Z-enriched	top-enriched
N_ℓ (loose)	3	3	3	3
$p_T^{\ell_{0,1,2}}$	$> 10, 20, 20$ GeV	$> 10, 20, 20$ GeV	$> 10, 20, 20$ GeV	$> 10, 20, 20$ GeV
N_{jets}	> 1	$= 1$	> 0	> 1
N_{b-jet}	$= 0$	–	$= 0$	> 0
P_T^{jet}	> 25 GeV	> 25 GeV	> 25 GeV	> 25 GeV
Z-window	$\lvert M_{\ell\ell}^{os} - M_Z\rvert > 10$ GeV	$\lvert M_{\ell\ell}^{os} - M_Z\rvert > 10$ GeV	$\lvert M_{\ell\ell}^{os} - M_Z\rvert < 10$ GeV	$\lvert M_{\ell\ell}^{os} - M_Z\rvert > 10$
$M_{\ell\ell}^{os}$	> 15 GeV	> 15 GeV	–	> 15 GeV
$E_{\mathrm{T}}^{\mathrm{miss}}$	> 30 GeV	–	– GeV	> 30 GeV
Signal-like Sample $N_{\ell_{1,2}}$ (tight)	2	2	2	2
Fake-enriched Sample : $N_{\ell_{1,2}}$ (tight)	1	1	1	1

Table 5.7: The selection criteria used for the pre-selection region and various control regions that are used for cross-checks. The last two lines differentiate each region into signal-like by requiring the same-sign leptons to be *tight*, and fake-enriched samples by requiring at least one lepton to be *loose* and not *tight*.

simulations. This calculation can be made in all the regions defined above, denoted by "in-situ" fake factors in the following, but the fake factors from the Y region are the nominal fake factors and are used in the subsequent signal region analysis. The control region definitions, their usage to extract fake factors and to perform cross checks are also illustrated in Figure 5.1.

The result of this procedure is shown in Table 5.8. The fake factors for electrons and muons are deduced using the first (e) and the last (μ) rows in the two sub-tables using the formula 5.1: $\theta_e = 0.39 \pm 0.07$ and $\theta_\mu = 0.17 \pm 0.06$ (statistical errors only). The fake-enriched YF region can be used to estimate the fake contribution in the signal enriched region YS, using the "fake factors" for electrons θ_e and muons θ_μ as follows:

$$N_{\mathrm{xe}\mu} = \theta_\mathrm{e} \times N_{\mathrm{x}\mu\not{e}} + \theta_\mu \times N_{\mathrm{xe}\not{\mu}} \tag{5.2}$$

$$N_{\mathrm{xee}} = \theta_\mathrm{e} \times N_{\mathrm{xe}\not{e}} \tag{5.3}$$

$$N_{\mathrm{x}\mu\mu} = \theta_\mu \times N_{\mathrm{x}\mu\not{\mu}} \tag{5.4}$$

where the data yields indicated by N always comprise a subtraction of the prompt contribution (estimated with MC). For this sample, Equations 5.3 and 5.4 are an inversion of the fake factor definition. Therefore, the column "Data-Prompt" is identical to "Data Driven Fakes" in Table 5.8 (bottom sub-table) for the rows corresponding to xee and $x\mu\mu$, by definition. However, the middle row ($xe\mu$) is a nontrivial check for closure of the procedure: 119.8 ± 24.04 compared to 206.3 ± 34.2. This difference, as well as the other closure comparisons, will be taken into account while estimating the systematic errors. For columns corresponding to MC Fakes, MC simulations are used directly to estimate the number of fakes. This column only serves as a comparison to the data-driven fakes. MC simulations are not used in the analysis to estimate fakes.

Background estimation in the pre-selection region

Since XS is the pre-final selection towards the signal region, the background estimates are particularly important in this region. The fake-enriched XF region can be used to estimate the fake contribution in the XS, using the "fake factors" for electrons θ_e and muons θ_μ in Equations 5.2, 5.3 and 5.4. The nominal fake factors (obtained in the Y region, as explained above) are applied to the XF region to calculate the data driven fake estimates in the XS region. The results are shown in Table 5.9. A good

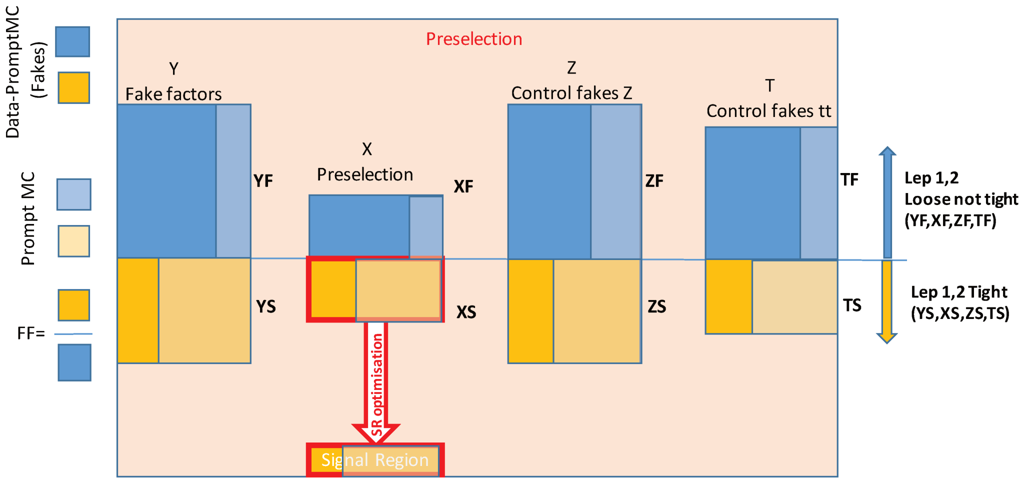

Fig. 5.1: An illustration of the work-flow used to estimate and control the background in the control samples. The amount of fakes in each region can be calculated using the fake factors estimated in the Y region and compared with the Data-Prompt value, as explained in the text.

Region	Data	Prompt	Data-Prompt	MC fakes		
YF $xe\not{e}$	366	103 ± 7.29	263 ± 20.5*	324 ± 72.2		
YF $x\mu\not{e}$	572	151 ± 8.58	421 ± 25.4	206 ± 30.9		
YF $xe\not{\mu}$	283	42.7 ± 4.21	240 ± 17.3	248 ± 23.6		
YF $x\mu\not{\mu}$	307	44 ± 4.17	263 ± 18*	211 ± 21.4		
Region	Data	Prompt	Data-Prompt	DD fakes	in-situ DD fakes	MC fakes
YS xee	234	131.3 ± 6.8	102.7 ± 16.75*	102.7 ± 20.21	102.7 ± 20.21	109 ± 37
YS $xe\mu$	462	342.2 ± 11	119.8 ± 24.04	206.3 ± 34.2	206.3 ± 34.2	259 ± 88.7
YS $x\mu\mu$	167	121.4 ± 6	45.65 ± 14.25*	45.65 ± 14.92	45.65 ± 14.92	19.9 ± 4.53
$\theta_e(in-situ)$	0.39 ± 0.07					
$\theta_m(in-situ)$	0.17 ± 0.06					

Table 5.8: Y samples yields in sub-regions enriched in fakes YF and signal YS. Note that the column "Data Driven Fakes" contains the fake lepton contribution estimated using the fake factors. The numbers in that column are directly comparable to the column "Data-Prompt"; the first and third line of the bottom table for these two columns are identical by definition. The middle ($xe\mu$) line provides however a non-trivial test, since this sample is disjoint from xee and $x\mu\mu$ samples, used to calculate the fake factors. The numbers indicate by * are used for evaluating the fake factors using equation 5.1. The errors indicated here are statistical.

agreement is observed between the estimates (column 'DDFakes' in table 5.8) and the "Data-Prompt MC" numbers, confirming the validity of this method. For completeness, the "in-situ" fake factors are given (and are in agreement with the fake factors deduced in the YR region), together with the "in-situ" data-driven fakes.

Region	Data	Prompt	Data-Prompt	MC fakes		
XF $x e \not{e}$	106	33.7 ± 4.53	72.3 ± 11.2	64.7 ± 6.67		
XF $x \mu \not{e}$	160	35.9 ± 3.02	124 ± 13	64 ± 8.69		
XF $x e \not{\mu}$	111	12.3 ± 1.83	98.7 ± 10.7	91 ± 4.58		
XF $x \mu \not{\mu}$	136	13.3 ± 2.14	123 ± 11.9	98.7 ± 5.53		
Region	Data	Prompt	Data-Prompt	DD fakes	in-situ DD fakes	MC fakes
XS xee	87	55.12 ± 3.4	31.88 ± 9.939	28.25 ± 6.736	31.88 ± 12.17	42.5 ± 21.4
XS $xe\mu$	215	135.4 ± 5.6	79.59 ± 15.69	65.64 ± 11.66	63.76 ± 21.63	32.5 ± 5.87
XS $x\mu\mu$	90	78.79 ± 4.1	11.21 ± 10.35	21.29 ± 7.108	11.21 ± 10.46	16.8 ± 5.86
$\theta_e(in - situ)$	0.44 ± 0.15					
$\theta_m(in - situ)$	0.09 ± 0.08					

Table 5.9: X samples yields in sub-regions enriched in fakes (XF) and signal (XS). Note that the column "Data Driven (DD) Fakes" contains the fake lepton contribution estimated using the fake factors measured in the Y region. The numbers in that column are directly comparable to the column "Data-Prompt", and a good agreement is observed. The fake factors formulae can also be used, similarly to the study in Y the region, to deduce "in-situ" fake factors and background estimates (the column "in situ DD fakes"). The latter are non-trivial for the middle line in ($xe\mu$), where they can be directly compared to the baseline "Data Driven Fakes" estimates and to the "Data-Prompt" yield. The errors indicated here are statistical.

Distribution of variables and fake prediction

The data and prompt MC events selected in the XF region defined above are used to build a sample of events (denoted "fakes" in the following). The selected events are weighted according to the fake factors defined above (depending on the flavour of the loose-not-tight lepton candidate in the event). The weights of the events from prompt MC samples are flipped in sign, since they need to be subtracted from the data. These fake events are used to emulate fake leptons in the XS region. The data-driven fake sample is, therefore, included in the SM prediction, replacing the MC samples that contribute due to fake leptons ($t\bar{t}$, V+jets,...), and used for further cuts optimization towards the signal region definition. In order to validate this procedure, the distributions of the variables used to select the Signal Region are shown in Figures 5.2 to 5.4. A good agreement is observed.

Figure 5.5 show the events selected in the pre-selected sample as a function of the lepton flavours combination. A good agreement of the data and the SM estimate including fakes is observed for all variables. Figure 5.5 shows the flavor composition of the events in the pre-selection region. Bins 3 and 4 correspond to events which do not contain same-flavor opposite sign leptons (SFOS 0), while bins 1, 2, 5, and 6 correspond to events which consist of same-flavor opposite sign leptons (SFOS 1,2). It is worth noting that the number of background events with SFOS 0 is significantly less than that with SFOS 1,2.

The background estimate is also verified in the control samples, Y, Z, and T, and shown in Appendix C.1.

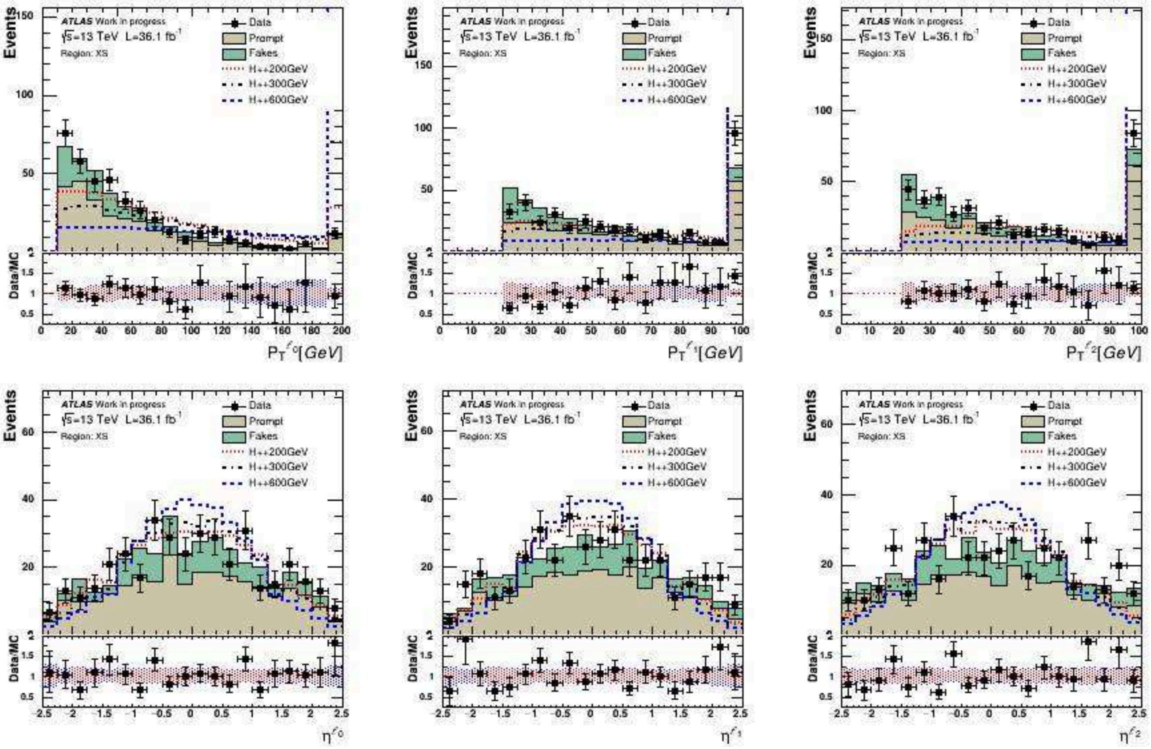

Fig. 5.2: Distributions of the events included in the pre-selection stage (XS). Note that the signal is scaled to data integral, for a better visibility. The bottom panels of each figure shows the ration between data and the total SM prediction (including prompt Monte Carlo and fakes estimates). The error band includes the Monte Carlo statistics and the total error obtained by adding in quadrature the uncertainty from the fakes estimates.

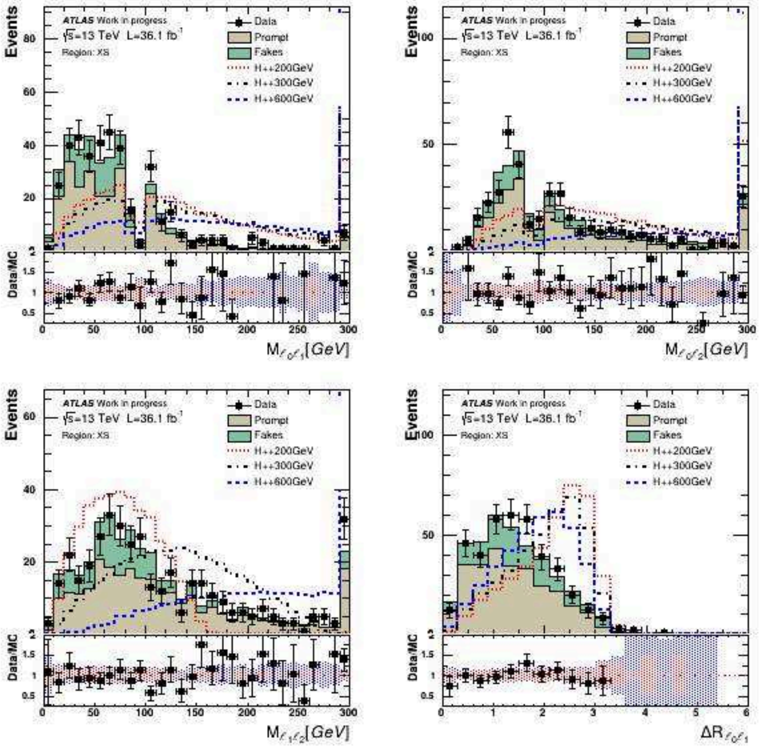

Fig. 5.3: Distribution of the events included in the pre-selection stage (XS). Note that the signal is scaled to data integral, for a better visibility. The bottom panels of each figure shows the ration between data and the total SM prediction (including prompt Monte Carlo and fakes estimates). The error band includes the Monte Carlo statistics and the total error obtained by adding in quadrature the uncertainty from the fakes estimates.

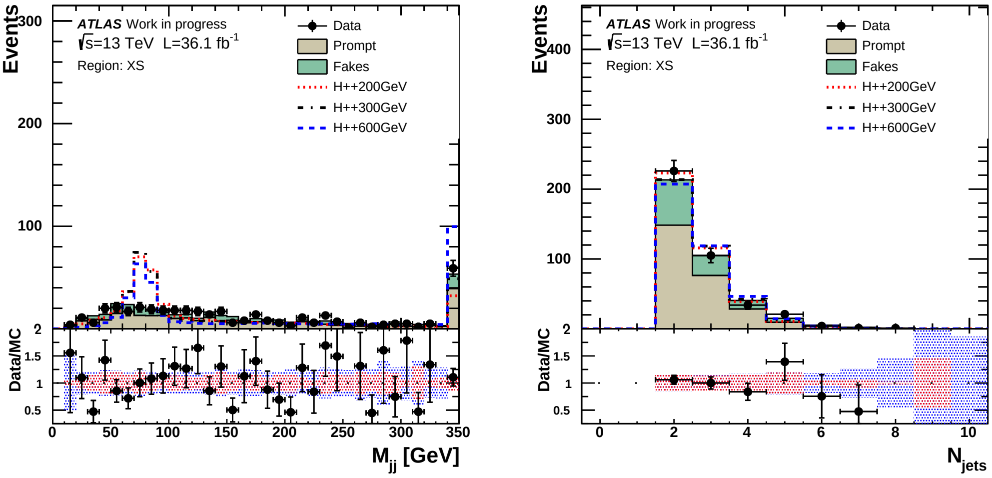

Fig. 5.4: Distribution of the events included in the pre-selection stage (XS). Note that the signal is scaled to data integral, for a better visibility. The bottom panels of each figure shows the ration between data and the total SM prediction (including prompt Monte Carlo and fakes estimates). The error band includes the Monte Carlo statistics and the total error obtained by adding in quadrature the uncertainty from the fakes estimates.

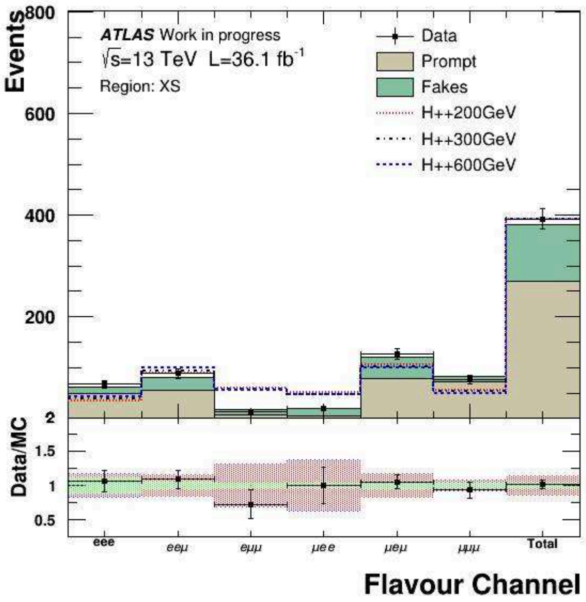

Fig. 5.5: Distribution of 3L at event pre-selection stage (XS) per flavour channel (with leptons ordered $\ell_0\ell_1\ell_2$). Note that the signal is scaled to the integral of data, for a better visibility. The bottom panel shows the ratio between data and the total SM prediction (including prompt Monte Carlo and fakes estimates). The error band includes the Monte Carlo statistics (black) and the total error obtained by adding in quadrature the uncertainty from the fakes estimates.

5.4.3. Signal region

While the cuts pre-selection region, shown in Table 5.6, orient the analysis towards the signal topology and greatly reduce various backgrounds, it is necessary to further reduce the background while preserving as much of the signal as possible, in order to increase the discovery potential. To this cause, several variables involving the kinematics and the angular correlations of the various physics objects were investigated. The signal region is obtained as a subset of the pre-selected events by using the cuts on these variables. The correlation between the variables, and a ranking of their power of discrimination was studied using the TMVA package. This study yielded five variables with the highest power of discrimination,

- $\Delta R_{\ell_1\ell_2}$: The angular separation between the same-sign leptons. These leptons result from W-bosons originating from the same $H^{\pm\pm}$ reflect the spin correlations in the $H^{\pm\pm}$ decays, thus providing a good S/B discrimination.

- $\Delta R_{\ell_0 j}$: The angular separation between the opposite-sign lepton and the leading jet. The opposite-sign lepton and the leading jet both are decay products of W bosons originating from the same $H^{\pm\pm}$ boson. This variable, like $\Delta R_{\ell_1\ell_2}$, is constrained and hence helps discriminate signal from background.

- $P_T^{\text{leading jet}}$: The transverse momentum of the leading jet, as described above, depends on the mass of $H^{\pm\pm}$.

- $M_{3\ell}$: The invariant mass of the three leptons.

- E_T^{miss}: Since the signal is characterized by the presence of three neutrinos, E_T^{miss} does not show a sharp peak. Instead, since the W-bosons originate from the heavy doubly charged Higgs bosons, the signal events have an average E_T^{miss} that is higher than that in the dominant SM processes such as WZ. Furthermore, as $m_{H^{\pm\pm}}$ increases, the discrimination achieved by the variable also increases.

The distributions of these variables at the pre-selection level is shown in Figure 5.6, and their correlations for the signal and background events are shown in Table 5.11.

Other variables that are good at discriminating between signal and background are the invariant masses of same-sign and opposite-sign leptons, sum of the p_T of the three leptons, the ΔR between opposite-sign leptons, and the invariant mass of the leading and sub-leading jets (the two jets that could reconstruct the W mass). The invariant masses of the same-sign is strongly correlated with $\Delta R_{\ell_1\ell_2}$ while being slightly less discriminating. The sum of the p_T of the three leptons is strongly correlated with invariant mass of all three leptons. For those reasons, even though the additional variables are discriminating by themselves, they add little value to the optimization and hence, for the sake of simplicity, are dropped.

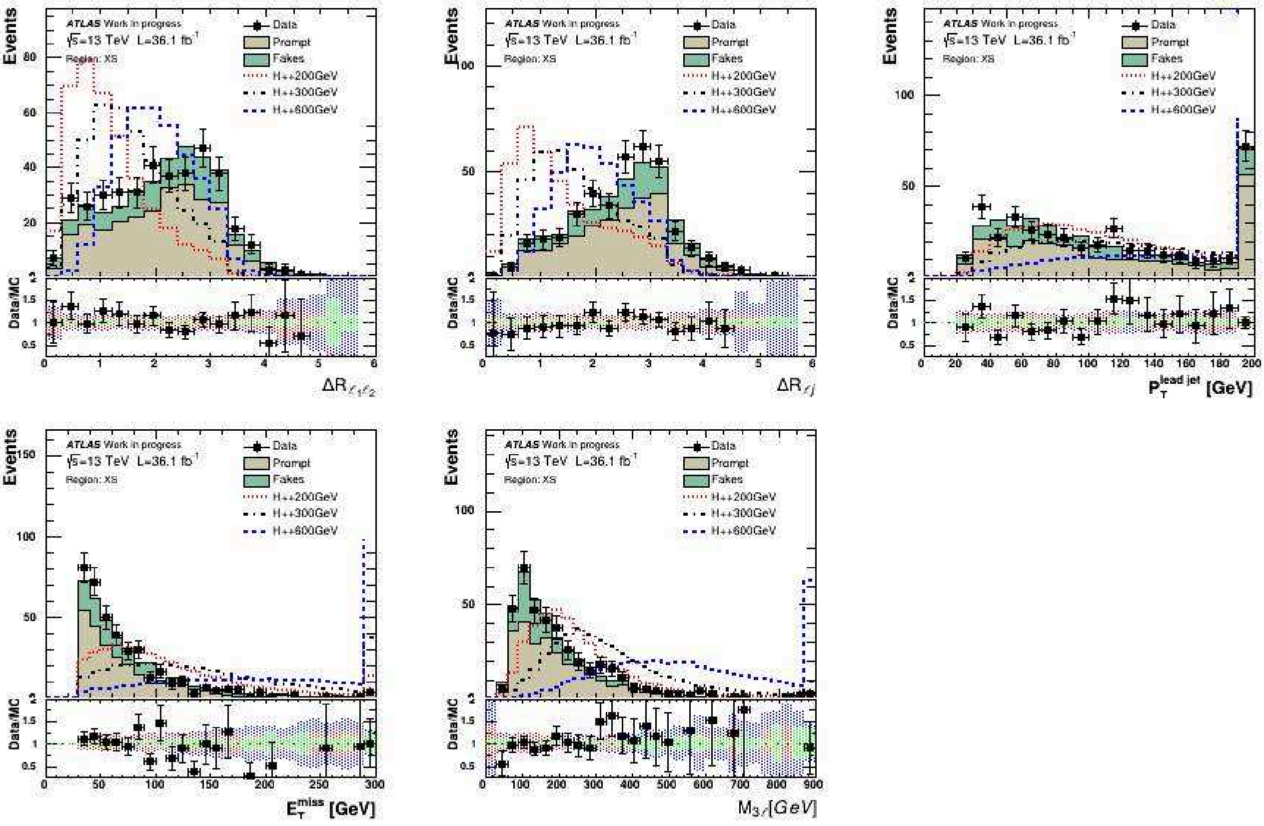

Fig. 5.6: Data compared to prediction for the five most discriminating variables.

The optimized set of cuts is obtained in several steps, using the TMVA CutsSA method as follows:

- The background composition and the S/B ratio depend on the presence or absence of same-flavor opposite sign (SFOS) leptons. To take this account, the training for each group is further split into two regions, SFOS 0 when SFOS leptons are absent and SFOS 1,2 denoting the presence of SFOS leptons.

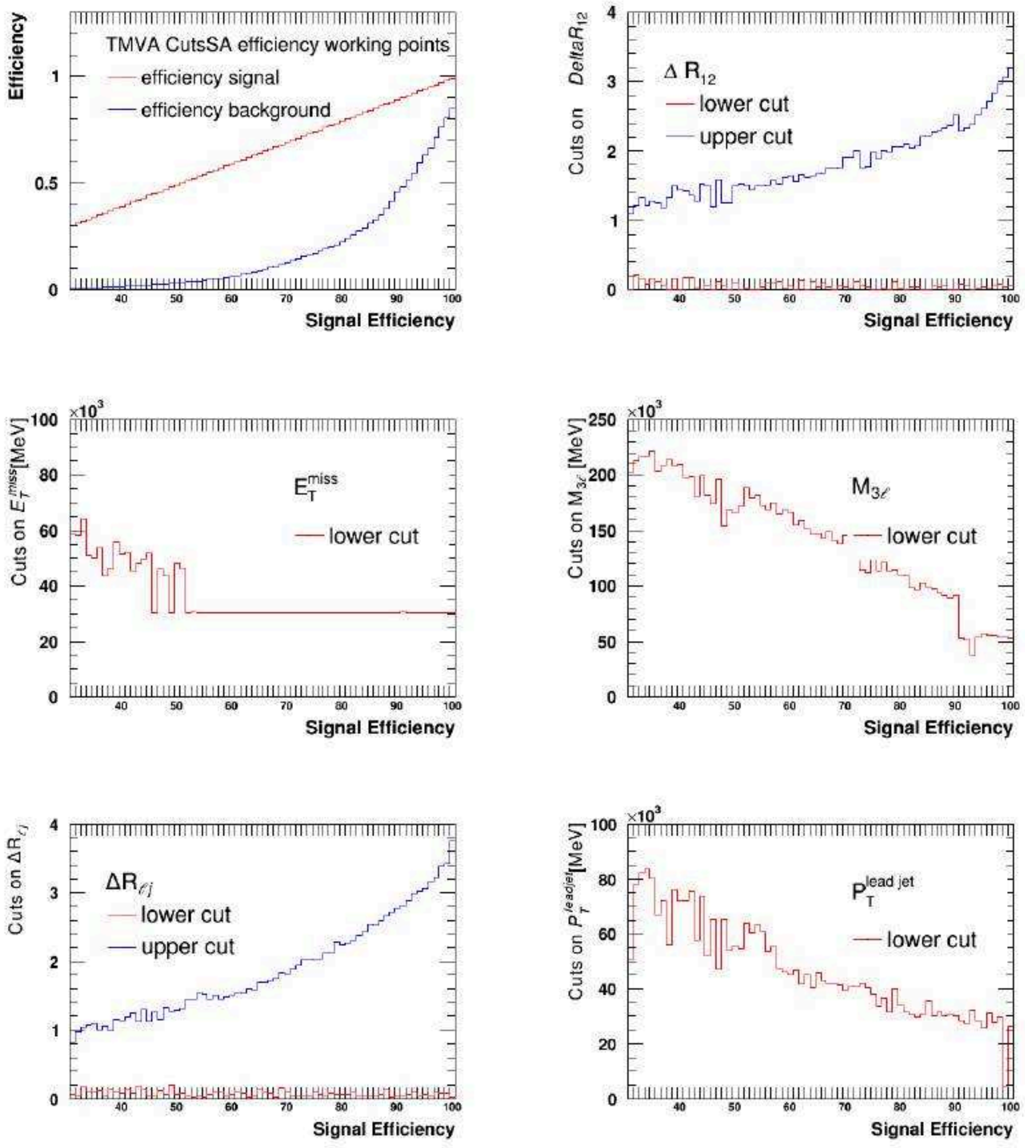

Fig. 5.7: Scanning of cuts as a function of the target efficiency of the signal for the two groups of cuts for SFOS12 flavour composition. On top are the variations of background efficiency as a function of signal efficiency (trivially also shown as a diagonal). The values in y for all cuts corresponding to the same x value define a "working point" (selection configuration) where the signal efficiency is given by that x value.

$p_T^{\text{lead jet}}$	-23	45	11	10	100
$\Delta R_{\ell j}$	21	-12	-27	100	10
$M_{3\ell}$	-26	13	100	-27	11
E_T^{miss}	-14	100	13	-12	45
$\Delta R_{\ell\ell^{ss}}$	100	-14	13	-12	45
	$\Delta R_{\ell\ell^{ss}}$	E_T^{miss}	$M_{3\ell}$	$\Delta R_{\ell j}$	$p_T^{\text{lead jet}}$

Table 5.10: The correlation coefficients (in %) for the variables used to define the signal region for the signal simulation.

$p_T^{\text{lead jet}}$	-22	40	18	7	100
$\Delta R_{\ell j}$	3	3	1	100	7
$M_{3\ell}$	21	23	100	1	18
E_T^{miss}	10	100	23	3	40
$\Delta R_{\ell\ell^{ss}}$	100	10	21	3	40
	$\Delta R_{\ell\ell^{ss}}$	E_T^{miss}	$M_{3\ell}$	$\Delta R_{\ell j}$	$p_T^{\text{lead jet}}$

Table 5.11: The correlation coefficients (in %) for the variables used to define the signal region for the background simulations.

- When all the variables are trained together, the TMVA becomes more sensitive to statistical fluctuations. Therefore, the variables are grouped in two (a group with three variables and the second with two variables) for training, and scanning of cuts.

- The cuts are scanned as function of the signal efficiency (also referred to as target efficiency). The target efficiency is defined as the efficiency of a given group of cuts with respect to the pre-selection region. The values of the cuts as a function of the signal target efficiency are shown in Figure 5.7. Note that the real efficiency (the efficiency when all cuts are applied at the same time) is roughly equal to the product of the *target* efficiencies, barring the correlation between the variables.

- Below 40% target efficiency, the background shows a lot of statistical fluctuations and TMVA becomes more sensitive to these fluctuations. To avoid this situation, the scanning begins from 40%, and selects a working point which maximizes the significance. This also serves to ensure that small changes in the working point correspond to small changes in the cut values. The significance as a function of the signal efficiency is shown in Figure 5.9.

- TMVA, by default, applies cuts as lower bounds as well as upper bounds. When the lower bound is inactive, it is set to zero. Similarly, when the upper bound is inactive, the cut value is set to a very large default value.

- Figure 5.6 shows that the distribution of the signal vary significantly for different $m_{H^{\pm\pm}}$. Thus, the optimization is repeated for all the mass points. The target efficiency for the higher mass points of $500, 600, 700$ GeV is set to 0.6 to avoid regions of very low signal rates since the cross-sections for these masses are very low.

- In order to simplify the sets of cuts applied for the signal region, some post-processing is applied on the cuts obtained after the above mentioned steps.
  - The cuts for the mass points of 200 GeV and 300 GeV are not changed.

- The cuts corresponding to 400 GeV and 500 GeV are taken as averages of the neighbouring mass points, starting from the lower masses, towards higher masses. This is done to ensure that the cuts are monotonic as a function of the mass of $H^{\pm\pm}$.
- The cuts for 600 GeV and 700 GeV points are required to be the same as those for 500 GeV in order to reduce the number of signal regions and keep the analysis simple.
- The values of cuts obtained directly from TMVA have an arbitrary number of digits. These numbers are rounded to have a resolution of 1 GeV for the invariant mass of the three leptons and the p_T of the leading jet. The solid angles, ΔR's are rounded to two decimal digits.

The cuts obtained after the procedure are shown in Figure 5.10 and summarized in Table 5.12. The overall signal efficiencies obtained as a function of mass are summarised in Table 5.13. The efficiency as a function of flavor channel for each mass are shown in Figure 5.8. These efficiencies are rather flat (variation of about 10% at most) as a function of flavor.

Selection criteria	SFOS 0	SFOS 1,2
	$M_{H^{\pm\pm}} = 200$ GeV	
$E_{\mathrm{T}}^{\mathrm{miss}}[GeV]$	> 45	> 45
$M_{3\ell}$[GeV]	> 160	> 170
$\Delta R_{\ell^\pm\ell^\pm}$	[0.15 : 1.57]	[0.00 : 1.52]
$\Delta R_{\ell-\mathrm{jet}}$	[0.08 : 1.88]	[0.07 : 1.31]
$P_T^{\text{leading jet}}$[GeV]	> 80	> 55
	$M_{H^{\pm\pm}} = 300$ GeV	
$E_{\mathrm{T}}^{\mathrm{miss}}[GeV]$	> 65	> 55
$M_{3\ell}$[GeV]	> 170	> 210
$\Delta R_{\ell^\pm\ell^\pm}$	[0.18 : 2.23]	[0.08 : 2.23]
$\Delta R_{\ell j}$	[0.27 : 2.37]	[0.21 : 2.08]
$P_T^{\text{leading jet}}$[GeV]	> 95	> 80
	$M_{H^{\pm\pm}} = 400$ GeV	
$E_{\mathrm{T}}^{\mathrm{miss}}[GeV]$	> 65	> 85
$M_{3\ell}$[GeV]	> 230	> 250
$\Delta R_{\ell^\pm\ell^\pm}$	[0.22 : 2.39]	[0.29 : 2.69]
$\Delta R_{\ell j}$	[0.30 : 2.59]	[0.31 : 2.30]
$P_T^{\text{leading jet}}$[GeV]	> 120	> 100
	$M_{H^{\pm\pm}} = 500 - 700$ GeV	
$E_{\mathrm{T}}^{\mathrm{miss}}[GeV]$	> 120	> 100
$M_{3\ell}$[GeV]	> 230	> 300
$\Delta R_{\ell^\pm\ell^\pm}$	[0.39 : 3.11]	[0.29 : 2.85]
$\Delta R_{\ell j}$	[0.60 : 2.68]	[0.31 : 2.53]
$P_T^{\text{leading jet}}$[GeV]	> 130	> 130

Table 5.12: The selection criteria used for the two signal regions, SFOS 0 and SFOS 1,2.

Effect of optimized cuts on data and background estimates

Once the cuts are optimized, it is important to check that none of the cuts result in a disagreement between data and background estimate. The yields for each cut applied individually and sequentially (cutflow) are shown in figures 5.11 and 5.12 respectively. A good agreement is observed in both the cases.

Mass point	$N_\ell = 3$	XS efficiency	SR/XS	filter efficiency	TotEff
$M_{H^{\pm\pm}} = 200$	0.0753	0.34	0.33	0.29	0.00244
$M_{H^{\pm\pm}} = 300$	0.0852	0.44	0.40	0.30	0.00450
$M_{H^{\pm\pm}} = 400$	0.0879	0.48	0.40	0.32	0.00541
$M_{H^{\pm\pm}} = 500$	0.0884	0.49	0.40	0.33	0.00567
$M_{H^{\pm\pm}} = 600$	0.0887	0.50	0.46	0.34	0.00689
$M_{H^{\pm\pm}} = 700$	0.0879	0.51	0.49	0.35	0.00760

Table 5.13: The efficiencies obtained for the optimisation in each mass point. The second column corresponds to the efficiency obtained when the number of reconstructed leptons is required to be 3. The XS efficiency is obtained by dividing the signal yield in the preselection region by the number of events that survive the three lepton requirement. The SR/XS column shows the efficiency of the signal region cuts relative to the yield at the pre-selection stage. The filter requests at least two leptons in the sample. Note that the total efficiency implicitly includes the branching ratio to three leptons.

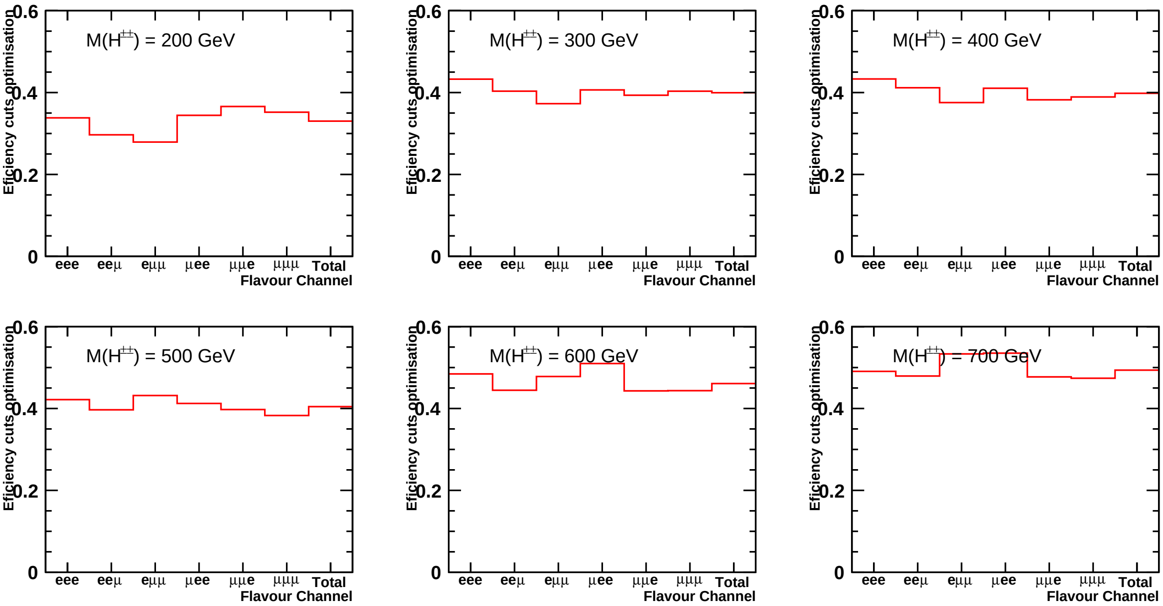

Fig. 5.8: The signal efficiency for the 6 mass points shown as a function of the channel number.

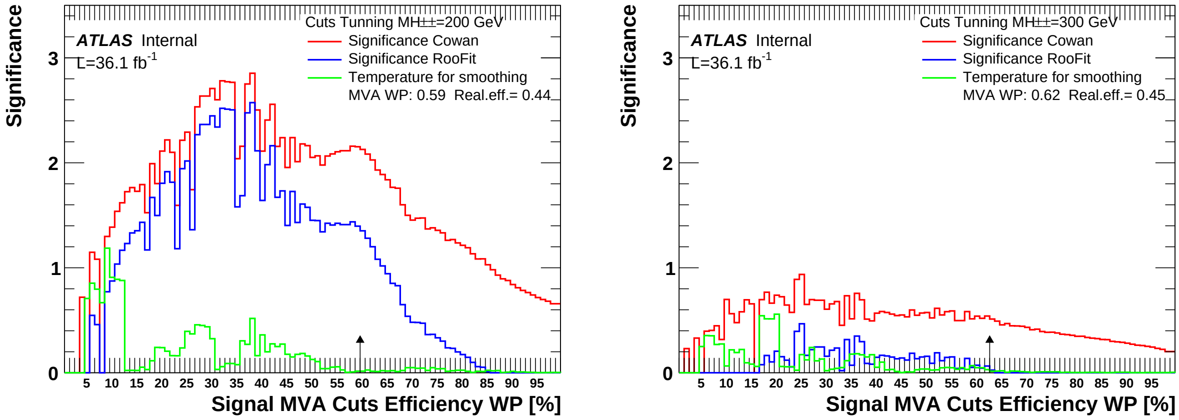

Fig. 5.9: The significance scan as a function of efficiency, shown for two signal masses as examples $M_{H^{\pm\pm}} = 200$ GeV (left) and $M_{H^{\pm\pm}} = 300$ GeV (right). Here the SFOS12 configuration is shown. The arrows indicate the chosen working points, The significance is calculated with two algorithms (Cowan, defined by the formula $\sqrt{2*((s+b)*log(1+s/b)-s)}$ [49], and Roofit [50] which has an in-built function to calculate the significance) green curve indicate the "temperature", i.e. the RMS in the previous 5 bins, and is used as an indicator of the significance stability and in order to avoid working points where the significance estimate is unstable due to low background statistics (typically at low efficiency).

Fake estimates in the signal region

While the fake factor method used to estimate the number of fakes at the pre-selection level works well, it cannot be used directly in the signal region due to lack of statistics. As a way around this problem, individual efficiencies of the cuts can be evaluated and multiplied. This method assumes that the variables are not correlated.

The total efficiency obtained by multiplying the product of efficiencies of single cuts, efficiencies when cuts are grouped and factorized efficiencies resulting from the grouping for the mass point of 200 GeV are shown in Table 5.14. It should be noted that the 'All cuts' row estimates the number of fakes to be zero with a high statistical fluctuation. Therefore, the variables are grouped into three; the first and second groups with two variables each and the third group with one variable. This also helps reducing the effect of correlations. The resulting extrapolation efficiency is given by,

$$\epsilon_{2-2-1} = \epsilon_{1,2} \times \epsilon_{3,4} \times \epsilon_5. \tag{5.5}$$

The nominal $2-2-1$ configuration is such that, in the above equation, $1,2$ corresponds to $\Delta R_{\ell\ell^{ss}}$ and E_T^{miss}, $3,4$ corresponds to $M_{3\ell}$ and $\Delta R_{\ell^0 j}$, and 5 corresponds to $P_T^{\text{leading jet}}$. The yields obtained when the cuts are applied by groups are shown in Figure 5.13 for all mass points. A good agreement is observed between data and prediction for the three groups.

5.4.4. Systematic uncertainties

Various sources of uncertainties affect both the signal and the background processes. These sources are described in this section.

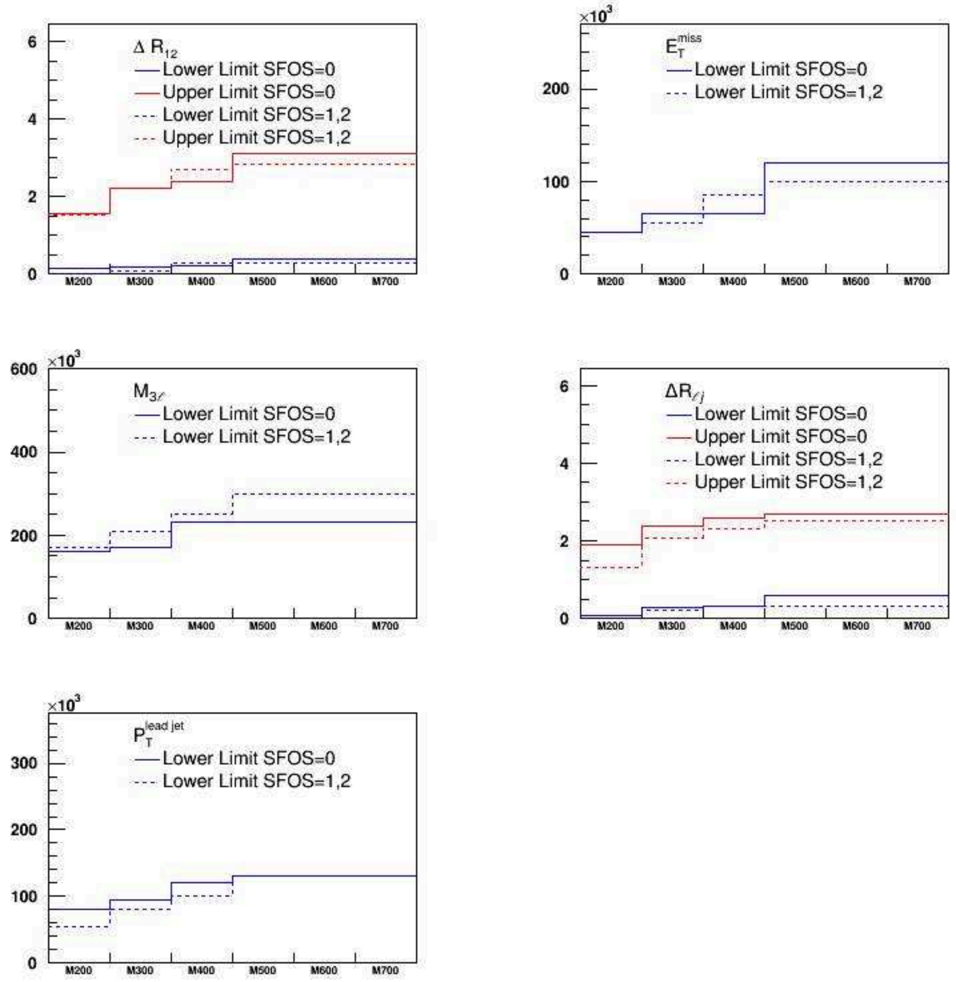

Fig. 5.10: The cuts obtained after an optimization run using TMVA package as explained in the text. The cuts are smoothen and rounded, as explained in the text, and same cuts are used for $M_{H^{\pm\pm}} \geq 500$ GeV.

	SFOS 0	SFOS 1,2	ϵ_{Data}	ϵ_{Prompt}	ϵ_{Fakes}	ϵ_{signal} (200 GeV)
1	$0.15 < \Delta R_{\ell\ell^{ss}} < 1.57$ and $E_{\text{T}}^{\text{miss}} > 45$ GeV	$0.00 < \Delta R_{\ell\ell^{ss}} < 1.52$ and $E_{\text{T}}^{\text{miss}} > 45$ GeV	0.198 ± 0.046	0.191 ± 0.025	0.16 ± 0.06	0.670 ± 0.004
2	$M_{3\ell} > 160$ GeV and $0.08 < \Delta R_{\ell j} < 1.88$	$M_{3\ell} > 170$ GeV and $0.07 < \Delta R_{\ell j} < 1.31$	0.061 ± 0.050	0.084 ± 0.027	0.038 ± 0.057	0.498 ± 0.005
3	$P_T^{\text{leading jet}} > 80$ GeV	$P_T^{\text{leading jet}} > 55$ GeV	0.751 ± 0.026	0.772 ± 0.014	0.709 ± 0.034	0.821 ± 0.003
4		All cuts	0.008 ± 0.05	0.006 ± 0.019	0.003 ± 0.073	0.330 ± 0.006
5		Factorised efficiency	0.011 ± 0.005	0.012 ± 0.006	0.004 ± 0.005	0.274 ± 0.1

Table 5.14: The cuts applied at the signal region level and their individual efficiencies. The correlated variables are grouped together. The "All cuts" line displays the nominal efficiency when all cuts are applied while the last line "Factorised efficiency" shows the product of the efficiencies of the three groups. Only statistical errors are shown. The systematic uncertainties are not included in this table.

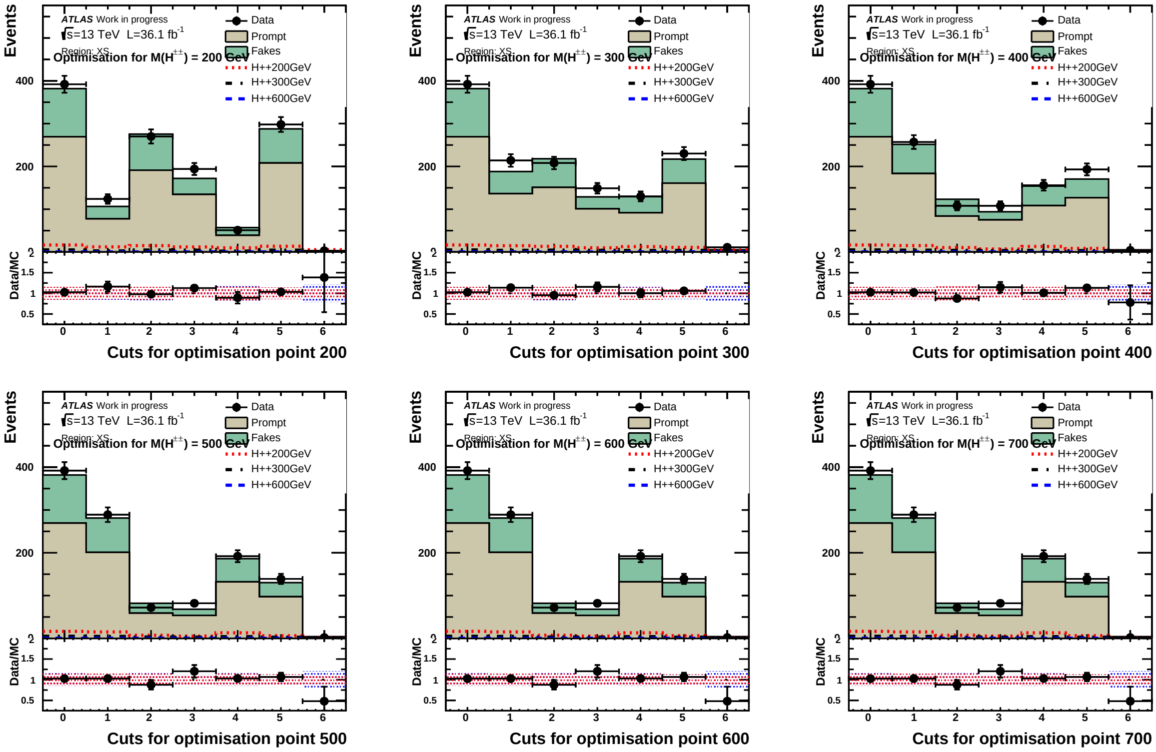

Fig. 5.11: The yields obtained for each cut in a given optimization point. Bin 0 corresponds to the yields in the preselection region. Bins $1-5$ correspond to the cuts on $\Delta R_{\ell\ell^{ss}}$, $E_{\mathrm{T}}^{\mathrm{miss}}$, $M_{3\ell}$, $\Delta R_{\ell j}$ and $P_T^{\text{leading jet}}$ respectively.

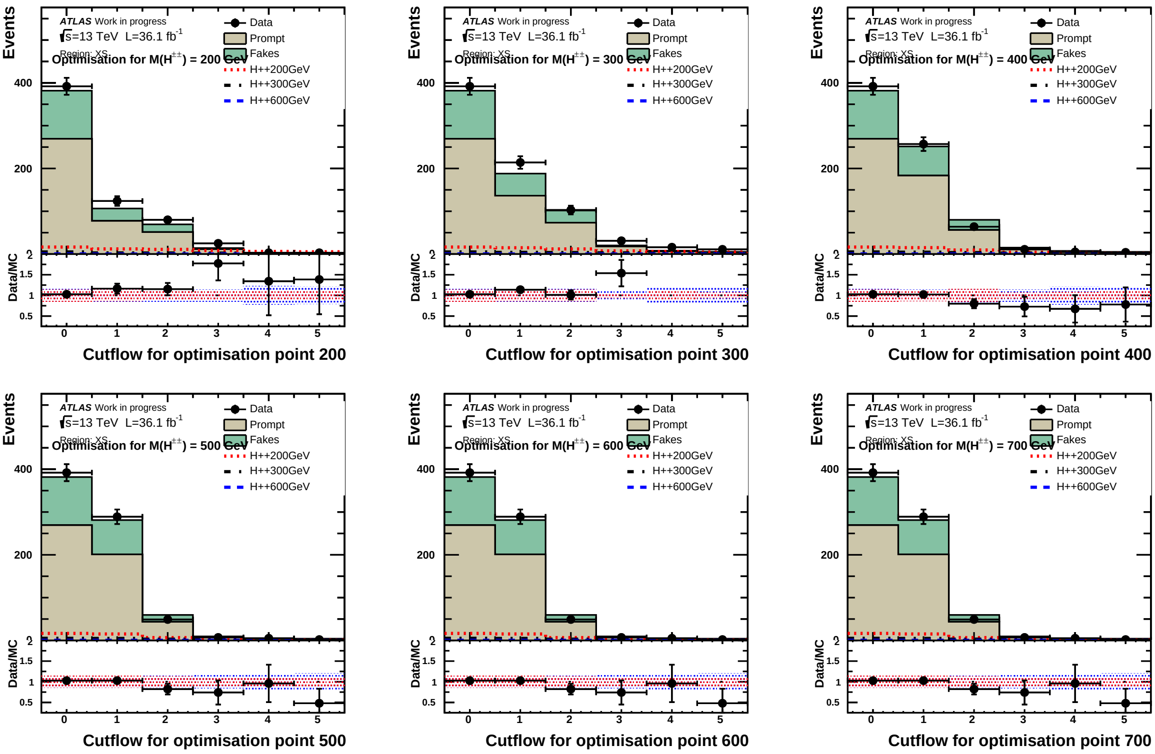

Fig. 5.12: The yields obtained sequentially after each cut in the six mass-dependent optimisation points. The first bin (0) represents the pre-selection level (same in all figures). Bins $1-5$ correspond to the cuts on $\Delta R_{\ell\ell^{ss}}$, $E_{\mathrm{T}}^{\mathrm{miss}}$, $M_{3\ell}$, $\Delta R_{\ell j}$ and $P_T^{\text{leading jet}}$ respectively, when the cuts are applied sequentially.

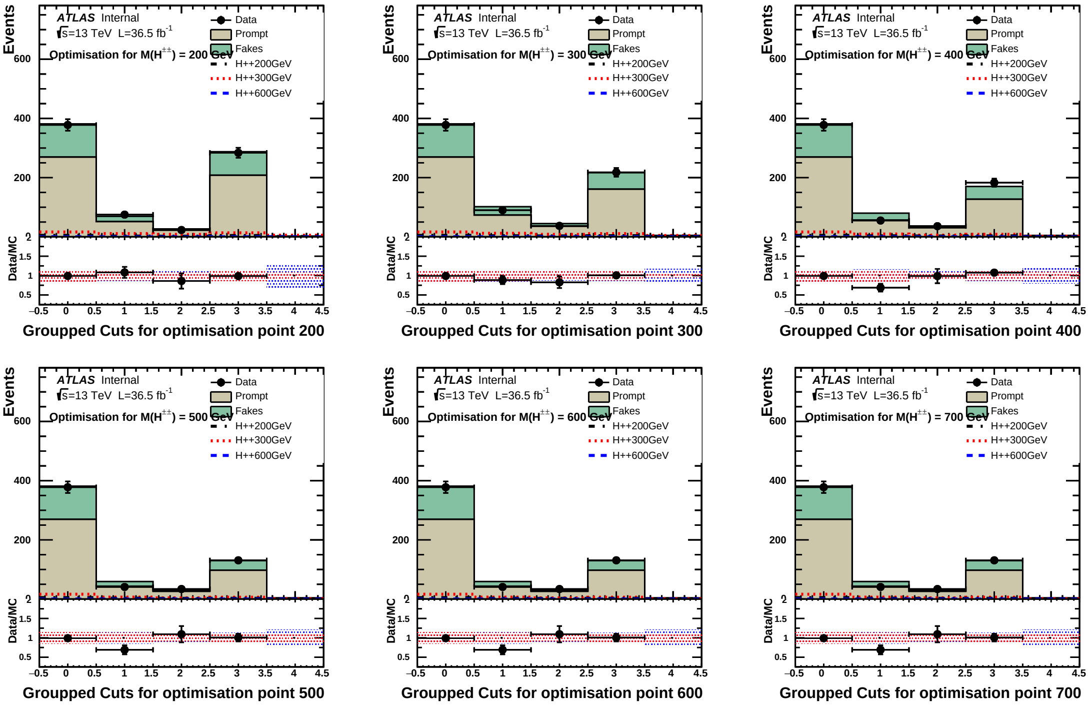

Fig. 5.13: The event yields after the "group" cuts (2-2-1 out of the 5 cuts, as illustrated in Table 5.14) are applied. The six signal region optimization points $M_{H^{\pm\pm}} = 200, 300, 400, 500, 600, 700$ GeV are shown. The first bin represent the pre-selection level (same in all figures). The last bin represent the signal region with all cuts applied. The groups of cuts (variables) definitions for 1, 2 and 3 are illustrated in Table 5.14.

Theoretical uncertainties on the signal

The uncertainties due to the choice of the parton distribution function for the signal are evaluated using the LHAPDF6 library. Re-weighting the events using information from an alternative PDF is equivalent to generating the events using the alternative PDF itself. The generated signal events are re-weighted at leading order using the following [51]:

$$\omega_i = \frac{x_1 f_{1i}(x_1; Q^2)}{x_1 f_{10}(x_1; Q^2)} \frac{x_2 f_{2i}(x_2; Q^2)}{x_2 f_{20}(x_2; Q^2)}, i = 1, 2, \cdots . \tag{5.6}$$

where x_i's denote the momentum fractions and f_{10} and f_{20} in the denominators correspond to the nominal PDFs for parton i in 1 and 2 at a factorization scale Q. The PDFs can be expressed as linear combination of eigenvectors. The re-weighting is based on the systematic variations of these eigenvector PDF members. The PDFs corresponding to these variations are denoted by $f_{1i}(x_1; Q^2)$ and $f_{2i}(x_2; Q^2)$. It is important to note that the re-weighting should be done using PDFs corresponding to an α_s (the strong coupling) similar to that of the nominal PDF. For example, LO and NLO PDFs tend to have difference values of α_s. Such a re-weighting was avoided while estimating the uncertainties. The uncertainties are taken as symmetric (average of up-down variations) for simplicity. The study is performed by applying the pre-selection cuts on the truth level quantities of the signal samples. The PDF uncertainties are found to range from 2.5% to 4.5%.

$m_{H^{\pm\pm}}$ (in GeV)	200	300	400	500	600	700
μ (auto)	70.59	14.18	4.11	1.469	0.594	0.2631
$\mu = m_{H^{\pm\pm}}$	73.28	15.21	4.504	1.633	0.6684	0.2866
$\mu = m_{H^{\pm\pm}}/2$	74.3	15.83	4.767	1.748	0.7237	0.3247
$\mu = 2m_{H^{\pm\pm}}$	72.01	14.63	4.268	1.528	0.6208	0.2751
$\Delta\sigma/2\sigma\,(\mu = m_{H^{\pm\pm}})$	1.56%	3.94%	5.54%	6.74%	7.70%	8.65%

Table 5.15: The variation of the inclusive cross section (in fb) as a function of the factorisation scale (taken to be equal to the normalisation scale).

The signal cross section can also vary with the assumed factorisation scale. A study is presented in Table 5.15. The variations due to the factorisation scale (taken to be equal to the renormalisation scale in this study) ranges from 1.5 to 8.7%. Based on the above studies, as well as on the comparison with a similar study of SUSY $2\ell^{ss}$ and 3ℓ analysis [52], an overall uncertainty of 15% is assumed for the signal normalisation.

Uncertainties on cross-sections of prompt backgrounds

The uncertainties found in the cross-section measurements of various prompt processes are used. For rare backgrounds (processes with very low cross-sections) which have no dedicated measurements yet, a conservative uncertainty of 50% was used. The WZ, VVV, and tZ uncertainties are 7.2% [53], 20% [54], and 15% (similar to the WZ analysis [53]) respectively. The WZ production is an important contribution to the signal region, and therefore the uncertainty estimate needs to take into account the fact that the analysis phase space covers the high jet multiplicity region. In the dedicated control study of the WZ process defined as,

- The three leptons should satisfy the tight requirements.
- The leading lepton should have $p_T > 25$ GeV.

- A pair of same-flavour, opposite sign leptons with an invariant mass in the $Z-$window, $|M_{\ell\ell} - M_Z| < 10$ GeV. If there are two pairs satisfying this condition, the pair with an invariant mass closer to the $Z-$mass is chosen as Z-candidates and the remaining lepton is chosen as the W-candidate.

- Transverse mass of the W candidate, $M_T > 40$ GeV.

the comparison between data and predicted background as a function of the number of jets is shown in Figure 5.14. The data agrees with the predicted number of events within 10% for $N_{jets} < 4$. The agreement is around 20% for $N_{jets} > 3$. The WZ uncertainty is therefore taken to be of 20%.The uncertainties for the other backgrounds are 19.2% for ZZ [55] and 10.1% for WW [56], 53.3% (33.3%) for $t\bar{t}W$ $(t\bar{t}Z)$ [57]. Since the ttV contributions are dominating some of the signal regions, the cited uncertainty correspond to the measurements and largely exceed the uncertainties of the corresponding theoretical predictions (11-13%). This conservative choice also covers the uncertainties associated with the specific final state topology requested for the signal region of the present analysis.

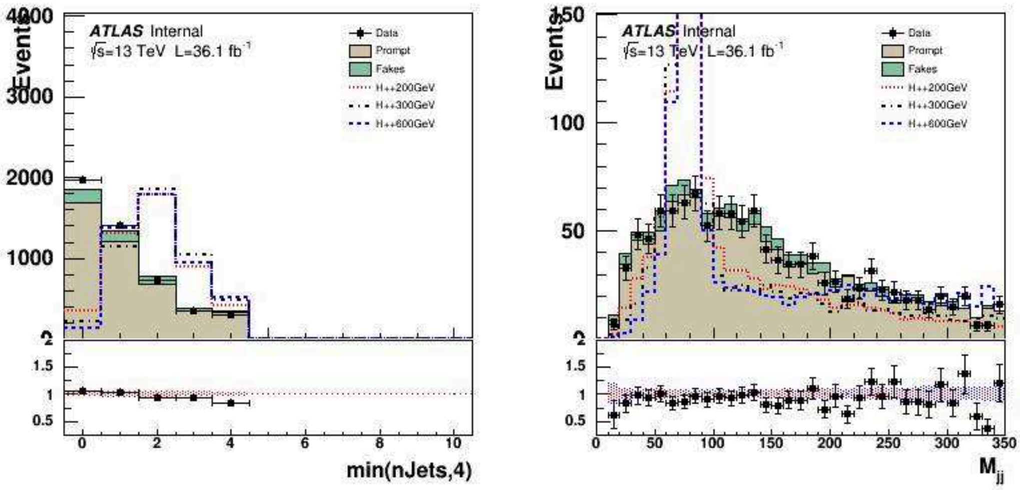

Fig. 5.14: Distributions in the WZ control region.

Uncertainties due to detector simulation

Imperfect detector simulation affects the shapes of the kinematic distributions of physics objects and thus, also affects the acceptance of the signal region selection. These uncertainties are implemented as a part of the corrections applied to the analysis and are described here. This type of uncertainty includes: uncertainties on the electron energy scale and energy resolution, uncertainties on the reconstruction of MET due to effects of soft tracks and uncertainties on the jet energy scale (JES) and resolutions (JER). The b-tagging related uncertainties are mixtures of statistical error from data, experimental error (JER), and modeling errors ($t\bar{t}$ events used to measure the b-tagging uncertainties). These uncertainties depend on the jet p_T, η and the b-tagging operating points used in the analysis. The impact on the event yields in the signal region due to these uncertainties is estimated by applying the same event selection on the simulated samples with these scales and resolutions varied by ± 1 standard deviation from the nominal.

Another type of systematic uncertainty arises from the uncertainties on the corrections to the efficiencies of the reconstruction and selection of the final states. This group affects the yields of all processes and includes uncertainties on the efficiency of lepton (electron and muon) reconstruction

and identification (labeled as "elSF" and "muSF" in the tables), uncertainties on the trigger efficiency (referred to as "trigSF"), and jet energy scale (19NP, labeled as "Jet"). The pile-up re-weighting (labeled as "Pileup") is also taken into account. The uncertainties of these effects are evaluated by varying the correctional factors by one standard deviation.
The prompt background processes are normalized to get the yield at the luminosity of the collected data. Hence, an uncertainty in the luminosity measurement also affects the yields in the signal region. This uncertainty in the luminosity measurement is also taken into account.

Uncertainties on fake background estimates

The systematic uncertainties on fake background estimates originate from various sources such as uncertainties on prompt processes, origin of the fake lepton, reliability of the fake factor method in the context of closure, and extrapolation of fake yields from the pre-selection region to the signal region. These effects are described below.

Uncertainties due to systematics on prompt processes:
As shown in method for evaluating fake estimates at the pre-selection stage, the MC-based prompt background processes enter the estimation of the number of fakes, both in the fake factor definition (equation 5.1) and in the extrapolation procedure (section 5.4.3). This implies that the uncertainties due to detector simulation also affect the contribution from fakes. These sources are collectively called ’Prompt uncertainties’ in Table 5.16.

Source of error on prompt contribution	Error on θ_e	Error on θ_μ
Systematic weights (JVT, pileup, scale factors etc.)	9.1%	12.6%
Systematic shapes (jets, MET, etc.)	7.7%	15.7%
Cross-section uncertainties (theory)	12.8%	47%
Total	17.5%	51.1%

Table 5.16: Systematics effects on the fake factors originating from prompt contributions.

Uncertainties due to origin and composition of fake backgrounds:
The three regions Y, Z, and T are mutually orthogonal and sources for fakes are different in these regions. For example, the fakes in the Z regions are mostly jets faking leptons in the detector, whereas the fakes in the T region originate from semi-leptonic b-decays. Since fakes in the X region can have mixed sources, the variation in the fake factors due to changes in composition needs to be taken into account. The stability of the fake factor across the samples Y, Z ,T is considered as a systematic uncertainty attributed to the sample composition dependence. The high value of the muon fake factor calculated in the Z sample (twice the nominal value but with large errors): it is attributed to a statistical fluctuation. Indeed, by investigating the MC fakes composition, the fake muons in all samples is seen to originate from heavy hadrons. In addition, recomputing the fake factors based on the MC samples (instead of data driven) lead to a value in the Z sample that is in much better agreement with the nominal value deduced from the Y sample. A potential deviation from a constant fake factor in all samples is taken as the average difference of the X, Z and T sample versus the nominal (Y) values. This variation is found to be below 10% for the electron, and 30% for the muon.

The origin of fakes has been studied using the MC fakes (dominated by Z+jets and $t\bar{t}$, but including all MC components where one lepton is identified as non-prompt. The differences in the origin of the

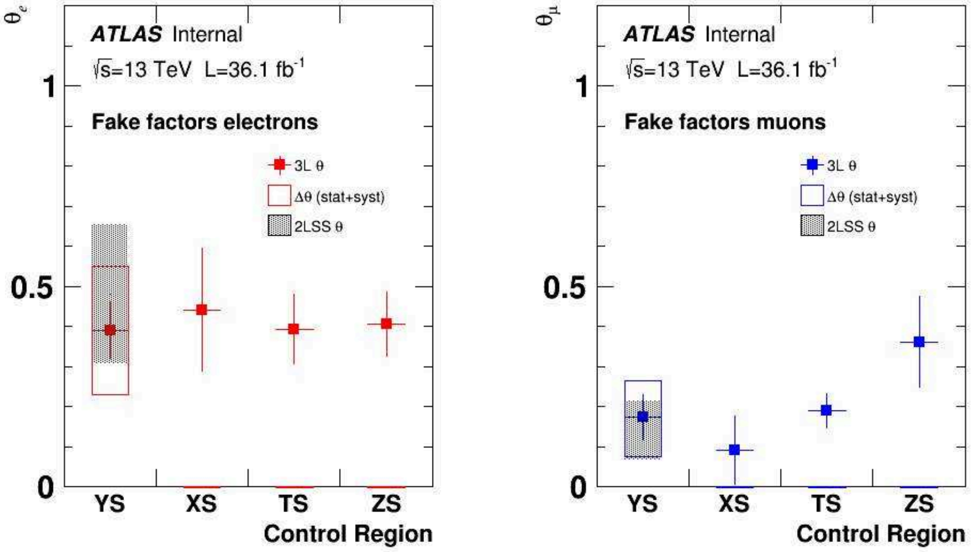

Fig. 5.15: The fake factors deduced in various control regions described in the text. The base-line values used for fakes estimated are calculated from the YR samples). The dark bands are fake factors calculated in the dilepton analysis using the same method. A good agreement between the trilepton and dilepton fake factors is also a validation of the method itself.

"loose-not-tight" versus "tight" regions, as well as the differences across the samples may lead to systematic effects. For instance, if the fractions of conversions versus heavy hadrons are different in the Y sample (where the fake factor is calculated) with respect to the pre-selection or signal region, this may induce an error in the estimate of the fake contributions. In order to further evaluate the impact of the difference in the origin of fake leptons, the MC simulation is used as follows: each of the main components (conversions, b-hadrons and c-hadrons) is varied individually by a factor ranging from 0.5 to 2, in steps of 0.5. The fake factors are then re-calculated for each of these variations in all the sections. The results are shown in Figure 5.16 for electrons and in Figure 5.17 for muons. The impact is mostly below 10% for both electrons and muons, except a maximum at 24% for the electron fake factor in the pre-selection region (X), where in fact the MC statistics is very low. These values are well below the assigned uncertainties to the nominal fake factors, which are of 50% and 80% for electrons and muons, respectively. However, the sample dependence uncertainty for electrons, estimated to be of below 10% from the variation of the fake factor in the control samples (X,Y,Z,T), is conservatively increased to 25%, leading to an increase of the total uncertainty of the fake factor for electrons from 50% to 55%. The sample variation for muons was set to 30% covering the effect observed here, so no extra systematics is assigned using this variation.

Uncertainties due to validity of the fake factor method in the context of closure:
The fake factors are determined in the $xe\not{e}$ and $x\mu\not{\mu}$ channels for electron and muons, respectively. The method assumes that this measurement would give a good agreement between $N_{\text{Data}} - N_{\text{prompt}}$ and the data-driven fakes in the $xe\mu$ channel. But, there is a possibility that the method has an internal bias that could systematically affect the closure in all the regions, X,Y,Z, and T. The closure quality, verified in the $xe\mu$ channel, is shown in Figure 5.18 (bottom, right). No statistically deviations are found in X,Z, and T. The closure is not as good in the Y region. This lack of closure is attributed to

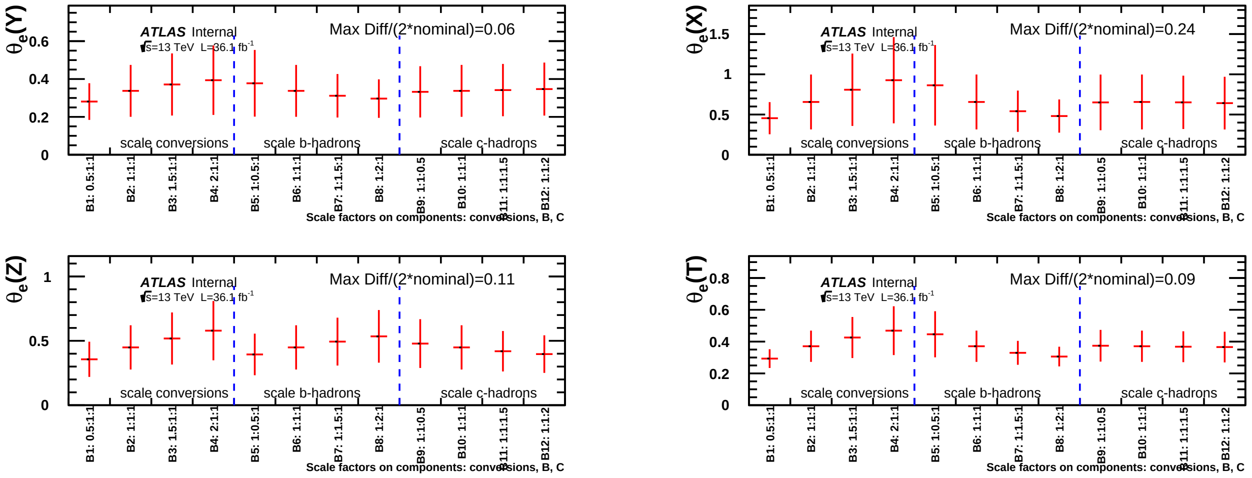

Fig. 5.16: The fake factors for electrons calculated with the MC fakes in all control regions for 3ℓ analysis as a function of the scale applied to one of the three main components. Each bin is labeled as "BN:I:J;K", where N is the serial number of the bin, I represent the overall scale applied to conversions component, J the scale applied to b-hadrons component and K the scale applied to c-hadrons component. 1:1:1 represents the nominal value for a given fake factor.

statistical fluctuation. The systematic uncertainty due to closure is defined as the stability of the fake-factor method for the $xe\mu$ channel, when the fake factors θ_e and θ_μ are deduced from xee and $x\mu\mu$ channels. Therefore the systematic is deduced from the differences observed in the $xe\mu$ channel with 'in-situ' (bottom-right figure in Figure 5.18) . The model for evaluating the systematic uncertainty is the following: it is taken as a common relative shift over the θ_e and θ_μ. By definition, the data-driven estimate N_D^r in each region r (X,Y,Z or T) is a linear combination of the "in-situ" fake factors θ_e^r and θ_μ^r and therefore is shifted in each region when a common "method-related closure bias" is considered as: $\theta_{e,\mu}^r = (1+\alpha_{e,\mu})\theta_{e,\mu}^r$. A χ^2 is built using the difference between these "data driven" estimates N_D (based on the fake factor method in each sample, represented in blue in the bottom-right Figure 5.18) and the $N_{\text{Data}} - N_{\text{prompt}}$, denoted by N_F (represented in red in the bottom-right Figure 5.18) in the $xe\mu$ channel, as follows:

$$\chi^2 = \sum_{r=X,Y,Z,T} \frac{(N_D^r - N_F^r)^2}{\sigma^2_{N_D^r} + \sigma^2_{N_F^r}} \tag{5.7}$$

where $\sigma^2_{N_D^r}$ and $\sigma^2_{N_F^r}$ are the uncertainties of the two estimates for each region r (X,Y,Z or T). The distribution of the probability $P(\chi^2, 4)$ as a function of the two shift , and the respective projections, are shown in Figure 5.19. The nominal values is in the centre $(0,0)$. The χ^2 probability indicates than a scan of the shift parameters $\alpha_{e,\mu}$ defined above does not define a significantly different preference. However, the highest probability is obtained within a shift of below 30%. Conservatively, this value is taken as a closure systematics.

Uncertainty due to usage of loose lepton ID for ℓ^0:
The fake factor method assumes as well that the "opposite-charge" lepton ℓ_0 is "pure". This hypothesis is verified with the main background contributions of the MC (Z+jets and $t\bar{t}$). The lepton ℓ_0 is found to be fake at a rate of less than 5%, a value taken as systematic effect on the fake factors.

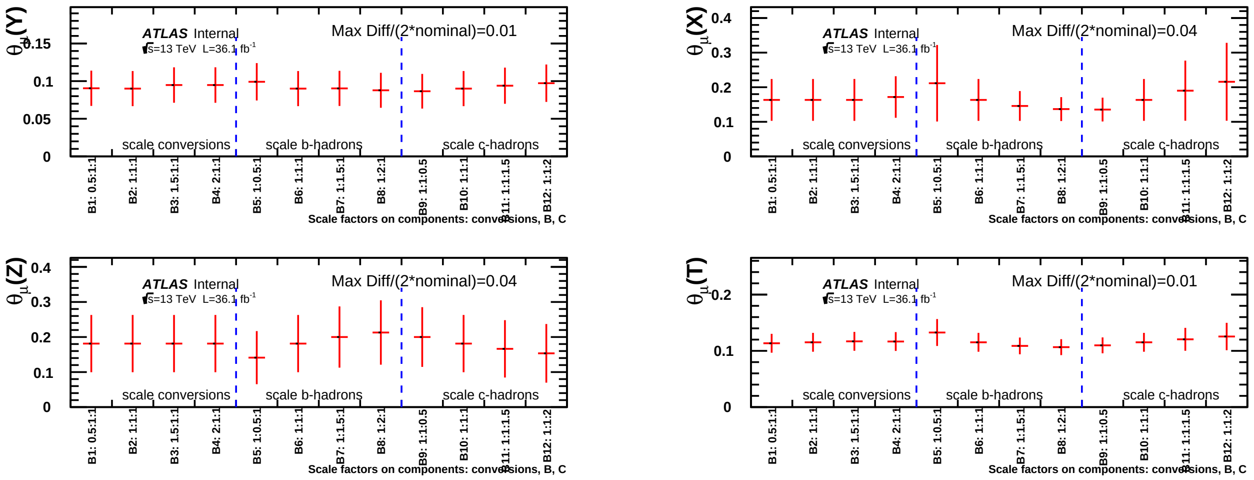

Fig. 5.17: The fake factors for muons calculated with the MC fakes in all control regions for 3ℓ analysis as a function of the scale applied to one of the three main components. Each bin is labeled as "BN:I:J;K", where N is the serial number of the bin, I represent the overall scale applied to conversions component, J the scale applied to b-hadrons component and K the scale applied to c-hadrons component (note that 1:1:1 represents the nominal value for a given fake factor).

Uncertainty due to a cut on jet multiplicity:
The distributions of the kinematic and topology variables in the preselection region (Figures 5.2 to 5.5) show a good agreement between data and prediction. This remains true for the other control samples (figures in appendix).

In particular, the good agreement observed for jet multiplicity distribution in the pre-selection sample, shown in figure 5.4 does not suggest a fake factor dependence on this observable. This also holds true in the Z-enriched (ZS) and $t\bar{t}$ enriched sample (TS), as illustrated in Figures 5.20 and 5.21 respectively. Therefore, the fake factors are considered as uniform over the whole phase space and no extra systematic uncertainty is attributed to the dependence of the fake factor on kinematics or jet multiplicity.

Uncertainty due to extrapolation of fake estimates to the signal region:
The extrapolation from the pre-selection level to the signal region, is estimated using the factorised efficiencies of partial cuts combinations, as described in section 5.4.3. An additional systematic uncertainty needs to be considered estimating the fake contributions. The grouping shown in Table 5.14 is not unique, and hence the efficiencies in the table can also vary. This would affect the fake estimates in the signal region as well. The cuts are grouped in various combinations (5 cuts grouped in 2-2-1, giving 15 different paving combinations, on which the average and the RMS are calculated). This average is then compared with the nominal configuration that is used in the analysis. This comparison is shown in figure 5.22. The uncertainty deduced from this extrapolation is thus taken to be 30%. The systematics uncertainty associated to the fake leptons contributions to the signal region are summarised in Table 5.17.

The effect of the various systematic uncertainties described in this section are summarized in Tables 5.18 and 5.19 for the mass point of 200 GeV.

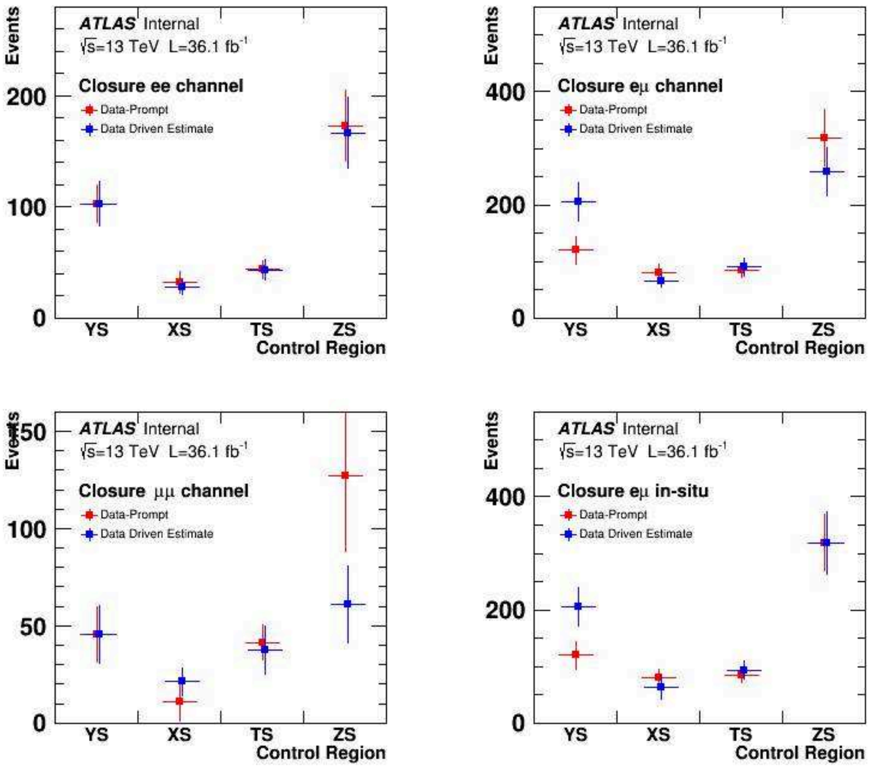

Fig. 5.18: The comparison between the difference between data and the prompt MC and the data-driven fake estimates for the four control regions. The base-line values used for fakes estimated are calculated from the Y samples (the values obtained in the first bins in the left figures are trivially in agreement). The three flavour contributions are shown in the first three figures. The "in-situ" verification is presented in the bottom-right figure: for this figure the data driven estimate is obtained using the "in-situ" fake factors obtained in the $xe\not{e}/x\mu\not{\mu}$ configurations in each control region.

Source	fake factor electron	fake factor muon
Sample dependence	25%	30%
Closure $e\mu$	30%	30%
Prompt uncertainties	17.5%	51.1%
ℓ_0 purity	5%	5%
Extrapolation to the signal region	30%	30%
Total systematics	46%	73%
Total stat+systematics	55%	81%

Table 5.17: Systematic uncertainties taken into account for the fake rate in the signal region.

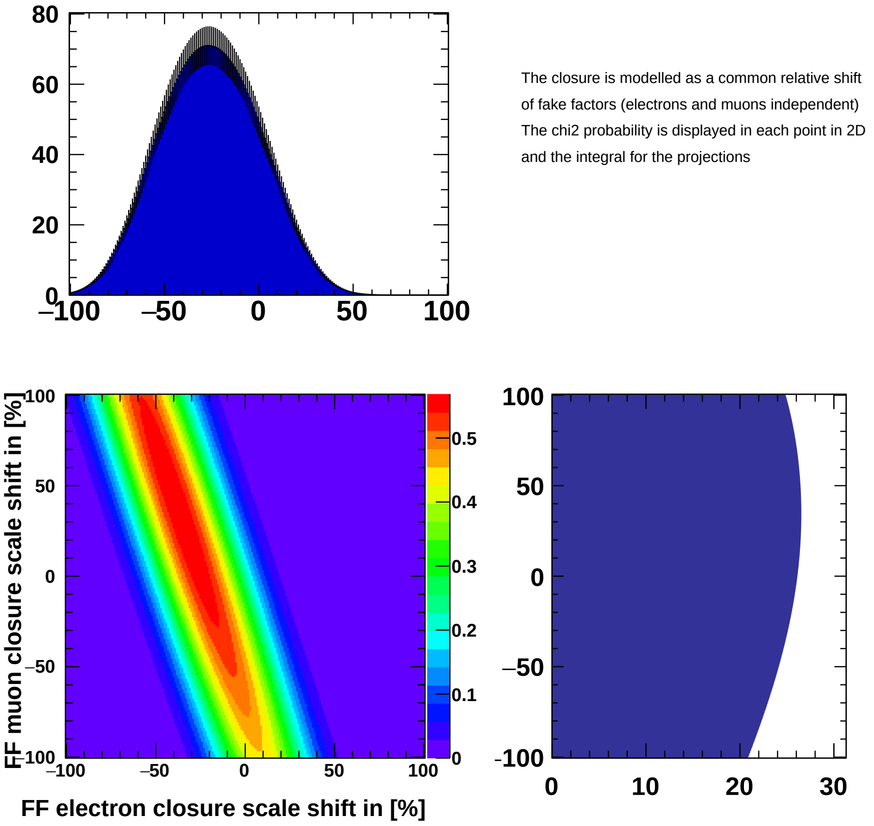

The closure is modelled as a common relative shift
of fake factors (electrons and muons independent)
The chi2 probability is displayed in each point in 2D
and the integral for the projections

Fig. 5.19: The χ^2 probability distribution as a function of a common shifts for of the fake factors in each sample.

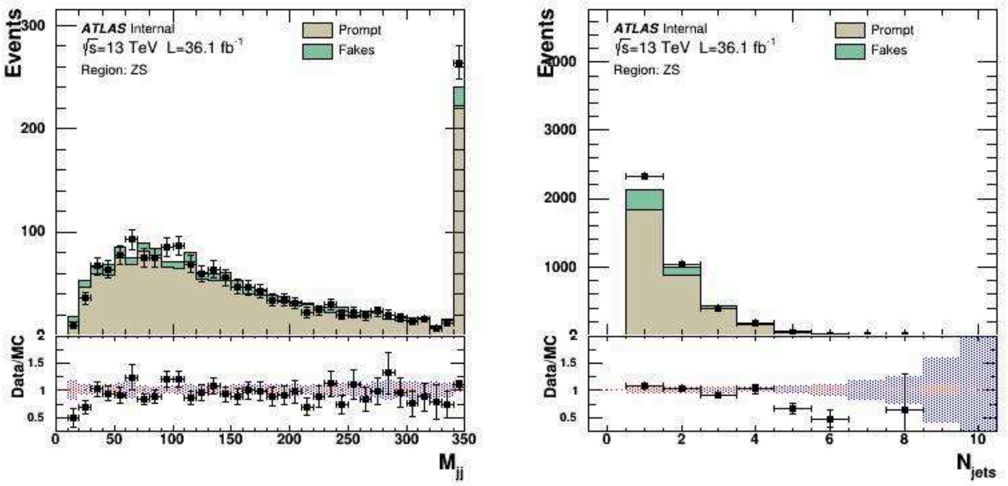

Fig. 5.20: Data compared to prediction for the di-jet invariant mass M_{jj} (left) and jet multiplicity N_{jet} (right) distributions in the Z-enriched (ZS) sample

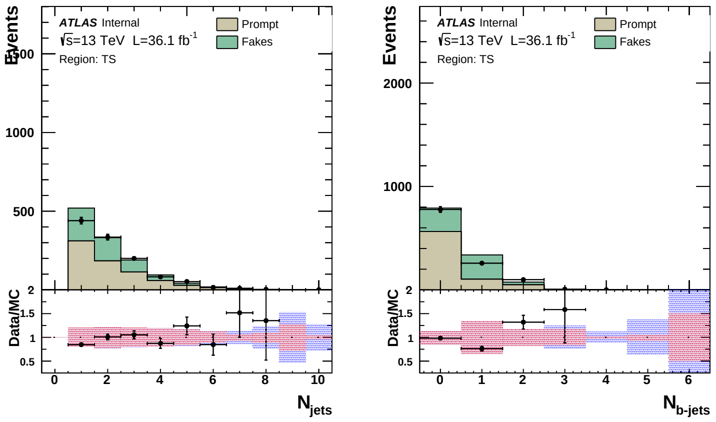

Fig. 5.21: Data compared to prediction for the di-jet invariant mass M_{jj} (left) and jet multiplicity N_{jet} (right) distributions in the $t\bar{t}$ enriched sample (TS).

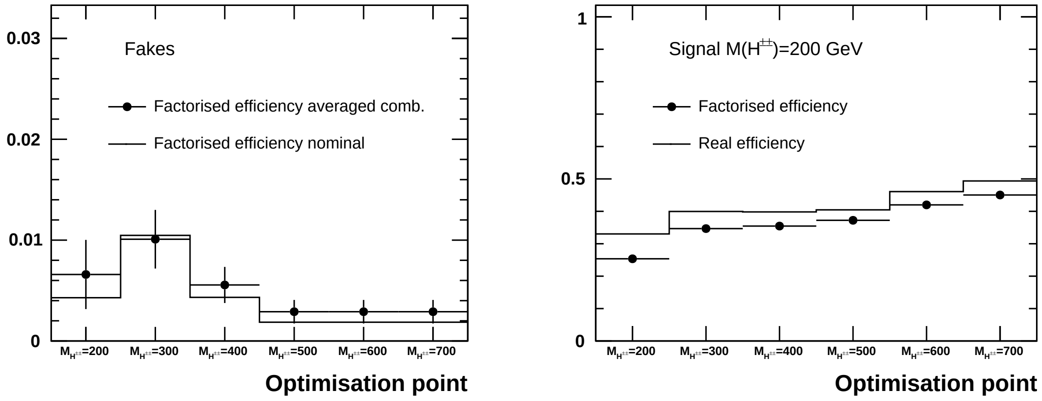

Fig. 5.22: The factorised efficiency averaged over all cuts combinations grouping 2-2-1. The average and the RMS values are represented. This is an estimate of the central value and the spread obtained when different grouping combinations are used for the 5 cuts in order to estimate the extrapolation efficiency for fakes. The agreement between the variations and the nominal values is within 30%.

	$H^{++}H^{--}$	FAKES	Prompt
Pileup	$--$	$--$	0.01
Electron scale factors	0.03	$--$	0.02
electron resolution	$--$	$--$	0.01
MET	$--$	$--$	0.01
Muon scale factors	0.01	$--$	0.01
Trigger scale factors	$--$	$--$	$--$
Jet (JES, JER)	0.03	$--$	0.04
JVT	0.03	$--$	0.04
MC normalization	$--$	$--$	0.22
Fake	$--$	0.36	$--$
Luminosity	0.03	$--$	0.03

Table 5.18: Relative effect of each systematic on the yields of the 3L SFOS0 channel in %.

	$H^{++}H^{--}$	FAKES	Prompt
Pileup	0.01	$--$	0.03
Electron scale factors	0.02	$--$	0.02
MET	0.00	$--$	0.04
Muon scale factors	0.01	$--$	0.02
Trigger scale factors	$--$	$--$	$--$
Jet (JES, JER)	0.03	$--$	0.12
JVT	0.03	$--$	0.04
MC normalization	$--$	$--$	0.17
Fake	$--$	0.46	$--$
Luminosity	0.03	$--$	0.03

Table 5.19: Relative effect of each systematic on the yields of the 3L SFOS12 channel in %.

5.4.5. Yields in the signal region

As an example, the yields in the signal region designed for $m_{H^{\pm\pm}} = 200$ GeV are shown in table 5.20. The corresponding distributions of the observed and predicted events are shown in figure 5.23.

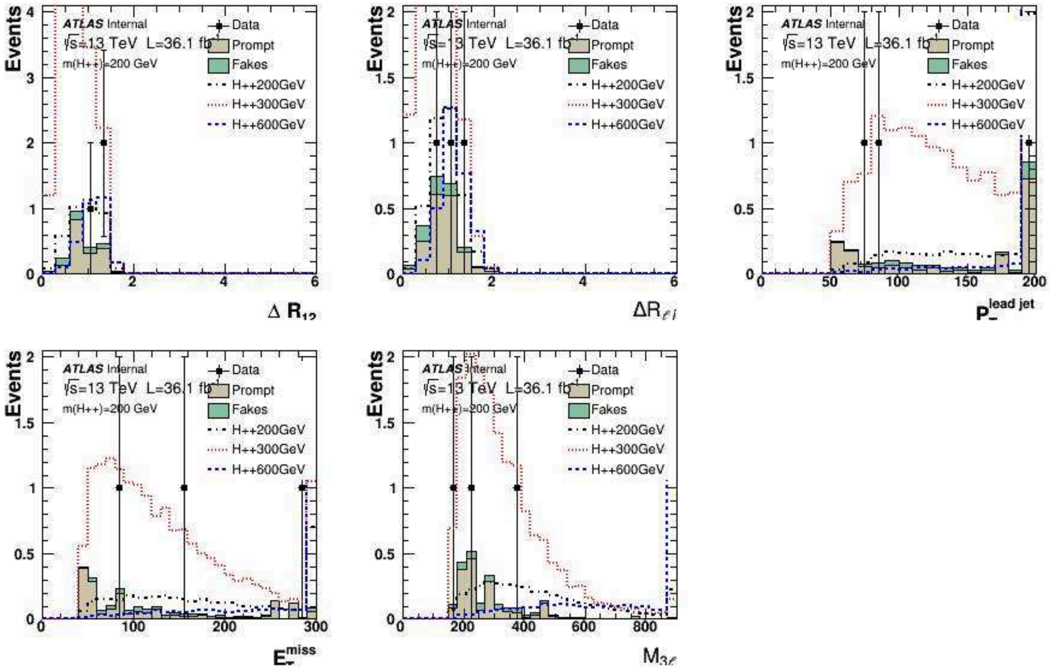

Fig. 5.23: Distributions in the 3ℓ signal region for $m_{H^{\pm\pm}} = 200GeV$. The normalisations for the signal expectations are arbitrary.

	Channel	Flavour	Data	Prediction	Prompt	Fakes	H++200GeV
1	eee	SFOS2	1	0.105 ± 0.038	$0.079 \pm 0.020 \pm 0.029$	0.025 ± 0.013	$0.474 \pm 0.021 \pm 0.040$
2	$ee\mu$	SFOS1	1	0.451 ± 0.194	$0.392 \pm 0.177 \pm 0.076$	0.058 ± 0.029	$1.095 \pm 0.032 \pm 0.059$
3	$e\mu\mu$	SFOS0	1	0.270 ± 0.075	$0.161 \pm 0.033 \pm 0.040$	0.109 ± 0.054	$0.685 \pm 0.025 \pm 0.031$
4	μee	SFOS0	0	0.224 ± 0.071	$0.106 \pm 0.024 \pm 0.031$	0.118 ± 0.059	$0.745 \pm 0.025 \pm 0.045$
5	$\mu e\mu$	SFOS1	0	0.587 ± 0.402	$0.501 \pm 0.231 \pm 0.326$	0.086 ± 0.043	$1.616 \pm 0.037 \pm 0.082$
6	$\mu\mu\mu$	SFOS2	0	0.531 ± 0.330	$0.488 \pm 0.275 \pm 0.181$	0.043 ± 0.021	$0.804 \pm 0.027 \pm 0.030$
7	Total		3	2.166 ± 0.586	$1.727 \pm 0.403 \pm 0.364$	0.439 ± 0.219	$5.419 \pm 0.069 \pm 0.261$

Table 5.20: Various options to select the signal region and the corresponding yields of prompt and fake backgrounds, and the signal with $M_{H^{\pm\pm}} = 200$ GeV. Note that in this table the systematic errors are considered separately for prompt and signal (second error) and the fake uncertainty includes the systematic uncertainties as well.

5.5. Combination of analysis in $2\ell^{ss}$, 3ℓ, and 4ℓ final states

In the previous sections, the analysis in the 3ℓ final state is described in detail. But, as mentioned earlier, analysis in $2\ell^{ss}$ and 4ℓ final states are also possible, and should increase the sensitivity. The analysis in these channels is summarized in this section. For comparison, the 3ℓ analysis is included in this summary.

5.5.1. Signal and background topologies

The searched signal events contains four $W^{\pm}$ bosons. Since at least two leptonic W-boson decays are needed to lead to the multi-lepton topologies considered in this analysis, all corresponding signal events are expected to present significant $E_{\mathrm{T}}^{\mathrm{miss}}$. For the $2\ell^{ss}$ signature, two out of the four W bosons decay to dijets, typically. Similarly, one W boson is expected to decay to jets for 3ℓ signature, while no jets issued from the hard interaction is expected for the 4ℓ channel. The signal event of $2\ell^{ss}$ and 3ℓ channels contains therefore a significant number of jets with high transverse momentum. Moreover, the same-sign di-leptons present in all searched topologies originate from the same scalar boson $H^{\pm\pm}$ and therefore tend to be close in $\eta-\phi$, while the other decay production (jets for $2\ell^{ss}$, jets and the opposite sign lepton for the 3ℓ case, and the other lepton pair for 4ℓ) are generally produced at larger distance in $\eta-\phi$. Additionally, the jets originating from W's are predominantly issued from light quarks $udsc$, leading therefore to events with no b-jets.

5.5.2. Event preselection

All analysis channels face various background contributions from the SM. The $2\ell^{ss}$ topology is populated with events containing one true lepton (from W, and to some lesser extent from Z bosons) and one fake lepton from the hadronic final state. The $2\ell^{ss}$ events with two same-sign electrons can also originate from the opposite sign pairs originating from Drell-Yan and $t\bar{t}$ production, where the charge of one of the electron is mis-identified (the charge mis-identification rate is negligible for muons). The background for the 4ℓ final state originates from processes such as $t\bar{t}V$, ZZ, $t\bar{t}$, Z+jets, and more rare backgrounds such as $t\bar{t}H$, and VH. A set of cuts is defined in order to reject as many events as possible from these sources.

The selection is divided in two steps: the pre-selection, where data samples are compared to the predictions (including Monte Carlo simulations and data-driven background estimates) and the signal region. The latter is obtained from a multivariate rectangular cuts optimization and is adjusted as a function of the $H^{\pm\pm}$ mass.

For $2\ell^{ss}$ and 4ℓ channels, the leptons are ranked with increasing P_T as $\ell^{0,1,2..}$. The lepton ranking for the 3ℓ topology is defined in section 5.4.1. The pre-selection for all the channels in presented in table 5.21.

5.5.3. Background estimate

The SM processes contribute to the analysis phase space when the final state include reconstructed leptons , missing energy and several jets (for $2\ell^{ss}$). A significant contribution is expected from processes where the reconstructed leptons correspond to leptons that are promptly produced in the hard interaction or originate from a weak boson decay. These processes, called "prompt" in the following, are predicted using MC simulations. The SM processes leading predominantly to prompt contributions are indicated in table 5.2 and the procedure to pre-select prompt events from the MC files is explained in section 5.1.

Selection criteria	$2\ell^{ss}$	3ℓ	4ℓ
Trigger	At least one lepton with $P_T^{\ell} > 30$ GeV matched to the single-lepton trigger signals		
N_ℓ(loose,$P_T > 10$ GeV,$\lvert\eta_\ell\rvert < 2.47$)	2	3	4
$\lvert\sum Q_\ell\rvert$	2	1	0
P_T threshold leptons	$P_T^{\ell_0 \ell_1} > 30, 20$ GeV	$P_T^{\ell_0,\ell_1,\ell_2} > 10, 20, 20$ GeV	$P_T^{\ell_0,\ell_1,\ell_2,\ell_3} > 10$ GeV
$E_{\mathrm{T}}^{\mathrm{miss}}$	> 70 GeV	> 30 GeV	> 30 GeV
N_{jets}	> 2	> 12	–
Z-boson decays veto	$\lvert M_{ee} - M_Z\rvert > 10$ GeV	$\lvert M_{\ell^\pm\ell^\mp} - M_Z\rvert > 10$ GeV	
Low di-lepton mass veto	–	$M_{\ell^\pm\ell^\mp} > 15$ GeV	$M_{\ell^\pm\ell^\mp} > 12$ GeV
b-jet veto	$N_b - jet = 0$	$N_b - jet = 0$	$N_b - jet = 0$
N_ℓ (tight)	2	2 (ell_1 and ℓ_2)	> 0

Table 5.21: The preselection for the searched event topologies. The 3ℓ pre-selection is shown here for reference.

Further contributions originate from mis-measurements of the leptons: the charge mis-identification of prompt leptons, that mainly occurs for electrons and affects predominantly the $2\ell^{ss}$ channel, and the so called fake leptons contributions that originate from hadrons decay, from photon conversions within the detector or are misidentified hadrons. Those contributions are described in the following.

Charge mis-measurement contributions

In the $2\ell^{ss}$ channel contributions are expected from events with opposite-sign lepton pairs where one of the lepton charge is mis-measured. The rate of charge mis-identification is only relevant for electrons, due to the higher sensitivity to the material, while for muons it is found to be negligible. The mis-identification rate is measured using large samples of di-lepton events origination predominantly from $Z \to e^+e^-$ decays. The sample of selected events is largely dominated by opposite (OS) sign di-leptons, while a small fraction contain same-sign (SS) di-leptons. The main phenomenon responsible for the charge mis-identification is the radiative interaction with the detector material, leading to secondary electron tracks of opposite charge associated to the initial electron. This fraction of SS di-leptons increases from 10^{-5} in the central region to a few percent at large rapidity, mainly due to the increase with the rapidity of the detector material crossed by electrons. Using this sample, the rate of charge mis-identification for electrons $r^{\mathrm{Q-flip}}$ can be measured as a function of η and p_T. Moreover, $r^{\mathrm{Q-flip}}$ is measured as a function of the electron type. The rate of events OS events selected with the same kinematic criteria as for the main analysis is then multiplied to the measured charge mis-identification rate to obtain the charge mis-identification contribution in the analysis phase space: $N_{SS}^{\mathrm{Q-flip}} = r^{\mathrm{Q-flip}} N_{OS}$.

Fake leptons contributions

The fake lepton contributions are estimated using data-driven methods. Due to the fact that background composition and rates vary for the analysis channels, the background estimation methods are different for $2\ell^{ss}$, 3ℓ and 4ℓ channels. For the $2\ell^{ss}$ and 3ℓ channels the fake factor method is applied.

The fake factors are used to extrapolate the contribution from background enriched regions defined with then same kinematics requirements as the analysis phase space, but with inverted the lepton identification criteria, thereby enriched in fake leptons. The fake factors are calculated using control samples independent from the nominal selection: for $2\ell^{ss}$ the sample is defined by inverting the $E_{\mathrm{T}}^{\mathrm{miss}}$requirement. The rest of the procedure is similar to that used for the 3ℓ method and is described below.

For the 4ℓ channel, for which the statistics is low, the MC simulation is used, after a scaling procedure based on control regions built in order to test various background contributions. Since the two main backgrounds are expected to be associated with fake leptons originating from Z+jets and $t\bar{t}$ processed, two samples A and B with three leptons are defined such that they are enriched in fake leptons originating from those two processes respectively. The three-lepton control samples are built such that the fake lepton candidate is identified by topology (for instance the lepton not part of the Z-candidate for A sample). The comparison of data to the simulation allows to estimate the scale factors for the MC processes leading to the fakes contributions, as explained below.

The control samples used to extract the fake factors and the scale factors are described in Table 5.22.

Cut name	$2\ell^{ss}$	3ℓ	4ℓ-A	4ℓ-B
N_ℓ (loose)	2	3	3	3
p_T^ℓ	$> 30, 30$ GeV	$> 10, 20, 20$ GeV	$> 10, 10, 10$ GeV	$> 10, 10, 10$ GeV
N_{jets}	> 2	$= 1$	$= 1 (or = 2)$	$= 1 (or = 2)$
N_{b-jet}	$= 0$	–	–	–
P_T^{jet}	> 25 GeV	> 25 GeV	> 25 GeV	$> 30(25)$ GeV
Z-window	$\lvert M_{\ell\ell}^{os} - M_Z\rvert > 10$ GeV	$\lvert M_{\ell\ell}^{os} - M_Z\rvert > 10$ GeV	$\lvert M_{\ell\ell}^{os} - M_Z\rvert < 10$ GeV	No same-flavor opposite sign pair
$M_{\ell\ell}^{os}$	–	> 15 GeV	–	–
$E_{\mathrm{T}}^{\mathrm{miss}}$	< 70 GeV	–	< 50 GeV	–
M_T	–	–	< 50 GeV	–
Control Sample N_ℓ (tight)	2	2 (ℓ_1 and ℓ_2)	–	–
Fake-enriched Sample : N_ℓ (tight)	1	1 (ℓ_1 or ℓ_2)	–	–

Table 5.22: The selection criteria used for control samples definitions. The column for 3ℓ corresponds to the Y region defined in the previous section.

Fake lepton contribution estimate for $2\ell^{ss}$ channel For the $2\ell^{ss}$ channel, the fake factors need to take into account the charge-mis-identification contributions in the control samples. The fake factor calculation proceeds in two steps: first the muon fake factor is deduced from $\mu\mu$ events:

$$\theta_\mu^{2\ell ss} = \frac{(N^{\mathrm{Data}} - N^{\mathrm{Prompt}})_{\mu\mu}}{(N^{\mathrm{Data}} - N^{\mathrm{Prompt}})_{\mu\not\mu}} \tag{5.8}$$

This fake factor is the used to predict the contribution of fake muons for the $e\mu$ channel as follows:

$$N_{\mathrm{e}\mu}^{\mathrm{fake}-\mu} = \theta_\mu^{2\ell ss}(N^{\mathrm{Data}} - N^{\mathrm{Prompt}})_{\mathrm{e}\not\mu} \tag{5.9}$$

The fake factors for electrons are then deduced from the $e\mu$ sample as follows:

$$\theta_{\mathrm{e}}^{2\ell ss} = \frac{(N^{\mathrm{Data}} - N^{\mathrm{Prompt}} - N^{\mathrm{Q-flip}} - N^{\mathrm{fake}-\mu})_{\mathrm{e}\mu}}{(N^{\mathrm{Data}} - N^{\mathrm{Q-flip}} - N^{\mathrm{Prompt}})_{\not e\mu}} \tag{5.10}$$

The measured muon fake factor is found to be 0.14 ± 0.03, while the measured electron fake factor is 0.48 ± 0.07, where the error here are statistical only.

Fake lepton contribution estimate for 4ℓ channel The fake lepton contributions for the 4ℓ channel are estimated using MC predictions that are scaled. The scaling takes into account the agreement between data and simulation in control regions, enriched in fake contributions. The misidentified leptons are classified according to the origin of the events as heavy H (light L) if a top quark is present (absent). These two main sources of fake contributions are tested in two orthogonal regions A and B, enriched in Z+jets processes (dominated by "light" fakes) and in $t\bar{t}$ (mostly attributed to "heavy" fakes) , respectively. The scaling factors for electrons and muons in heavy and light environments $\lambda^{\ell}_{L,H}$ are extracted for each lepton flavor $\ell = e, \mu$ by solving the system of two equations: $N^{\ell}_{Data|A,B} - N^{\ell}_{Prompt|A,B} = \lambda^{\ell}_{H} N^{\ell}_{t\bar{t}|A,B} + \lambda^{\ell}_{L} Ne, \mu_{\text{Z+jets|A,B}}$, where the number of events for N^{ℓ} is labeled in the lower index by the nature of the contribution (Data, Prompt, $t\bar{t}$ and Z+jets) and the equation is derived in each of the respective control region (A, B). The obtained scale factors range from 0.94 to 1.12 and are statistically compatible with unity.

5.5.4. Signal region definitions

Several discriminant variables can be defined in each event in addition to the reconstructed variables such as $E_{\mathrm{T}}^{\mathrm{miss}}$, N_{jets}, N^{b}_{jets}, and the ones described in section 5.4.3:

- M^{W}_{jj}: the invariant mass of two jets closest to the W-boson mass.
- M_{jets}: the invariant mass of all jets in the event. When there are more than four jets in the event, only the leading 4 jets are considered for the calculation of the invariant mass.
- $M_{\ell_i \ell_j}$: di-lepton invariant mass. While a complete reconstruction of the $H^{\pm\pm}$ bosons is not possible using leptons due to escaping neutrinos, the variable still reflects the mass scale of the boson.
- $\Delta R_{\ell_i \ell_j}$: the distance in $\eta - \phi$ between two same-sign leptons. The same sign leptons tend to close for the signal, while some part the background favours a back-to-back topology. In 4ℓ channel, two such variables can be calculated per event, and the minimal and maximal value are used to discriminate the signal from the background. This and the previous variables can be used for any lepton pair in all analysis channels.
- $\Delta\Phi_{\text{MET}-\ell\ell}$: the difference in azimuth between the di-lepton system and the $E_{\mathrm{T}}^{\mathrm{miss}}$. This variable is used in the $2\ell^{ss}$ analysis.
- RMS: this is a variable used by the $2\ell^{ss}$ channel to describe the spread of the azimuthal angles of leptons, $E_{\mathrm{T}}^{\mathrm{miss}}$, and jets, defined as the R.M.S of the ϕ's of the leptons and $E_{\mathrm{T}}^{\mathrm{miss}}$ times that of the jets divided by the R.M.S. of the ϕ's of leptons, $E_{\mathrm{T}}^{\mathrm{miss}}$, and jets:

$$\text{RMS} = \frac{\text{R.M.S.}(\phi_{\ell_1}, \phi_{\ell_2}, \phi_{E_{\mathrm{T}}^{\mathrm{miss}}}) * \text{R.M.S.}(\phi_{j1}, \phi_{j2}, \cdots)}{\text{R.M.S.}(\phi_{\ell_1,}, \phi_{\ell_2}, \phi_{E_{\mathrm{T}}^{\mathrm{miss}}}, \phi_{j1}, \phi_{j2}, \cdots)}. \tag{5.11}$$

In the $2\ell^{ss}$ channel, the W bosons originating from one Higgs particle should decay to charged leptons and neutrinos, and the W bosons from the other Higgs particle should both decay to hadronic jets. Due to the spin correlations, the two charged leptons tend to be close in the azimuthal plane. The directions of $E_{\mathrm{T}}^{\mathrm{miss}}$and leptons should be centred around the direction of the Higgs particle. So smaller spread in the azimuthal angles of leptons in the events are expected. The same correlations are expected for the jets from the other Higgs particle. The ratio of the R.M.S defined above characterizes the feature of signal events.

- $\Delta\Phi_{\mathrm{MET-jet}}$: the distance in azimuth between the MET and the leading jet.
- $M_{4\ell}$: the invariant mass of four leptons (for the 4ℓ channel).

The distributions of the chosen variables in each channel are shown in Figures 5.24 and 5.25. The data is compared to predictions based on MC simulations and data-driven fake lepton estimate. A good agreement is observed. The distributions expected from the signal for various $H^{\pm\pm}$ masses is also shown, and illustrate the discriminant power of the chosen variables.

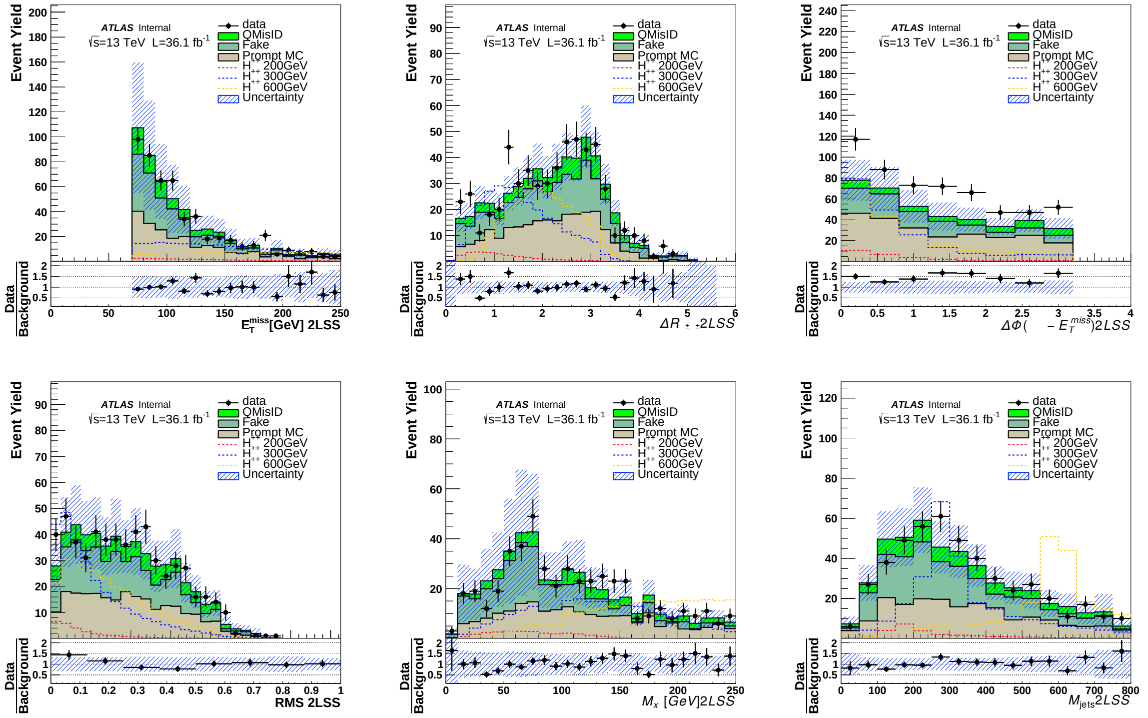

Fig. 5.24: Discriminating variables for all $2\ell^{ss}$ channel at event pre-selection stage, signal is rescaled to data for better vision, all uncertainties included.

The signal is extracted using a rectangular set cuts, optimized using the TMVA package. The optimization, as is the case for 3ℓ, is performed as a function of the $H^{\pm\pm}$ mass for $M_{H^{\pm\pm}} = 200, 300, 400$ and 500 GeV. The last optimization point is applied to $M_{H^{\pm\pm}} = 600$ and $M_{H^{\pm\pm}} = 700$ as well, since the expected cross sections are very small and the signal and background features do not vary significantly. The signal regions are optimized separately for the three lepton flavor composition for $2\ell^{ss}$ channel. The 4ℓ channel is not split into several channels.

The selection criteria used for the signal region are described in Table 5.23.

	$2\ell^{ss}$			3ℓ		4ℓ
Selection criteria	$e^{\pm}e^{\pm}$	$e^{\pm}\mu^{\pm}$	$\mu^{\pm}\mu^{\pm}$	SFOS 0	SFOS 1,2	
	$M_{H^{\pm\pm}}$ = 200 GeV					
$E_{\mathrm{T}}^{\mathrm{miss}}[GeV]$	> 100	> 100	> 100	> 45	> 45	> 60
$M_{x\ell}$[GeV]	[25 : 130]	[15 : 150]	[35 : 150]	> 160	> 170	> 230
$\Delta R_{\ell^{\pm}\ell^{\pm}}$	< 0.8	< 1.8	< 0.9	[0.15 : 1.57]	[0.00 : 1.52]	
$\Delta\Phi(\ell\ell - E_{\mathrm{T}}^{\mathrm{miss}})$	< 1.1	< 1.3	< 1.3			
RMS	< 0.3	< 0.3	< 0.2			
M_{jets}	[140 : 770]	[95 : 330]	[95 : 640]			
$\Delta R_{\ell-\mathrm{jet}}$				[0.08 : 1.88]	[0.07 : 1.31]	
$P_T^{\mathrm{leading\ jet}}$[GeV]				> 80	> 55	
$P_T^{\ell 0}$ [GeV]						> 65
$\Delta R^{min}_{\ell^{\pm}\ell^{\pm}}$						[0.16 : 1.21]
$\Delta R^{max}_{\ell^{\pm}\ell^{\pm}}$						[0.27 : 2.03]
	$M_{H^{\pm\pm}}$ = 300 GeV					
$E_{\mathrm{T}}^{\mathrm{miss}}[GeV]$	> 200	> 200	> 200	> 65	> 55	> 60
$M_{x\ell}$[GeV]	[105 : 340]	[80 : 320]	[80 : 320]	> 170	> 210	> 270
$\Delta R_{\ell^{\pm}\ell^{\pm}}$	< 1.4	< 1.8	< 1.8	[0.18 : 2.23]	[0.08 : 2.23]	
$\Delta\phi(\ell\ell, E_{\mathrm{T}}^{\mathrm{miss}})$	< 2.1	< 2.4	< 2.4			
RMS	< 0.4	< 0.4	< 0.4			
M_{jets}	[180 : 770]	[130 : 640]	[130 : 640]			
$\Delta R_{\ell j}$				[0.27 : 2.37]	[0.21 : 2.08]	
$P_T^{\mathrm{leading\ jet}}$[GeV]				> 95	> 80	
$P_T^{\ell 0}$ [GeV]						> 45
$\Delta R^{min}_{\ell^{\pm}\ell^{\pm}}$						[0.09 : 1.97]
$\Delta R^{max}_{\ell^{\pm}\ell^{\pm}}$						[0.44 : 2.68]
	$M_{H^{\pm\pm}}$ = 400 GeV					
$E_{\mathrm{T}}^{\mathrm{miss}}[GeV]$	> 200	> 200	> 200	> 65	> 85	> 60
$M_{x\ell}$[GeV]	[105 : 340]	[80 : 350]	[80 : 350]	> 230	> 250	> 270
$\Delta R_{\ell^{\pm}\ell^{\pm}}$	< 2.2	< 1.8	< 1.8	[0.22 : 2.39]	[0.29 : 2.69]	
$\Delta\phi(\ell\ell, E_{\mathrm{T}}^{\mathrm{miss}})$	< 2.4	< 2.4	< 2.4			
RMS	< 0.6	< 0.6	< 0.5			
M_{jets}	[280 : 1200]	[220 : 1200]	[220 : 1200]			
$\Delta R_{\ell j}$				[0.30 : 2.59]	[0.31 : 2.30]	
$P_T^{\mathrm{leading\ jet}}$[GeV]				> 120	> 100	
$P_T^{\ell 0}$ [GeV]						> 110
$\Delta R^{min}_{\ell^{\pm}\ell^{\pm}}$						[0.39 : 2.22]
$\Delta R^{max}_{\ell^{\pm}\ell^{\pm}}$						[0.55 : 2.90]
	$M_{H^{\pm\pm}}$ = 500 − 700 GeV					
$E_{\mathrm{T}}^{\mathrm{miss}}[GeV]$	> 250	> 250	> 250	> 120	> 100	> 60
$M_{x\ell}$[GeV]	[105 : 730]	[110 : 440	[110 : 440]	> 230	> 300	> 370
$\Delta R_{\ell^{\pm}\ell^{\pm}}$	< 2.6	< 2.2	< 2.2	[0.39 : 3.11]	[0.29 : 2.85]	
$\Delta\phi(\ell\ell, E_{\mathrm{T}}^{\mathrm{miss}})$	< 2.6	< 2.4	< 2.4			
RMS	< 1.1	< 1.1	< 1.1			
M_{jets}	> 440	> 470	> 470			
$\Delta R_{\ell j}$				[0.60 : 2.68]	[0.31 : 2.53]	
$P_T^{\mathrm{leading\ jet}}$[GeV]				> 130	> 130	
$P_T^{\ell 0}$ [GeV]						> 160
$\Delta R^{min}_{\ell^{\pm}\ell^{\pm}}$						[0.53 : 3.24]
$\Delta R^{max}_{\ell^{\pm}\ell^{\pm}}$						[0.59 : 2.94]

Table 5.23: The selection criteria used for the signal regions.

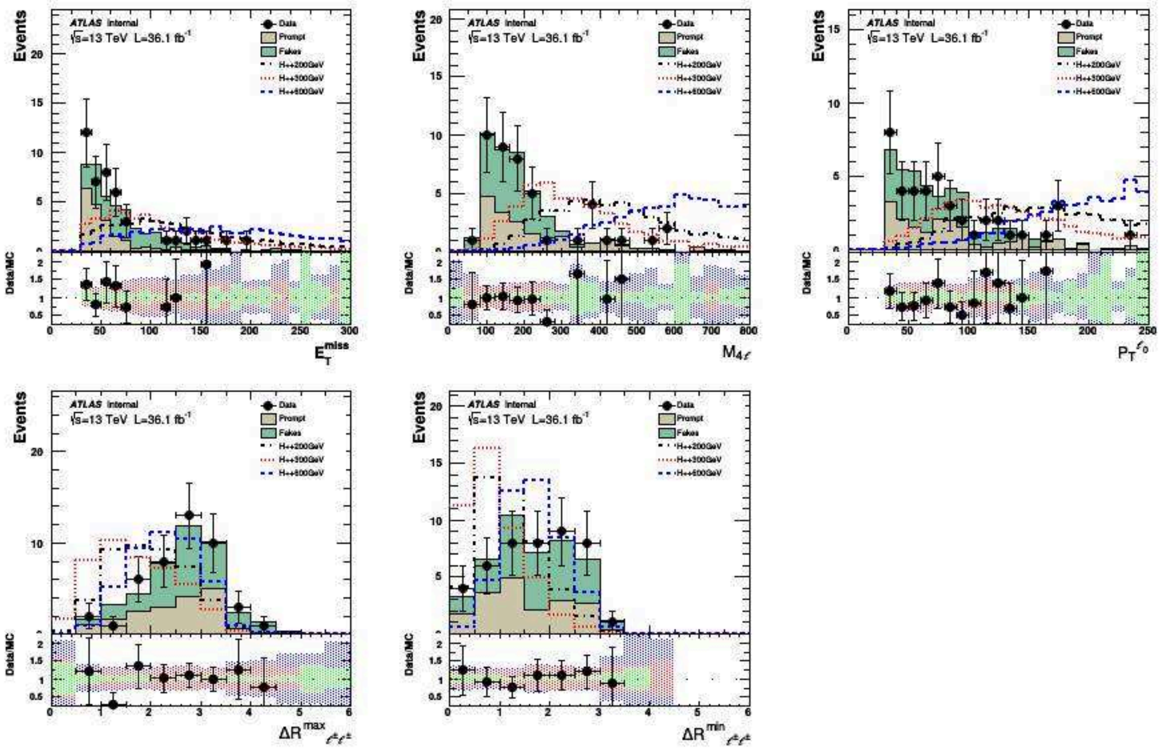

Fig. 5.25: Distributions of discriminating variables for the 4ℓ channel.

6.Statistical Analysis and Results

6.1. Event yields

The expected and observed event yields in the signal regions of the 200-500 GeV mass points are shown in Figure 6.1 and Table6.1. The performance is similar in all channels, with the signal prediction being comparable or larger than the expected background in most cases for the mass point of 200 GeV.

	$2\ell^{ss}$			3ℓ		4ℓ
subchannel	$e^\pm e^\pm$	$e^\pm\mu^\pm$	$\mu^\pm\mu^\pm$	SFOS 0	SFOS 1,2	
			$M_{H^{\pm\pm}} = 200$ GeV			
Prompt	0.50 ± 0.24	0.29 ± 0.20	1.25 ± 0.56	0.27 ± 0.08	1.4 ± 0.54	0.07 ± 0.03
QMisID	0.62 ± 0.21	0.35 ± 0.14	–	–	–	–
Fake	1.10 ± 1.02	< 0.01	0.39 ± 0.33	0.23 ± 0.11	0.21 ± 0.11	0.03 ± 0.02
Total background	2.21 ± 1.05	0.64 ± 0.26	1.66 ± 0.68	0.49 ± 0.13	1.67 ± 0.55	0.11 ± 0.05
Signal	0.86 ± 0.17	1.87 ± 0.34	1.91 ± 0.34	1.43 ± 0.26	3.99 ± 0.72	0.91 ± 0.17
Data	3	2	2	1	2	0
			$M_{H^{\pm\pm}} = 300$ GeV			
Prompt	0.13 ± 0.12	0.91 ± 0.42	0.02 ± 0.02	0.44 ± 0.13	3.99 ± 1.21	0.25 ± 0.14
QMisID	0.14 ± 0.09	0.07 ± 0.04	–	–	–	–
Fake	0.44 ± 0.49	< 0.01	< 0.01	0.31 ± 0.19	0.84 ± 0.39	0.20 ± 0.18
Total background	0.71 ± 0.51	0.99 ± 0.46	0.02 ± 0.02	0.75 ± 0.23	4.83 ± 1.78	0.45 ± 0.23
Signal	0.13 ± 0.03	0.50 ± 0.09	0.24 ± 0.04	0.51 ± 0.09	1.46 ± 0.26	0.34 ± 0.06
Data	0	3	0	0	11	0
			$M_{H^{\pm\pm}} = 400$ GeV			
Prompt	0.68 ± 0.30	1.03 ± 0.44	0.25 ± 0.14	0.30 ± 0.08	3.73 ± 1.16	0.33 ± 0.12
QMisID	0.32 ± 0.14	0.18 ± 0.08	–	–	–	–
Fake	0.38 ± 0.49	< 0.01	< 0.01	0.30 ± 0.16	0.21 ± 0.11	0.05 ± 0.04
Total background	1.37 ± 0.59	1.21 ± 0.45	0.25 ± 0.14	0.59 ± 0.18	3.94 ± 1.17	0.38 ± 0.13
Signal	0.16 ± 0.03	0.31 ± 0.06	0.15 ± 0.03	0.18 ± 0.03	0.52 ± 0.09	0.13 ± 0.02
Data	2	6	1	0	4	1
			$M_{H^{\pm\pm}} = 500, 600, 700$ GeV			
Prompt	1.00 ± 0.38	0.73 ± 0.30	0.34 ± 0.19	0.38 ± 0.10	2.93 ± 0.84	0.24 ± 0.07
QMisID	0.31 ± 0.12	0.15 ± 0.07	–	–	–	–
Fake	0.24 ± 0.49	0.29 ± 0.49	< 0.01	0.11 ± 0.06	0.10 ± 0.05	0.17 ± 0.17
Total background	1.56 ± 0.63	1.16 ± 0.58	0.34 ± 0.17	0.49 ± 0.12	3.02 ± 0.84	0.41 ± 0.18
Signal	0.09 ± 0.02	0.13 ± 0.02	0.06 ± 0.01	0.07 ± 0.01	0.20 ± 0.03	0.05 ± 0.01
Data	4	3	0	0	2	3

Table 6.1: The number of events in the various signal regions.

6.2. Statistical analysis

The relative signal strength to the SM prediction, $\mu = \sigma/\sigma_{\mathrm{SM}}$, is extracted from data, using a statistical fitting procedure based on the ROOSTATS framework [58, 59]. A binned maximum likelihood function is constructed like the following equation, as the product of Poisson-probability terms over the bins of the input distributions including the numbers of data events and expected signal and background yields, taking into account the effects of the floating background normalizations and systematic uncertainties:

$$\mathcal{L}(\mu,\boldsymbol{\theta}) = \prod_{j} \prod_{i=\text{bin}} \text{Poisson}\left(N_i(j)|\mu\left(s_i^{SFOS0}(j) + s_i^{SFOS1,2}(j)\right) + b_i(j)\right) \prod_{\boldsymbol{\theta}} \text{func}(t|\boldsymbol{\theta},1), \tag{6.1}$$

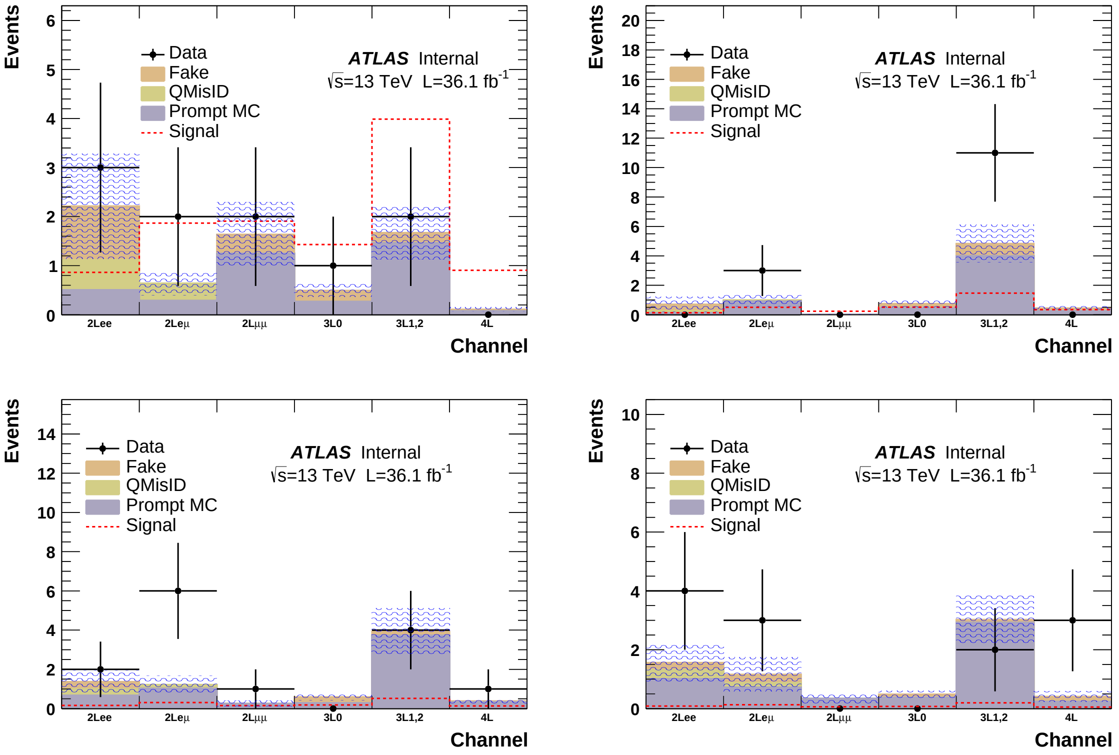

Fig. 6.1: The yields obtained in all analysis channels of the analysis for the signal regions m_{H++} = 200, 300, 400 and 500 GeV. Data is represented as point with errors, while the prediction of various components are represented as histograms. The error band represent the full uncertainty (statistic and systematic) of the total prediction. The signal prediction normalized to the luminosity of the analyzed data sample is represented as well.

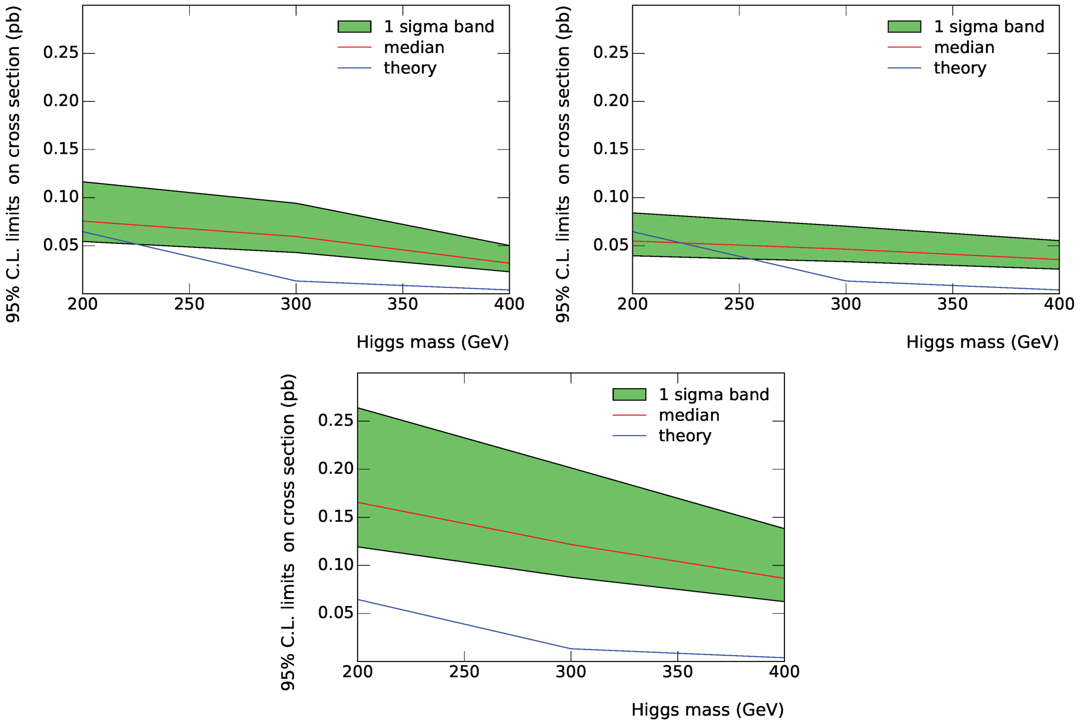

Fig. 6.2: Expected limits assuming 36.1 fb^{-1} of data in the $2\ell^{ss}$, 3ℓ, and 4ℓ channels (from left to right).

where μ is the signal strength, $\boldsymbol{\theta}$ is the nuisance parameters (NPs), func is given by Gaussian or log-normal probability density functions (PDFs), and t is the measured values in the calibrations. $N_i(j)$ is the number of observed events in the ith bin in the jth signal region, and $s_i^{SFOS0}(j)$, $s_i^{SFOS1,2}(j)$ and $b_i(j)$ are the expected number of $SFOS0$, $SFOS-1,2$ signal and background events, respectively. Here, $s_i(j)$ and $b_i(j)$ are given by a function of NP. The impact of systematic uncertainties on the signal and background expectations is described by NPs, $\boldsymbol{\theta}$, which are constrained by Gaussian or log-normal PDFs, the latter being used for normalization uncertainties to prevent normalization factors from becoming negative in the fit. The expected number of signal and background in each bin are given by functions of $\boldsymbol{\theta}$. The NP parameterization is chosen such that the predicted signal and background yields in each bin are log-normally distributed for a normally distributed θ. The test statistic, q_μ, is defined by the profile likelihood ratio,

$$q_\mu = -2\ln(\mathcal{L}(\mu, \hat{\hat{\boldsymbol{\theta}}}_\mu)/\mathcal{L}(\hat{\mu}, \hat{\boldsymbol{\theta}})), \tag{6.2}$$

where $\hat{\mu}$ and $\hat{\boldsymbol{\theta}}$ are the parameters that maximize the likelihood (with the constraint $0 \leq \hat{\mu} \leq \mu$), and $\hat{\hat{\boldsymbol{\theta}}}_\mu$ are NP values that maximize the likelihood for a given μ. This test statistic is used for exclusion intervals derived with the CL_s method [60, 61]. The systematic uncertainties are treated as nuisance parameters implemented in the likelihood functions.

6.3. Results

The upper limit on the signal strength is set at 95% C.L., and is presented in cross sections. The expected and observed limits of the combination of $2\ell^{ss}$, 3ℓ and 4ℓ channel for the six $H^{\pm\pm}$ mass

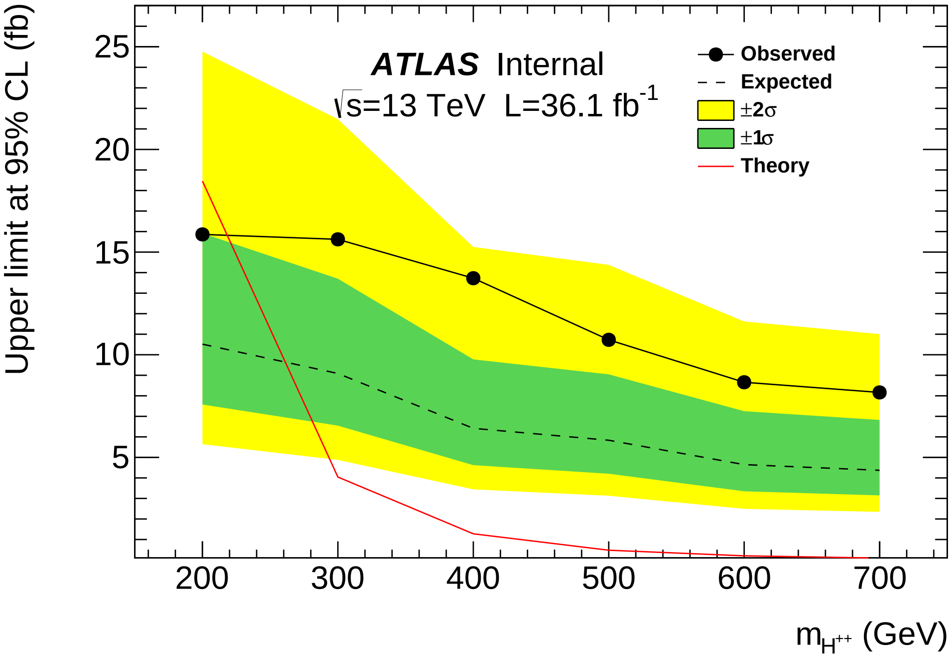

Fig. 6.3: Expected and observed limits for the combination of $2\ell^{ss}$, 3ℓ and 4ℓ channels.

hypothesis are shown in Figure 6.3. Assuming a linear interpolation of the sensitivity between near mass hypothesis, the expected upper limit is $m_{H^{\pm\pm}} < 260$ GeV at 95% CL, while the observed upper limit is $m_{H^{\pm\pm}} < 220$ GeV at $95\% CL$.

7.Future prospects

In the analysis presented in this thesis, it was assumed that the singly charged Higgs boson is heavier than the doubly charged Higgs boson. But, they can be degenerate or nearly-degenerate without violating any constraints. In such cases, the cross-section of associated production is twice as high as that of pair-production of doubly-charged Higgs bosons.

In order to further study this, masses of the singly and doubly charged Higgs bosons were considered to be nearly degenerate, and the masses of all Higgs bosons was assumed to be lower than that of the doubly charged Higgs boson. This simplifies the relations between the couplings and the masses. Furthermore, the mixing between the CP-even Higgs bosons was assumed to be zero in order to ensure that h^0 is the SM-like Higgs boson. With these assumptions, a list of parameters that satisfy all theoretical constraints were calculated. The resulting masses are shown in table 7.1. The cross-section of production of the charged Higgs bosons for these points can be seen in Figure 7.1 which shows that the cross-section of the associated production mode is at least a factor of two higher than that of the pair-production mode. This fact can be used to enhance the sensitivity of the model.

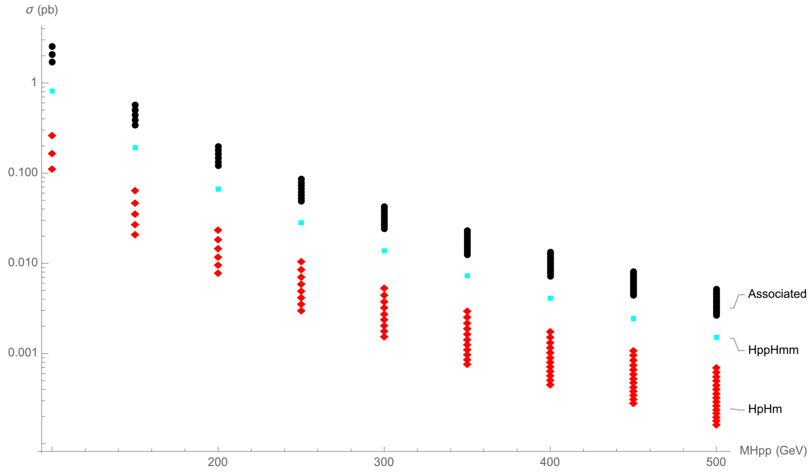

Fig. 7.1: Cross-section of pair-production of doubly- and singly-charged Higgses, and of the associated production of the two charged Higgses.

Among these parameters, the points with least mass difference between the masses of the singly and doubly charged Higgs boson were selected as inputs to CalcHEP. In this parameter space, it was found that $\mathcal{BR}(H^\pm \to W^\pm Z) = 64\%$, while $\mathcal{BR}(H^\pm \to t\bar{b}) = 36\%$. The signal regions in the new production mode are complicated and have several orthogonal possibilities that need to be treated individually. These can be classified as,

- $pp \to H^{\pm\pm}H^\mp \to W^\pm W^\pm W^\mp Z$
  - All W bosons decay to leptons and the Z boson also decays to leptons. This gives a 5 lepton final state.
  - All W bosons decay to leptons and the Z boson decays via the hadronic mode. This mode has 3 leptons in the final state, and is of interest to add sensitivity in the 3ℓ channel.
  - The W and Z bosons originating from $H^\pm$ decay leptonically while the other two W bosons give 4 jets. This can further add sensitivity to the 3ℓ final state.

$m_{H^{\pm\pm}}$	$m_{H^{\pm}}$	m_{H^0}	m_{A^0}
200	142.83	28.355	28.354
200	152.83	81.960	81.959
200	162.83	114.15	114.15
200	172.83	140.51	140.51
200	182.83	163.88	163.88
200	192.83	185.39	185.39
250	178.54	35.443	35.443
250	188.54	92.725	92.725
250	198.54	127.82	127.82
250	208.54	156.46	156.46
250	218.54	181.72	181.72
250	228.54	204.85	204.85
250	238.54	226.51	226.51
250	248.54	247.08	247.08
300	214.25	42.532	42.532
300	224.25	102.85	102.85
300	234.25	140.53	140.53
300	244.25	171.22	171.22
300	254.25	198.21	198.21
300	264.25	222.84	222.84
300	274.25	245.82	245.82
300	284.25	267.58	267.58
300	294.25	288.39	288.39
350	249.96	49.621	49.621
350	259.96	112.52	112.51
350	269.96	152.50	152.50
350	279.96	185.08	185.08
350	289.96	213.67	213.67
350	299.96	239.69	239.69
350	309.96	263.91	263.91
350	319.96	286.79	286.79
350	329.96	308.62	308.62
350	339.96	329.61	329.61
350	349.96	349.92	349.92
400	285.67	56.709	56.709
400	295.67	121.83	121.83
400	305.67	163.91	163.91
400	315.67	198.23	198.23
400	325.67	228.30	228.30
400	335.67	255.63	255.63
400	345.67	281.02	281.02
400	355.67	304.96	304.96
400	365.67	327.76	327.76
400	375.67	349.65	349.65
400	385.67	370.78	370.78
400	395.67	391.29	391.29
450	321.38	63.798	63.798
450	331.38	130.86	130.86
450	341.38	174.87	174.87
450	351.38	210.79	210.79
450	361.38	242.26	242.26
450	371.38	270.82	270.82
450	381.38	297.32	297.32
450	391.38	322.26	322.26
450	401.38	345.99	345.99
450	411.38	368.73	368.73
450	421.38	390.66	390.66
450	431.38	411.91	411.91
450	441.38	432.58	432.58
500	357.08	70.887	70.887
500	367.08	139.67	139.67
500	377.08	185.45	185.45
500	387.08	222.88	222.88
500	397.08	255.65	255.65
500	407.08	285.38	285.38
500	417.08	312.93	312.93
500	427.08	338.83	338.83
500	437.08	363.44	363.44
500	447.08	387.01	387.01
500	457.08	409.70	409.70
500	467.08	431.67	431.67
500	477.08	453.02	453.02
500	487.08	473.82	473.82
500	497.08	494.16	494.16

Table 7.1: Masses of Higgs using parameters allowed by all theoretical constraints, with additional assumptions.

  - The W bosons originating from $H^{\pm\pm}$ decay via the leptonic mode, while W and Z bosons decaying from $H^{\pm}$ give two jets each. This channel can add sensitivity to the $2\ell^{ss}$ channel.
  - One W from $H^{\pm\pm}$, and both W and Z from $H^{\mp}$ decay via the leptonic mode. This gives 4 leptons in the final state, along with two hard jets originating from the remaining W boson.
  - The same-sign W bosons and the Z boson decay leptonically while the remaining W decays hadronically. This results in a 4 lepton final state as well. The big difference being that the total charge in this case would be ± 1.

- $pp \to H^{\pm\pm}H^{\mp} \to W^{\pm}W^{\pm}\bar{t}b$ with $t \to W^{\mp}\bar{b}$
  - The same sign W bosons decay leptonically while the remaining W boson decays hadronically. This gives $2\ell^{ss}$ and 2 b jets in the final state.
  - All three W bosons decay into leptons resulting in a $3\ell + 2b$ final state.

All the above possibilities would, in principle, have different topologies and require a dedicated optimization. But, all the possibilities can potentially have a big impact on the sensitivity of the model. In an attempt to list out the various final states, cases with 0, 1 or 2ℓ with opposite sign leptons were ignored because the SM background for these channels is extremely high.

8. Conclusion

The scalar sector of the Standard Model is one of the main candidates to host new particles beyond the Standard Model. The extension of the scalar sector to include new scalar triplet is usually mentioned in the context of the so-called "see-saw" models, that have the ability to explain a finite mass of neutrinos. Those models include new scalars, some of which have masses in the electroweak scale range, being therefore detectable at LHC. A variant of such an extension is addressed in the present paper. A model is explored for which the scalar sector includes a hypercharge $Y = 2$ scalar triplet, Δ, in addition to the SM scalar doublet H. Within this framework, the symmetry breaking leads to seven scalars $H^{\pm\pm}$, $H^{\pm}$, A^0 (CP odd), H^0 (CP even), h^0 (CP even), where the latter can be identified as being the SM Higgs boson.

A search for the pair production of doubly charged Higgs bosons with each decaying to same sign W bosons is performed with 36.1 fb^{-1} of proton-proton collision data at center-of-mass energy of 13 TeV collected by the ATLAS collaboration during the year 2015 and 2016. The search proceed through the selection of multi-lepton events (dilepton of same sign, tri-leptons and four leptons) with missing transverse energy and several jets. A multi-variate cut-based search strategy is adopted in order to discriminate the signal from the Standard Model background. A significant fraction of this background in particular for dilepton and trilepton topologies originates from misidentified (fake) leptons and from charge mis-identification. These contributions are determined using data driven methods. Seven signal regions are defined depending on the flavour structure of the multi-lepton events, in order to exploit the different signal features and background conditions as a function of the flavour composition. Combining those channels, the model is excluded at 95% C.L. for masses in the range $200 - 300$ GeV. The excluded domain is significantly lower than that excluded in the exclusive di-lepton decay hypothesis probed at various colliders.

The predicted 300 fb^{-1} of data by the end of Run 2 will increase the sensitivity at higher masses. The addition of the associated production mode provides a good potential to increase the sensitivity in the charged sector of the model.

Bibliography

[1] F. R. Klinkhamer, *Neutrino mass and the Standard Model*, Mod. Phys. Lett. **A28** (2013) 1350010, `arXiv:1112.2669 [hep-ph]`, KA-TP-41-2011.

[2] F. F. Freitas, C. A. de S. Pires, and P. S. Rodrigues da Silva, *Inverse type II seesaw mechanism and its signature at the LHC and ILC*, `arXiv:1408.5878 [hep-ph]`.

[3] A. Arhrib, R. Benbrik, M. Chabab, G. Moultaka, M. C. Peyranère, L. Rahili, and J. Ramadan, *Higgs potential in the type II seesaw model*, Phys. Rev. D **84** (2011) 095005. `http://link.aps.org/doi/10.1103/PhysRevD.84.095005`.

[4] S. Kanemura, K. Yagyu, and H. Yokoya, *First constraint on the mass of doubly-charged Higgs bosons in the same-sign diboson decay scenario at the LHC*, Phys. Lett. **B726** (2013) 316–319, `arXiv:1305.2383 [hep-ph]`, UT-HET-080.

[5] E. J. Chun, H. M. Lee, and P. Sharma, *Vacuum Stability, Perturbativity, EWPD and Higgs-to-diphoton rate in Type II Seesaw Models*, JHEP **11** (2012) 106, `arXiv:1209.1303 [hep-ph]`, KIAS-P12055.

[6] A. Belyaev, N. D. Christensen, and A. Pukhov, *CalcHEP 3.4 for collider physics within and beyond the Standard Model*, Comput. Phys. Commun. **184** (2013) 1729–1769, `arXiv:1207.6082 [hep-ph]`, PITT-PACC-1209.

[7] L. Evans and P. Bryant, *LHC Machine*, JINST **3** (2008) S08001.

[8] ATLAS Collaboration, *The ATLAS Experiment at the CERN Large Hadron Collider*, JINST **3** (2008) S08003.

[9] ATLAS Collaboration, *ATLAS pixel detector electronics and sensors*, JINST **3** (2008) P07007.

[10] ATLAS Collaboration, *dE/dx measurement in the ATLAS Pixel Detector and its use for particle identification*, ATLAS-CONF-2011-016. `https://cds.cern.ch/record/1336519`.

[11] ATLAS Collaboration, *ATLAS Insertable B-Layer Technical Design Report*, CERN-LHCC-2010-013. `https://cds.cern.ch/record/1291633`.

[12] ATLAS Collaboration, *ATLAS event at 13 TeV – First stable beam, 3 June 2015 – run: 266904, evt: 25884805*, ATLAS-PHO-Event-2015-016. `https://cds.cern.ch/record/2022202`.

[13] ATLAS Japan SCT working group Collaboration, T. Kondo, *Selected Photos of ATLAS Silicon Microstrip Modules*,. `http://atlas.kek.jp/sub/photos/SCTJ/SCTJModule/SCTJModule.html`.

[14] ATLAS Japan SCT working group Collaboration, T. Kondo, *Selected Photos of ATLAS SCT: Design*,. `http://atlas.kek.jp/sub/photos/SCTJ/SCTJDesign/SCTJDesign.html`.

[15] ATLAS Collaboration, *ATLAS: technical proposal for a general-purpose pp experiment at the Large Hadron Collider at CERN*, CERN-LHCC-94-43. `https://cds.cern.ch/record/290968`.

[16] ATLAS Collaboration, *ATLAS level-1 trigger: Technical Design Report*, CERN-LHCC-98-014. `https://cds.cern.ch/record/381429`.

[17] W. Lampl, S. Laplace, D. Lelas, P. Loch, H. Ma, S. Menke, S. Rajagopalan, D. Rousseau, S. Snyder, and G. Unal, *Calorimeter Clustering Algorithms: Description and Performance*, ATL-LARG-PUB-2008-002. ATL-COM-LARG-2008-003, CERN, Geneva, Apr, 2008. `https://cds.cern.ch/record/1099735`.

[18] T. G. Cornelissen, M. Elsing, I. Gavrilenko, J.-F. Laporte, W. Liebig, M. Limper, K. Nikolopoulos, A. Poppleton, and A. Salzburger, *The global chi2 track fitter in ATLAS*, Journal of Physics: Conference Series **119** no. 3, (2008) 032013. `http://stacks.iop.org/1742-6596/119/i=3/a=032013`.

[19] ATLAS Collaboration Collaboration, *Improved electron reconstruction in ATLAS using the Gaussian Sum Filter-based model for bremsstrahlung*, ATLAS-CONF-2012-047, CERN, Geneva, May, 2012. `http://cds.cern.ch/record/1449796`.

[20] G. e. Aad, *Electron and photon energy calibration with the ATLAS detector using LHC Run 1 data*, The European Physical Journal C **74** no. 10, (2014) 3071. `https://doi.org/10.1140/epjc/s10052-014-3071-4`.

[21] ATLAS Collaboration Collaboration, *Electron efficiency measurements with the ATLAS detector using the 2015 LHC proton-proton collision data*, ATLAS-CONF-2016-024, CERN, Geneva, Jun, 2016. `https://cds.cern.ch/record/2157687`.

[22] ATLAS Collaboration, G. Aad et al., *Muon reconstruction performance of the ATLAS detector in proton–proton collision data at* $\sqrt{s}$ *=13 TeV*, Eur. Phys. J. **C76** no. 5, (2016) 292, `arXiv:1603.05598 [hep-ex]`, CERN-EP-2016-033.

[23] ATLAS Collaboration, W. Lampl, S. Laplace, D. Lelas, P. Loch, H. Ma, et al., *Calorimeter clustering algorithms: Description and performance*, ATL-LARG-PUB-2008-002. `https://cds.cern.ch/record/1099735`.

[24] M. Cacciari, G. P. Salam, and G. Soyez, *The anti-*k_t *jet clustering algorithm*, JHEP **04** (2008) 063, `arXiv:0802.1189 [hep-ph]`.

[25] *Pile-up subtraction and suppression for jets in ATLAS*, ATLAS-CONF-2013-083. `https://cds.cern.ch/record/1570994`.

[26] *Pile-up subtraction and suppression for jets in ATLAS*, ATLAS-CONF-2013-083, CERN, Geneva, Aug, 2013. `https://cds.cern.ch/record/1570994`.

[27] *Tagging and suppression of pileup jets with the ATLAS detector*, ATLAS-CONF-2014-018. `https://cds.cern.ch/record/1700870`.

[28] *Expected performance of the ATLAS* b*-tagging algorithms in Run-2*, ATL-PHYS-PUB-2015-022. `https://cds.cern.ch/record/2037697`.

[29] T. Sjostrand, S. Mrenna, and P. Z. Skands, *A brief introduction to PYTHIA 8.1*, Comput. Phys. Commun. **178** (2008) 852–867, `arXiv:0710.3820 [hep-ph]`, CERN-LCGAPP-2007-04, LU-TP-07-28, FERMILAB-PUB-07-512-CD-T.

[30] ATLAS Collaboration, ATLAS Collaboration, *ATLAS Run 1 Pythia8 tunes*,. http://cds.cern.ch/record/1966419.

[31] A. Martin, W. J. Stirling, R. S. Thorne, and G. Watt, *Parton distributions for the LHC*, Eur. Phys. J. C **63** (2009) 189, `arXiv:0901.0002 [hep-ph]`, IPPP-08-95, DCPT-08-190, CAVENDISH-HEP-08-16.

[32] ATLAS Collaboration, ATLAS Collaboration, *Further ATLAS tunes of Pythia 6 and Pythia 8*,. `http://cds.cern.ch/record/1400677`. ATL-PHYS-PUB-2011-014.

[33] J. Alwall et al., *The automated computation of tree-level and next-to-leading order differential cross sections, and their matching to parton shower simulations*, JHEP **07** (2014) 079, `arXiv:1405.0301 [hep-ph]`, CERN-PH-TH-2014-064, CP3-14-18, LPN14-066, MCNET-14-09, ZU-TH-14-14.

[34] NNPDF Collaboration, R. D. Ball et al., *Parton distributions for the LHC Run II*, JHEP **04** (2015) 040, `arXiv:1410.8849 [hep-ph]`, EDINBURGH-2014-15, IFUM-1034-FT, CERN-PH-TH-2013-253, OUTP-14-11P, CAVENDISH-HEP-14-11.

[35] R. D. Ball et al., *Parton distributions with LHC data*, Nucl. Phys. **B867** (2013) 244–289, `arXiv:1207.1303 [hep-ph]`.

[36] H.-L. Lai et al., *New parton distributions for collider physics*, Phys. Rev. D **82** (2010) 074024, `arXiv:1007.2241 [hep-ph]`.

[37] T. Sjöstrand et al., *High-energy-physics event generation with Pythia 6.1*, Comput. Phys. Commun. **135** (2001) 238, `arXiv:hep-ph/0010017 [hep-ph]`.

[38] P. Skands, *Tuning Monte Carlo Generators: The Perugia Tunes*, Phys. Rev. D **82** (2010) 074018, `arXiv:1005.3457 [hep-ph]`, MCNET-10-08, CERN-PH-TH-2010-113.

[39] S. Frixione, G. Ridolfi, and P. Nason, *A positive-weight next-to-leading-order Monte Carlo for heavy flavour hadroproduction*, JHEP **09** (2007) 126, `arXiv:0707.3088 [hep-ph]`.

[40] E. Re, *Single-top Wt-channel production matched with parton showers using the POWHEG method*, Eur. Phys. J. C **71** (2011) 1547, `arXiv:1009.2450 [hep-ph]`.

[41] S. Alioli, P. Nason, C. Oleari, and E. Re, *NLO single-top production matched with shower in POWHEG: $s-$ and $t-$channel contributions*, JHEP **09** (2009) 111, `arXiv:0907.4076 [hep-ph]`.

[42] Gleisberg, T. and Hoeche, Stefan. and Krauss, F. and Schonherr, M. and Schumann, S. and Siegert, F. and Winter, J., *Event generation with SHERPA 1.1*, JHEP **02** (2009) 007, `arXiv:0811.4622 [hep-ph]`.

[43] D. J. Lange, *The EvtGen particle decay simulation package*, Nucl. Instrum. Meth. Phys. Res. A **462** (2001) 152.

[44] ATLAS Collaboration, *Monte Carlo Generators for the Production of a W or Z/γ^* Boson in Association with Jets at ATLAS in Run 2*,. `https://cds.cern.ch/record/2120133`. ATL-PHYS-PUB-2016-003.

[45] ATLAS Collaboration, *Multi-Boson Simulation for 13 TeV ATLAS Analyses*,. `https://cds.cern.ch/record/2119986`. ATL-PHYS-PUB-2016-002.

[46] ATLAS Collaboration, *Simulation of top quark production for the ATLAS experiment at $\sqrt{s}$ = 13 TeV*,. `https://cds.cern.ch/record/2120417`. ATL-PHYS-PUB-2016-004.

[47] ATLAS Collaboration, *Modelling of the $t\bar{t}H$ and $t\bar{t}V$ $(V = W, Z)$ processes for $\sqrt{s}$ = 13 TeV ATLAS analyses*,. `https://cds.cern.ch/record/2120826`. ATL-PHYS-PUB-2016-005.

[48] S. Agostinelli et al., *Geant4: a simulation toolkit*, Nucl. Instrum. Meth. Phys. Res. A **506** (2003) 250.

[49] G. Cowan, K. Cranmer, E. Gross, and O. Vitells, *Asymptotic formulae for likelihood-based tests of new physics*, The European Physical Journal C **71** no. 2, (2011) 1554. `https://doi.org/10.1140/epjc/s10052-011-1554-0`.

[50] W. Verkerke and D. P. Kirkby, *The RooFit toolkit for data modeling*, eConf **C0303241** (2003) MOLT007, `arXiv:physics/0306116 [physics]`, CHEP-2003-MOLT007. [,186(2003)].

[51] A. Buckley, J. Ferrando, S. Lloyd, K. Nordström, B. Page, M. Rüfenacht, M. Schönherr, and G. Watt, *LHAPDF6: parton density access in the LHC precision era*, The European Physical Journal C **75** no. 3, (2015) 132.

[52] ATLAS Collaboration Collaboration, *Search for supersymmetry in final states with two same-sign or three leptons and jets using 36 fb of s=13 TeV pp collision data with the ATLAS detector*, ATLAS-CONF-2017-030, CERN, Geneva, May, 2017. `http://cds.cern.ch/record/2262920`.

[53] ATLAS Collaboration, The ATLAS Collaboration, *Measurement of the $W^{\pm}Z$ boson pair-production cross section in pp collisions at $\sqrt{s} = 13$ TeV with the ATLAS Detector*, Phys. Lett. **B762** (2016) 1–22, `arXiv:1606.04017 [hep-ex]`, CERN-EP-2016-108.

[54] *Multi-Boson Simulation for 13 TeV ATLAS Analyses*, ATL-PHYS-PUB-2016-002, CERN, Geneva, Jan, 2016. `https://cds.cern.ch/record/2119986`.

[55] ATLAS Collaboration, The ATLAS Collaboration, *Measurement of the ZZ Production Cross Section in pp Collisions at $\sqrt{s}$ = 13 TeV with the ATLAS Detector*, Phys. Rev. Lett. **116** no. 10, (2016) 101801, `arXiv:1512.05314 [hep-ex]`, CERN-PH-EP-2015-318.

[56] ATLAS Collaboration, The ATLAS Collaboration, *Measurement of the $W^{+}W^{-}$ production cross section in pp collisions at a centre-of-mass energy of $\sqrt{s}$ = 13 TeV with the ATLAS experiment*, `arXiv:1702.04519 [hep-ex]`, CERN-EP-2016-267.

[57] ATLAS Collaboration, The ATLAS Collaboration, *Measurement of the $t\bar{t}Z$ and $t\bar{t}W$ production cross sections in multilepton final states using 3.2 fb^{-1} of pp collisions at $\sqrt{s}$ = 13 TeV with the ATLAS detector*, Eur. Phys. J. **C77** no. 1, (2017) 40, `arXiv:1609.01599 [hep-ex]`, CERN-EP-2016-185.

[58] L. Moneta, K. Belasco, K. S. Cranmer, S. Kreiss, A. Lazzaro, D. Piparo, G. Schott, W. Verkerke, and M. Wolf, *The RooStats Project*, PoS**ACAT2010** 057, `arXiv:1009.1003 [physics.data-an]`.

[59] W. Verkerke and D. Kirkby, *The RooFit toolkit for data modeling*, in *2003 Computing in High Energy and Nuclear Physics, CHEP03*. 2003. `arXiv:physics/0306116`.

[60] A. L. Read, *Presentation of search results: The CL(s) technique*, J.Phys. **G28** (2002) 2693–2704.

[61] G. Cowan, K. Cranmer, E. Gross, and O. Vitells, *Asymptotic formulae for likelihood-based tests of new physics*, Eur. Phys. J. C **71** (2011) 1554, `arXiv:1007.1727v2 [physics.data-an]`.

A.Parameters used for event generation

In chapter 2, only the parameters that affect either the cross-section of pair-production of $H^{\pm\pm}$ or its branching ratio are described. The complete set of parameters needed to generate events is shown in table A.1. The strong coupling constant is allowed to run with scale. CalcHEP recomputes this value and is not fixed to the exact value as shown in the table.

The quatities from the neutrino sector such as the $\sin\theta^N_{ij}$, mass of the lightest neutrino, mass hierarchy in the neutrino sector, and the mass differences enter the event generation as parameters. These are not constrained theoretically, but have to respect the current experimental bounds. In principle, the parameters related to neutrinos do not affect the analysis presented in this thesis. They become important for low v_t regimes.

The mass of the SM-like Higgs boson (h^0 in this case) is set to 125 GeV. This is enforced by the fact that the mixing between the neutral CP-even Higgses is considered to be negligible. The masses of the BSM Higgses shown in table A.1 are illustrative. When the benchmark mass of the doubly charged Higgs boson is changed, the rest of the masses change and the widths are calculated by CalcHEP accordingly.

Parameter	Value
Fermi constant	0.0000116637
Strong coupling constant at the Z pole.	0.1184
Down Yukawa mass	0.00504
Up Yukawa mass	0.00254999999
Strange Yukawa mass	0.101
Charm Yukawa mass	1.27
Bottom Yukawa mass	4.7
Top Yukawa mass	173.34
Electron Yukawa mass	0.00051100000
Muon Yukawa mass	0.10566
Tau Yukawa mass	1.777
Triplet VEV	0.1
Sign degeneracy in CP-even neutral scalar mixing angle	1
Sign degeneracy in CP-odd neutral scalar mixing angle	1
Sign degeneracy in singly-charged scalar mixing angle	1
Sine of CP-odd neutral Higgses mixing angle	0.0
$\sin\theta_{12}$, PDG-94	0.221
$\sin\theta_{23}$, PDG-94	0.04
$\sin\theta_{13}$, PDG-94	0.0035
Neutrino Solar Mass Difference (in eV^2)	0.0086
Neutrino Atmosferic Mass Difference (in eV^2)	0.048
Inverted hierarchy	0
Lightest neutrino mass (in eV)	0.1
$\sin\theta_{12}^N$	0.54
$\sin\theta_{23}^N$	0.70
$\sin\theta_{13}^N$	0.15
Strong coupling constant	1.21
Mass of e.	0.00051100000
Mass of μ	0.10566
Mass of τ.	1.777
Mass of u.	0.00254999999
Mass of c.	1.27
Mass of t.	173.34
Mass of d.	0.00504
Mass of s.	0.101
Mass of b.	4.7
Mass of ϕ.	91.1876
Mass of h^0	125
Mass of H^0.	185.39
Mass of A^0.	185.39
Mass of $H^\pm$.	192.83
Mass of $H^{\pm\pm}$.	200
Width of t.	1.338
Width of ϕ.	2.4952
Width of W.	2.085
Width of h^0.	0.00407

Table A.1: The complete set of parameters used as inputs to CalcHEP for event generation. The masses and widths are shown in GeV.

B. Optimization of electron identification

B.1. Monte Carlo Samples

The process of optimization begins with monitoring of different signal and background signatures. A suitable signal simulation is selected to study 'good' quality electrons, and a comparison is made with a suitable background simulations. Variables are ranked depending on their signal-background discrimination power. The signal MC samples used for the studies are $J/\psi \rightarrow ee$ and $Z \rightarrow ee$ events with only truth-matched electrons used for the studies. A variety of $J/\psi \rightarrow ee$ with different truth p_T cuts are available for the studies. J/ψe3e3, J/ψe3e8 and J/ψe3e13 have truth p_T cuts of 3GeV on the first electron, and 3 GeV, 8 GeV, and 13 GeV on the second electron respectively. The $Z \rightarrow ee$ simulation has a dilepton filter which applies truth p_T cuts of 15 GeV on both electrons.

A minimum bias MC sample was used as background at low $\mathrm{E_T}$. The statistics is very low for $\mathrm{E_T} > 15$ GeV. So, the di-jet sample was added for $\mathrm{E_T} > 17$ GeV. The di-jet sample has a truth pt cut at 17 GeV and hence cannot be used for $\mathrm{E_T} < 17$ GeV. Any true electrons in these background samples were removed for the optimization studies. To further select good quality electrons, a loose isolation cut was applied. This causes an efficiency increase of about 5%. The resultant statistics in every $\mathrm{E_T}$ bin after the truth matching are provided in the table below.

B.2. Structure

During Run-1, several variables were tested to assess their discrimination between signal and background electrons. The variables identified to have the highest discrimination are shown in Table 4.1. For Run 2, several improvements to the input variables used for electron ID have been introduced. Taking advantage of the IBL, the number of hits in this innermost pixel layer is used for discriminating between electrons and converted photons. This criterion was also used in Run 1, but with what is now the second-to-innermost pixel layer. As mentioned in section 4, there are two methods available for identifying electrons in ATLAS, the likelihood method and the cut-based method. This appendix focuses on the cut-based method.

The variables defined in Table 4.1 are dependent on the kinematics of the electron, specifically $\mathrm{E_T}$ and η. In order to take this into account, the following binning was adopted for optimization and usage,

- $\mathrm{E_T}$ bins in GeV: $[5, 10]$, $[10, 15]$, $[15, 20]$, $[20, 30]$, $[30, 40]$, $[40, 50]$, $[50, 60]$, $[60, 70]$, $[70, 80]$, $[> 80]$.
- $|\eta|$ bins: $[0, 0.1]$, $[0.1, 0.6]$, $[0.6, 0.8]$, $[0.8, 1.15]$, $[1.15, 1.37]$, $[1.37, 1.52]$, $[1.52, 1.81]$, $[1.81, 2.01]$, $[2.01, 2.47]$

The last η bin was previously split into two, $2.01 - 2.37$ and $2.37 - 2.47$. But the last bin, in this case, is statistically limited. The plots still show the bins separately in order to see the effect of optimizing the two bins together.

B.3. Performance of LikelihoodPCA

LikelihoodPCA is selected due to its good performance as a Multi-Variate-Analysis method and thus provides a good baseline for the cut-based method. TMVA can take advantage of the characteristics of the discriminating variables that allow them distinguish between signal and background more efficiently than others. This test serves as a cross check for the cut-based method and a good reference for choosing the working point at the same time. Distributions of some of the variables are shown below as an example.

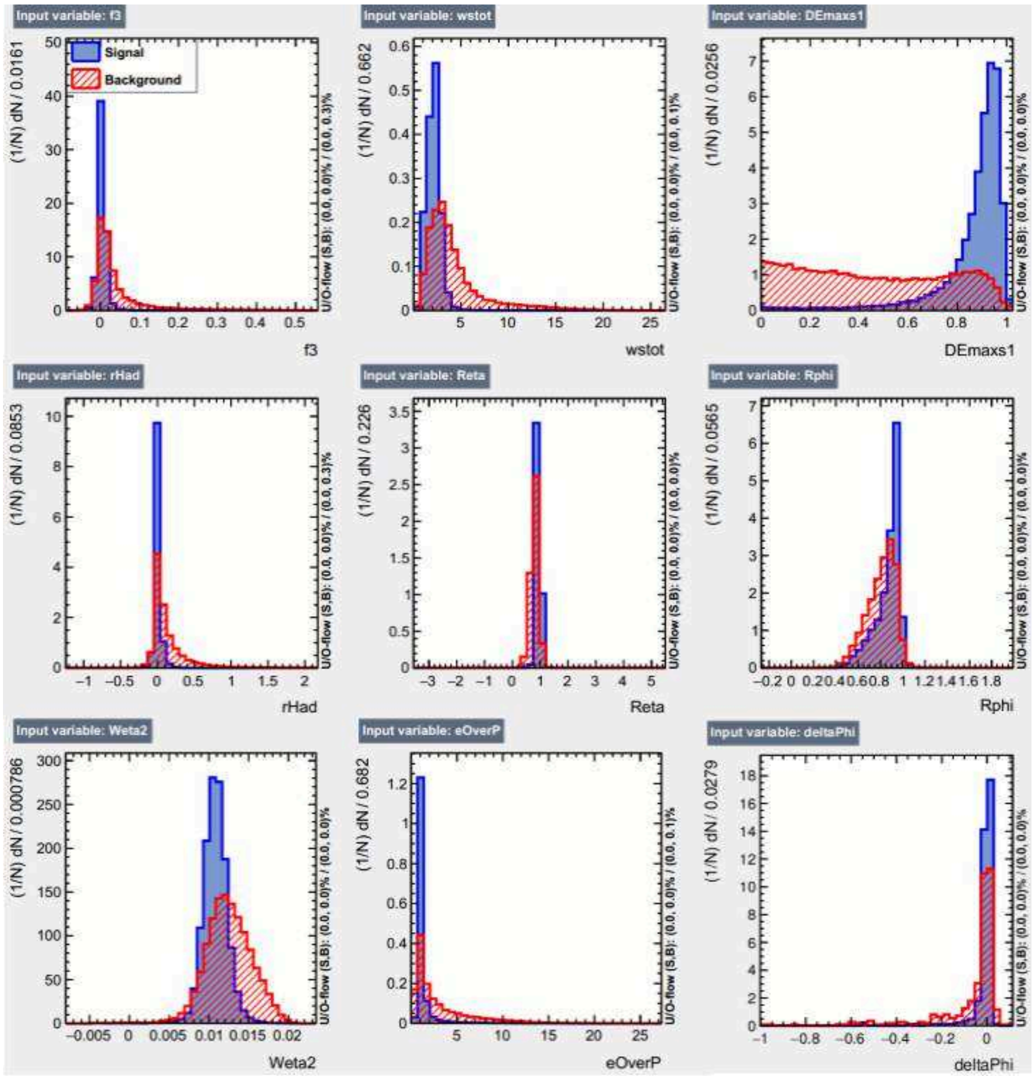

Fig. B.1: Variables distribution for signal and background

From the Figure B.2 and Figure B.3, a high correlation can be seen between DEmaxs1 (ΔE_{max}) and wstot ($W_{s,tot}$), and this will be a reference for forming groups of variables to be optimized independently during the optimization process.

Figure B.4 shows that the LikelihoodPCA can give a very good performance by using those variables.

B.4. Cut-based Optimisation Methodology

B.4.1. Work before optimizing

Once the samples are decided, preparing for the optimization involves studies that can be mainly categorized into two:

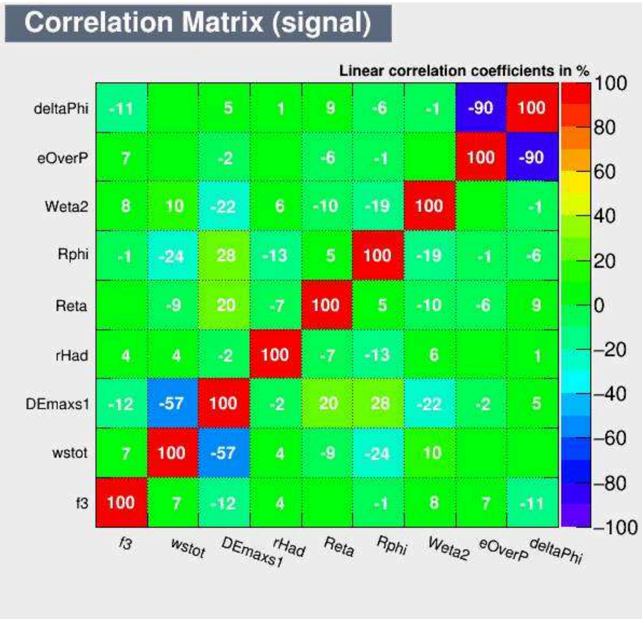

	f3	wstot	DEmaxs1	rHad	Reta	Rphi	Weta2	eOverP	deltaPhi
deltaPhi	-11		5	1	9	-6	-1	-90	100
eOverP	7		-2		-6	-1		100	-90
Weta2	8	10	-22	6	-10	-19	100		-1
Rphi	-1	-24	28	-13	5	100	-19	-1	-6
Reta		-9	20	-7	100	5	-10	-6	9
rHad	4	4	-2	100	-7	-13	6		1
DEmaxs1	-12	-57	100	-2	20	28	-22	-2	5
wstot	7	100	-57	4	-9	-24	10		
f3	100	7	-12	4		-1	8	7	-11

Fig. B.2: Correlation between the variables for the signal simulation

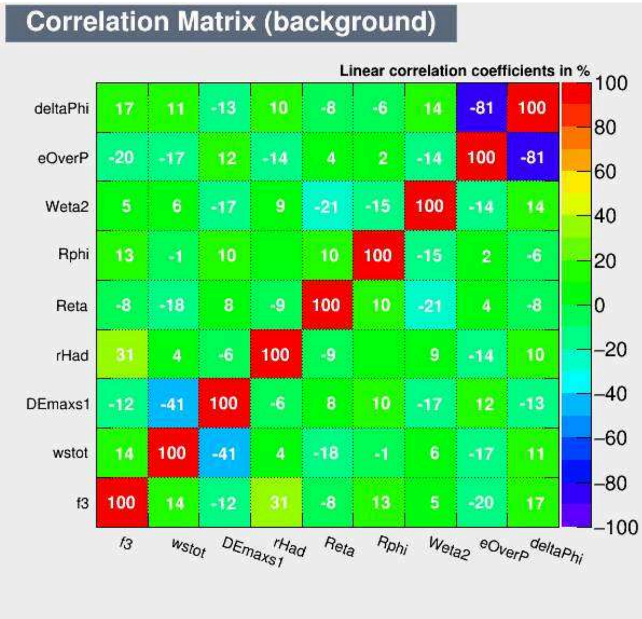

	f3	wstot	DEmaxs1	rHad	Reta	Rphi	Weta2	eOverP	deltaPhi
deltaPhi	17	11	-13	10	-8	-6	14	-81	100
eOverP	-20	-17	12	-14	4	2	-14	100	-81
Weta2	5	6	-17	9	-21	-15	100	-14	14
Rphi	13	-1	10		10	100	-15	2	-6
Reta	-8	-18	8	-9	100	10	-21	4	-8
rHad	31	4	-6	100	-9		9	-14	10
DEmaxs1	-12	-41	100	-6	8	10	-17	12	-13
wstot	14	100	-41	4	-18	-1	6	-17	11
f3	100	14	-12	31	-8	13	5	-20	17

Fig. B.3: Correlation between the variables for the background simulation

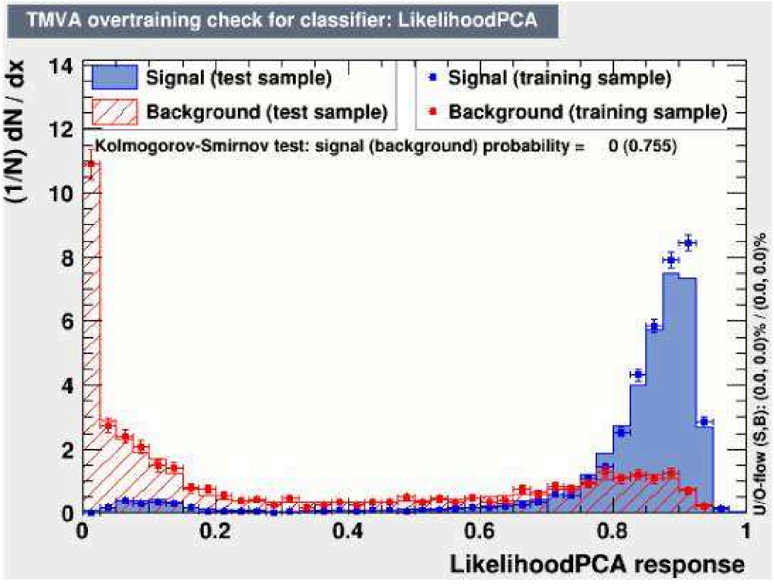

Fig. B.4: LikelihoodPCA response built using the variables shown above.

- Pile-up (μ) dependence of each cut used in electronID
- Correlation between the variables

The pile-up dependence can be studied in two ways:

- Applying only one cut, and measuring the slope of the efficiency vs μ curve.
- Applying all but one cut, measure the efficiency, and take the difference between the slopes of efficiency vs μ when all cuts are applied and when all cuts but one are applied.

The variables deemed sensitive using these methods were treated with extra care. Once the pile-up sensitive variables are identified, a pre-cleaning process is applied on some variables to avoid having cuts in the tails.[a]

For each variable preliminary cuts are applied such that the efficiency of the background decreases by 10% for each cut while keeping the decrease in signal efficiency less than 2%.

As a next step, the variable correlations are taken into account to form groups of variables:

Group1	$f_3\ w_{s,tot}\ \Delta E_{max}\ R_{had}$
Group2	$R_\eta\ R_{phi}\ W_{\eta 2}$
Group3	$E/P\ \Delta\phi$

The TRT PID variable, eProbabilityHT, is treated separately; this is justified by the fact that its linear correlation with other variables is negligible. This process is explained in the later sections.

The performance of the Run 1[b] cut-based menus is used as a benchmark. For each E_T bin, the same signal efficiency as the 2012 menu is used for the three working points, loose, medium, and tight. In addition, a flatness in the efficiency as a function of η is enforced.

B.4.2. Optimization flow

Signal and background events are pre-selected. Furthermore, all cuts from the 2012 menu are applied except the variables which need to be optimized (Example- group 1 variables). A primary selection efficiency(ϵ_1) can be obtained after this step. Then those optimized variables will be the input variables for cut-based method. The general optimization work flow is shown in Figure B.5.

After the MVA training and testing, a new signal efficiency(ϵ_2) is obtained. The total signal efficiency (ϵ_3) can then be calculated with equation $\epsilon_3 = \epsilon_1 * \epsilon_2$.
which is the target efficiency in the table above. Values of all cuts corresponding to the signal efficiency(ϵ_2) can also be found with MVA cut-based output.

Variables are separated into three groups and the optimization chain is Group-1 → Group-2 → Group-3. It means that during the Group-2 optimization process, cut-based method will use the new first Group variables' cut value which are obtained from Group-1 process and so on. To give more optimization room for each group, a proper efficiency target is needed for the optimization of each group. In the exact optimization process, signal efficiencies are set differently for Groups to leave a balanced optimization room. And after whole optimizing process, targeted signal efficiency will be

---

[a] Cut values could jump a lot with negligible changes in efficiency if this is not taken care of. This is not very desirable since it could make the optimization sensitive to statistical fluctuations.

[b] The Run-1 algorithms were called isEM2012 while the current optimizations give isEM2015

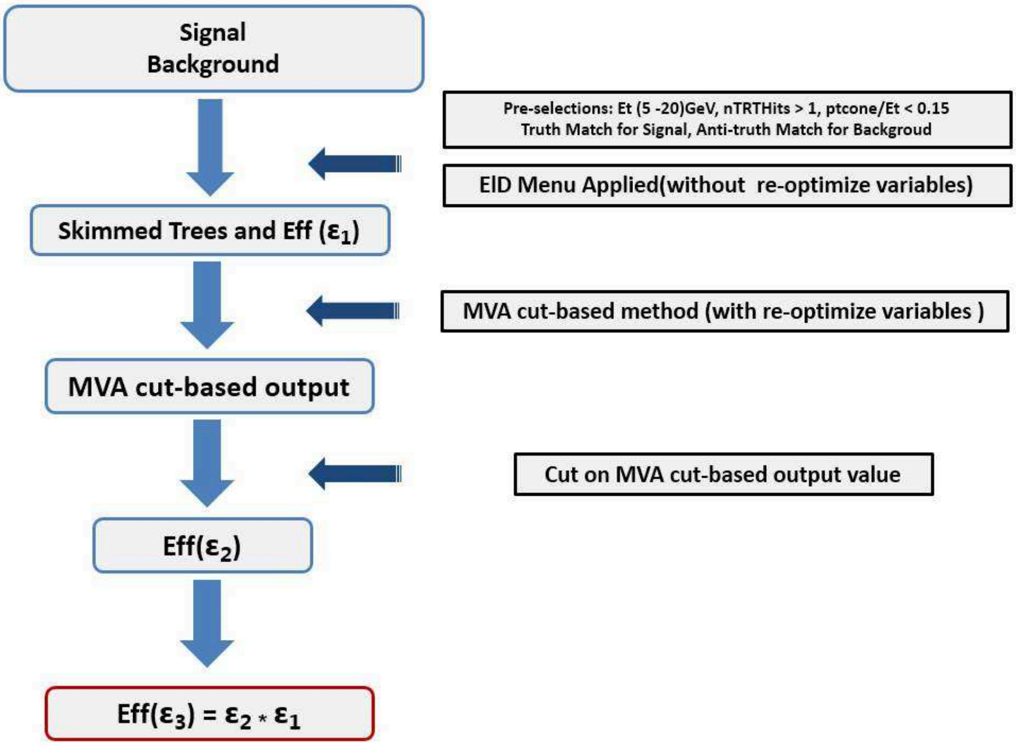

Fig. B.5: Optimization Work Flow

achieved as expected. Example for Tight menu optimization which contains all 3 group variables:
1). Efficiency with pre-cleaning: ϵ_C
2). G1 optimization:Prepare samples with pre-cleaning and target efficiency:
$\epsilon_{G1} = \epsilon_0 + 0.66 * (\epsilon_C - \epsilon_0)(\epsilon_0$
3). G2 optimization:Prepare samples with pre-cleaning+G1 and target efficiency:
$\epsilon_{G2} = \epsilon_0 + 0.33 * (\epsilon_C - \epsilon_{G1})$
4). G3 optimization:Prepare samples with pre-cleaning+G1+G2 and target efficiency:
$\epsilon_{G3} = \epsilon_0$

The cut values of the variables corresponding to the signal efficiency are chosen to replace the old ones. It should be noted that some variables such as f_3 are badly modeled in the last η bin. For this reason, the relatively loose cuts were applied in the last bin for the badly modeled variables.

B.4.3. Smoothing and monotonicity process

After inspecting the cut-values in different η bins in any given $\mathrm{E_T}$ bin, it was found that some cut values changed a lot from one η-bin to the next. This is not desired, so post-optimization a smoothening procedure was applied to avoid these jumps without loss in efficiency or the flatness. The procedure is as follows:

- Move cuts in small steps. The step value was defined using the maximum and minimum values of the cut among all η bins in a given $\mathrm{E_T}$ bin (call this C_{max} and C_{min}). The step size is then defined as $\frac{C_{max} - C_{min}}{200}$.
- This change in cut values is stopped as soon as the efficiency reduces by 1%.

But it was observed that this resulted in a global decrease of about 4%. To get around this, an extra condition was applied on the efficiency by forcing it to depend on the working point efficiency by requiring the following relation:

$$\epsilon_T = \epsilon_{T,MAX}\left(1 - C\epsilon_{WP}^2\right) \tag{B.1}$$

where $\epsilon_{T,MAX} = 0.01$ and $C = 0.05$.

Besides this cut smoothing process, inclusiveness of menus should be ensured which means Loose menu is looser than Medium and Medium looser than Tight. This has a significant impact on the final performance. Monotonicity of cut values as a function of $\mathrm{E_T}$ is also taken into consideration to avoid trigger inefficiencies.

B.4.4. Coping with the changes in the TRT

During Run-I, the gas in the TRT used to be only Xenon, which is very expensive. This was problematic because there were major leaks in the TRT. A cheaper solution was to use a Xenon-Argon mixture instead. This had major effects on electron identification because of the TRT-related variables. Two new scenarios called the Baseline scenario and the Pessimistic scenario were simulated based on the amount of Argon being used in the Xe-Ar mixture. The electron ID includes cuts on the total number of TRT hits, and the fraction of high threshold Xenon hits (defined as $f_{HT} = \frac{\#(\text{HT Xe hits})}{\text{Total }\#\text{of TRT hits}}$). The comparison between different scenarios is shown in Figure B.6.

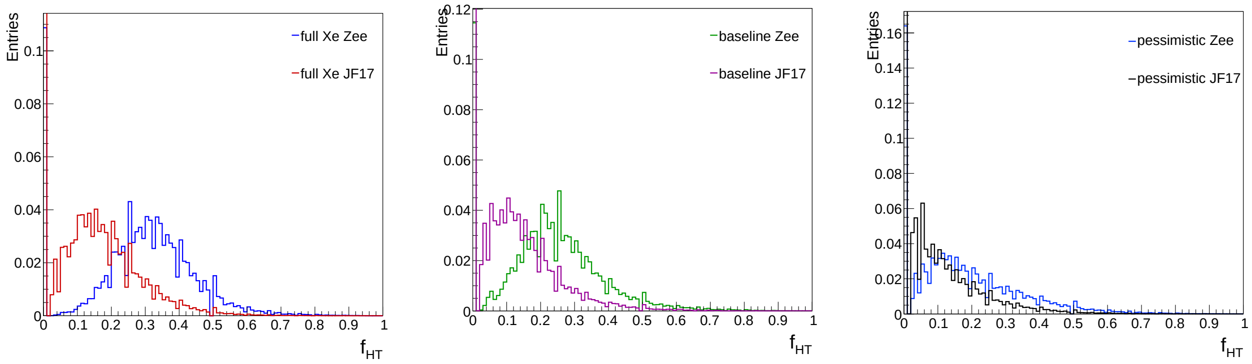

Fig. B.6: The effect of changing the TRT gas on the fraction of the high threshold TRT hits.

It is clear that the discrimination power of the variable is significantly reduced in shifting from full Xe to the baseline Xe-Ar scenario to the pessimistic Xe-Ar scenario. To cope with this, a new variable, called eProbabilityHT, which also uses the high threshold hits information was introduced. eProbabilityHT is a likelihood-type variable defined as,

$$p^{e,\pi} = \Pi p_{HT}^{e,\pi} \times \Pi\left(1 - p_{HT}^{e,\pi}\right), \tag{B.2}$$

$$p_{final}^{e,\pi} = \frac{p^{e,\pi}}{p^e + p^\pi} \tag{B.3}$$

The main purpose of this variable is to distinguish electrons from hadrons, especially pions and hence, plays an important role in electron ID. The cut-based menu had to be re-tuned to replace f_{HT} by eProbabilityHT. To do this, it is important to understand the distribution for the signal and background. This is shown in Figure B.7 for the baseline and pessimistic scenarios. These are inclusive in E_T and η

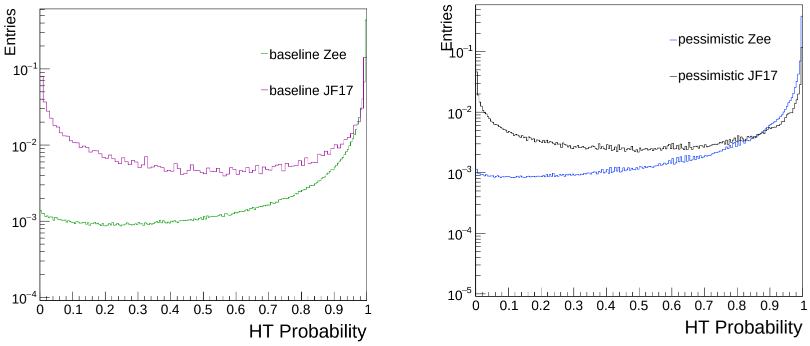

Fig. B.7: The comparison between signal and background distributions of eProbabilityHT in the baseline (left) and pessimistic (right) scenarios.

The true electrons tend to have values closer to 1, as seen in the plots. After having understood the distribution, it is necessary to replace f_{HT} by eProbabilityHT. This was done in two steps,

- The effect of removing the f_{HT} cut on the efficiency was evaluated in all the E_T and η bins in which electron ID is optimized.
- The eProbabilityHT distributions in these bins are scanned and cuts are proposed to cause the same effect in the efficiency as f_{HT}.

A notable feature of the TRT variables is that they are very pileup sensitive and need to be treated with special care. A positive aspect of the swap of variables was that the efficiency is more stable w.r.t. μ. A comparison of the performance of the latest menus was made between the baseline and pessimistic scenarios. It was found that the performance was similar, which is not expected given the difference in the eProbabilityHT distribution in the two scenarios and is not yet understood. The following plots show the efficiencies as a function of the μ for signal and background for the two scenarios. The efficiencies of the eProbabilityHT cut alone in the $-2 < \eta < 2$ range for signal and background are shown in Figure B.8[c]. The differences can be further attributed mostly to the $-1 < \eta < 1$ region. This is evident from Figure B.10,

The bin-wise cuts for eProbabilityHT and the efficiency comparison between the T_{Ratio} cut and the eProbabilityHT cut can be seen in Figure B.11.

B.4.5. Results

The results of the optimization are shown in Figure B.12. As intended, the efficiency is significantly flatter after the new optimization. The performance of the identification algorithms have also improved.

---

[c] The loose menu does not have the eProbabilityHT cut and the plots corresponding to the loose menu represent the complete loose menu applied

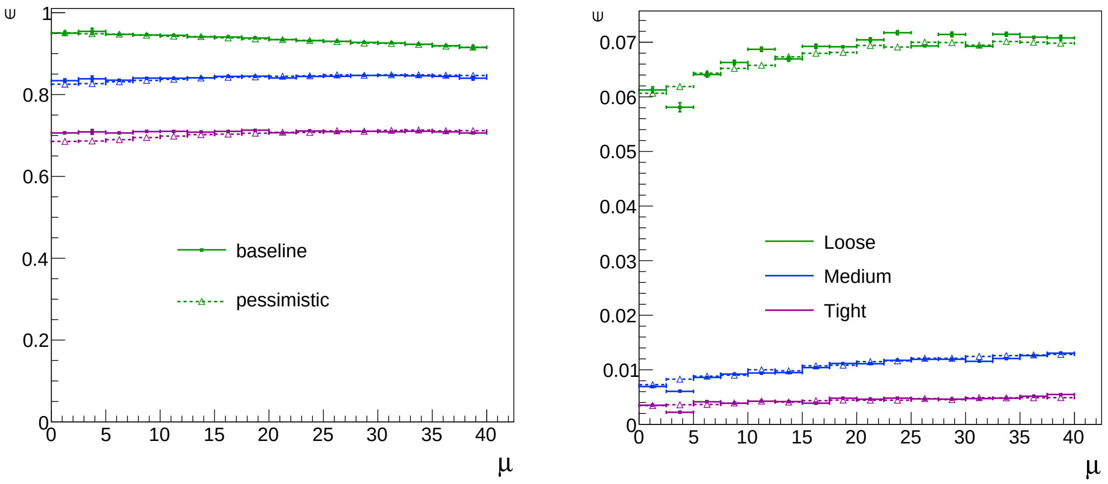

Fig. B.8: $|\eta| < 2.47$ and $E_T > 5$ GeV: Efficiency vs μ for signal (left) and background (right)

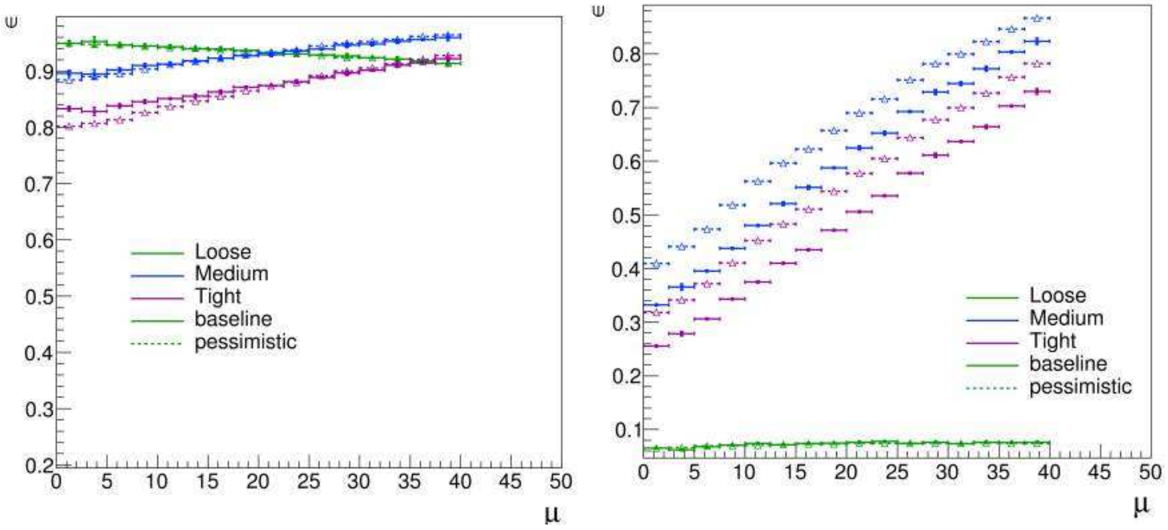

Fig. B.9: $|\eta| < 2$: Efficiency vs μ for signal (left) and background (right)

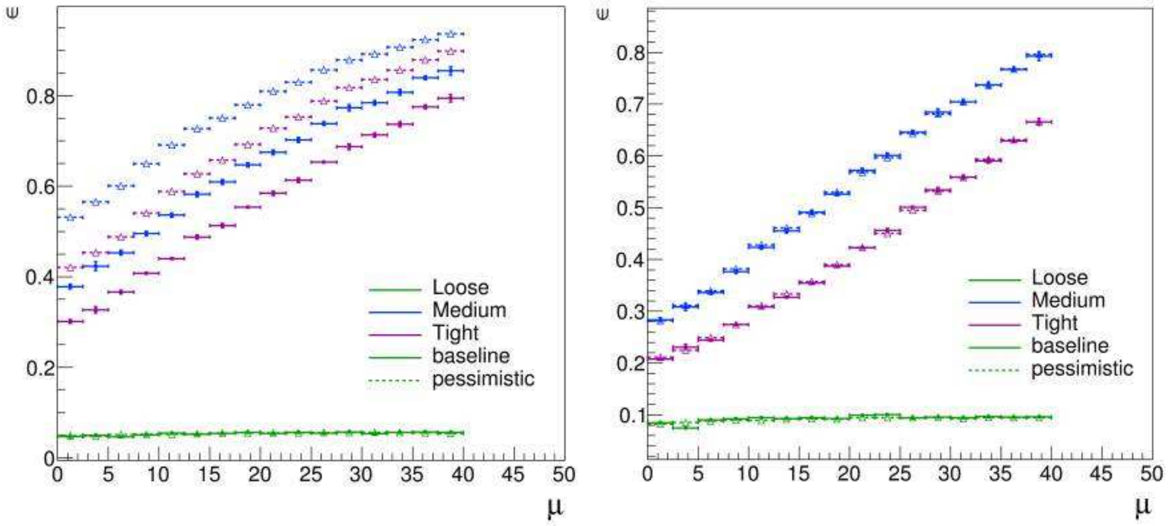

Fig. B.10: $|\eta| < 1$ (left) and $|\eta| > 1$ (right): Efficiency vs μ for background.

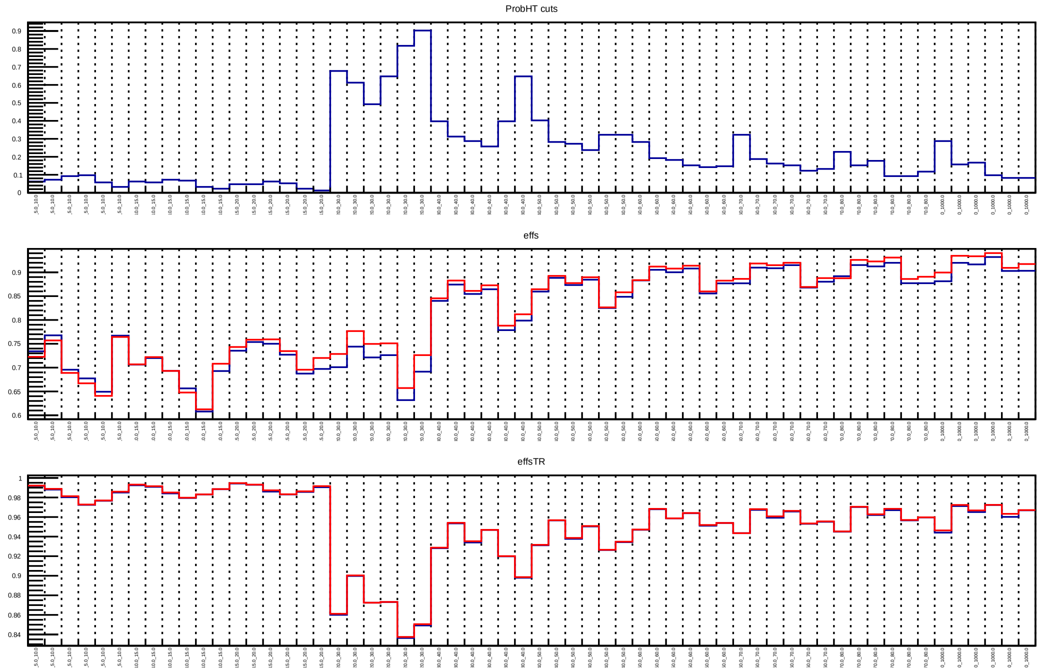

Fig. B.11: Top: Cut values for eProbabilityHT; Middle: Total efficiency comparison; Bottom: Comparison of efficiency of T_{Ratio} and eProbabilityHT cuts

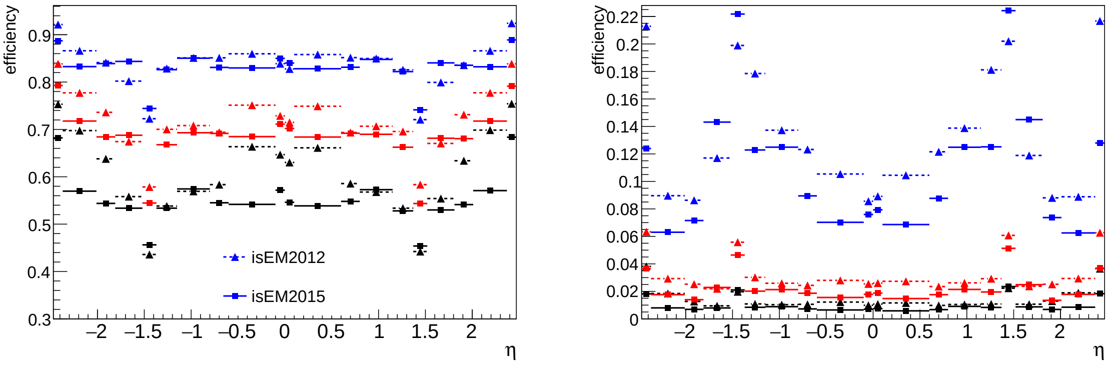

Fig. B.12: $|\eta| < 1$ (left) and $|\eta| > 1$ (right): Efficiency vs μ for background

C.Auxilliary material for the analysis

C.1. Control regions in the 3L channel

C.1.1. Cross-checks of background estimation

Region	Data	Prompt	Data-Prompt	MC fakes		
ZF $xe\not{e}$	689	263 ± 9.77	426 ± 28	226 ± 62.1		
ZF $x\mu\not{e}$	832	294 ± 8.68	538 ± 30.1	704 ± 168		
ZF $xe\not{\mu}$	339	63 ± 4.32	276 ± 18.9	227 ± 58		
ZF $x\mu\not{\mu}$	443	90.9 ± 14.2	352 ± 25.4	386 ± 68.1		
Region	Data	Prompt	Data-Prompt	DD fakes	in-situ DD fakes	MC fakes
ZS xee	848	674.7 ± 14	173.3 ± 32.23	166.5 ± 32.01	173.3 ± 36.03	101 ± 26.8
ZS $xe\mu$	1957	1638 ± 23	318.6 ± 49.99	258.2 ± 42.74	318.8 ± 55.17	96.2 ± 19.8
ZS $x\mu\mu$	1180	1053 ± 18	127.4 ± 38.92	61.11 ± 20.02	127.4 ± 41.04	70.1 ± 29
$\theta_e(in - situ)$	0.41 ± 0.08					
$\theta_\mu(in - situ)$	0.36 ± 0.11					

Table C.1: Z samples yields in sub-regions enriched in fakes (ZF) and signal (ZS). Note that the column "Data Driven (DD) Fakes" contains the fake lepton contribution estimated using the fake factors measured in the Y region. The numbers in that column are directly comparable to the column "Data-Prompt", and a good agreement is observed. The fake factors formulae can also be used, similarly to the study in Y the region, to deduce "in-situ" fake factors and background estimates (the column "in situ DD fakes"). The latter are non-trivial for the middle line in ($xe\mu$), where a good agreement is also observed to the baseline "Data Driven Fakes" estimates and to the "Data-Prompt" yield. The errors indicated here are statistical.

In order to further study this method in regions with different multiplicities of jets/b-jets, and implicitly different Z+jets and $t\bar{t}$ contributions, the regions Z and T are employed. The results are given in Tables C.1 and C.2. A good agreement is observed between the fake estimates and the "Data-Prompt" yields. The "in-situ" fake factors are also in agreement with the ones deduced from YR, as shown in Figure 5.15, thereby proving the stability of the proposed procedure to estimate the fake leptons contributions (note that the "in-situ" fake factors are only for verification, and are not used in the analysis beyond these checks.). The closure for all control regions is illustrated in Figure 5.18.

C.1.2. Distributions of variables in the control regions

It is important to verify that the distributions of various variables produced using data and the predicted background agree well with each other. Figures C.2 - C.13 show the variables such as invariant masses and angular correlations between various objects such as leptons, jets, and $E_{\mathrm{T}}^{\mathrm{miss}}$. These show a good agreement in all control regions and are reassuring to the method used to predict the background.

C.2. Monte Carlo based tests for validation of fakes estimation

Region	Data	Prompt	Data-Prompt	MC fakes		
TF $xe\not{e}$	120	9.28 ± 0.767	111 ± 11	83 ± 4.89		
TF $x\mu\not{e}$	169	11.6 ± 0.647	157 ± 13	109 ± 4.92		
TF $xe\not{\mu}$	169	3.21 ± 0.412	166 ± 13	145 ± 6.1		
TF $x\mu\not{\mu}$	223	5.06 ± 0.659	218 ± 15	158 ± 5.66		
Region	Data	Prompt	Data-Prompt	DD fakes	in-situ DD fakes	MC fakes
TS xee	72	28.41 ± 0.81	43.59 ± 8.524	43.27 ± 8.918	43.59 ± 10.49	26.5 ± 1.9
TS $xe\mu$	155	70.49 ± 1.3	84.51 ± 12.52	90.31 ± 15.46	93.51 ± 16.42	39.1 ± 2.66
TS $x\mu\mu$	82	40.57 ± 0.91	41.43 ± 9.101	37.82 ± 12.36	41.43 ± 9.949	17.6 ± 1.7
$\theta_e(in - situ)$	0.39 ± 0.09					
$\theta_\mu(in - situ)$	0.19 ± 0.04					

Table C.2: T samples yields in sub-regions enriched in fakes (TF) and signal (TS). Note that the column "Data Driven (DD) Fakes" contains the fake lepton contribution estimated using the fake factors measured in the Y region. The numbers in that column are directly comparable to the column "Data-Prompt", and a good agreement is observed. The fake factors formulae can also be used, similarly to the study in Y the region, to deduce "in-situ" fake factors and background estimates (the column "in situ DD fakes"). The latter are non-trivial for the middle line in ($xe\mu$), where a good agreement is also observed to the baseline "Data Driven Fakes" estimates and to the "Data-Prompt" yield. The errors indicated here are statistical.

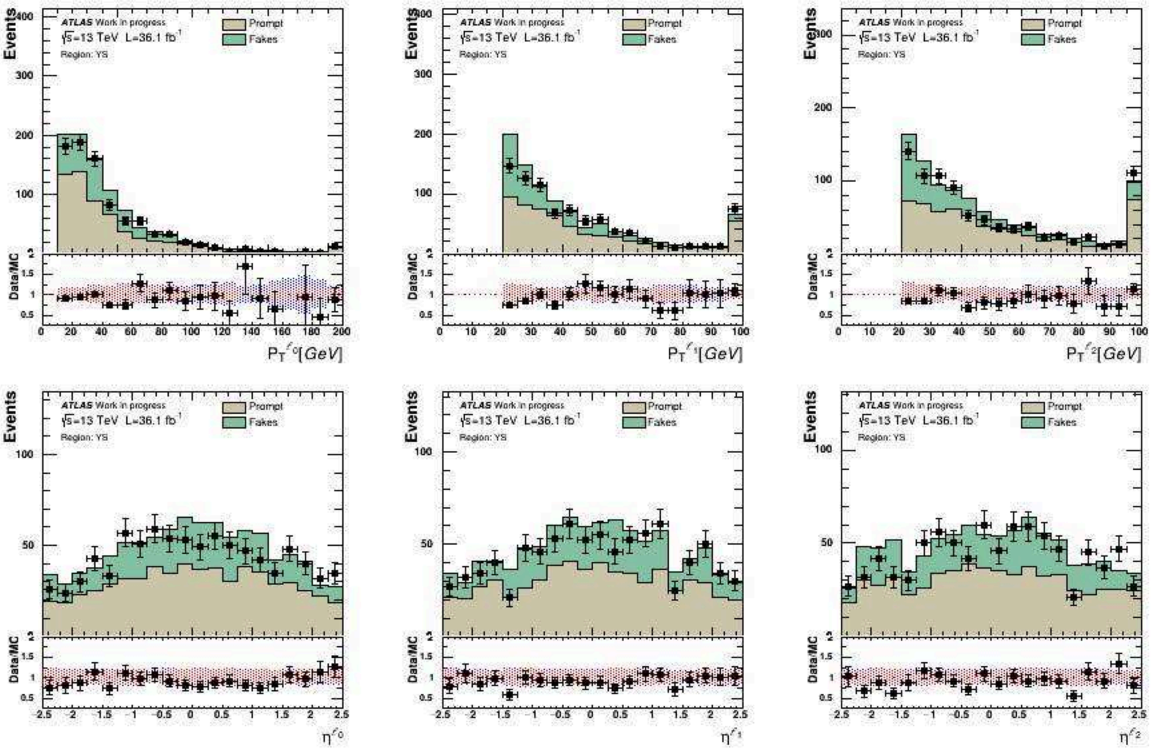

Fig. C.1: Distribution of 3L in the control sample (YS)

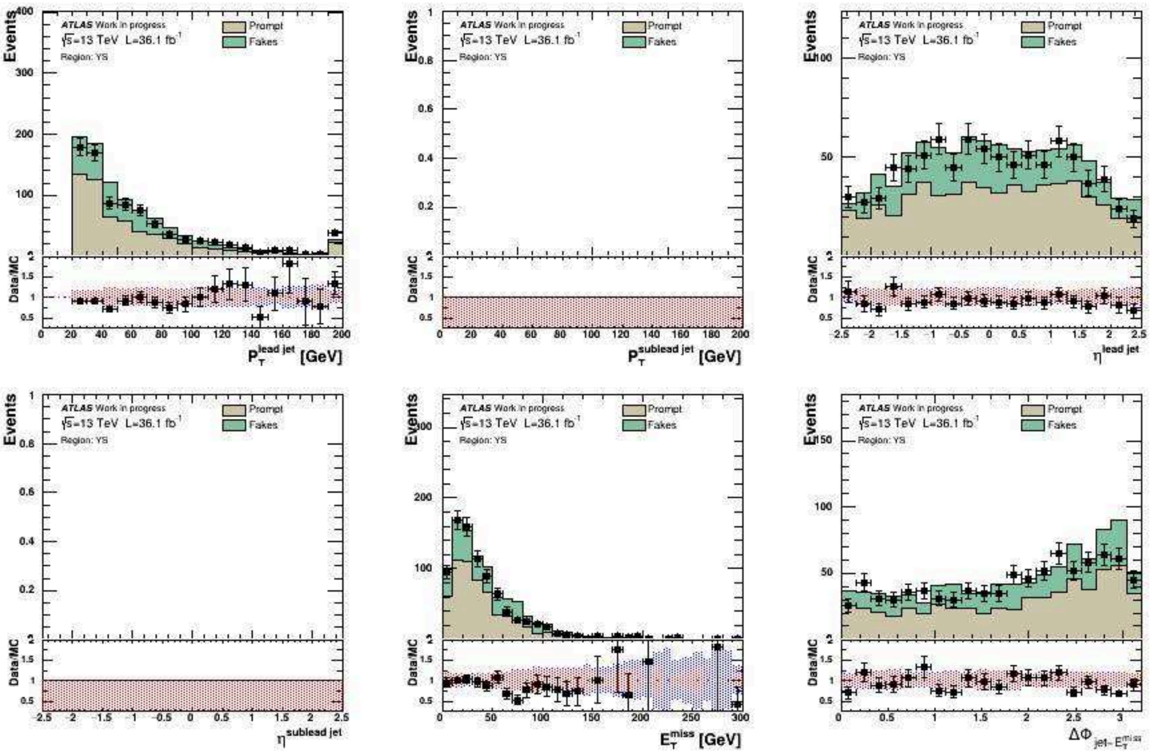

Fig. C.2: Distribution of 3L in the control sample (YS)

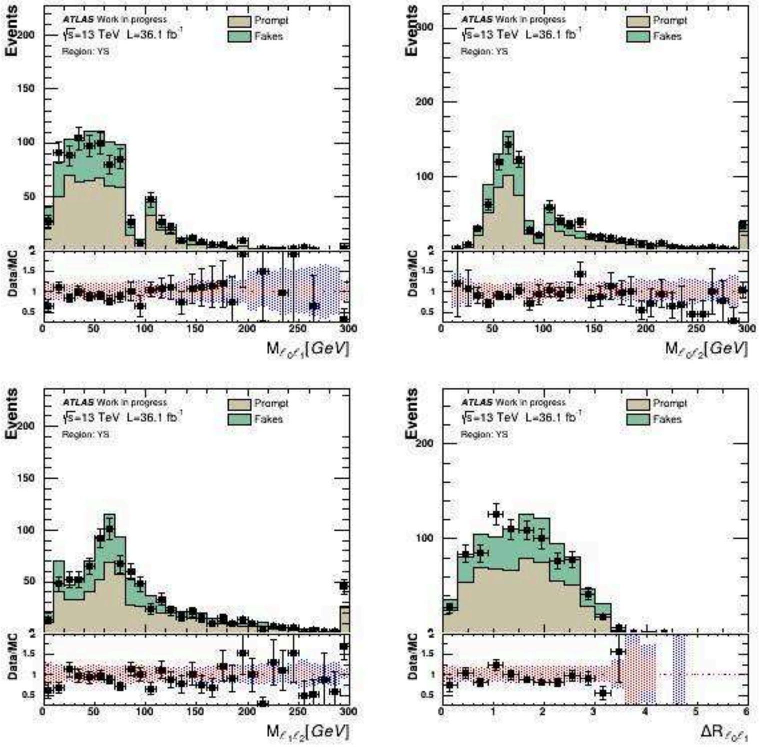

Fig. C.3: Distribution of 3L in the control sample(YS)

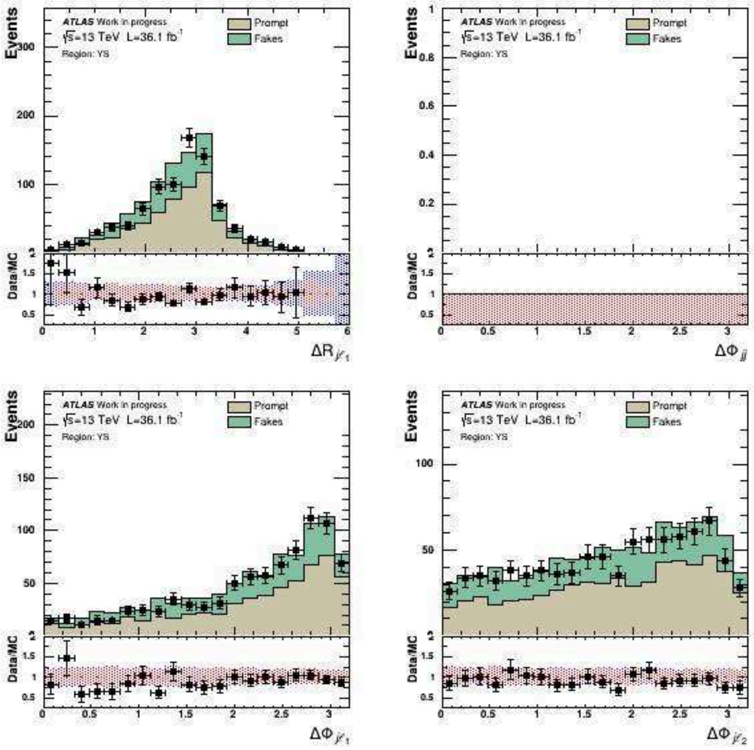

Fig. C.4: Distribution of 3L in the control sample (YS)

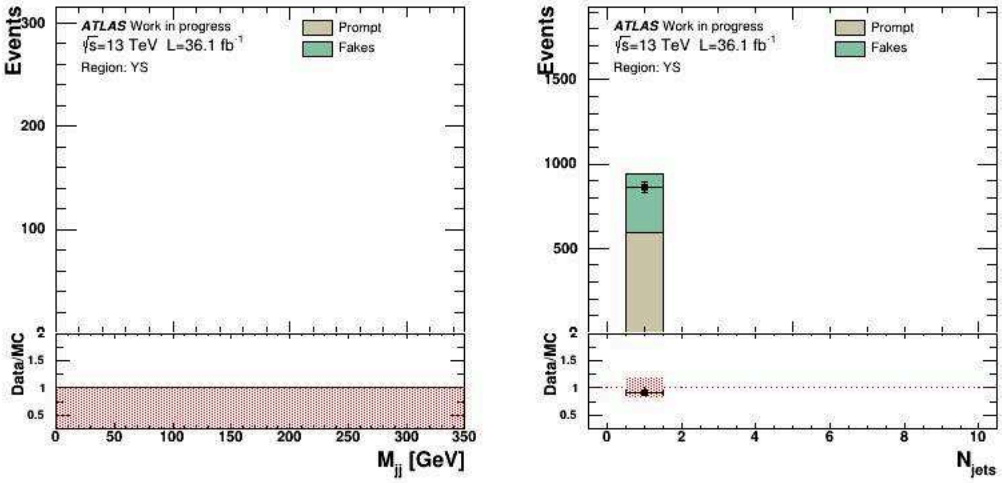

Fig. C.5: Distribution of 3L at event in the control sample(YS)

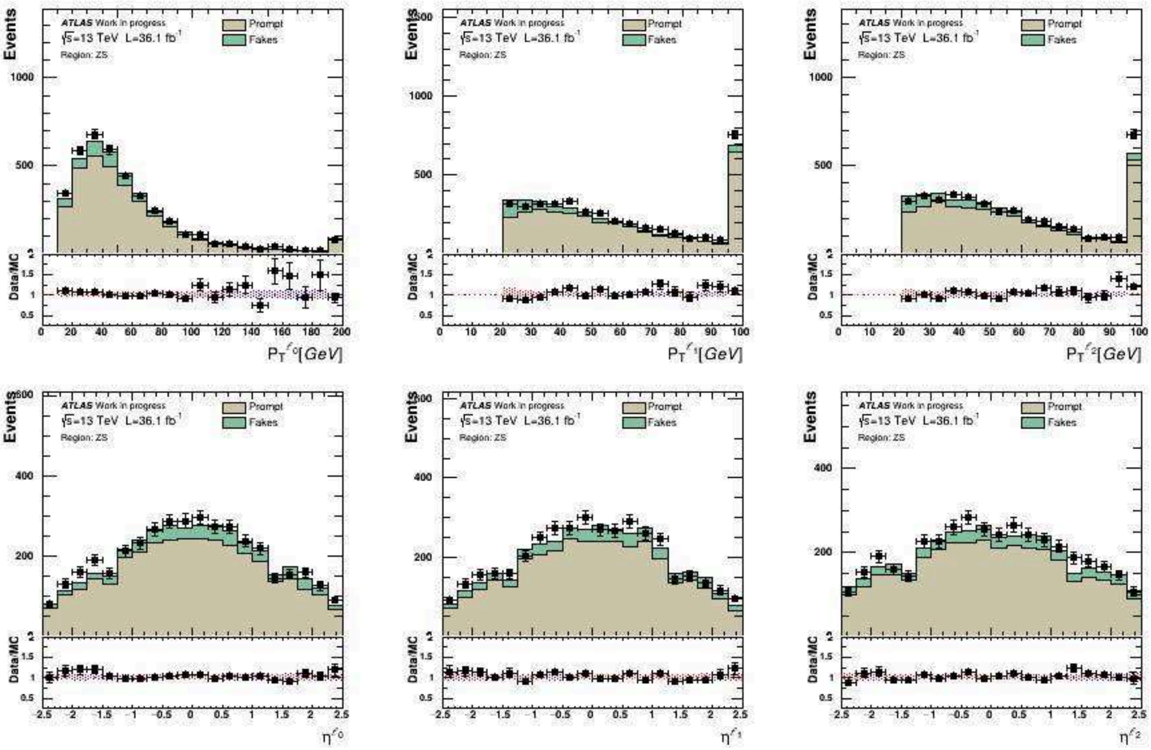

Fig. C.6: Distribution of 3L in the control sample (ZS)

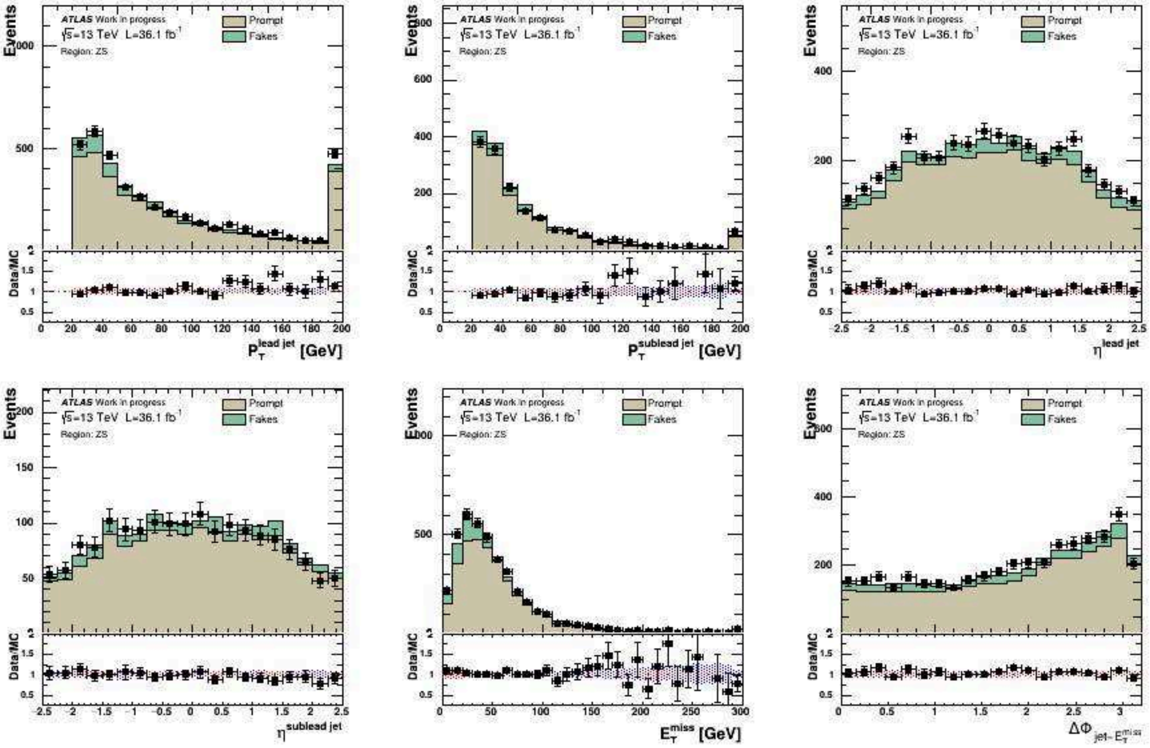

Fig. C.7: Distribution of 3L in the control sample (ZS)

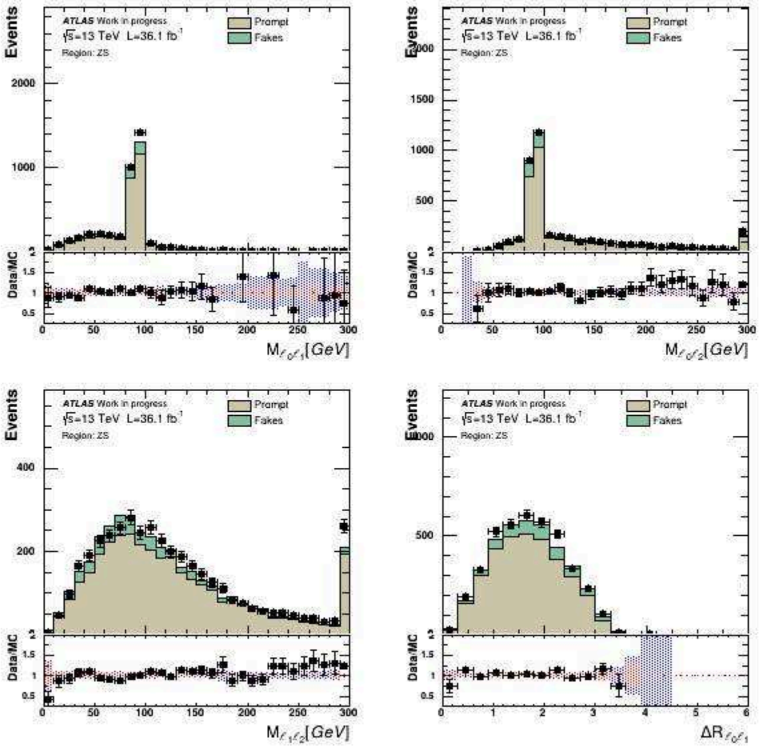

Fig. C.8: Distribution of 3L in the control sample(ZS)

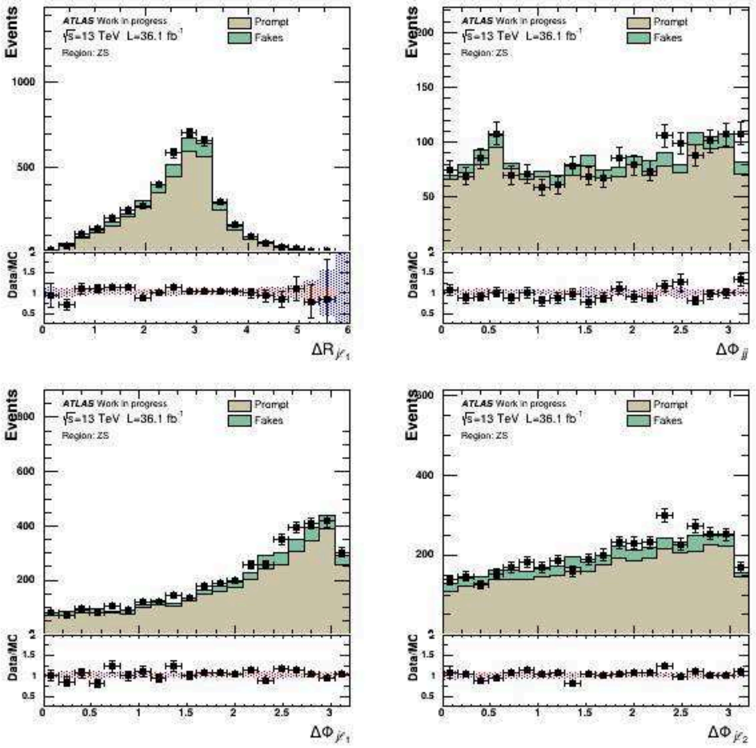

Fig. C.9: Distribution of 3L in the control sample (ZS)

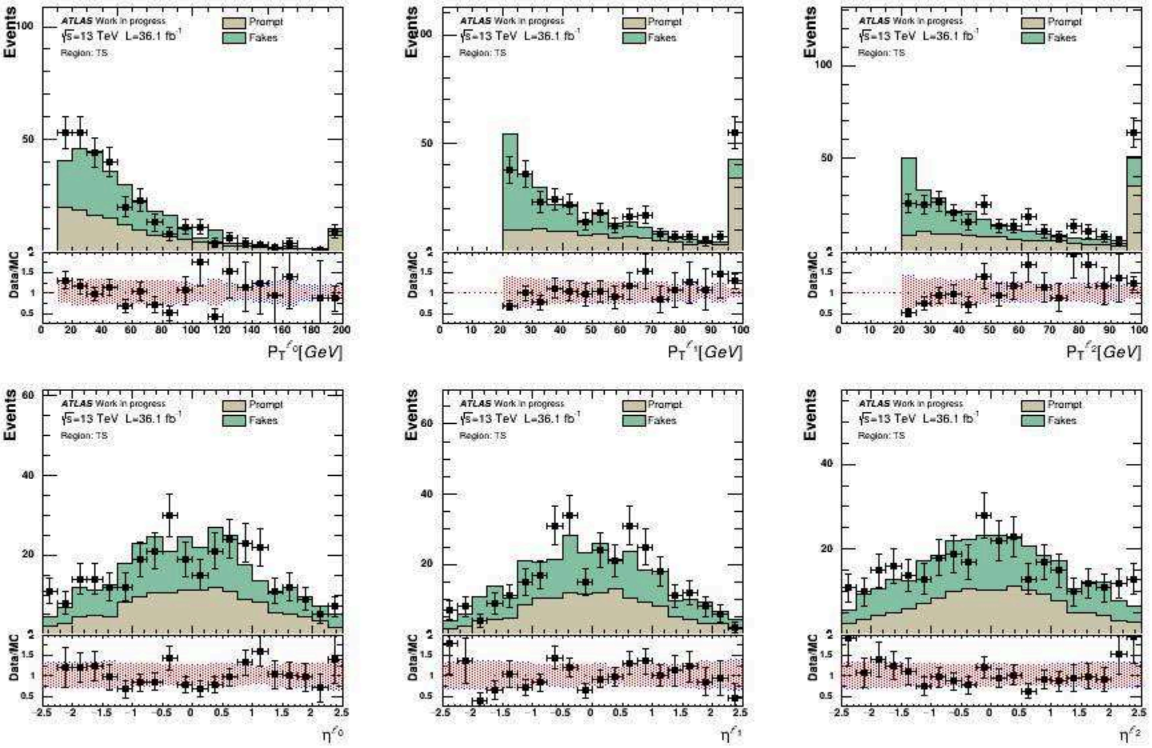

Fig. C.10: Distribution of 3L in the control sample (TS)

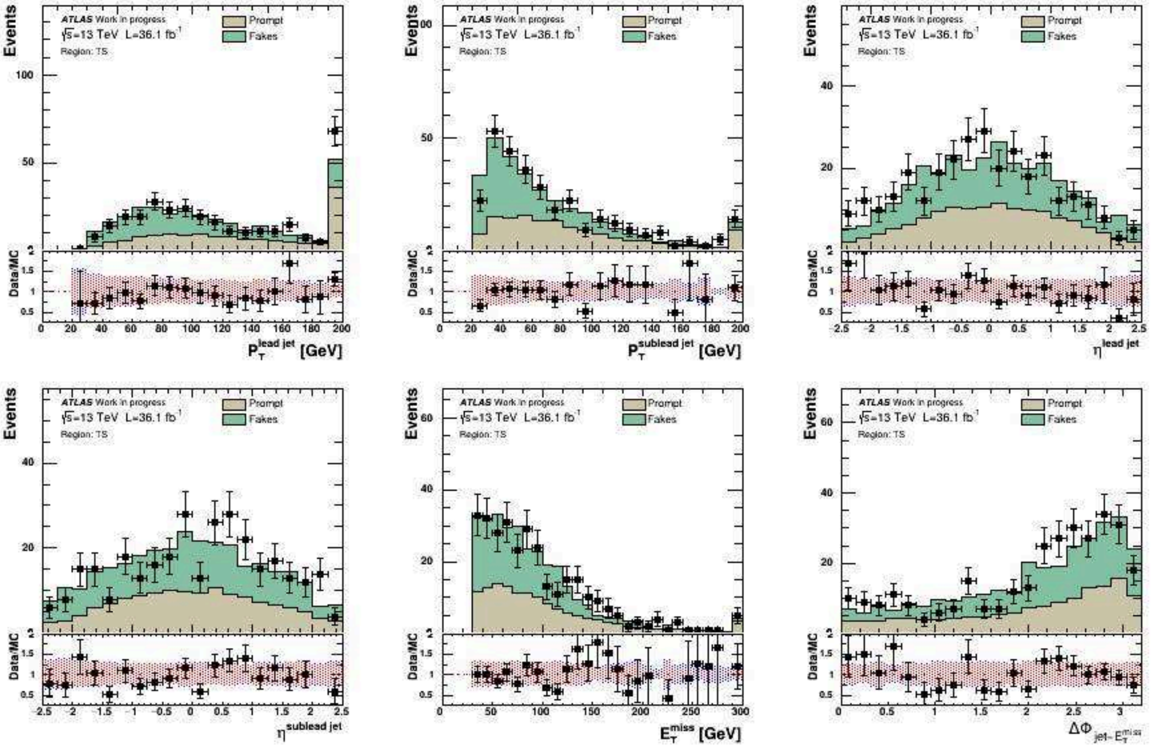

Fig. C.11: Distribution of 3L in the control sample (TS)

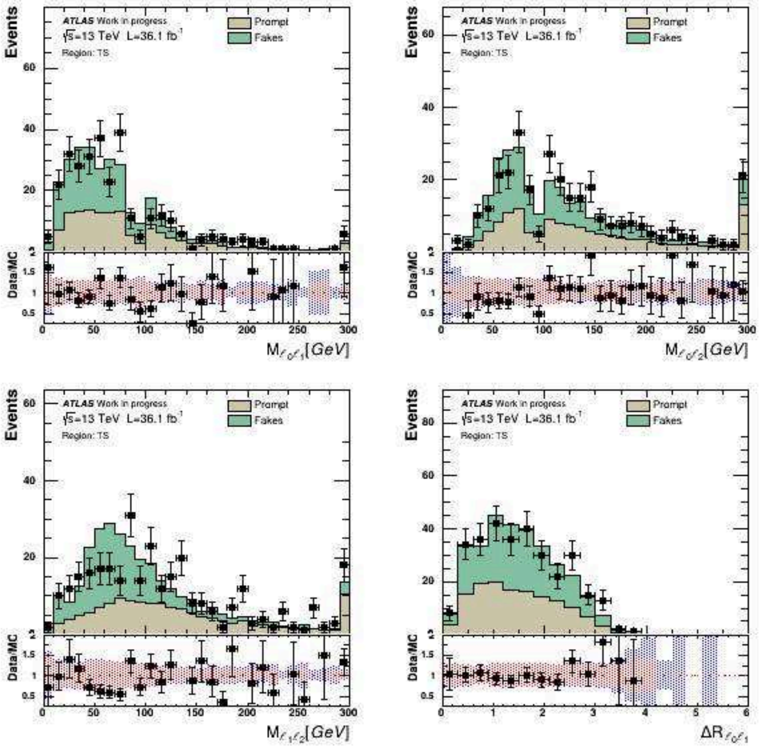

Fig. C.12: Distribution of 3L in the control sample(TS)

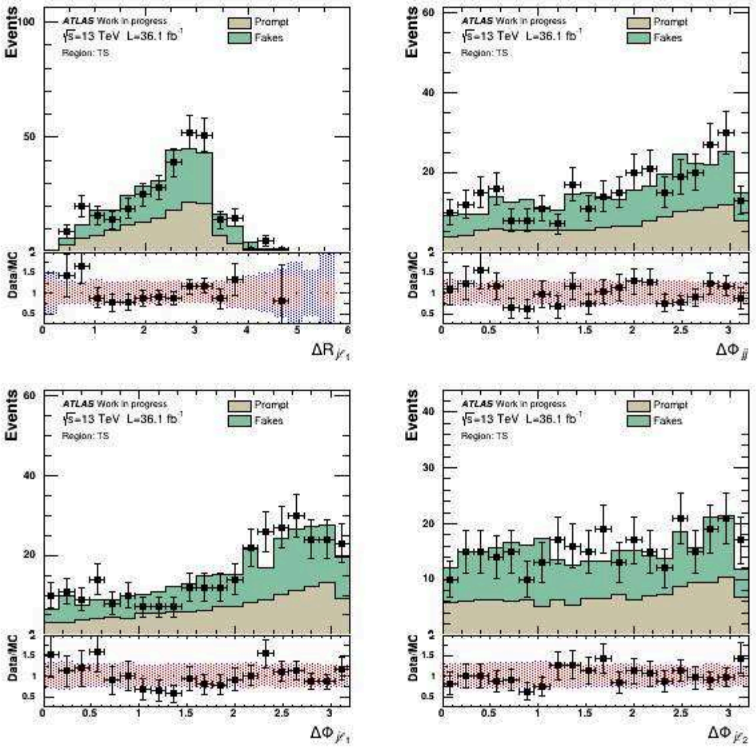

Fig. C.13: Distribution of 3L in the control sample (TS)

C.2.1. Validation of the fake factor method using MC simulation

In order to validate the fake factor method used in Section 5.4.2, the method was used on MC simulations of the backgrounds. All processes with less than three prompt prompt leptons contributed to 'MC Fakes' in the following studies. Table C.3 shows a good agreement between the data-driven fake factors and MC-based fake factors within statistical uncertainty. (also displayed in Figure C.14). The full breakdown of the MC fakes in each control sample is shown in Tables C.4, C.5, C.6 and C.7.

Region	θ_e DD	θ_e MC
Y	0.39 ± 0.07	0.34 ± 0.14
X	0.44 ± 0.15	0.66 ± 0.34
Z	0.41 ± 0.08	0.45 ± 0.17
T	0.39 ± 0.08	0.32 ± 0.03

Region	θ_μ DD	θ_μ MC
Y	0.17 ± 0.06	0.09 ± 0.10
X	0.09 ± 0.08	0.17 ± 0.18
Z	0.36 ± 0.11	0.18 ± 0.2
T	0.19 ± 0.04	0.11 ± 0.11

Table C.3: Comparison between fake factors measured using the data-driven method and fake factors measured using MC simulation. Only statistical errors are shown here.

Channel	MC Fakes		
YF $xe\not e$	324 ± 72.2		
YF $x\mu\not e$	206 ± 30.9		
YF $xe\not\mu$	248 ± 23.6		
YF $x\mu\not\mu$	211 ± 21.4		
Channel	MC Fakes	Estimated Fakes	Estimated in-situ Fakes
YS xee	109 ± 37	109 ± 50.6	
YS $xe\mu$	259 ± 88.7	93 ± 38.5	93 ± 38.5
YS $x\mu\mu$	19.9 ± 4.53	19.9 ± 20.5	
$\theta_e =$	0.34 ± 0.14		
$\theta_m =$	0.09 ± 0.10		

Table C.4: Y samples yields using MC simulation in sub-regions enriched in fakes YF and signal YS. These yields are used to calculate the MC simulation based fake factors as a cross-check. Only statistical errors are shown here.

In order to further check the MC fakes reliability, the data is compared to the prediction obtained by replacing the data-driven fakes estimate by the MC fakes. The distribution of the number of jets is shown in figure C.15. A good overall description is observed, thereby lending confidence to the studies based on MC fakes shown above.

The dominant and sub-dominant contributions in the Y and X regions are shown in Table C.8 and C.9.

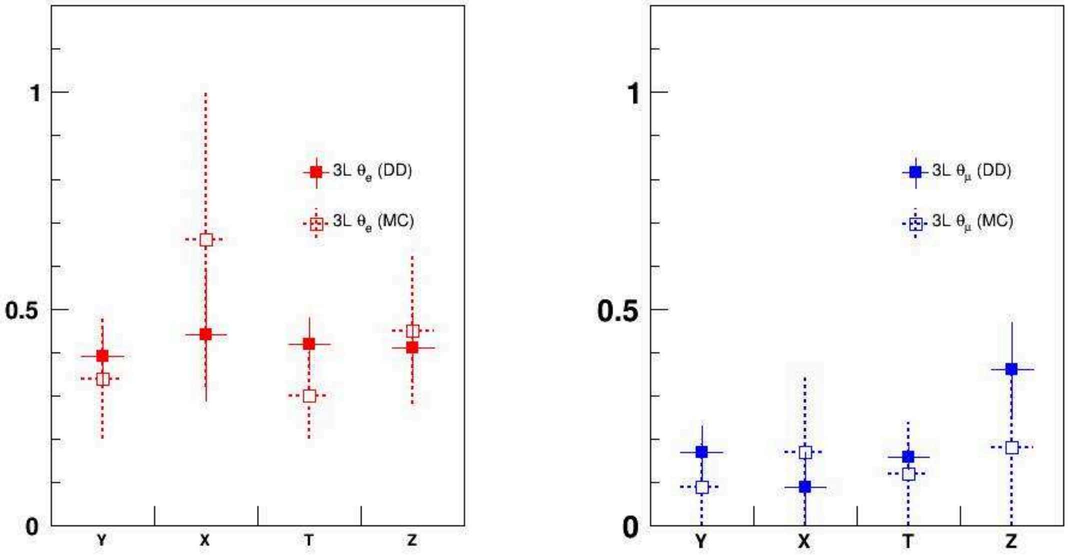

Fig. C.14: Fake factors from MC "fakes" (errors shown as dotted) compared with nominal fake factors (errors shown as full lines) corresponding to Table C.3.

Channel	MC Fakes
XF $xe\not{e}$	64.7 ± 6.67
XF $x\mu\not{e}$	64 ± 8.69
XF $xe\not{\mu}$	91 ± 4.58
XF $x\mu\not{\mu}$	98.7 ± 5.53

Channel	MC Fakes	Estimated Fakes	Estimated in-situ Fakes
XS xee	42.5 ± 21.4	21.9 ± 9.13	
XS $xe\mu$	32.5 ± 5.87	30.2 ± 12.8	57.5 ± 27.7
XS $x\mu\mu$	16.8 ± 5.86	9.3 ± 9.55	
$\theta_e =$	0.66 ± 0.34		
$\theta_m =$	0.17 ± 0.18		

Table C.5: X samples yields using MC simulation in sub-regions enriched in fakes XF and signal XS. These yields are used to calculate the MC simulation based fake factors as a cross-check. Only statistical errors are shown here.

Channel	MC Fakes
TF $xeef$	83 ± 4.89
TF $x\mu\not{e}$	109 ± 4.92
TF $xe\not{\mu}$	145 ± 6.1
TF $x\mu\not{\mu}$	158 ± 5.66

Channel	MC Fakes	Estimated Fakes	Estimated in-situ Fakes
TS xee	26.5 ± 1.9	28 ± 11.5	
TS $xe\mu$	39.1 ± 2.66	50.6 ± 20.6	51.1 ± 16.7
TS $x\mu\mu$	17.6 ± 1.7	14.9 ± 15.3	
$\theta_e =$	0.32 ± 0.03		
$\theta_m =$	0.11 ± 0.11		

Table C.6: T samples yields using MC simulation in subregions enriched in fakes TF and signal TS. These yields are used to calculate the MC simulation based fake factors as a cross-check. Only statistical errors are shown here.

Channel	MC Fakes
ZF $xe\not{e}$	226 ± 62.1
ZF $x\mu\not{e}$	704 ± 168
ZF $xe\not{\mu}$	227 ± 58
ZF $x\mu\not{\mu}$	386 ± 68.1

Channel	MC Fakes	Estimated Fakes	Estimated in-situ Fakes
ZS xee	101 ± 26.8	76.3 ± 37.3	
ZS $xe\mu$	96.2 ± 19.8	259 ± 114	356 ± 149
ZS $x\mu\mu$	70.1 ± 29	36.4 ± 37.9	
$\theta_e =$	0.45 ± 0.17		
$\theta_m =$	0.18 ± 0.19		

Table C.7: Z samples yields using MC simulation in subregions enriched in fakes ZF and signal ZS. These yields are used to calculate the MC simulation based fake factors as a cross-check. Only statistical errors are shown here.

Region	Dominant	Sub-dominant
YS	$t\bar{t}$	Z+jets
YF	$t\bar{t}$	Z+jets
XS	$Z + jets$	$ttH + ttV$
XF	$t\bar{t}$	WZ

Table C.8: The processes contributing to fake background in SFOS0 channel of the X and Y regions. The XS region has very low statistics and the corresponding row is not reliable.

Region	Dominant	Sub-dominant
YS	$t\bar{t}$	Z+jets
YF	Z+jets	$t\bar{t}$
XS	WZ	ttH
XF	Z+jets	$t\bar{t}$

Table C.9: The processes contributing to fake background in SFOS 1,2 channel of the X and Y regions. The X regions contain low statistics for fakes and the corresponding rows are not reliable.

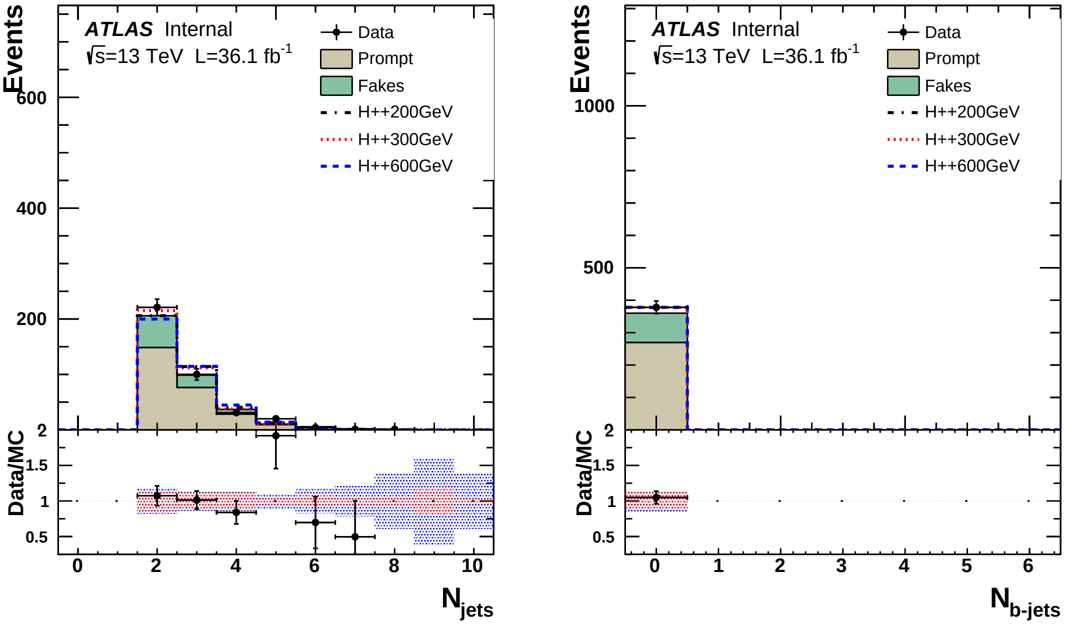

Fig. C.15: The distribution of jet multiplicity for the preselection region (X) in data compared to the prediction where the MC fakes are used instead of data-driven estimate.

C.3. Charge-flip check in the 3ℓ channel

A potential background (from WZ for instance) may occur in the 3ℓ channel if one electron from Z charge-flips and escapes the SFOS mass window veto. This background should appear in the Z boson mass window for the same sign di-electron mass. The di-lepton mass distributions is shown in Figure C.16. A good agreement is observed for both electrons and muons, in particular around the Z boson nominal mass.

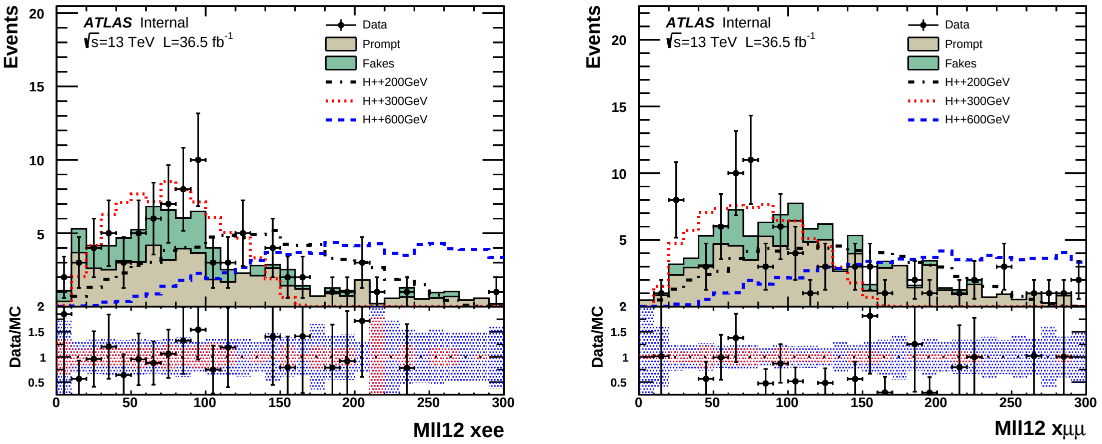

Fig. C.16: The same sign di-leptons (leptons 1 and 2 in the analysis notation) mass distributions for same flavour dileptons: left di-electrons and right di-muons in the XS region.

C.3.1. Comparison between the CutsSA method and other MVA methods

To evaluate the performance of this cut-based procedure, a comparison is made with other MVA methods. A Boosted Decision Tree with a gradient boost (BDTG) and a linear discriminant (LD) are optimized and used for this comparison. The comparison is given in Table C.10. For events with SFOS 0, the performance of the CutsSA method is similar to that of the BDTG method. On the other hand, BDTG performs better than CutsSA for events with SFOS 1,2. But, within statistical errors, they are not very different. The systematic errors make the two methods more compatible. The Linear Discriminant, on the other hand, doesn't perform as well as the other two methods. Therefore, taking into account a better handle on the optimization and final limit extraction procedures, the signal region only uses the CutsSA method.

Selection	Data	SM Background	Signal
SFOS 0			
All input MVA	33	12.74 ± 1.49	4.670 ± 0.065
Tuned Cuts	1	0.27 ± 0.04	1.446 ± 0.035
BDTG method $D > 0.996$ Signal $\simeq$ Cuts Tuned	0	0.35 ± 0.16	1.452 ± 0.035
LD method $D > 0.554$ Signal $\simeq$ Cuts Tuned	0	0.44 ± 0.22	1.446 ± 0.035
SFOS 1,2			
All input MVA	359	259.54 ± 7.68	11.919 ± 0.101
Tuned Cuts	2	1.48 ± 0.41	4.032 ± 0.061
BDTG method $D > 0.993$ Signal $\simeq$ Cuts Tuned	0	0.56 ± 0.20	4.047 ± 0.060
LD method $D > 0.651$ Signal $\simeq$ Cuts Tuned	0	2.49 ± 0.68	4.007 ± 0.060

Table C.10: Various options to select the signal region, using cuts and multivariate discriminants for $M(H^{\pm\pm}) = 200$ GeV. The signal region with a cut on the discriminant (D) value is selected such that the signal rate is approximately the same as the one in the cut-based optimization. The upper half of the table shows the SFOS0 channels, while the lower half shows the channels with SFOS 1,2. The errors shown are only statistical errors.

Abstract

Keywords : LHC, ATLAS, Higgs boson, phenomenology

Le secteur scalaire du Modèle Standard (MS) est l'un des meilleurs candidats pour contenir les nouvelles particules au-delà du Modèle Standard. Les mesures de précision des propriétés du boson de Higgs ainsi que la recherche de nouveaux scalaires est d'une ultime importance. L'ajout d'un triplet de scalaires aux champs du MS dans le contexte des modèles dits "Type 2 Seesaw" explique pourquoi les neutrinos sont massifs tout en prédisant de nouveaux scalaires, parmi lesquels certains ont une masse à l'échelle électrofaible, et donc, seraient détectables au LHC. La montée en énergie et en luminosité du Run 2 du LHC augmente significativement le potentiel de découverte de cette extension du secteur scalaire.

Une variante d'une telle extension est explorée dans cette thèse : le triplet scalaire, Δ, est doté d'une hypercharge $Y = 2$, en complément du doublet scalaire H du MS. Ce secteur scalaire mixte entre doublet et triplet est dirigé par 6 couplages, définissant les multiples interactions entre les champs scalaires respectifs. Les composantes neutres du doublet et du triplet prennent une valeur v_d et v_t (la VEV, ou valeur attendue dans le vide) au minimum du potentiel, causant par la même la brisure de symétrie électrofaible. En particulier, la vev du triplet est contrainte par les mesures de précisions électrofaibles et doit se situer sous l'échelle du GeV. La brisure de symétrie produit une phénoménologie riche, incluant sept scalaires, dont un peut être identifié au boson de Higgs du MS : $H^{\pm\pm}$ et $H^{\pm}$ des bosons de Higgs simplement ou doublement chargés, A^0 un boson de Higgs neutre CP odd et deux autre CP even h^0 et H^0.

La recherche de bosons de Higgs doublement chargés a déjà été réalisée au LHC en utilisant des états finaux plus inclusifs, à savoir le canal dileptonique. Ces analyses ont été ré-interprétées dans le cas où la désintégration en deux bosons est favorisée, affaiblissant ces limites. Il est donc nécessaire de réaliser une analyse dédiée qui exploite la totalité des capacités expérimentales pour explorer ce modèle, notemment en prenant en compte la présence d'énergie transverse manquante et de multi-jets issus de l'état final multibosonique dans l'optimisation de la sélection.

Cette thèse se focalise sur la phénoménologie des bosons scalaires doublement chargés $H^{\pm\pm}$, dans le cas où le couplage aux leptons est défavorisé au profit des bosons vecteurs du MS, c'est à dire dans le canal de désintégration $H^{\pm\pm} \to W^{\pm}W^{\pm}$. Les bosons de Higgs doublement chargés peuvent être produits par paires, ce qui est caractérisé par un état final à quatre bosons W. La recherche de ces particules est réalisée pour six masses du $H^{\pm\pm}$: 200, 300, 400, 500, 600, and 700 GeV. Cette étude est possible dans différents états finaux, comme l'état final à deux leptons de même signe, à trois leptons et quatre leptons. La signature expérimentale étudiée dans cette thèse concerne l'état final avec trois leptons, de l'énergie transverse manquante et deux jets. Les bruits de fond dominants proviennent de processus du MS tels que WZ, ZZ, $Z+$jets et $t\bar{t}$. Les bruits de fonds primaires (ou "prompts") sont estimés à l'aide de simulations Monte Carlo. Mais dans le cas où un jet passe pour un lepton ou si l'origine d'un lepton est une désintégration secondaire (ou "non-prompte"), comme pour les désintégrations semi-leptoniques des b, les simulations ne sont pas suffisantes et il est nécessaire, pour ces bruits, d'utiliser des méthodes d'extraction depuis les données, notemment la méthode dite des "fake factor". Celle-ci n'utilise que les données et les simulations de processus primaires qui sont correctement décrits.

Lorsque le bruit de fond est bien décrit, un ensemble de coupures de sélection est appliqué pour supprimer une fraction significative de processus caractéristiques. Par exemple, un veto sur le nombre de b-jets supprime les événements du type $t\bar{t}$ car le quark top se désintègre en un boson W et un quark

b. Malgré ces coupures, la sensibilité de l'analyse est faible, ce qui requiert une étape supplémentaire de discrimination entre le signal et le bruit de fond. Ceci est obtenu en identifiant cinq variables discriminantes. Il s'agit de la séparation angulaire entre les leptons de même charge, entre le jet de plus haut p_T et le troisième lepton (celui qui a un signe opposé aux deux autres), l'énergie transverse manquante, l'impulsion transverse du jet de plus haut p_T et la masse invariante des trois leptons. Ces variables sont illustrées Figure C.17.

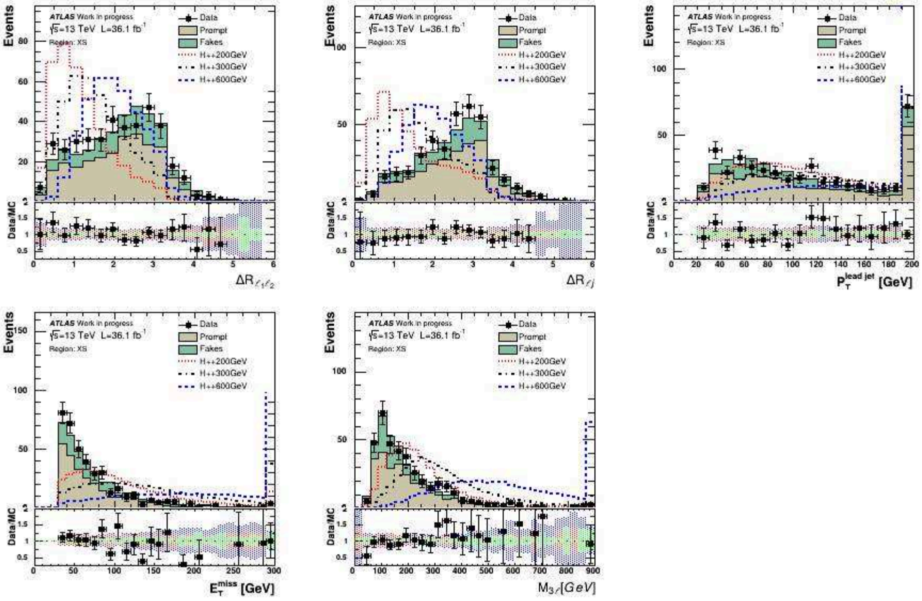

Fig. C.17: Variables discriminantes utilisées dans l'analyse trileptonique.

A l'aide de ces variables, la sensibilité de l'analyse augmente considérablement. Pour parachever le tout, les trois canaux leptoniques mentionnés plus haut sont combinés pour cette recherche de boson de Higgs doublement chargés. L'interprétation statistique des résultats donne une limite inférieure en masse de 220 GeV, comme montrée Figure ??. Il s'agit de la première recherche de particules de ce modèle dans cet espace de paramètres auprès des collisionneurs.

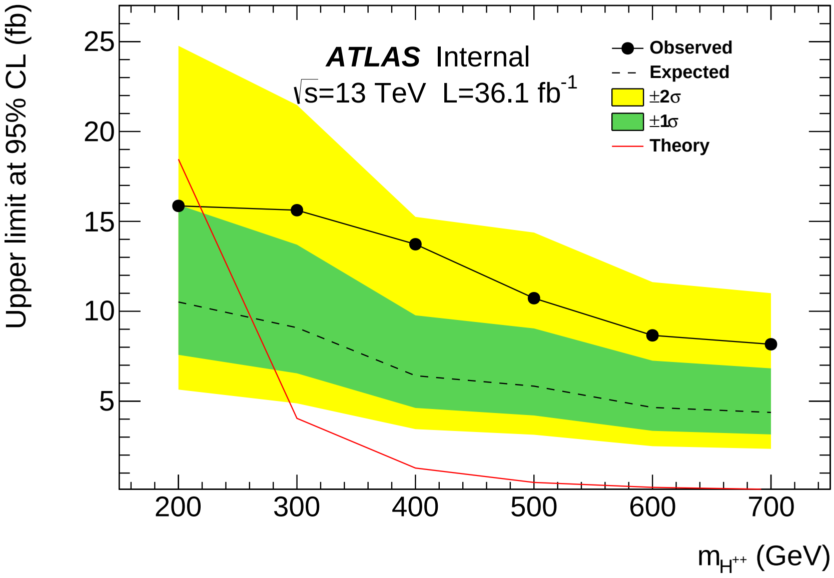

Fig. C.18: Limites attendues et observées pour les canaux $2\ell^{ss}$, 3ℓ and 4ℓ combinés.